Synthesis and characterisation of homometallic and heterometallic Co(II)/*4f* complexes: investigation of magnetic properties

Alexandra Foteini Tsampika Collet

M.Sc.

Submitted in fulfilment of the requirements for the Degree of Doctor of Philosophy

School of Chemistry

College of Science and Engineering

University of Glasgow

August 2019

Abstract

The work presented in this thesis describes the directed synthesis, structural and magnetic characterisation of new Co(II), Co(II)-4*f* and 4*f* complexes, using a range of polydentate ligands. The aim of this work was to synthesise new Co(II)-based complexes, in the presence or absence of 4*f* ions, where the cobalt centre would adopt different coordination numbers and geometries, in an attempt to tune the magnetic properties. We managed to isolate twenty new complexes and depending on the ligand employed they can be categorised in five groups.

Complexes $[Co^{II}(H_2bic)Cl]$ (**1**), $[Co^{II}_9(Hbic)_4(bic)_2Cl_4]$ (**2**) and $[Co^{II}_9(Hbic)_4(bic)_2Cl_4]\cdot 12H_2O$ (**2**$\cdot 12H_2O$) were synthesised using the ligand bicine (= H_3bic, *N,N*-Bis(2-hydroxyethyl)glycine) by employing solvothermal and microwave−assisted synthesis. Complexes **1**, **2** and **2**$\cdot 12H_2O$ were magnetically characterised and only **2** shows the onset of out-of-phase ac signals at low temperature. The second family consists of three Co(II)/Co(III) complexes with the same triangular motif and with the Co(II) in a trigonal bipyramidal geometry: $[Co^{II}Co^{III}_2(\mu_3\text{-OH})(\mu\text{-pz})_4(DBM)_3]\cdot 2THF$ (**3**$\cdot$2THF), $[Co^{II}Co^{III}_2(\mu_3\text{-OH})(\mu\text{-pz})_4(DBM)_3]\cdot 2MeCN$ (**4**$\cdot$2MeCN) and $[Co^{II}Co^{III}_2(\mu_3\text{-OH})(\mu\text{-pz})_4(acac)_3]$ (**5**), where Hpz = pyrazole, HDBM = dibenzoylmethane and Hacac = acetylacetone. Magneto-structural analysis showed that complexes **3**$\cdot$2THF and **4** show field-induced slow magnetic relaxation, while **5** shows only the onset of the out-of-phase signals at low temperature. The third group consists of polynuclear Co(II)-based complexes incorporating substituted phosphonate ligands along with dimethylpyrazole (= Hdmpz), exhibiting nuclearities from two to nine metal centres. These complexes are: $[Co^{II}_9(t\text{BuPO}_3)_3(dmpz)_{12}(Hdmpz)_6]\cdot x\text{MeCN}\cdot y\text{H}_2\text{O}$ (**6**$\cdot x$MeCN$\cdot y$H$_2$O), $[Co^{II}_3(t\text{BuPO}_3)_2(Hdmpz)_4Br_2]$ (**7**), $[Co^{II}_8(\text{EtPO}_3)_3(dmpz)_{10}(Hdmpz)_6]\cdot x\text{MeCN}\cdot y\text{H}_2\text{O}$ (**8**(MeCN)), $[HNEt_3][Co^{II}_8(\text{EtPO}_3)_3(dmpz)_{10}(Hdmpz)_6][ClO_4]\cdot x\text{DCM}\cdot y\text{H}_2\text{O}$ (**9a**(DCM)), $[HNEt_3][Co^{II}_8(\text{EtPO}_3)_3(dmpz)_{10}(Hdmpz)_6][ClO_4]\cdot 0.75(Hdmpz)\cdot 2.25\text{DCE}\cdot\text{H}_2\text{O}$ (**9b**(DCE)), $[Co^{II}_3(dmpz)_4(Hdmpz)_2Cl_2]$ (**10**), $[HNEt_3][Co^{II}_6(\text{PhPO}_3)_3(dmpz)_6(Hdmpz)_6][ClO_4]\cdot$DCM (**11**$\cdot$DCM) and $[HNEt_4]_2[Co^{II}_2(dmpz)_2Cl_4]$ (**12**), where $t\text{BuPO}_3\text{H}_2$ = *tert*-butylphosphonic acid, EtPO_3H_2 = ethylphosphonic acid and PhPO_3H_2 = phenylphosphonic acid. Complexes **6** and **7** were magnetically characterised and ac magnetic studies showed only the onset of out-of-phase ac signals for **6**, whereas complex **7** does not display slow magnetic relaxation. The next group is a family of six-coordinate mononuclear Ln^{III} complexes which was obtained by utilising the ligand tricyclohexylphosphine oxide (= Cy_3PO), with molecular formula $[Ln^{III}(Cy_3PO)_2Cl_3(EtOH)]\cdot y\text{EtOH}$, where Ln^{III} = Tb (**13**), Dy (**14**), Ho (**15**), Er (**16**) and Y (**17**), and y = 0.5 for **14** and y = 1 for **13**, **15−17**. Magnetic studies for complexes Tb (**13**), Dy (**14**) and Ho (**15**) revealed that only Dy (**14**) displays field-induced slow magnetic relaxation. The last family of complexes incorporates the ligand 2,6-bis[4(1-*N*-phenyl-3-methyl-pyrazolium-5-one)carbonyl]pyridinium trichloride (= $[H_5L]\cdot 3Cl$) leading

to a variety of 4*f* and Co(II)-4*f* complexes with nuclearities from one to nine metal centres. These complexes are $[La^{III}_9(L^{2-})_7(NO_3)_4(CO_3)_4(OH)(H_2O)_8]\cdot xMeCN\cdot yH_2O$ (**18**·xMeCN·yH_2O), $[HNEt_3][Ce^{III}_3(HL^{-})_2(NO_3)_7(H_2O)_2][Cl]\cdot xMeCN\cdot yH_2O\cdot zEt_2O$ (**19a**) and $[HNEt_3][Ce^{III}_3(HL^{2-})(H_2L)(NO_3)_7(H_2O)_2][Cl]\cdot xMeCN\cdot yH_2O\cdot zEt_2O$ (**19b**), $[Dy^{III}(HL^{-})_2(H_2O)_4][Cl]\cdot xMeCN\cdot yH_2O$ (**20**·xMeCN·yH_2O), $[Co^{II}_2Ln^{III}(L^{2-})_2(NO_3)_{2.3}Cl_{0.7}(MeCN)]$ where Ln = La (**21**) and Ce (**22**), $[HNEt_3][Co^{II}Dy^{III}_2(L^{2-})_4(HL^{-})(H_2O)_2]\cdot xMeCN\cdot yH_2O$ (**23**·xMeCN·yH_2O) and $[Gd^{III}_6(L^{2-})_4(OH)_4(O^{2-})(MeOH)_6(H_2O)_2][NO_3]_{3.75}[Cl]_{0.25}\cdot xMeOH\cdot yH_2O$ (**24**·xMeOH·yH_2O). Magnetic studies were carried out only for the Co(II)-4*f* complexes, with complex **23** exhibiting field-induced slow magnetic relaxation.

Contents

Acknowledgements

Firstly, I would like to thank my supervisor Prof. Mark Murrie for giving me the opportunity to do my PhD in his group. Thank you Mark for all the advice and guidance during my PhD, and for being so kind and patient with me, especially during the last months of my thesis writing (and all the extended deadlines!). Also, I still believe that Chewie should be the official mascot of the group and be in the group photo! I would also like to thank my second supervisor Dr Mark Symes for all the helpful feedback on my work, and of course the University of Glasgow for the funding.

Thanks to all the past and present members of the Murrie group: Gavin, Maria-Jose, Moya, Angelos, Emma and Lucy! Gavin, MJ and Moya, thank you for welcoming me to the group and for all the good times we shared together − usually in a pub with drinks! MJ, volia respondre amb una frase en català: gràcies per totes les nostres converses prenent una tassa de te i pastís. Emma and Lucy your calming and encouraging words during the writing of my thesis helped a lot, and I feel lucky to have met you during my PhD! Thank you also to my project students Sarah-Jane and Kate, I really enjoyed working with you.

I would like to thank our collaborator Prof. Stephen Hill for the high-field/frequency EPR measurements. Thanks also to the Gregory group, especially Davide and Hallam, for all the help with the preparation of the air-sensitive samples in their glove-box. Also, thanks to Angelos for helping with the preparation of the air-sensitive holder for the magnetic measurements. Thanks to all the technicians and staff in the Chemistry department, especially Claire for all the training and support with crystallography (you were always patient and willing to help!) and Jim for the EDX measurements, the maintenance of the SQUID and of course all our talks during the He fills! I would also like to mention Stuart for the help with all the pc and laptop crises (we are lucky to have you next door!), and Karen, you are one of the friendliest people in the department and always willing to help!

A special mention to my master thesis supervisor, Prof. Constantinos Milios in the Chemistry department at the University of Crete. Thank you for encouraging me to continue my studies by doing a PhD!

Thanks to all my friends back home (the E.P.A group). Especially Mariza and Dimitra, you were there for me during all the happy, sad, difficult, frustrating or exciting moments! I am very lucky to have you in my life. Thanks to my partner Angelos, you have always inspired me with your passion for chemistry; thanks for always being there for me.

Last but not least, I would like to thank all my family back home, especially my mother Eirini Potsaki, my father Jean-Louis Collet and my brothers Fotis, David and Mathieu. Mum and Dad, I would have not been able to do this PhD without you. Thank you for your constant love, support and encouragement.

Author’s declaration

I certify that the thesis presented here for examination for a PhD degree of the University of Glasgow is solely my own work other than where I have clearly indicated that it is the work of others and that the thesis has not been edited by a third party beyond what is permitted by the University’s PGR Code of Practice.

I declare that the thesis does not include work forming part of a thesis presented successfully for another degree.

I declare that this thesis has been produced in accordance with the University of Glasgow’s Code of Good Practice in Research. I acknowledge that if any issues are raised regarding good research practice based on review of the thesis, the examination may be postponed pending the outcome of any investigation of the issues.

Publication list

Chapter 3:

Microwave-assisted synthesis: from a mononuclear {Co^{II}} complex to {Co^{II}_9} solvomorphs. **A. Collet**, C. Wilson and M. Murrie, *Dalton Transactions*, 2019, **48**, 854-858.

Chapter 4:

Slow magnetic relaxation in a {$Co^{II}Co^{III}_2$} complex containing a high magnetic anisotropy trigonal bipyramidal Co^{II} centre. **A. Collet**, G. A. Craig, M. J. Heras Ojea, L. Bhaskaran, C. Wilson, S. Hill and M. Murrie, *Dalton Transactions*, 2018, **47**, 9237-9240.

Chapter 5:

Tuning the nuclearity using phosphonate ligands in the {Co^{II}_3}, {Co^{II}_6} and {Co^{II}_9} cyclic complexes: investigation of magnetic properties. **A. Collet**, C. Wilson and M. Murrie, *for submission*.

Others:

Constructing Cr^{III}-centered heterometallic complexes: [$Ni^{II}_6Cr^{III}$] and [$Co^{II}_6Cr^{III}$] wheels. F. E. Kakaroni, **A. Collet**, E. Sakellari, D. I. Tzimopoulos, M. Siczek, T. Lis, M. Murrie and C. J. Milios, *Dalton Transactions*, 2018, **47**, 58-61.

α-Amino acids: Natural and artificial building blocks for discrete polymetallic clusters. A. B. Canaj, F. E. Kakaroni, **A. Collet** and C. J. Milios, *Polyhedron*, 2018, **151**, 1-32.

Abbreviations and symbols

$[H_5L]\cdot 3Cl$	2,6-bis[4(1-*N*-phenyl-3-methyl-pyrazolium-5-one)carbonyl]pyridinium trichloride
ac	Alternating current
BVS	Bond Valence Sum
CSD	Cambridge Structural Database
CShMs	Continuous shape measures
Cy_3PO	Tricyclohexylphosphine oxide
D	Axial zero field splitting parameter
dc	Direct current
DCE	1,2-Dichloroethane
DCM	Dichloromethane
E	Rhombic zero field splitting parameter
EDX	Electron dispersive X-ray
EPR	Electron paramagnetic resonance
Et_2O	Diethyl ether
EtOH	Ethanol
$EtPO_3H_2$	Ethylphosphonic acid
g	Landé tensor (or *g*-factor)
H	Magnetic field
H_3bic (bicine)	*N,N*-Bis(2-hydroxyethyl)glycine
Hacac	Acetylacetone
HDBM	Dibenzoylmethane
Hdmpz	dimethylpyrazole
Hpz	Pyrazole
J	Magnetic exchange interaction
JT	Jahn−Teller
k_B	Boltzmann constant
M	Magnetisation
MeCN	Acetonitrile
MeOH	Methanol

NEt_3	Triethylamine
$NMe_4OH·5H_2O$	Tetramethylammonium hydroxide pentahydrate
O_h	Octahedral
PBP	Pentagonal bypiramidal
$PhPO_3H_2$	phenylphosphonic acid
PXRD	Powder X-ray diffraction
QTM	Quantum tunnelling of the magnetisation
SCXRD	Single-crystal X-ray diffraction
SIM	Single-Ion Magnet
SMM	Single-Molecule Magnet
SPY	Square pyramidal
SQUID	Superconducting Quantum Interference Device
T	Temperature
T_B	Blocking temperature
TBP	Trigonal bipyramidal
t$BuPO_3H_2$	*tert*-butylphosphonic acid
THF	Tetrahydrofurane
TIP	Temperature independent paramagnetic
ZFS	Zero−Field Splitting
zj	Intermolecular magnetic interaction
χ'	Real component of the ac magnetic susceptibility
χ''	Imaginary component of the ac magnetic susceptibility
χ_M	Molar magnetic susceptibility

Chapter 1

Introduction

Contents

1. Introduction

Polynuclear transition-metal and/or lanthanide compounds have always attracted much attention due to the wide range of properties that they could display. Biochemistry[1, 2], catalysis[3-5], molecular magnetism[6], magnetic refrigerants[7, 8] and MRI contrast agents[9], are some of the many fields where such complexes could find usage. Hence, the development of optimised molecule-based materials for future applications in these scientific areas grows continuously.

More specifically, within the field of molecular magnetism a class of compounds, known as single-molecule magnets (SMMs), display some interesting properties with potential applications in high-density data storage, spintronic devices and quantum computing.[10-12] SMMs show magnetic behaviour similar to conventional bulk magnets, but of molecular origin. Such molecules display slow relaxation of the magnetisation in the absence of an external magnetic field at low temperatures. The slow magnetic relaxation occurs due to the presence of an energy barrier preventing the spin reversal, and therefore magnetic hysteresis can be observed. In the sections that follow, some fundamental aspects of molecular magnetism, features and characterisation of SMMs and single-ion magnets (SIMs, where the magnetic behaviour originates from a single ion) will be discussed. In addition, some representative recent SMM and SIM examples will be presented.

1.1 Basic concepts of molecular magnetism

At the macroscopic level when a current circulates round a loop of wire, then a magnetic moment is generated with magnitude equal to the area of the loop times the magnitude of the current; this is the principle of an electromagnet.[13] In the microscopic world, the electrons can be considered to produce a magnetic moment as the result of two types of motion (spin and orbit), which give rise to spin angular momentum (*S*) and orbital angular momentum (*L*). Considering an isolated atom, a total angular momentum, *J*, results from the combination of *S* and *L*.[13] If a material or substance does not contain any unpaired electrons, then it is defined as diamagnetic, whereas if it contains unpaired electrons then it is defined as paramagnetic. When a diamagnetic material is placed in a magnetic field, it will be repelled by the field and so its induced magnetic moment will be negative; when a paramagnetic material is placed in a magnetic field, it will be attracted to the field and so its induced magnetic moment will be positive. Note that even if the material is paramagnetic, it will still have some paired electrons and therefore will display a diamagnetic contribution.[13]

The magnetic susceptibility, χ, is the quantitative measure of the response of a material to an applied (*i.e.* external) magnetic field. The magnetic susceptibility is defined as:

$$\chi = \frac{dM}{d\mathrm{H}} \qquad (1.1)$$

where *M* is the magnetisation (magnetic moment per unit of volume) and H is the magnetic field strength. Note that when the magnetic field is weak then χ is independent of the H and the equation is written as: $\chi = \frac{M}{\mathrm{H}}$. χ is dimensionless, but is expressed as emu/cm^3. By multiplying χ with the molar volume, *v* (in cm^3/mol), we obtain the molar susceptibility χ_M. The magnetic susceptibility comprises the diamagnetic (χ^D) and paramagnetic (χ^P) susceptibilities.[14]

$$\chi = \chi^D + \chi^P \qquad (1.2)$$

χ^D does not depend on field strength and is temperature independent. The experimental χ is corrected by the diamagnetic correction in order to obtain the actual χ^P. The diamagnetic correction is generally much smaller than the paramagnetic susceptibility and can be calculated with the application of Pascal's constants. However, a rough order of magnitude can be estimated as −(molecular weight/2)x10^{-6} cm^3 mol^{-1}.[13, 15]

Consider a free isotropic ion (where $L = 0$) with a spin *S*, and 2*S*+1 degenerate sublevels with quantum number m_s. The application of an external magnetic field (Zeeman perturbation) will lift the degeneracy of the m_s states, with an energy $E = m_s g \mu_B \mathrm{H}$ (Fig. 1.1) of each state.[14]

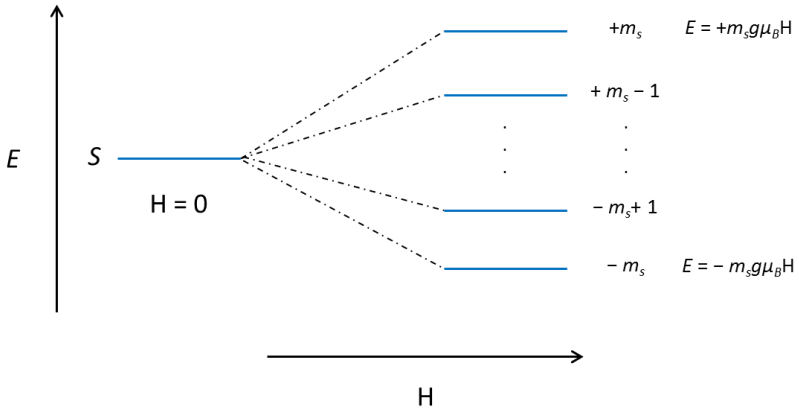

Figure 1.1 Diagram of the splitting of the m_s states with a spin *S* due to the Zeeman effect. Figure adapted from reference 14.[14]

The Curie law

In a paramagnetic sample there will be a number of individual magnetic moments arising from the individual molecules in the sample. The total magnetisation resulting from the sum of each individual magnetic moment is expressed as:

$$M = \frac{N\sum_n \frac{dE_n}{dH}\exp(-E_n/k_BT)}{\sum_n \exp(-E_n/k_BT)} \qquad (1.3)$$

where *N* is Avogadro's number, *n* is the energy level with energy E_n, k_B is the Boltzmann constant, T is the absolute temperature and H the applied magnetic field.[13] Van Vleck proposed a few approximations in order to simplify eqn 1.3 in order to avoid the need for the calculation of the E_n energies. The first of these approximations is to expand the energies E_n according to the increasing powers of H[15]:

$$E_n = E_n^{(0)} + E_n^{(1)}H + E_n^{(2)}H^2 + \cdots$$

where $E_n^{(0)}$ is the energy of level n in zero field, while $E_n^{(1)}$ and $E_n^{(2)}$ are the first- and second order Zeeman coefficients, respectively. Therefore, eqn 1.3 is written as[15]:

$$\chi = \frac{N\sum_n [\frac{(E_n^{(1)})^2}{k_BT} - 2E_n^{(2)}]\exp(-E_n^{(0)}/k_BT)}{\sum_n \exp(-E_n^{(0)}/k_BT)} \qquad (1.4)$$

Further approximations of this equation lead to the Curie law[15], with the Currie constant *C*:

$$\chi = \frac{Ng^2\mu_B^2}{3k_BT}S(S+1) \quad \text{or} \quad \chi = \frac{C}{T} \qquad (1.5)$$

N is Avogadro's number, μ_B is the Bohr magneton, *g* is the gyromagnetic ratio, T is absolute temperature, k_B is the Boltzmann constant, and *S* is the spin ground state.[15] All paramagnets should obey the Curie law, displaying a plot of χT *versus* T as shown in Figure 1.2 (left). However, it has been experimentally observed that there are deviations from this behaviour and the reason is twofold. Firstly, the Curie law does not take into account the interaction between the spins, and secondly the presence of an orbital angular momentum can contribute to the magnetic moment and introduce magnetic anisotropy.[13] In order to account for the interaction between the spins, a parameter θ is introduced in equation 1.5, known as the Curie−Weiss law:

$$\chi = \frac{C}{T-\theta} \qquad (1.6)$$

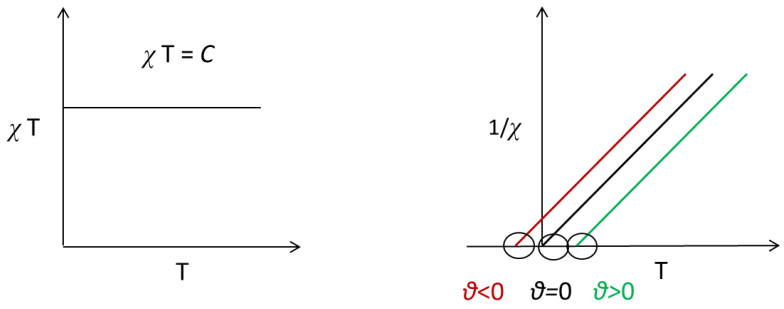

Figure 1.2 *Left)* The χT vs. T plot for a paramagnet. *Right)* The 1/χ vs. T plots for a paramagnet (black), a ferromagnet (green) and an antiferromagnet (red). Figure adapted from reference 13.[13]

When the neighbouring spins exhibit ferromagnetic coupling, *i.e.* parallel alignment of the spins (Fig. 1.3b) then θ is positive; whereas when the neighbouring spins exhibit antiferromagnetic coupling, *i.e.* antiparallel alignment of the spins (Fig. 1.3c) then θ is negative. The antiferromagnetic interaction between unequal spins leads to ferrimagnetic behaviour (Fig. 1.3d).[13] In many materials, the above-mentioned interactions occur at sufficiently low temperatures, whereas at higher temperatures, due to the thermal energy, the spins will not interact and will follow a paramagnetic behaviour (Fig. 1.3a).[13] The temperature below which ferromagnetic behaviour is observed is known as the Curie temperature, while the temperature below which antiferromagnetic behaviour is observed is known as the Néel temperature.[16]

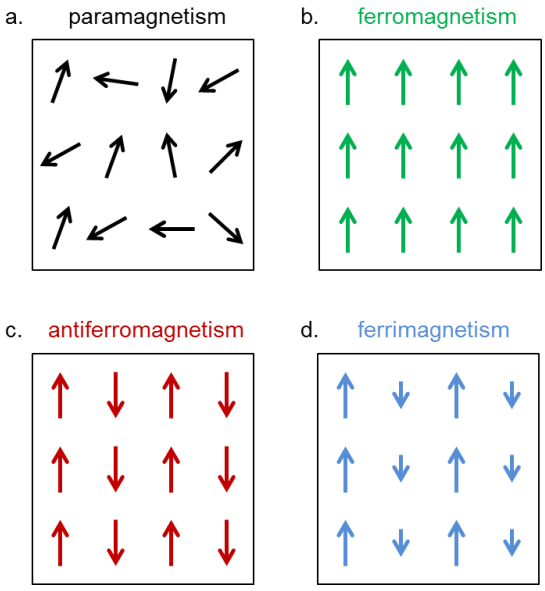

Figure 1.3 Illustration of the alignment of the spins: a) paramagnetism, b) ferromagnetism, c) antiferromagnetism and d) ferrimagnetism. Figure adapted from reference 13.[13]

1.2 The spin Hamiltonian approach

The Schrödinger equation describes the wavefunction of a system (*e.g.* an atom) which includes all the information on the energy of this system. The full Hamiltonian contains all the interactions within the system. The spin Hamiltonian (SH) approach approximates the complete Hamiltonian with an effective Hamiltonian. The SH approach eliminates all the orbital coordinates needed to define the system, and replaces them with spin coordinates. A few approximations are applied, with the main one being that the orbital moment is essentially quenched and is treated as a perturbation. However, there are cases where this approximation is not applicable, *e.g.* in the case of heavier atoms like 4*f* where the orbital contribution is significant.[17]

1.2.1 Zeeman Hamiltonian

As discussed previously in Section 1.1, the application of an external magnetic field to a magnetic centre with spin *S*, will lift the degeneracy of the 2*S*+1 states (m_s states), with energy $E = m_s g \mu_B H$ of each state.[14] Therefore, the Zeeman Hamiltonian will be represented as shown below (eqn 1.7),[18] where $\hat{B}$ is the external magnetic field; μ_B is the Bohr magneton; $\overleftrightarrow{g}$ is the gyromagnetic tensor and $\hat{S}$ is the spin operator:

$$\hat{H}_{ZE} = \mu_B \sum_i \hat{B} \cdot \overleftrightarrow{g}_i \cdot \hat{S}_i \qquad (1.7)$$

1.2.2 Spin-orbit coupling Hamiltonian

As mentioned previously, electrons possess two magnetic moments, the spin and the orbital magnetic moment. The spin-orbit coupling interaction can be described by the below Hamiltonian, where ζ is the spin-orbit coupling constant, and l_i and s_i are the orbital and spin operators, respectively, for electron i:[17]

$$\hat{H}_{SO} = \sum_i \zeta \hat{l_i} \cdot \hat{s_i} \qquad (1.8)$$

The spin-orbit coupling constant increases from the lighter to the heavier elements, and therefore this term is negligible for lighter atoms, but becomes significant for heavier atoms. Equation 1.8 can be simplified to eqn 1.9 with the application of the Russell–Saunders term ^{2S+1}L:[17]

$$\hat{H}_{SO} = \lambda \hat{L} \cdot \hat{S} \qquad (1.9)$$

L and *S* are the total orbital and spin operators and $\lambda = \pm\zeta/(2S)$. Note that for *d*−elements λ is positive for a less than half filled shell, whereas λ is negative for a more than half filled shell.[17]

1.2.3 Crystal field Hamiltonian

A good approximation for the crystal field spin Hamiltonian is to assume a quadratic form of the spin operators. Therefore, it can be expressed as:[17]

$$\widehat{H}_{CF} = \vec{\hat{S}} \cdot \overline{\overline{D}} \cdot \vec{\hat{S}} \qquad (1.10)$$

Eqn 1.10 can also be in the form of 1.11, due to the fact that *D* is a real symmetric tensor, and therefore has three orthogonal eigenvectors.[17]

$$\widehat{H}_{CF} = D_{xx}\hat{S}_x^2 + D_{yy}\hat{S}_y^2 + D_{zz}\hat{S}_z^2 \qquad (1.11)$$

Further simplification of 1.11 is obtained by the subtraction of constants (hence the physical properties are not changed) in two steps, to give:[17]

$$\widehat{H}_{CF} = D[\hat{S}_z^2 - \frac{1}{3}S(S+1)] + E\left(\hat{S}_x^2 - \hat{S}_y^2\right) \qquad (1.12)$$

D and *E* are the axial and rhombic zero-field splitting (ZFS) parameters, respectively. According to the ZFS phenomenon the degeneracy of the m_s states of the ground state *S*, is lifted in the absence of an external magnetic field leading to the presence of magnetic anisotropy. This is caused by the mixing of the ground state *S* (where *S*≥1) with excited states due to spin-orbit coupling.[16] Note that when $D_{zz} = D_{xx} = D_{yy}$ (cubic symmetry) then *D* is zero, and when $D_{xx} = D_{yy}$ (axial symmetry) then *E* is zero. Additionally, the limit $|E/D| \leq 1/3$ has to be considered in order to apply the Hamiltonian 1.12.[17]

The spin Hamiltonian (1.12), which is an approximation considering a quadratic form of the spin operators (using only the second order terms), is the simplest possible crystal field Hamiltonian. However, in some cases (*e.g.* 4*f* ions) the introduction of fourth, sixth, etc. order terms is necessary in order to adequately reproduce the energy levels.[16]

$$\widehat{H}_{CF} = \sum_{i=1}^{N} \sum_{k=2,4,6} \sum_{q=-k}^{k} B_{k\,i}^{q} \theta_k \hat{O}_{k\,i}^{q}$$

where B_k^q is the crystal field parameter, θ_k is the operator equivalent factor, and $\hat{O}_k^q$ is the operator equivalent in Steven's notation containing the orbital reduction parameter.[16] The

ZFS parameters *D* and *E* can also be expressed using the Stevens operators as shown below:[16]

$$D = 3B_2^0 \quad \text{and} \quad E = B_2^2$$

1.2.4 Hamiltonian for interacting spin centres

When two magnetic centres interact, then the spin Hamiltonian is written as:[17]

$$\hat{H}_{EX} = -J_{12}\hat{S}_1 \cdot \hat{S}_2 + \hat{S}_1 \cdot D \cdot \hat{S}_2 + d_{12} \cdot (\hat{S}_1 \mathrm{x}\, \hat{S}_2) \qquad (1.14)$$

The first term is referred to as the isotropic contribution to the magnetic interaction, while the second and third terms are referred to as the anisotropic and the antisymmetric spin-spin contributions, respectively. The isotropic term is responsible for the parallel or antiparallel alignment of the spins, while the third term cant the spins by 90 º. The second term tends to orient the spins along a given orientation space.[17] However, in most cases the isotropic term is considered as dominant, whereas the other two are considered as perturbations. Hence, the spin Hamiltonian for two or more magnetic centres is often written as:[18]

$$\hat{H}_{EX} = -2J \sum_{ij} \hat{S}_i \cdot \hat{S}_j \qquad (1.15)$$

1.3 Single-Molecule Magnets (SMMs)

The term Single-Molecule Magnet (SMM) was introduced for the first time at the beginning of the 1990s to describe molecules that can retain their magnetisation at low temperatures, which originates from the application of an external magnetic field, upon the removal of this external magnetic field. Although this was not the first time that slow relaxation of magnetisation was observed at a molecular level, it was the first time that such behaviour was due to isolated, discrete molecules.[16, 19] These materials combine the classical macroscale properties of a magnet (*e.g.* magnetisation hysteresis) with quantum mechanical properties of molecular origin (*e.g.* quantum tunnelling phenomena).[13]

Such molecules display slow relaxation of the magnetisation due to the presence of an energy barrier (ΔE) between the $\pm m_s$ ($-S \leq m_s \leq +S$) states (Fig. 1.4). This energy barrier depends on the total spin ground state *S* and the magnetic anisotropy, expressed with the ZFS parameter *D*, with the following equations: $\Delta E = S^2|D|$ for an integer spin and $\Delta E = (S^2 - \frac{1}{4})|D|$ for a half-integer spin.[16]

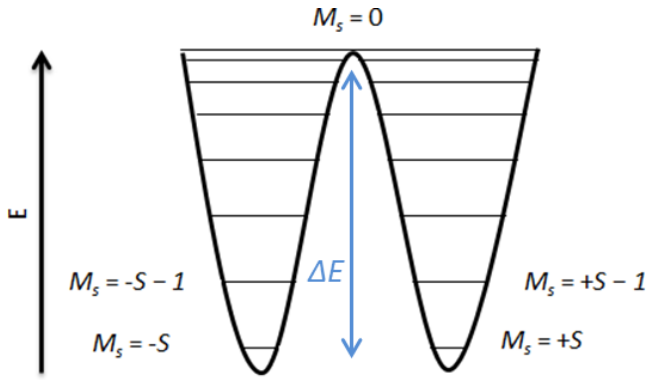

Figure 1.4 Illustration of the splitting of the m_s states by a negative axial ZFS and the energy barrier ΔE (for an integer spin S). Figure adapted from reference 16.[16]

The sign of D is crucial, since it defines the type of magnetic anisotropy. A negative D (easy-axis anisotropy) will stabilise the highest m_s state as ground state, as depicted in Fig. 1.4; whereas a positive D (easy-plane anisotropy) will stabilise the lowest m_s state as ground state, which is zero for an integer spin (and hence no barrier is observed) and $\pm\frac{1}{2}$ for a half-integer spin.[20] A negative D is desirable for a SMM, since it will provide the necessary bistability of the ground state for the existence of the energy barrier, and a large spin ground state (hence higher energy barrier). In the absence of an external magnetic field and D<0, both $\pm m_s$ states are equally populated as shown in Fig. 1.5 (left). The application of a magnetic field lifts the degeneracy of the $\pm m_s$ states and only the $-m_s$ are populated (Fig. 1.5 middle). After the removal of the field in order to achieve equilibrium again, half of the spins will have to re-orientate to the $+m_s$ state; however, due to the presence of the energy barrier the spins have a 'difficulty' to re-orientate and therefore a slow relaxation is observed (Fig. 1.5 right).[20]

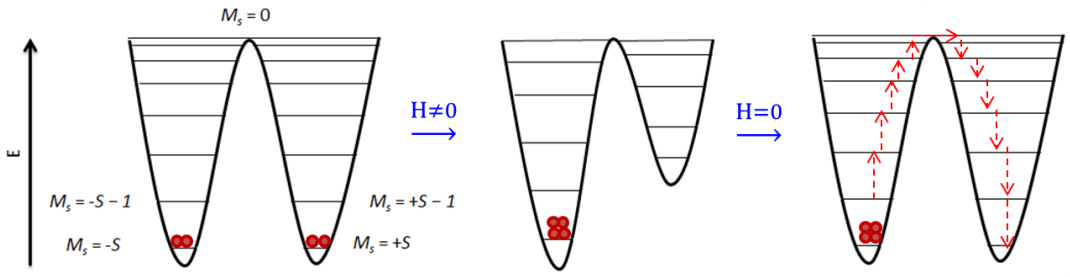

Figure 1.5 Illustration of the double well demonstrating the magnetization (middle) and the thermally activated relaxation (right) in a SMM. Figure adapted from reference 20.[20]

This mechanism, *i.e.* the relaxation over the barrier, occurs through transfer of energy with the environment and is called thermally activated relaxation.[13] In theory the higher the energy barrier, the longer the relaxation time will be. However, there are other relaxation processes that may occur besides the thermally activated relaxation; these mechanisms are discussed in the following section.

1.3.1 Relaxation mechanisms

When there is sufficient thermal energy (k_BT), then the molecule can absorb heat from the vibrational system of the lattice. The lattice vibrational modes are often referred to as phonons, and the absorption/emission of phonons is used to describe heat being transferred from/to the lattice.[13] There are three spin-lattice relaxation mechanisms involving the absorption/emission of phonons (Fig. 1.6): i) the direct process (one-phonon process), where the relaxation occurs between the $-m_s$ to $+m_s$ with the emission of a phonon; ii) the Orbach process (two-phonon process), which involves the absorption of a phonon (to a real state) followed by the emission of a phonon; iii) the Raman process (two-phonon process), which is analogous to Orbach but a virtual state is involved instead of a real state.[21] Another possible pathway of magnetic relaxation is quantum tunnelling of the magnetisation (QTM) (Fig. 1.7). According to this phenomenon the wavefunctions of the $\pm m_s$ states are superposed and the spin can travel 'through' the barrier, resulting in a faster magnetic relaxation. The QTM of the ground state (Fig. 1.7) is thermally independent, and it can be induced by low symmetry components of the crystal field, any effective transverse magnetic field or hyperfine interactions with nuclear spins.[13] Additionally, thermally-assisted QTM can also occur as shown in Figure 1.7. The probability of QTM to occur is higher for smaller states m_s states.[13]

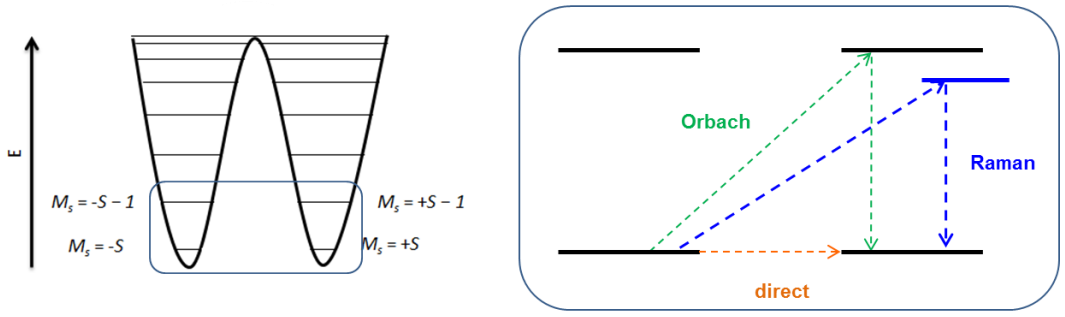

Figure 1.6 Schematic representation of the spin-lattice relaxation processes: direct (orange), Raman (blue) and Orbach (green). Figure adapted from reference 21.[21]

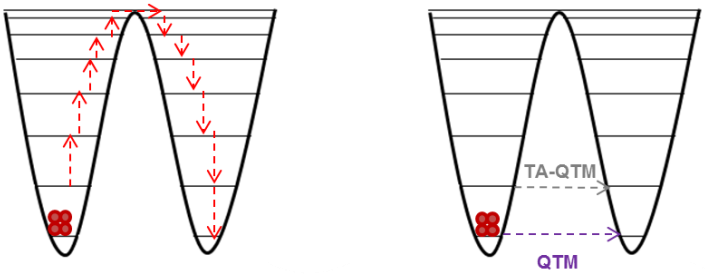

Figure 1.7 *Left)* Schematic representation of the thermally activated relaxation. *Right)* The QTM of the ground state (purple) and the thermally-assisted QTM (grey).

1.3.2 Magnetic characterisation of SMMs

One of the main experimental measurements that are performed in order to determine if a sample exhibits SMM behaviour is the alternating current (ac) susceptibility measurement; according to this measurement a small alternating magnetic field (usually 1–5 Oe) is applied to the sample, which induces an alternating magnetisation. This experiment can be performed in zero or an applied static dc field and reveals information about the magnetic relaxation dynamics.[13, 22] The alternating magnetic field can be defined as follows:

$$H_{(t)} = H_0 + h\cos(\omega t) \quad (1.16), \quad \text{where} \quad \omega = 2\pi v$$

H_0 is a zero/nonzero constant indicating the zero/nonzero dc magnetic field parallel to the oscillating field h; h is the amplitude of the ac magnetic field, and v corresponds to the oscillating frequency of the ac magnetic field.[22] The measured ac suceptibiltiy (χ_{ac}) at given temperature will contain a real (χ') and an imaginary (χ'') component as a function of the oscillating frequency (v) of the ac magnetic field:

$$\chi_{ac}(\omega) = \chi'(\omega) - i\chi''(\omega) \quad (1.17)$$

The decrease in the in-phase component $\chi'(\omega)$ of the ac susceptibility will be concomitant with the appearance of peaks in the out-of-phase component $\chi''(\omega)$, indicating slow magnetic relaxation (Fig. 1.8 left).[22] In order to investigate further the relaxation process, an Argand or Cole−Cole plot of $\chi''(\omega)$ vs $\chi'(\omega)$ can be constructed as shown in Figure 1.8 (right). The relaxation time and the width of its distribution can be extracted from this plot.

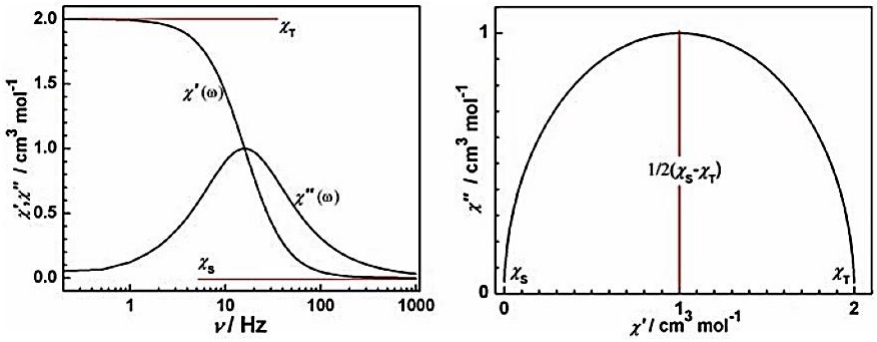

Figure 1.8 *Left*) The real (χ') and imaginary (χ'') components as a function of the oscillating frequency (ν) of ac magnetic field. *Right)* The Cole–Cole diagram with a single relaxation process characterized by a single relaxation time. [22]

If the system relaxes with a single relaxation process and is characterised by a single relaxation time ($\tau = \omega^{-1}$), then the following Debye model applies where χ_T and χ_S are the isothermal and the adiabatic susceptibility, respectively:[13, 22]

$$\chi_{ac}(\omega) = \chi_s + \frac{\chi_T - \chi_S}{1+i\omega\tau} \qquad (1.18)$$

If the whole magnetisation relaxes as stated above, then the Cole–Cole plot describes a semicircle whose centre lies on the χ' axis (Fig. 1.8 right). The frequency ω at which the absorption reaches its maximum $\chi_{max} = 1/2(\chi_T - \chi_S)$, determines the relaxation time of the relevant relaxation process. If there is a wider distribution of relaxation times then the semicircle will be flattened and the Debye model will be modified:[13, 22]

$$\chi_{ac}(\omega) = \chi_s + \frac{\chi_T - \chi_S}{1+(i\omega\tau)^{1-a}} \qquad (1.19)$$

The α parameter (0< α <1) or Cole−Cole parameter, equals zero for a relaxation with one time constant (Debye process), whereas the larger it becomes, the wider the distribution of the relaxation times is.[22] However, more complex systems (*e.g.* polynuclear systems) often possess multiple relaxation processes with different relaxation times. In that case the relaxations can be described by the sum of two modified Debye functions and the Cole–Cole plot will display two semicircles, which are often partially merged (Fig. 1.9) [22]:

$$\chi_{ac}(\omega) = \chi_{s1} + \chi_{s1} + \frac{\chi_{T1} - \chi_{S1}}{1+(i\omega\tau_1)^{1-a1}} + \frac{\chi_{T2} - \chi_{S2}}{1+(i\omega\tau_2)^{1-a2}} \qquad (1.20)$$

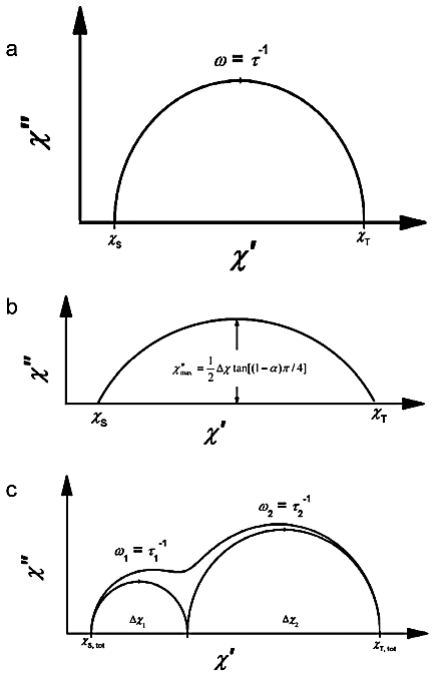

Figure 1.9 χ'' vs. χ' (Cole–Cole plot) for: (a) relaxation process with a single time constant τ (Debye process); (b) distribution of relaxation time constants according to modified Debye eqn 1.19; (c) relaxation process with two time constants τ_1 and τ_2.[23]

The extracted relaxation times from the Cole–Cole plot can be consequently plotted as a function of the temperature as τ^{-1} vs T or ln(τ) vs T^{-1}. The fit of these data can produce the effective energy barrier following the Arrhenius law (Orbach process):[22]

$$\tau^{-1} = \tau_0^{-1}\exp(-\frac{\Delta E}{k_B T}) \quad (1.21)$$

where τ_0 is the pre-exponential factor, ΔE the effective energy barrier, k_B the Boltzmann constant, T is the temperature. However, as discussed previously more than one relaxation processes may be present and therefore the complete equation for direct, Raman, QTM and Orbach processes, in that order is shown below[22]:

$$\tau^{-1} = AH^m T + CT^n + \frac{B_1}{1+B_2H^2} + \tau_0^{-1}\exp(-\frac{\Delta E}{k_B T}) \quad (1.22)$$

Parameters A, C, B_1 and B_2 are constants for the direct, Raman and QTM processes, respectively. Parameter m is equal to 4 for Kramers and 2 for non-Kramers ions, while n corresponds to 9 for Kramers and 7 for non-Kramers ions; however, lower values than 7 have also been reported for parameter n when acoustic and optical phonons are involved.[24-30]

A fundamental characteristic of molecules exhibiting slow relaxation of the magnetisation is the observation of hysteresis loops in the magnetisation *versus* field plots (Fig. 1.10 left). The application of an external magnetic field to a sample will cause the saturation of the magnetisation at a specific temperature. If the sample is paramagnetic the *M*(H) curve would retrace itself back to zero upon decreasing the field.[13] However, if there is slow magnetic relaxation then *M* will have some remnant value and it will not be reduced back to zero.[13] The application of a field in the opposite direction will force the magnetisation to zero ('at the coercive field') and finally will saturate in the opposite direction. The removal of the field leaves an equal but opposite remnant magnetisation. This implies bistability, *i.e.* in zero applied field the magnetisation can take either a positive or negative value.[13] This property rendered SMMs as ideal candidates for information storage in a molecular level. However, it was experimentally observed that usually not a perfect hysteresis loop is obtained; the presence of steps in the hysteresis, due to the QTM phenomenon, is often detected (Fig. 1.10 right).[16]

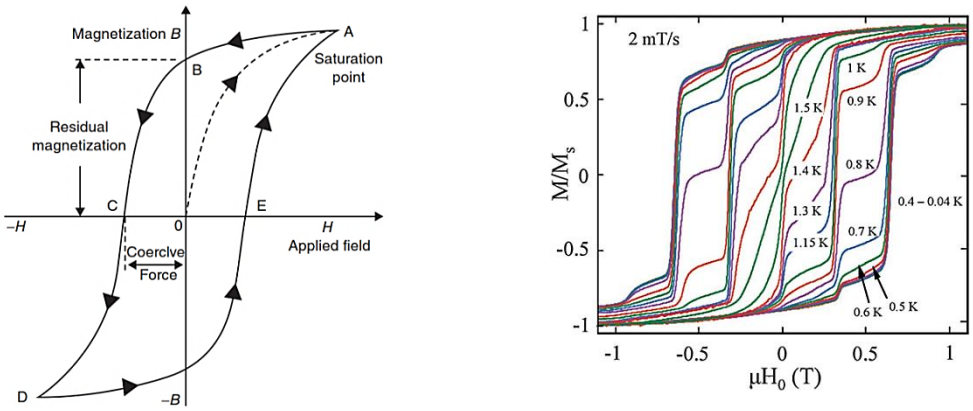

Figure 1.10 *Left)* Typical magnetic hysteresis loop.[16] *Right)* Temperature dependence of the hysteresis loops for a single crystal of $(NMe_4)_2[Mn_{12}O_{12}(O_2CC_6F_5)_{16}(H_2O)_4]\cdot 6C_7H_8$ at a fixed scan rate of 2 mT/s. Reprinted with permission from N. E. Chakov, M. Soler, W. Wernsdorfer, K. A. Abboud and G. Christou, *Inorg Chem*, 2005, **44**, 5304-5321. Copyright 2019 American Chemical Society.[31]

Another important characteristic of molecules that exhibit SMM behaviour is the blocking temperature, T_B. There are three definitions that are usually used in the literature: a) the temperature at which a peak is observed in the out-of-phase susceptibility (χ'') at a given frequency, b) the highest temperature at which hysteresis is observed in a plot of magnetisation *versus* field, or c) the temperature at which a maximum is observed in the zero-field cooled magnetization.[32] The second definition, which is closest to the behaviour

of a bulk ferromagnet, is usually reported; however when comparing reported T_B values, one should be careful of which definition is used by the author.[13]

1.3.3 The first SMM and some milestones of the field

The first SMM

The very first compound to be studied for SMM properties was the archetypal $[Mn_{12}O_{12}(MeCO_2)_{16}(H_2O)_4]\cdot 2MeCO_2H\cdot 4H_2O$, hereafter referred to as {Mn_{12}OAc}. Although {Mn_{12}OAc} has been reported in 1980 by Lis *et al.*[33], its thorough magnetic characterisation came much later at the beginning of 1990s.[34-36] {Mn_{12}OAc} is a dodecanuclear mixed-valence manganese complex which contains eight Mn^{III} and four Mn^{IV} ions (Fig. 1.11). The spin ground state of the molecule is S = 10, which results from the antiferromagnetic interaction between the eight outer Mn^{III} ions and the four inner Mn^{IV} ions, and the zero-field splitting of this ground state is D = –0.5 cm^{-1}. The magnetic anisotropy of the molecule originates from the near-parallel alignment of the Jahn-Teller (JT) axes on the eight Mn^{III} ions. {Mn_{12}OAc} displays frequency-dependent out-of-phase ac signals and it was the first complex to exhibit hysteresis loops of molecular origin.

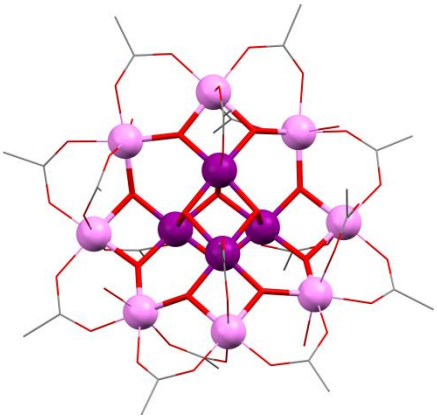

Figure 1.11 The molecular structure of {Mn_{12}OAc}. Colour code: Mn^{III}: light pink, Mn^{IV}: dark pink, O: red, C: grey. Hydrogen atoms are omitted for clarity.[33]

After the observation that {Mn_{12}OAc} exhibits slow relaxation of molecular origin, a great number of such molecules appeared employing 3*d* metal ions,[37] and the pursuit for the increase of the energy barrier began. The main goal of researchers was to stabilise a large spin ground state which in theory would increase the energy barrier (remember that $\Delta E = S^2|D|$), without focusing yet on the magnetic anisotropy (D). As a result a large number of polynuclear complexes were reported, amongst them a {Mn^{III}_{84}}[38] with S = 6

and a mixed valent Mn^{II}/Mn^{III} $\{Mn_{19}\}$[39] with S = 83/2, both of which display hysteresis loops, however at very low temperatures. More recent examples of polunclear high-spin complexes have been reported, such as a mixed valent Mn^{II}/Mn^{III} $\{Mn_{49}\}$[40] with S = 61/2, a mixed valent Fe^{II}/Fe^{III} $\{Fe_{42}\}$[41] with S = 45, a $\{Fe^{III}_{10}Gd^{III}_{10}\}$[42] with S = 60 and a $\{Ni^{II}_{21}Gd^{III}_{20}\}$[43] with the highest spin to date S = 91. Molecules with giant spins could also find applications in magnetic resonance imaging and as local coolers by utilising the magnetocaloric effect.[42]

The first Ln-based SMM

In 2003 the first lanthanide based SMMs were introduced by Ishikawa *et al.*[44], which also were the first monometallic complexes exhibiting SMM properties. Ishikawa *et al.* reported a series of phthalocyanine double-decker complexes $[Pc_2Ln^{III}]^-\cdot[TBA]^+$ (Fig. 1.12) (where Ln^{III} = Tb, Dy, Ho, Er, Tm, or Yb, H_2Pc = phthalocyanine and $[TBA]^+$ = $[N(C_4H_9)_4]^+$), of which only the Tb ($\{Pc_2Tb\}$) and Dy ($\{Pc_2Dy\}$) analogues displayed slow magnetic relaxation. To ensure that this behaviour is due to a molecular origin, the diluted samples of $\{Pc_2Tb\}$ and $\{Pc_2Dy\}$ were studied and were found to exhibit energy barriers of ~331 K and ~40 K, respectively.[44] The energy barrier of the Tb analogue was by far higher than the energy barriers reported for transition metal complexes. The magnetic relaxation in complexes $\{Pc_2Tb\}$ and $\{Pc_2Dy\}$ was proposed to occur through the first excited m_J state (*vide infra*) as shown in Figure 1.13.[44] This remarkable result marked the beginning of a new era in the SMM field and led not only to the introduction of lanthanides in SMMs, but also to a new class of molecules exhibiting slow magnetic relaxation arising from a single ion; these molecules are often referred to as single-ion magnets (SIMs), and this definition will be used throughout this thesis.[45] Selected examples of 3*d* and 4*f* SIMs will be discussed in section 1.4.

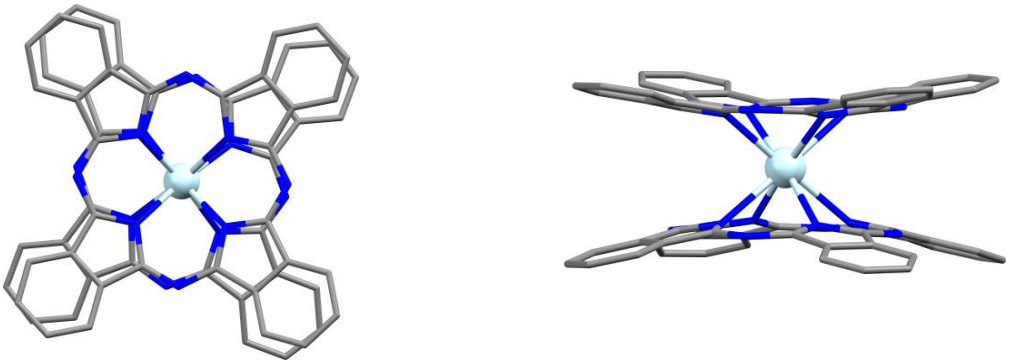

Figure 1.12 The molecular structure of the $[Pc_2Ln^{III}]^-$ anion. Colour code: Ln: light blue, N: blue, C: grey. Hydrogen atoms are omitted for clarity.[46]

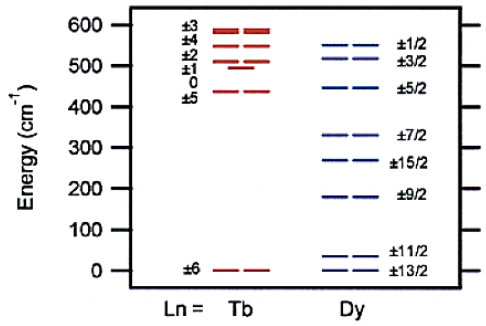

Figure 1.13 Energy and m_J values of the sublevels of the ground multiplets of {Pc_2Tb} and {Pc_2Dy}. Reprinted with permission from N. Ishikawa, M. Sugita, T. Ishikawa, S.-Y. Koshihara and Y. Kaizu, *J Am Chem Soc*, 2003, **125**, 8694-8695. Copyright 2019 American Chemical Society.[44]

Lanthanide ions possess a large and unquenched orbital contribution (except from those with electronic terms $^1S_0$ and $^8S_{7/2}$) which could lead to a large magnetic anisotropy. Although the spin-orbit coupling is more significant than the crystal field effect (due to the inner 4*f* electrons), the crystal field effect cannot be completely ignored and is treated as a small but significant perturbation.[47] Due to the unquenched angular momentum in lanthanides, *S* is no longer a 'good' quantum number to describe the system, and instead the total angular momentum *J* is used. The crystal field splits the ground state (*e.g.* $^6H_{15/2}$ for Dy^{III}) into (2*J*+1) m_J states as shown in Figure 1.14 (and Fig. 1.13), and therefore the ground state bistability arises from these m_J levels. Although the contribution of the crystal field is small, it has proved to be a key factor for the slow relaxation of the magnetisation (see Section 1.4: SIMs).[32]

The {Mn^{III}_6} family

Another breakthrough came along with the famous {Mn^{III}_6} family (over 30 structures)[19] with molecular formula [$Mn^{III}_6O_2(O_2CR^1)_2(R^2\text{-sao})_6L_x$] (Fig. 1.15), employing a variety of carboxylates (R^1) and the ligand salicylaldoxime and its derivatives (R^2 = methyl-, ethyl- and phenyl-salicylaldoxime). The metallic core of these complexes consists of two off-set stacked [$Mn^{III}_3O(O_2CR^2)(R^1\text{-sao})_3$] triangles, which are linked to each other via two oximate O atoms. Two of the Mn^{III} within each oxo-centred {Mn^{III}_3} subunit are six-coordinate (adopting a JT elongated octahedral geometry) and one is five-coordinate (adopting a square pyramidal geometry).[19]

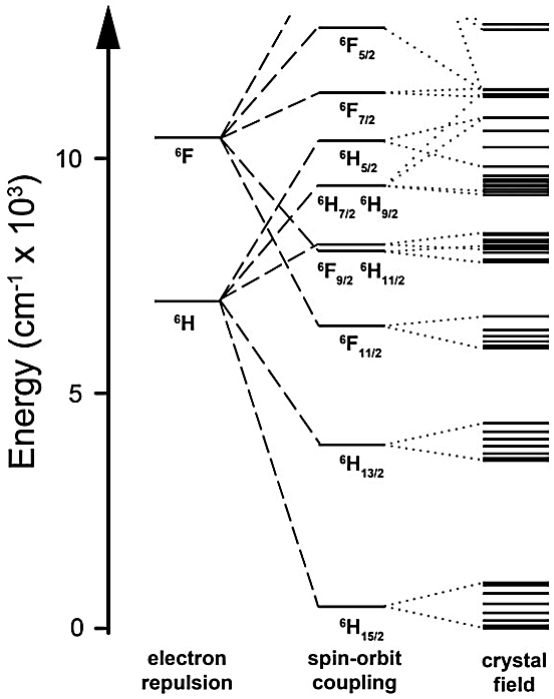

Figure 1.14 Low energy electronic structure of the Dy^{III} ion with sequential perturbations of electron-electron repulsion, spin–orbit coupling, and the crystal field. The crystal field splitting is constructed from a model for the complex, $Dy[(Me_3Si)_2N]_3$.[48] Energy is measured relative to the ground crystal field (m_J) state. Further complications due to mixing between states have been neglected in favour of clarity.[32]

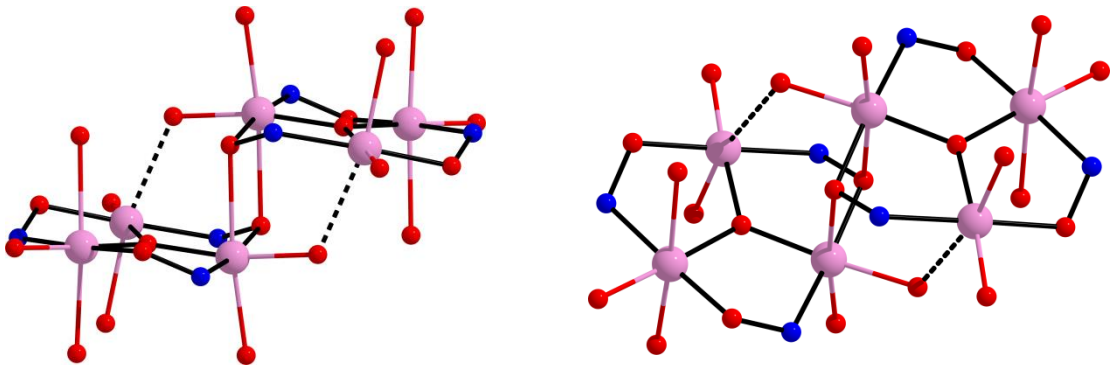

Figure 1.15 The $\{Mn^{III}_6\}$ metallic core of the $[Mn^{III}_6O_2(O_2CR^1)_2(R^2\text{-sao})_6L_x]$ family. The black bonds highlight the $\{Mn^{III}_3\}$ subunits, while the black dashed lines represent the link between the two subunits (the distance varies between ~2.5−3.5 Å for different complexes). Colour code: Mn^{III}: pink, O: red, N: blue. Hydrogen and carbon atoms are omitted for clarity.[49]

The studies performed on this family provided an important magnetostructural correlation of an extended family of SMMs, with the $[Mn^{III}_6O_2(Et\text{-}sao)_6(O_2CPh(Me)_2)_2(EtOH)_6]$ analogue exhibiting a then record high energy barrier for transition metal complexes of ~86 K.[49, 50] According to these magnetostructural studies the following observations were made:[19, 50] *a)* the exchange interactions between the $\{Mn^{III}_3\}$ subunits were found to be ferromagnetic in all cases, *b)* the exchange interaction between Mn^{III} pairs within the triangle is dominated by the Mn−O−N−Mn torsion angles; the larger the torsion angle, the more ferromagnetic the pairwise interaction; the smaller the Mn−O−N−Mn torsion angle the more antiferromagnetic the pairwise interaction, *c)* the magnetic coupling switches from antiferromagnetic to ferromagnetic above a torsion angle of ~31º, *d)* the individual torsion angles between neighbouring Mn^{III} ions dictates the behaviour of the complex, instead of the average torsion angle, *e)* the presence of carboxylates (either in bridging mode or terminally bound) has a small effect on the exchange interactions and *f)* if each of the Mn^{III} pairs are ferromagnetically coupled (hence S = 12 for the complex), then the larger the Mn−O−N−Mn torsion angle, the larger the effective energy barrier.[51, 52]

3d-4f SMMs

Shortly after the report of $\{Pc_2Tb\}$ and $\{Pc_2Dy\}$ the first 3*d*-4*f* SMM was published, which is a cyclic tetranuclear $\{Cu^{II}_2Tb^{III}_2\}$ with molecular formula $[Cu^{II}Tb^{III}L(hfac)_2]_2$ (Fig.1.16) (H_3L = 1-(2-hydroxybenzamido)-2-(2-hydroxy-3-methoxy-benzylideneamino)-ethane).[53] The Cu-Tb centres show a ferromagnetic coupling and complex $\{Cu^{II}_2Tb^{III}_2\}$ displays frequency-dependent ac out-of-phase peaks with an energy barrier of 21 K (in the 2.0 – 2.8 K temperature range); however no hysteresis loops were observed. Additionally, by replacing the paramagnetic square-planar Cu^{II} ion with the diamagnetic square-planar Ni^{II} ion, the authors demonstrated that the slow magnetic relaxation is not intrinsic to the Tb^{III} centres. Similar behaviour was observed for the Dy^{III} analogue, although no maximum in the χ'' signal was observed down to 2 K.[53] The second 3*d*-4*f* complex which was found to exhibit slow magnetic relaxation, although no fully formed out-of-phase peaks were observed, was the dodecanuclear complex $[Mn^{III}_4Mn^{IV}_2Dy^{III}_6(H_2shi)_4(Hshi)_2(shi)_{10}(MeOH)_{10}(H_2O)_2]\cdot 9MeOH\cdot 8H_2O$ $\{Mn_6Dy_6\}$ (H_3shi = salicylhydroxamic acid). Additionally, the Tb^{III} and Gd^{III} analogues were studied, however they did not display any out-of-phase signal; this was an indication that the nature of the lanthanide ion was important in order for SMM properties to be observed.[54]

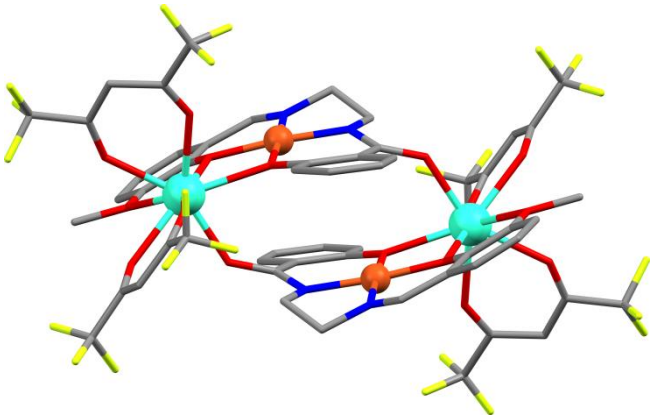

Figure 1.16 The molecular structure of $[Cu^{II}Tb^{III}L(hfac)_2]_2$. Colour code: Cu: orange, Tb: turquoise, O: red, N: blue, C: grey, F: light green. Hydrogens are omitted for clarity.[53]

After the report of these results the number of 3*d*-4*f* complexes which were studied for SMM properties grew exponentially over the next few years.[55-59] The nuclearities of such complexes varied from 2 up to 136 metal centres[57] and exhibited a rich structural diversity with topologies such as: butterfly, cubanes and double-cubanes, cages, propeller shape and many more.[55-58] Studies on 3*d*-4*f* systems, incorporating appropriate ligands, led to the following advantages: i) a large magnetic anisotropy could be introduced by the use of Ln ions due to their intrinsic spin-orbit coupling; ii) the magnetic exchange between 3*d*-4*f* ions could effectively supress QTM, and therefore could lead to higher energy barriers for the reversal of the magnetisation; and iii) the combination of high spin isotropic 3*d* ions with high magnetic anisotropy 4*f* ions could help to better control the overall anisotropy of the system.[55-58, 60-64] However, the interpretation of the magnetic interactions within heterometallic complexes is still complicated, especially for high nuclearity clusters. Therefore, in order to elucidate the magneto-structural correlations, more simple structures with limited 3*d* and 4*f* ions are required.[60, 65, 66]

Pure 4f polynuclear complexes

Although the magnetic coupling between lanthanide ions is expected to be weak due to the inner 4*f* orbitals, pure 4*f* polynuclear complexes present some interesting magnetic properties.[22] One of the most fascinating and ground-breaking examples is the case of the triangular $\{Dy_3\}$ complexes exhibiting spin chirality. In 2006 the Powell group reported the triangular $[Dy^{III}_3(\mu_3\text{-}OH)_2L_3Cl_2(H_2O)_4]^+$ and $[Dy^{III}_3(\mu_3\text{-}OH)_2L_3Cl(H_2O)_5]^+$ (HL = o-vanillin) cations (Fig. 1.27), which can form complexes $[Dy^{III}_3(\mu_3\text{-}OH)_2L_3Cl_2(H_2O)_4][Dy^{III}_3(\mu_3\text{-}OH)_2L_3Cl(H_2O)_5][Cl]_5\cdot 19H_2O$ (**I**) and $[Dy^{III}_3(\mu_3OH)_2L_3Cl(H_2O)_5][Cl]_3\cdot 4H_2O\cdot 2MeOH\cdot 0.7MeCN$

(**II**); complex **I** contains a 50:50 mixture of the two cations.[67] The three Dy centres are connected by two μ_3-OH bridges, along with three singly deprotonated o-vanilin ligands. All Dy centres in both cations are eight-coordinate; in one cation the coordination sphere of two of the Dy is completed by two water molecules, while a mixture of Cl^- and H_2O molecules complete the coordination sphere of the third Dy; in the other cation again two water molecules are coordinated to two of the Dy centres, while two Cl^- ions are bound on the third Dy. Despite the small structural differences both complexes display the same magnetic behaviour.

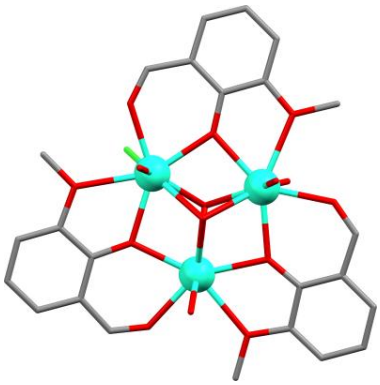

Figure 1.27 The molecular structure of the $[Dy^{III}_3(\mu_3\text{-}OH)_2L_3Cl(H_2O)_5]^+$ cation. Colour code: Dy: turquoise, O: red, Cl: green, C: grey. Hydrogen atoms are omitted.[67]

The dc susceptibility measurements (Fig. 1.28) revealed antiferromagnetic interactions and a diamagnetic ground state. This observation was surprising since a non-zero ground state is expected for an odd number of unpaired electrons which are antiferromagnetically coupled. The magnetic susceptibility shows a maximum around 7 K suggesting the presence of a non-magnetic ground state (Fig. 1.28 left inset), which is further confirmed by the almost zero magnetisation at low fields (Fig. 1.28 right). At higher fields the magnetisation shows a jump and reaches saturation. This behaviour is not the typical spin frustrated situation, where the magnetic moments are perpendicular to the Dy_3 plane; it can only be explained if the magnetic moments are not collinear and lie in the Dy_3 plane.[67, 68] This is caused by a strong magnetic anisotropy, which forces the magnetic moment to lie in the plane. The overall spin structure is described as toroidal or, alternatively, as vortex spin-chirality.[47] Another surprising observation was that although the ground state was non-magnetic, the complexes displayed slow magnetic relaxation which was associated with the population of an excited m_J state. This new phenomenon observed in the $\{Dy_3\}$ triangles has an important implication as the chiral nature of the spin in such materials could represent an advance toward the development of non-collinear molecular spintronics and qubits.[47, 68]

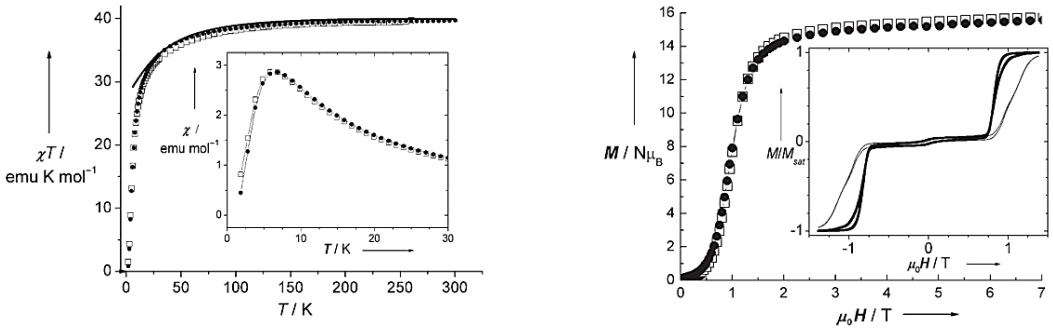

Figure 1.28 *Left)* χT versus T plot for **I** (open squares) and **II** (solid circles). The solid line represents the calculated value for three non-interacting Dy^{III} ions. *Inset*: low-temperature susceptibility χ. *Right)* Magnetisation versus applied field data of **I** (open squares) and **II** (solid circles) at 1.8 K. Inset: micro-SQUID measurements at 0.1 K and 28 mTs^{-1} on a single crystal of **II** applying the magnetic field in the plane (light line) and perpendicular to the plane (bold line) of the Dy^{III} ions.[67]

Two important results, which shed light on the magnetic relaxation pathways in Ln-based SMMs, were published by the Winpenny group including a square pyramidal $\{Dy_5\}$ and a $\{Dy_4K_2\}$ complex.[69, 70] The first example is the complex $[Dy^{III}{}_5O(O^iPr)_{13}]$[69] (Fig. 1.29 left), which will be referred to as $\{Dy_5\}$, incorporating *iso*-propoxide and one oxide bridges. Complex $\{Dy_5\}$ crystallises in two polymorphs that display the same magnetic behaviour. Each Dy centre is six-coordinate adopting a distorted octahedral geometry, with the Dy centre being located above the $\{O_4\}$ plane (the O atoms originate from the alkoxide ligands) and towards the terminal alkoxide ligand (hence longer distance with the central oxide). The authors based the design of the $\{Dy_5\}$ complex considering the following factors: the presence of a local fourfold symmetry on the Dy centres, which was found to play an important role in the magnetic behaviour of the previously reported $[Pc_2Ln^{III}]^-\cdot[TBA]^+$ [44] and $Na_9[Er(W_5O_{18})_2]$[71] complexes; and the presence of $\{Dy_3\}$ triangles, which could exhibit unusual effects as discussed above.[67, 68]

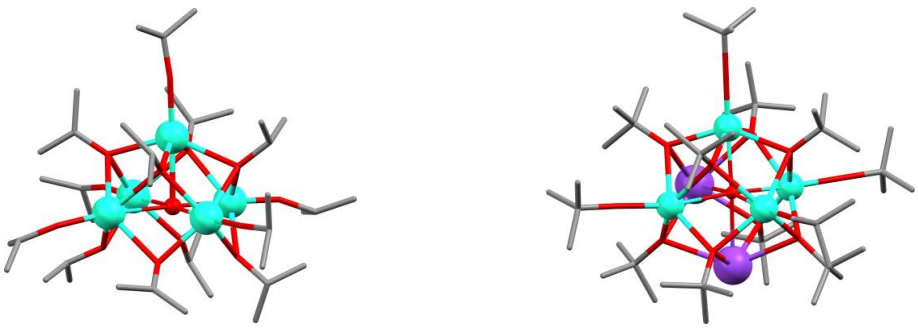

Figure 1.29 *Left)* The molecular structure of $[Dy^{III}{}_5O(O^iPr)_{13}]$.[69] *Right)* The molecular structure of $[Dy^{III}{}_4K_2O(O^tBu)_{12}]$.[70] Colour code: Dy: turquoise, K: purple, O: red, C: grey. Hydrogen atoms are omitted for clarity.

Dynamic ac susceptibility measurements revealed slow magnetic relaxation until 40 K in zero dc field, and an energy barrier of 528 K (a then record energy barrier) at higher temperatures. The authors suggested that the SMM property is associated with the individual magnetic anisotropy of each Dy centre. This was later confirmed with *ab initio* calculations which revealed that the slow magnetic relaxation occurred through the first excited state and that the magnetic anisotropy axis was in the same direction as the (μ_5O)−Dy−(terminal alkoxide) direction (the energy is minimised when the quantisation axis is coincident with this direction).[22, 70] The second example is complex $[Dy^{III}_4K_2O(O^tBu)_{12}]$[70] (Fig. 1.29 right), which will be referred to as {Dy_4K_2}. The Dy centres have similar local geometry as in {Dy_5} with a short terminal alkoxide *trans* to the central oxide and four equatorial alkoxides. Dynamic ac susceptibility studies showed slow magnetic relaxation with the presence of two out-of-phase peaks, which was attributed to two different relaxation processes. The energy barrier was found to be 692 K and is consistent with the energy of the first excited state as confirmed by theoretical calculations. Additionally, the magnetic dilution of {Dy_5} and {Dy_4K_2} with their yttrium analogues, resulted in even higher energy barriers of 804 and 842 K, for {Dy_5} and {Dy_4K_2} respectively. These values are consistent with the energies of the second excited states for each complex, as confirmed by theoretical calculations, something that was observed for the first time.[70] These results showed that the relaxation pathway from the first excited state can be effectively blocked, and therefore lead to higher energy barriers. Moreover, it was shown that the key feature in this system is a strong axial ligand field that maximises the gaps between m_J states; hence the mixing of the m_J states is minimised and a co-parallel alignment of the lowest Kramers doublets is enforced even where there is no symmetry.[70]

The last example that will be discussed in this section is a series of radical-bridged {Ln_2} complexes, reported by the Long group, with molecular formula $[K(18\text{-crown-}6)(THF)_2][Ln^{III}_2(N_2)\{N(SiMe_3)_2\}_4(THF)_2]$ (Ln = Gd, Tb, Dy, Ho, Er) (Fig. 1.30).[72, 73] The coordination environment of each lanthanide is pseudo-tetrahedral, with one vertex being occupied by the bridging N_2^{3-} ligand.[72] A fit of the dc susceptibility data of the Gd analogue revealed a strong magnetic coupling J = −27 cm^{-1}, while the Dy and Tb analogues exhibit SMM behaviour with high magnetic blocking temperatures (14 K for τ = 100 s) and large coercive fields. Dc and ac susceptibility studies were also performed to the non-radical N_2^{2-}analogues which exhibited poor SMM properties compared with the radical ones. These results confirm that the key factor in this system is the extremely strong direct exchange coupling between the N_2^{3-} radical and lanthanide ions, rather than a strict local symmetry.[72-74]

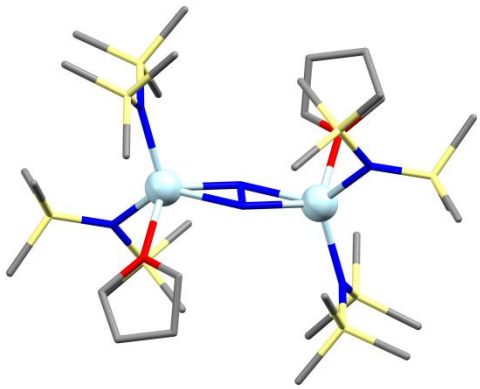

Figure 1.30 The molecular structure of the $[Ln^{III}_2(N_2)\{N(SiMe_3)_2\}_4(THF)_2]^-$ anion. Colour code: Ln: light blue, O: red, N: blue, Si: light yellow, C: grey. Hydrogen atoms are omitted for clarity.[72, 73]

As mentioned previously, in the early years of the SMM field researchers were focusing on maximising the spin ground state, in order to obtain higher energy barriers, by targeting the synthesis of polynuclear complexes where the magnetic centres would display strong ferromagnetic coupling. Strong and ferromagnetic coupling could lead to well isolated ground states and consequently the quenching of QTM (by avoiding the mixing of the ground state with low-lying excited states).[58] However, studies showed that the increase of the total spin did not translate into high energy barriers;[20, 38, 39, 75, 76] additionally O. Waldman demonstrated that the magnetic anisotropy was inversely proportional to S^2.[77] Moreover, the control of the overall anisotropy in polynuclear clusters has proven to be difficult, since the individual magnetic anisotropies of the paramagnetic centres may be antagonistic and this could lead to a diminished overall magnetic anisotropy.[45, 78] Taking into consideration these studies along with the observation that mononuclear complexes could display SMM behaviour, there has been a growing realization that the single-ion anisotropy is a crucial factor in the design of SMMs with high energy barriers.[47] Hence, the focus of the field shifted from polynuclear complexes to mononuclear 4*f* and 3*d* complexes.

1.4 Representative examples of Single-Ion Magnets (SIMs)

1.4.1 Lanthanide SIMs

The bistability of the ground state in lanthanides arises from the ground $\pm m_J$ states and the magnetic relaxation occurs via the excited m_J states. Hence, in order to maximise the energy barrier and the blocking temperature the following features should be considered: (i) the ground $\pm m_J$ states should be degenerate with the highest m_J value, (ii) the energy difference between the ground and the excited states should be large, and (iii) the m_J

states should be pure (strong axiality) in order to avoid QTM by minimizing the transverse anisotropy, the dipolar interaction and the hyperfine effect.[32, 74] A qualitative electrostatic model related to the interaction between the electron density of the 4*f* electrons and the surrounding ligands, was proposed by J.D. Rinehart and J.R. Long[32], based on J. Sievers publication '*Asphericity of 4f-Shells in Their Hund's Rule Ground States*'.[79] According to this model the overall shape of the free-ion electron density for Ce(III), Pr(III), Nd(III), Tb(III), Dy(III), and Ho(III) is oblate, whereas for Pm(III), Sm(III), Er(III), Tm(III), and Yb(III) is prolate (Fig. 1.31). To maximize the magnetic anisotropy of an oblate ion and stabilise the largest m_J state (the first prerequisite for SIM behaviour in lanthanides), a strong axial crystal-field below and above the *xy* basal plane is required; whereas an equatorial ligand field is preferable for a prolate ion in order to minimize the charge repulsion with the axial electron density.[32]

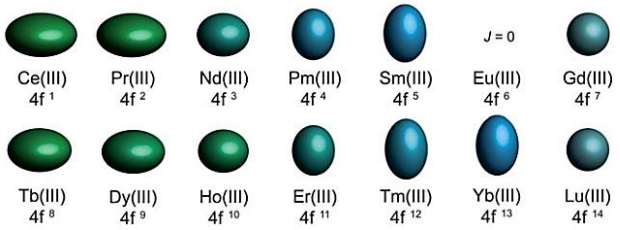

Figure 1.31 Quadrupole approximations of the 4*f*-shell electron distribution for the tripositive lanthanides. Europium is not depicted due to a $J = 0$ ground state.[32]

The energetic separation between the ground and the excited states depends on the individual m_J states (Fig. 1.32). Consider the case of the Tb^{III} adopting the sandwich type geometry as in the $[Pc_2Tb^{III}]^-\cdot[TBA]^+$ complex[44]. The $m_J = \pm6$ state has an extremely oblate density, which is favourable in the sandwich geometry, whereas the $m_J = \pm5, \pm4, \pm3, \pm2, \pm1$ and 0 states have prolate densities which are highly unfavourable (Fig. 1.32). This extreme contrast leads to a large separation of the ground state from the lowest excited state, and thus satisfying the second prerequisite for SIM behaviour in lanthanides.[32] Finally, the transverse anisotropy could be minimized by imposing symmetries that quench, in theory, the transverse crystal-field parameters B_k^q ($q \neq 0$) in the crystal-field Hamiltonian, such as C_n ($n > 7$), S_8 / D_{4d} (*e.g.* square antiprism geometry) C_{5h} / D_{5h} (*e.g.* pentagonal bipyramid) and S_{12} / D_{6d} (*e.g.* hexagonal bipyramid).[80] The dipolar interactions could be suppressed by magnetic dilution (using a diamagnetic analogue), while the hyperfine effect could be eliminated by using the pure isotope without nuclear spins.[80] Note that Dy(III) ($^6H_{15/2}$) is the most used ion in the synthesis of SIMs; it is considered an ideal candidate due to the fact that is a Kramers ion, and therefore the degeneracy of the ground state is ensured, and also possesses a large magnetic moment with significant anisotropy.[32]

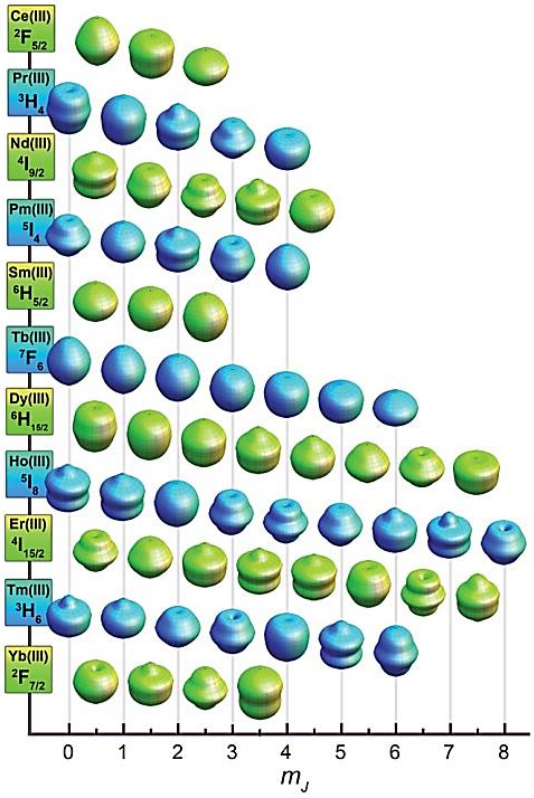

Figure 1.32 Approximations of the angular dependence of the total 4*f* charge density for m_J states composing the lowest spin–orbit coupled (*J*) state for each lanthanide. In the absence of a crystal field, all m_J states for each lanthanide ion are degenerate.[32]

The square antiprismatic (SAP) and the pentagonal bipyramidal (PBP) are amongst the most interesting geometries for the observation of SIM behaviour in lanthanides. In fact, the first Ln-based SIM complexes of Ishikawa *et al.*[44], $[Pc_2Ln^{III}]^-\cdot[TBA]^+$ (Ln = Tb, Dy), adopt a highly-symmetric SAP geometry, which leads to a large separation of the ground and first excited state for the terbium analogue, and hence a large energy barrier. Derivatives of this system showed enhanced SIM properties, with larger energy barriers, as a result of modifications to the phthalocyanine ligand.[81-85] A number of complexes with SAP geometry (near-perfect or distorted) have been reported exhibiting SIM behaviour[74, 80]; such complexes are a series of Dy-β-diketone complexes[86, 87] and complex $Na_9[Er(W_5O_{18})_2]$[71]. More recently, the PBP geometry has attracted a great interest; the first SIM in this geometry was reported in 2013 by J.-L. Liu *et al.*[88], complex $[Zn_2DyL^1_2]NO_3\cdot H_2O$ (L^1 = 2,2',2''-(((nitrilo-tris(ethane-2,1-diyl))tris(azanediyl))tris(methylene))tris-(4-bromo-phenol)). Since then, a number of results including mononuclear complexes in PBP geometry have been reported.[89-95] Experimental and theoretical studies of these results revealed that the energy barrier is enhanced when negatively-charged ligands along the main axis are present, along with weak equatorial bonds.[96]

In 2017 two groups reported the organometallic complex $[(Cp^{ttt})_2Dy^{III}][B(C_6F_5)_4]$ (Cp^{ttt} = 1,2,4-tri(tert-butyl)cyclopentadienide), hereafter referred to as $\{(Cp^{ttt})_2Dy\}$ (Fig. 1.33 left).[97, 98] The synthesis of $\{(Cp^{ttt})_2Dy\}$ includes the abstraction of a chloride ligand from the dysprosium metallocene $[(Cp^{ttt})_2DyCl]$ with the silylium reagent $[H(SiEt_3)_2][B(C_6F_5)_4]$. The $[(Cp^{ttt})_2DyCl]$ complex does not exhibit SMM behaviour, due to the equatorially coordinated chloride on the Dy centre, which leads to strong mixing between the m_J states and therefore significant QTM.[98] However, $\{(Cp^{ttt})_2Dy\}$ displays SIM behaviour with out-of-phase signals up to ~100 K and blocking temperature at ~60 K (open hysteresis loops up to this temperature at sweep rates 22 Oe s^{-1} [97] and 39 Oe s^{-1} [98]).[97, 98] Theoretical calculations revealed the strong axiality of the lower m_J states which efficiently supresses QTM, and hence the thermal relaxation occurs via the higher excited m_J states. This results from the exceptional axiality of the Dy centre with the bis(cyclopentadienyl) ligands and the absence of any ligands in the equatorial plane.[97, 98] The extracted energy barrier was found at ~1807[98] and ~1760[97] K for the different reported results. Furthermore, dynamic studies were also performed on the magnetic diluted samples of $\{(Cp^{ttt})_2Dy\}$, proving that the SIM behaviour is intrinsic to the $[Dy(Cp^{ttt})_2]^+$ cation and is not a result of long-range ordering.[97] Both the energy barrier and the blocking temperature (blocking temperature close to the boiling point of liquid nitrogen, 77 K) were the highest at that point among any reported SMM, thus establishing a new benchmark in the field of molecular-magnetism.[93, 94]

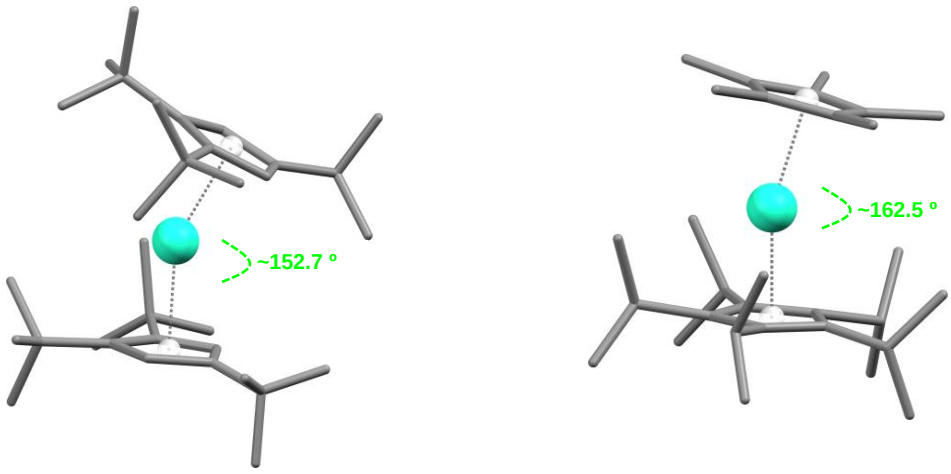

Figure 1.33 *Left)* The molecular structure of the $[Dy(Cp^{ttt})_2]^+$ cation. The centroids of the ligands (= Cp^{ttt}_c) are depicted by white spheres and the green dashed line represents the Cp^{ttt}_c–Dy–Cp^{ttt}_c angle.[97, 98] *Right)* The molecular structure of the $[(\eta^5\text{-}Cp^*)Dy(\eta^5\text{-}Cp^{iPr5})]^+$ cation. The centroids of the ligands (= Cp^*_c and Cp^{iPr5}_c) are depicted by white spheres and the green dashed line represents the Cp^*_c–Dy–Cp^{iPr5}_c angle. [99]

Only one year later, another organometallic complex related to $[(Cp^{ttt})_2Dy^{III}][B(C_6F_5)_4]$ was reported by the Layfield group, complex $[(\eta^5\text{-}Cp^{*})Dy(\eta^5\text{-}Cp^{iPr5})][B(C_6F_5)_4]$ (Cp^{iPr5} = penta-iso-propylcyclopentadienyl and Cp* = pentamethylcyclopentadienyl), hereafter abbreviated as $[Dy\text{-}5^{*}][B(C_6F_5)_4]$ (Fig. 1.33 right).[99] Crystallographic analysis revealed that the distances between the ligands and the Dy centre are on average 0.026 Å shorter than the Dy−ligands distances in $[(Cp^{ttt})_2Dy^{III}][B(C_6F_5)_4]$, while the Cp^{*}_{c}–Dy–Cp^{iPr5}_{c} angle (Cp^{*}_{c} and Cp^{iPr5}_{c} represent the centroids of the ligands) is ~9.7 º wider than the Cp^{ttt}_{c}–Dy–Cp^{ttt}_{c} angle in complex $[(Cp^{ttt})_2Dy^{III}][B(C_6F_5)_4]$ (Cp^{ttt}_{c} represents the centroids of the ligands) as shown in Figure 1.33. Comparing the structural parameters of the two complexes, the SIM properties of $[Dy\text{-}5^{*}][B(C_6F_5)_4]$ are expected to be improved due to the stronger and more axial crystal field (CF) present in $[Dy\text{-}5^{*}][B(C_6F_5)_4]$.[99] Indeed, dynamic studies revealed SIM behaviour with out-of-phase signals up to ~130 K and blocking temperature at ~80 K (open hysteresis loops up to this temperature at sweep rate of 25 Oe s^{-1}). The energy barrier was experimentally and theoretically found to be ~2200 K, which surpasses the energy barrier of $[(Cp^{ttt})_2Dy^{III}][B(C_6F_5)_4]$, and the magnetic relaxation occurs via the fourth exited doublet. Moreover, *ab initio* calculations revealed that due to the low symmetry (C_1 point group) of $[Dy\text{-}5^{*}][B(C_6F_5)_4]$, non-negligible CF parameters are present; however the second-rank parameter B_2^0 is at least two orders of magnitude higher than any other parameter. Hence, a highly axial CF environment is created despite the absence of point symmetry (or pseudosymmetry) that would be needed for a strictly axial CF.[99] This demonstrates that strict point symmetry is not required to achieve a highly axial CF, provided that the axial parameters are sufficiently strong in comparison to the other CF parameters arising from low-symmetry components. Complex $[Dy\text{-}5^{*}][B(C_6F_5)_4]$ overcomes an essential barrier toward the development of nanomagnet devices that function at practical temperatures.[99]

1.4.2 Transition metal SIMs

In contrast to lanthanides, first row transition metal ions possess smaller magnetic moments, lower spin-orbit coupling constants, and strong coupling of the *d*-orbitals to the ligand field.[21, 45] In most cases, due to the low symmetry of the ligand field (LF), the orbital angular momentum is easily quenched thus removing the first-order spin-orbit coupling (SOC). Hence, a strict symmetry of the LF is required in order to preserve the first-order SOC and achieve high magnetic anisotropy.[80] If the LF symmetry is low, the ground state can mix with the excited states through second-order SOC and therefore lead to magnetic anisotropy. In order to enhance 2nd order SOC two factors should be considered: i) increasing the $|D|$ parameter by lowering the energy gap of the first exited state, and ii)

stabilizing the largest m_s state and minimizing the transverse parameter E (the presence of E promotes magnetic relaxation through QTM).[80, 100] Overall, a strong geometrical control around the metal centre is required in order to achieve the desired high magnetic anisotropy.

The first 3*d*-based SIM was the high spin Fe(II) compound K[(tpa^{Mes})Fe] (H_3tpa^{Mes} = Tris((5-mesityl-1Hpyrrol-2-yl)methyl)amine), where the Fe(II) ion centre adopts a trigonal pyramidal geometry with orbital splitting as shown in Figure 1.34.[101] The unequal occupation of the 1e orbitals results in an unquenched orbital angular momentum, therefore a large magnetic anisotropy. Fit of the dc susceptibility data resulted in the axial and the rhombic ZFS parameters, D = −39.6 cm^{-1} and E = −0.4 cm^{-1}, respectively. The nonzero value of E likely arises from the slight distortion away from threefold symmetry of the Fe(II) centre. Dynamic studies revealed slow magnetic relaxation only under an applied dc field with an energy barrier of ~60 K.

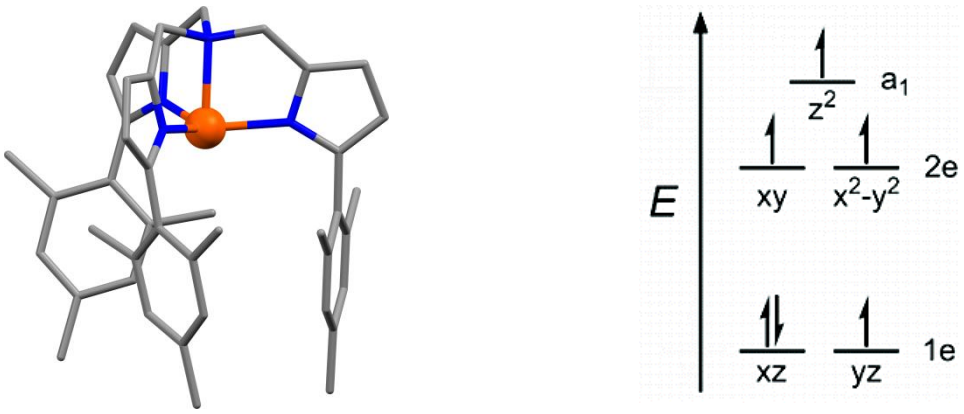

Figure 1.34 *Left)* The structure of the anion [(tpa^{Mes})Fe]$^-$. Colour code: Fe: orange, N: blue and C: grey. Hydrogen atoms are omitted for clarity.[101] *Right)* The splitting of the 3*d* orbital energies for a high-spin Fe^{II} centre in a trigonal pyramidal ligand field. Reprinted with permission from D. E. Freedman, W. H. Harman, T. D. Harris, G. J. Long, C. J. Chang and J. R. Long, *J Am Chem Soc*, 2010, **132**, 1224-1225. Copyright 2019 American Chemical Society.[101]

A theoretical study by S. Gomez-Coca *et al*.[100] shows how the magnetic anisotropy in first-row transition metal complexes can be predicted based on the coordination mode and the electronic configuration of the metal centres. Figure 1.35 shows the estimation of the D values for high-spin mononuclear transition-metal complexes with different electronic configurations and coordination modes using ammonia ligands. Since the first examples of 3*d* complexes exhibiting slow magnetic relaxation were reported[102-106], the number of such compounds studied for SIM properties grew exponentially.[21, 45, 80]

Figure 1.35 Estimation of the *D* values for high-spin mononuclear transition-metal complexes with different electronic configurations and coordination modes using ammonia ligands (using the molecular orbitals of $Fe^{II}(NH_3)_x$ models). Green and blue squares indicate large and small negative values, in that order, while red and orange represent large and small positive values, respectively. Cases with more than one colour indicate that the non-distorted structure has a zero *D* value, and different options are possible depending on the symmetry of the Jahn−Teller distortion. Reprinted with permission from S. Gomez-Coca, E. Cremades, N. Aliaga-Alcalde and E. Ruiz, *J Am Chem Soc*, 2013, **135**, 7010-7018. Copyright 2019 American Chemical Society.[100]

Figure 1.36 shows a summary of transition-metal SIMs, including the energy barriers and the type of magnetic anisotropy.[80] Although the majority of the 3*d*-SIMs are field induced (due to the predominant QTM phenomenon), the study of these complexes gives us an insight into the enhancement of the magnetic anisotropy and the relaxation dynamics; moreover, such complexes give the ability to create strongly coupled spin systems which

potentially offer access to 1, 2 and 3-dimensional materials with interesting structural and physical properties.[21]

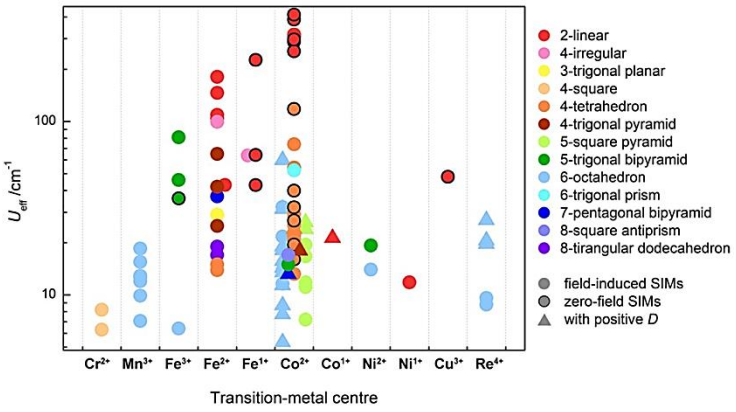

Figure 1.36 The effective barriers of different TM-SIMs with different coordination geometries (presented in different colours). Open form: field-induced SIMs, closed form: zero-field SIMs, triangle: SIMs with positive *D* value, circle: SIMs with negative *D* value and SIMs with unreported *D* value.[80]

Co(II) is a good candidate for the synthesis of complexes exhibiting SIM properties, due to its strong SOC and the fact that it is a Kramers ion (i.e. the QTM mechanism is in theory forbidden).[107] Depending on the coordination number and the geometry adopted, Co(II) can exhibit first- or second-order SOC leading to a large magnetic anisotropy. It is clear from Figure 1.36 that Co(II) is one of the most explored transition metals for SIM behaviour. In fact a two-coordinate linear Co(II) complex holds, so far, the record for the highest energy barrier in 3*d*-SIMs. Complex [(sIPr)Co^{II}NDmp][108] (sIPr = 1,3-bis(2,6-diisopropylphenyl)-4,5-dihydro-imidazole-2-ylidene, Dmp = 2,6-dimesitylphenyl) adopts a near linear C_{arene}−N_{imido}−Co−$C_{carbene}$ alignment (Fig. 1.37), with Co−N_{imido} and Co−$C_{carbene}$ distances of ~1.68 Å and ~1.97 Å, respectively. Structural analysis suggests high covalency of the Co−N_{imido} bond. Dynamic ac susceptibility studies revealed slow magnetic relaxation in zero applied dc field with an energy barrier of ~594 K (413 cm^{-1}) and open hysteresis loops until 9.5 K. Interestingly, the dc magnetic data were not able to be fitted with the spin-only Hamiltonian of *S* = 3/2, which indicates that the large ZFS results from the first-order SOC. This was ascribed to the [CoN]$^{+}$ moiety and was confirmed by theoretical calculations (although the authors do not exclude the simple ion model).[108] The large unquenched orbital angular momentum results in a m_J = ±7/2 ground state, and the calculated energy gap between the ground and first excited states is in agreement with the experimentally found energy barrier.

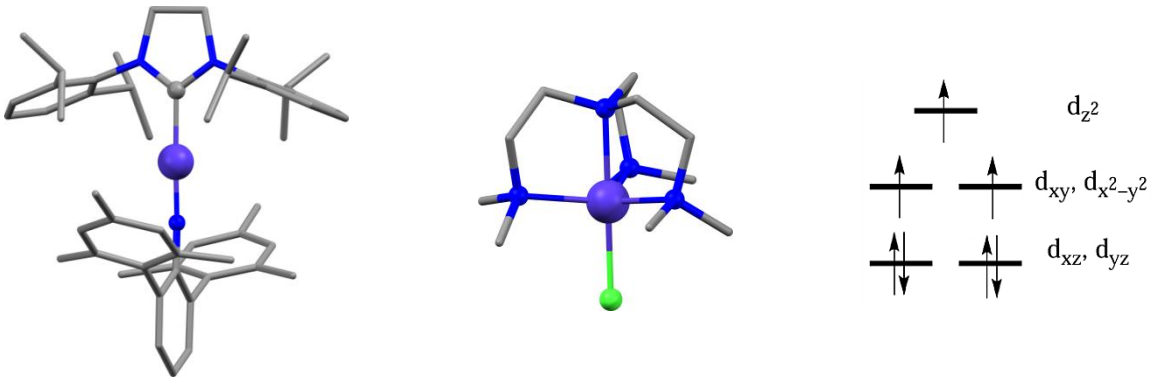

Figure 1.37 *Left)* The molecular structure of complex [(sIPr)Co^{II}NDmp].[108] *Middle)* The molecular structure of [Co(Me$_6$tren)Cl]$^+$ cation.[109] Colour code: Co: violet, N: blue, Cl: green, C: grey. Hydrogen atoms are omitted for clarity. *Right)* Removal of the degeneracy of the *d* orbitals in a trigonal bipyramidal (C_{3v}) crystal field.[109]

Recently, the trigonal bipyramidal (TBP) geometry has attracted a great interest in 3*d*-SIMs, especially for Ni(II) and Co(II) complexes[109-114] for which a large negative and large positive *D* value is predicted, respectively (Fig. 1.35).[100] Despite the positive *D* predicted for Co(II) complexes, it has been experimentally and theoretically observed that by enforcing C_3 symmetry an easy-axis (or Ising-type) magnetic anisotropy can be promoted, while the transverse parameter *E* could potentially be negligible. R. Ruamps *et al.* reported complexes [Co(Me$_6$tren)Cl]ClO$_4$ and [Co(Me$_6$tren)Br]Br (Me$_6$tren = tris[2-(dimethylamino)ethyl]amine), in which Co adopts a TBP geometry imposing an axial symmetry, with three N atoms in the equatorial plane, while one N and one halide atom (Cl^- or Br^-) occupy the axial positions.[109] Both complexes exhibit slow magnetic relaxation in zero applied dc field and hysteresis loops at very low T for [Co(Me$_6$tren)Cl]ClO$_4$. Theoretical and experimental investigations demonstrated the following: i) an easy-axis magnetic anisotropy is promoted by the axial symmetry imposed by the coordinating ligands, ii) the energy difference between the (d_{xz}, d_{yz}) and ($d_{x^2-y^2}$, d_{xy}) orbital sets is responsible for the magnitude of *D*, and iii) the presence of strong π-donating ligands at axial positions and weaker σ-donating ligands in equatorial positions yields an overall high and negative magnetic anisotropy.[109] Taking into consideration the above, ligand tris-(2-(isopropylthio)ethyl)amine (= NS$_3^{iPr}$) was chosen by F. Shao *et al.* in order to impose TBP geometry with weaker σ-donor atoms in the equatorial plane, and the complex [Co(NS$_3^{iPr}$)Cl](BPh$_4$) was obtained.[113] Indeed, the Co centre adopts a pseudo C_3 molecular symmetry axis, with three S atoms in the equatorial plane and one N and one Cl^- ligand in axial positions. Experimental and theoretical studies confirmed that the presence of weaker σ-donor atoms causes the decrease of the energy difference between the (d_{xz}, d_{yz}) and ($d_{x^2-y^2}$, d_{xy}) orbital sets and the increase of the energy gap between the ground state

orbitals (d_{xz}, d_{yz}) and the d_{z^2}. This results in the enhancement of the magnetic anisotropy, $D \approx -20$ cm^{-1}, in comparison with complex [Co(Me$_6$tren)Cl]ClO$_4$ with $D \approx -8$ cm^{-1}; this also translates into a higher energy barrier of 46 K compared with that of 23 K of complex [Co(Me$_6$tren)Cl]ClO$_4$ (despite the presence of non-zero E parameter).[113] Some representative examples of Co(II) complexes in TBP geometry can be found in Table 1.1. Finally, a variety of Co(II) geometries such as tetrahedral, square pyramidal and trigonal prism have also been found to exhibit slow magnetic relaxation and interesting SIM properties.[115]

Table 1.1 Selected examples of Co(II) complexes in TBP geometry with their coordination environment and the type of magnetic anisotropy (easy-axis, D<0, or easy plane, D>0).

Complex	Coordination environment	*D*	Ref.
[Co(terpy)(NCS)$_2$]	{N$_5$}	–	116
[(γ-CD)$_2$Co$_4$Li(H$_2$O)$_{12}$]	{O$_5$}	+	117
[Co(tbta)N$_3$]ClO$_4$·3MeCN	{N$_5$}	–	118
[Co(phen)(DMSO)Cl$_2$]	{N$_2$Cl$_2$O}	–	119
[Co(TPMA)(MeCN)](BF$_4$)$_2$·MeCN	{N$_5$}	+	120
[Co(TPMA)Cl]·Cl	{N$_4$Cl}	–	120
[Co(TPMA)Br]·Br	{N$_4$Br}	–	120
[Co(TPMA)I]·I	{N$_4$I}	–	120
[Co(TPTA)(N$_3$)](ClO$_4$)	{N$_5$}	–	121
[Co(Me$_4$cyclam)N$_3$]ClO$_4$	{N$_5$}	+	114
[Co(bbp)(NCS)$_2$]	{N$_5$}	+	28
[CoCl$_3$(HDABCO)(DABCO)]	{N$_2$Cl$_3$}	+	122

terpy = terpyridine
γ-CD = γ-cyclodextrin
tbta = tris[(1-benzyl-1H-1,2,3-triazol-4-yl)methyl]amine
phen = 1,10-phenanthroline
TPMA = tris(2-pyridylmethyl)amine
TPTA = tris[(1-phenyl-1H-1,2,3-triazol-4-yl)methyl]amine
Me$_4$cyclam = tetramethylcyclam
bbp = 2,6-bis(2- benzimidazolyl)pyridine
DABCO = 1,4-diazabicyclo[2.2.2]octane

1.5 References

1. R. H. Holm, P. Kennepohl and E. I. Solomon, *Chemical Reviews*, 1996, **96**, 2239-2314.
2. S. Vaddypally, S. K. Kondaveeti and M. J. Zdilla, *Inorganic Chemistry*, 2012, **51**, 3950-3952.
3. N. S. McCool, D. M. Robinson, J. E. Sheats and G. C. Dismukes, *Journal of the American Chemical Society*, 2011, **133**, 11446-11449.
4. H. Seino and M. Hidai, *Chemical Science*, 2011, **2**, 847-857.
5. B. Gerey, E. Gouré, J. Fortage, J. Pécaut and M.-N. Collomb, *Coordination Chemistry Reviews*, 2016, **319**, 1-24.
6. J. Ferrando-Soria, J. Vallejo, M. Castellano, J. Martínez-Lillo, E. Pardo, J. Cano, I. Castro, F. Lloret, R. Ruiz-García and M. Julve, *Coordination Chemistry Reviews*, 2017, **339**, 17-103.
7. Y.-Z. Zheng, G.-J. Zhou, Z. Zheng and R. E. P. Winpenny, *Chemical Society Reviews*, 2014, **43**, 1462-1475.
8. Y.-Z. Zheng, E. M. Pineda, M. Helliwell and R. E. P. Winpenny, *Chemistry – A European Journal*, 2012, **18**, 4161-4165.
9. G. Guthausen, J. R. Machado, B. Luy, A. Baniodeh, A. K. Powell, S. Krämer, F. Ranzinger, M. P. Herrling, S. Lackner and H. Horn, *Dalton Transactions*, 2015, **44**, 5032-5040.
10. A. Dei and D. Gatteschi, *Angewandte Chemie International Edition*, 2011, **50**, 11852-11858.
11. R. Vincent, S. Klyatskaya, M. Ruben, W. Wernsdorfer and F. Balestro, *Nature*, 2012, **488**, 357.
12. V. K. Joshi, *Engineering Science and Technology, an International Journal*, 2016, **19**, 1503-1513.
13. D. W. Bruce, D. O'Hare and R. I. Walton, *Molecular Materials*, John Wiley & Sons, Ltd, Chichester, 2010.
14. R. L. Carlin, *Magnetochemistry*, Springer-Verlag Berlin Heidelberg, 1986.
15. O. Kahn, *Molecular Magnetism*, VCH Publishers, New York, 1993.
16. C. Benelli and D. Gatteschi, *Introduction to Molecular Magnetism*, Wiley-VCH Verlag GmbH & Co. KGaA, Boschstr. 12, 69469 Weinheim, Germany, 2015.
17. D. Gatteschi, R. Sessoli and J. Villain, *Molecular Nanomagnets*, OUP Oxford, Oxford, 2006.
18. T. Gupta and G. Rajaraman, *Chemical Communications*, 2016, **52**, 8972-9008.
19. C. J. Milios and R. E. P. Winpenny, in *Molecular Nanomagnets and Related Phenomena*, ed. S. Gao, Springer Berlin Heidelberg, Berlin, Heidelberg, 2015, pp. 1-109.
20. F. Neese and D. A. Pantazis, *Faraday Discussions*, 2011, **148**, 229-238.
21. J. M. Frost, K. L. M. Harriman and M. Murugesu, *Chemical Science*, 2016, **7**, 2470-2491.
22. J. Tang and P. Zhang, *Lanthanide Single Molecule Magnets*, Springer, Berlin, Heidelberg, Springer-Verlag Berlin Heidelberg 2015, 2015.
23. Y.-N. Guo, G.-F. Xu, Y. Guo and J. Tang, *Dalton Transactions*, 2011, **40**, 9953-9963.

24. Y.-Z. Zhang, S. Gómez-Coca, A. J. Brown, M. R. Saber, X. Zhang and K. R. Dunbar, *Chemical Science*, 2016, **7**, 6519-6527.
25. E. Colacio, J. Ruiz, E. Ruiz, E. Cremades, J. Krzystek, S. Carretta, J. Cano, T. Guidi, W. Wernsdorfer and E. K. Brechin, *Angewandte Chemie International Edition*, 2013, **52**, 9130-9134.
26. L. Chen, S.-Y. Chen, Y.-C. Sun, Y.-M. Guo, L. Yu, X.-T. Chen, Z. Wang, Z. W. Ouyang, Y. Song and Z.-L. Xue, *Dalton Transactions*, 2015, **44**, 11482-11490.
27. D. Shao, S.-L. Zhang, L. Shi, Y.-Q. Zhang and X.-Y. Wang, *Inorganic Chemistry*, 2016, **55**, 10859-10869.
28. A. K. Mondal, T. Goswami, A. Misra and S. Konar, *Inorganic Chemistry*, 2017, **56**, 6870-6878.
29. K. S. Pedersen, J. Dreiser, H. Weihe, R. Sibille, H. V. Johannesen, M. A. Sørensen, B. E. Nielsen, M. Sigrist, H. Mutka, S. Rols, J. Bendix and S. Piligkos, *Inorganic Chemistry*, 2015, **54**, 7600-7606.
30. D. Errulat, R. Marin, D. A. Gálico, K. L. M. Harriman, A. Pialat, B. Gabidullin, F. Iikawa, O. D. D. Couto, J. O. Moilanen, E. Hemmer, F. A. Sigoli and M. Murugesu, *ACS Central Science*, 2019.
31. N. E. Chakov, M. Soler, W. Wernsdorfer, K. A. Abboud and G. Christou, *Inorganic Chemistry*, 2005, **44**, 5304-5321.
32. J. D. Rinehart and J. R. Long, *Chemical Science*, 2011, **2**, 2078-2085.
33. T. Lis, *Acta Crystallographica Section B*, 1980, **36**, 2042-2046.
34. R. Sessoli, D. Gatteschi, A. Caneschi and M. A. Novak, *Nature*, 1993, **365**, 141-143.
35. R. Sessoli, H. L. Tsai, A. R. Schake, S. Wang, J. B. Vincent, K. Folting, D. Gatteschi, G. Christou and D. N. Hendrickson, *Journal of the American Chemical Society*, 1993, **115**, 1804-1816.
36. A. Caneschi, D. Gatteschi, R. Sessoli, A. L. Barra, L. C. Brunel and M. Guillot, *Journal of the American Chemical Society*, 1991, **113**, 5873-5874.
37. G. Aromí and E. K. Brechin, in *Single-Molecule Magnets and Related Phenomena*, ed. R. Winpenny, Springer Berlin Heidelberg, Berlin, Heidelberg, 2006, pp. 1-67.
38. A. J. Tasiopoulos, A. Vinslava, W. Wernsdorfer, K. A. Abboud and G. Christou, *Angewandte Chemie International Edition*, 2004, **43**, 2117-2121.
39. A. M. Ako, I. J. Hewitt, V. Mereacre, R. Clérac, W. Wernsdorfer, C. E. Anson and A. K. Powell, *Angewandte Chemie International Edition*, 2006, **45**, 4926-4929.
40. M. Manoli, S. Alexandrou, L. Pham, G. Lorusso, W. Wernsdorfer, M. Evangelisti, G. Christou and A. J. Tasiopoulos, *Angewandte Chemie International Edition*, 2016, **55**, 679-684.
41. S. Kang, H. Zheng, T. Liu, K. Hamachi, S. Kanegawa, K. Sugimoto, Y. Shiota, S. Hayami, M. Mito, T. Nakamura, M. Nakano, M. L. Baker, H. Nojiri, K. Yoshizawa, C. Duan and O. Sato, *Nature Communications*, 2015, **6**, 5955.
42. A. Baniodeh, N. Magnani, Y. Lan, G. Buth, C. E. Anson, J. Richter, M. Affronte, J. Schnack and A. K. Powell, *npj Quantum Materials*, 2018, **3**, 10.

43. W.-P. Chen, J. Singleton, L. Qin, A. Camón, L. Engelhardt, F. Luis, R. E. P. Winpenny and Y.-Z. Zheng, *Nature Communications*, 2018, **9**, 2107.
44. N. Ishikawa, M. Sugita, T. Ishikawa, S.-y. Koshihara and Y. Kaizu, *Journal of the American Chemical Society*, 2003, **125**, 8694-8695.
45. G. A. Craig and M. Murrie, *Chemical Society Reviews*, 2015, **44**, 2135-2147.
46. N. Koike, H. Uekusa, Y. Ohashi, C. Harnoode, F. Kitamura, T. Ohsaka and K. Tokuda, *Inorganic Chemistry*, 1996, **35**, 5798-5804.
47. D. N. Woodruff, R. E. P. Winpenny and R. A. Layfield, *Chemical Reviews*, 2013, **113**, 5110-5148.
48. S. Jank, H. Reddmann and H. D. Amberger, *Inorganica Chimica Acta*, 2008, **361**, 2154-2158.
49. C. J. Milios, A. Vinslava, W. Wernsdorfer, S. Moggach, S. Parsons, S. P. Perlepes, G. Christou and E. K. Brechin, *Journal of the American Chemical Society*, 2007, **129**, 2754-2755.
50. C. J. Milios, R. Inglis, A. Vinslava, R. Bagai, W. Wernsdorfer, S. Parsons, S. P. Perlepes, G. Christou and E. K. Brechin, *Journal of the American Chemical Society*, 2007, **129**, 12505-12511.
51. S. Carretta, T. Guidi, P. Santini, G. Amoretti, O. Pieper, B. Lake, J. van Slageren, F. E. Hallak, W. Wernsdorfer, H. Mutka, M. Russina, C. J. Milios and E. K. Brechin, *Physical Review Letters*, 2008, **100**, 157203.
52. S. Bahr, C. J. Milios, L. F. Jones, E. K. Brechin, V. Mosser and W. Wernsdorfer, *Physical Review B*, 2008, **78**, 132401.
53. S. Osa, T. Kido, N. Matsumoto, N. Re, A. Pochaba and J. Mrozinski, *Journal of the American Chemical Society*, 2004, **126**, 420-421.
54. C. M. Zaleski, E. C. Depperman, J. W. Kampf, M. L. Kirk and V. L. Pecoraro, *Angewandte Chemie International Edition*, 2004, **43**, 3912-3914.
55. R. Sessoli and A. K. Powell, *Coordination Chemistry Reviews*, 2009, **253**, 2328-2341.
56. J. W. Sharples and D. Collison, *Coordination Chemistry Reviews*, 2014, **260**, 1-20.
57. K. Liu, W. Shi and P. Cheng, *Coordination Chemistry Reviews*, 2015, **289-290**, 74-122.
58. L. Rosado Piquer and E. C. Sañudo, *Dalton Transactions*, 2015, **44**, 8771-8780.
59. V. Mereacre, A. M. Ako, R. Clérac, W. Wernsdorfer, I. J. Hewitt, C. E. Anson and A. K. Powell, *Chemistry – A European Journal*, 2008, **14**, 3577-3584.
60. Y. Peng, M. K. Singh, V. Mereacre, C. E. Anson, G. Rajaraman and A. K. Powell, *Chemical Science*, 2019, **10**, 5528-5538.
61. S. K. Langley, N. F. Chilton, L. Ungur, B. Moubaraki, L. F. Chibotaru and K. S. Murray, *Inorganic Chemistry*, 2012, **51**, 11873-11881.
62. K. R. Vignesh, S. K. Langley, K. S. Murray and G. Rajaraman, *Chemistry – A European Journal*, 2017, **23**, 1654-1666.
63. S. K. Langley, D. P. Wielechowski, V. Vieru, N. F. Chilton, B. Moubaraki, B. F. Abrahams, L. F. Chibotaru and K. S. Murray, *Angewandte Chemie International Edition*, 2013, **52**, 12014-12019.

64. X.-L. Li, F.-Y. Min, C. Wang, S.-Y. Lin, Z. Liu and J. Tang, *Inorganic Chemistry*, 2015, **54**, 4337-4344.
65. F. Pointillart, K. Bernot, R. Sessoli and D. Gatteschi, *Chemistry – A European Journal*, 2007, **13**, 1602-1609.
66. J.-L. Liu, J.-Y. Wu, Y.-C. Chen, V. Mereacre, A. K. Powell, L. Ungur, L. F. Chibotaru, X.-M. Chen and M.-L. Tong, *Angewandte Chemie International Edition*, 2014, **53**, 12966-12970.
67. J. Tang, I. Hewitt, N. T. Madhu, G. Chastanet, W. Wernsdorfer, C. E. Anson, C. Benelli, R. Sessoli and A. K. Powell, *Angewandte Chemie International Edition*, 2006, **45**, 1729-1733.
68. J. Luzon, K. Bernot, I. J. Hewitt, C. E. Anson, A. K. Powell and R. Sessoli, *Physical Review Letters*, 2008, **100**, 247205.
69. R. J. Blagg, C. A. Muryn, E. J. L. McInnes, F. Tuna and R. E. P. Winpenny, *Angewandte Chemie International Edition*, 2011, **50**, 6530-6533.
70. R. J. Blagg, L. Ungur, F. Tuna, J. Speak, P. Comar, D. Collison, W. Wernsdorfer, E. J. L. McInnes, L. F. Chibotaru and R. E. P. Winpenny, *Nature Chemistry*, 2013, **5**, 673.
71. M. A. AlDamen, J. M. Clemente-Juan, E. Coronado, C. Martí-Gastaldo and A. Gaita-Ariño, *Journal of the American Chemical Society*, 2008, **130**, 8874-8875.
72. J. D. Rinehart, M. Fang, W. J. Evans and J. R. Long, *Nature Chemistry*, 2011, **3**, 538.
73. J. D. Rinehart, M. Fang, W. J. Evans and J. R. Long, *Journal of the American Chemical Society*, 2011, **133**, 14236-14239.
74. J.-L. Liu, Y.-C. Chen and M.-L. Tong, *Chemical Society Reviews*, 2018, **47**, 2431-2453.
75. J. C. Goodwin, R. Sessoli, D. Gatteschi, W. Wernsdorfer, A. K. Powell and S. L. Heath, *Journal of the Chemical Society, Dalton Transactions*, 2000, 1835-1840.
76. E. C. Sañudo, W. Wernsdorfer, K. A. Abboud and G. Christou, *Inorganic Chemistry*, 2004, **43**, 4137-4144.
77. O. Waldmann, *Inorganic Chemistry*, 2007, **46**, 10035-10037.
78. P. Parois, S. A. Moggach, J. Sanchez-Benitez, K. V. Kamenev, A. R. Lennie, J. E. Warren, E. K. Brechin, S. Parsons and M. Murrie, *Chemical Communications*, 2010, **46**, 1881-1883.
79. J. Sievers, *Zeitschrift für Physik B Condensed Matter*, 1982, **45**, 289-296.
80. M. Feng and M.-L. Tong, *Chemistry – A European Journal*, 2018, **24**, 7574-7594.
81. N. Ishikawa, M. Sugita, N. Tanaka, T. Ishikawa, S.-y. Koshihara and Y. Kaizu, *Inorganic Chemistry*, 2004, **43**, 5498-5500.
82. S. Takamatsu, T. Ishikawa, S.-Y. Koshihara and N. Ishikawa, *Inorganic Chemistry*, 2007, **46**, 7250-7252.
83. M. Gonidec, F. Luis, À. Vílchez, J. Esquena, D. B. Amabilino and J. Veciana, *Angewandte Chemie International Edition*, 2010, **49**, 1623-1626.
84. M. Gonidec, D. B. Amabilino and J. Veciana, *Dalton Transactions*, 2012, **41**, 13632-13639.
85. C. R. Ganivet, B. Ballesteros, G. de la Torre, J. M. Clemente-Juan, E. Coronado and T. Torres, *Chemistry – A European Journal*, 2013, **19**, 1457-1465.
86. S.-D. Jiang, B.-W. Wang, G. Su, Z.-M. Wang and S. Gao, *Angewandte Chemie International Edition*, 2010, **49**, 7448-7451.

87. Y. Bi , Y.-N. Guo, L. Zhao, Y. Guo, S.-Y. Lin, S.-D. Jiang, J. Tang, B.-W. Wang and S. Gao, *Chemistry – A European Journal*, 2011, **17**, 12476-12481.
88. J.-L. Liu, Y.-C. Chen, Y.-Z. Zheng, W.-Q. Lin, L. Ungur, W. Wernsdorfer, L. F. Chibotaru and M.-L. Tong, *Chemical Science*, 2013, **4**, 3310-3316.
89. Y.-C. Chen, J.-L. Liu, L. Ungur, J. Liu, Q.-W. Li, L.-F. Wang, Z.-P. Ni, L. F. Chibotaru, X.-M. Chen and M.-L. Tong, *Journal of the American Chemical Society*, 2016, **138**, 2829-2837.
90. Y.-S. Ding, N. F. Chilton, R. E. P. Winpenny and Y.-Z. Zheng, *Angewandte Chemie International Edition*, 2016, **55**, 16071-16074.
91. S. K. Gupta, T. Rajeshkumar, G. Rajaraman and R. Murugavel, *Chemical Science*, 2016, **7**, 5181-5191.
92. J. Liu, Y.-C. Chen, J.-L. Liu, V. Vieru, L. Ungur, J.-H. Jia, L. F. Chibotaru, Y. Lan, W. Wernsdorfer, S. Gao, X.-M. Chen and M.-L. Tong, *Journal of the American Chemical Society*, 2016, **138**, 5441-5450.
93. Y.-C. Chen, J.-L. Liu, Y. Lan, Z.-Q. Zhong, A. Mansikkamäki, L. Ungur, Q.-W. Li, J.-H. Jia, L. F. Chibotaru, J.-B. Han, W. Wernsdorfer, X.-M. Chen and M.-L. Tong, *Chemistry – A European Journal*, 2017, **23**, 5708-5715.
94. Y.-C. Chen, J.-L. Liu, W. Wernsdorfer, D. Liu, L. F. Chibotaru, X.-M. Chen and M.-L. Tong, *Angewandte Chemie International Edition*, 2017, **56**, 4996-5000.
95. A. B. Canaj, M. K. Singh, C. Wilson, G. Rajaraman and M. Murrie, *Chemical Communications*, 2018, **54**, 8273-8276.
96. S. G. McAdams, A.-M. Ariciu, A. K. Kostopoulos, J. P. S. Walsh and F. Tuna, *Coordination Chemistry Reviews*, 2017, **346**, 216-239.
97. C. A. P. Goodwin, F. Ortu, D. Reta, N. F. Chilton and D. P. Mills, *Nature*, 2017, **548**, 439.
98. F.-S. Guo, B. M. Day, Y.-C. Chen, M.-L. Tong, A. Mansikkamäki and R. A. Layfield, *Angewandte Chemie International Edition*, 2017, **56**, 11445-11449.
99. F.-S. Guo, B. M. Day, Y.-C. Chen, M.-L. Tong, A. Mansikkamäki and R. A. Layfield, *Science*, 2018, **362**, 1400-1403.
100. S. Gomez-Coca, E. Cremades, N. Aliaga-Alcalde and E. Ruiz, *Journal of the American Chemical Society*, 2013, **135**, 7010-7018.
101. D. E. Freedman, W. H. Harman, T. D. Harris, G. J. Long, C. J. Chang and J. R. Long, *Journal of the American Chemical Society*, 2010, **132**, 1224-1225.
102. T. Jurca, A. Farghal, P.-H. Lin, I. Korobkov, M. Murugesu and D. S. Richeson, *Journal of the American Chemical Society*, 2011, **133**, 15814-15817.
103. P.-H. Lin, N. C. Smythe, S. I. Gorelsky, S. Maguire, N. J. Henson, I. Korobkov, B. L. Scott, J. C. Gordon, R. T. Baker and M. Murugesu, *Journal of the American Chemical Society*, 2011, **133**, 15806-15809.
104. J. M. Zadrozny and J. R. Long, *Journal of the American Chemical Society*, 2011, **133**, 20732-20734.
105. J. Vallejo, I. Castro, R. Ruiz-García, J. Cano, M. Julve, F. Lloret, G. De Munno, W. Wernsdorfer and E. Pardo, *Journal of the American Chemical Society*, 2012, **134**, 15704-15707.

106. J. M. Zadrozny, D. J. Xiao, M. Atanasov, G. J. Long, F. Grandjean, F. Neese and J. R. Long, *Nature Chemistry*, 2013, **5**, 577.
107. D. Gatteschi and R. Sessoli, *Angewandte Chemie International Edition*, 2003, **42**, 268-297.
108. X.-N. Yao, J.-Z. Du, Y.-Q. Zhang, X.-B. Leng, M.-W. Yang, S.-D. Jiang, Z.-X. Wang, Z.-W. Ouyang, L. Deng, B.-W. Wang and S. Gao, *Journal of the American Chemical Society*, 2017, **139**, 373-380.
109. R. Ruamps, L. J. Batchelor, R. Guillot, G. Zakhia, A.-L. Barra, W. Wernsdorfer, N. Guihéry and T. Mallah, *Chem Sci*, 2014, **5**, 3418-3424.
110. R. Ruamps, R. Maurice, L. Batchelor, M. Boggio-Pasqua, R. Guillot, A. L. Barra, J. Liu, E.-E. Bendeif, S. Pillet, S. Hill, T. Mallah and N. Guihéry, *Journal of the American Chemical Society*, 2013, **135**, 3017-3026.
111. M. Gruden-Pavlović, M. Perić, M. Zlatar and P. García-Fernández, *Chemical Science*, 2014, **5**, 1453-1462.
112. K. E. R. Marriott, L. Bhaskaran, C. Wilson, M. Medarde, S. T. Ochsenbein, S. Hill and M. Murrie, *Chemical Science*, 2015, **6**, 6823-6828.
113. F. Shao, B. Cahier, N. Guihéry, E. Rivière, R. Guillot, A.-L. Barra, Y. Lan, W. Wernsdorfer, V. E. Campbell and T. Mallah, *Chemical Communications*, 2015, **51**, 16475-16478.
114. B. Cahier, M. Perfetti, G. Zakhia, D. Naoufal, F. El-Khatib, R. Guillot, E. Rivière, R. Sessoli, A.-L. Barra, N. Guihéry and T. Mallah, *Chemistry – A European Journal*, 2017, **23**, 3648-3657.
115. S. Tripathi, A. Dey, M. Shanmugam, R. Suriya Narayanan and V. Chandrsekhar, ch. Cobalt(II) Complexes as Single-Ion Magnets, in *Topics in Organometallic Chemistry.* , Springer, Berlin, Heidelberg, 2018.
116. F. Habib, O. R. Luca, V. Vieru, M. Shiddiq, I. Korobkov, S. I. Gorelsky, M. K. Takase, L. F. Chibotaru, S. Hill, R. H. Crabtree and M. Murugesu, *Angewandte Chemie International Edition*, 2013, **52**, 11290-11293.
117. N. Nedelko, A. Kornowicz, I. Justyniak, P. Aleshkevych, D. Prochowicz, P. Krupiński, O. Dorosh, A. Ślawska-Waniewska and J. Lewiński, *Inorganic Chemistry*, 2014, **53**, 12870-12876.
118. D. Schweinfurth, M. G. Sommer, M. Atanasov, S. Demeshko, S. Hohloch, F. Meyer, F. Neese and B. Sarkar, *Journal of the American Chemical Society*, 2015, **137**, 1993-2005.
119. I. Nemec, R. Marx, R. Herchel, P. Neugebauer, J. van Slageren and Z. Trávníček, *Dalton Transactions*, 2015, **44**, 15014-15021.
120. T. J. Woods, M. F. Ballesteros-Rivas, S. Gómez-Coca, E. Ruiz and K. R. Dunbar, *Journal of the American Chemical Society*, 2016, **138**, 16407-16416.
121. M. G. Sommer, R. Marx, D. Schweinfurth, Y. Rechkemmer, P. Neugebauer, M. van der Meer, S. Hohloch, S. Demeshko, F. Meyer, J. van Slageren and B. Sarkar, *Inorganic Chemistry*, 2017, **56**, 402-413.
122. M. A. Hay, A. Sarkar, G. A. Craig, L. Bhaskaran, J. Nehrkorn, M. Ozerov, K. E. R. Marriott, C. Wilson, G. Rajaraman, S. Hill and M. Murrie, *Chemical Science*, 2019, **10**, 6354-6361.

Chapter 2

Physical methods and techniques

Contents

Chapter 2: Physical methods and techniques

2. Physical methods and techniques

Note: In this chapter all complexes are mentioned only by the number of each complex without the co-crystallised solvents for simplicity (except **2**·12H_2O which is needed to be distinguished from complex **2**).

2.1 Elemental analysis

All CHN microanalyses were performed in-house by the analytical services at the School of Chemistry, University of Glasgow, on an Exeter CE-440 Elemental Analyser.

2.2 Energy-dispersive X-ray (EDX) spectroscopy

EDX experiments were performed on crystalline samples of complexes **21**, **22** and **23** using a Philips XL 30 Environmental Scanning Electron Microscope (ESEM) at various magnifications with images taken using W-Kα radiation (57981.77 eV) with a secondary electron detector and Oxford Instruments INCA 250Xact10 EDX detector. Prior to analysis the samples were gold-coated using a vacuum electric sputter coater (POLARON SC 7640), in order to avoid charging.

2.3 High-field/frequency Electron Paramagnetic Resonance (HFEPR)

HFEPR spectra were collected on a microcrystalline powder sample of **4**, which was immobilized in a polyethylene cup with a Teflon® stopper. The transmission-type spectrometer used in this study employed a 17 T superconducting magnet.[1] Microwave frequencies were generated in the 48 to 615 GHz range using a phase-locked Virginia Diodes source combined with a series of frequency multipliers. The field modulated EPR signal, *dI*/*dB* (where *I* represents the absorption intensity and *B* the magnetic field strength), was obtained via lock-in detection using an InSb hot-electron bolometer (QMC Ltd., Cardiff, U.K.). Variable temperature measurements were performed in the range from 2 to 20 K using an Oxford Instruments (Oxford, U.K.) continuous-flow cryostat.

2.4 Nuclear Magnetic Resonance (NMR) spectroscopy

The ^{1}H−NMR of the ligand [H_5L]·3Cl (= 2,6-bis[4(1-*N*-phenyl-3-methyl-pyrazolium-5-one)carbonyl]pyridinium trichloride) was obtained using a Bruker AVI 400M MHz.

2.5 Powder X-ray Diffraction (PXRD)

PXRD measurements were carried out at room temperature using a PANalytical X'Pert PRO MPD diffractometer (λ (CuKα) = 1.5405 Å) on a mounted bracket sample stage over the range of 3 º < 2θ < 40 º (the range may vary depending on the studied complex) using a step size of 0.0334°. The calculated patterns were generated from Mercury using the CIF of the crystal structures.[2] In the case of the air-sensitive complexes **2**, **13**, **15**, **16** and **17**, the samples were prepared under an inert atmosphere and the measurements were carried out using a Bruker airtight specimen holder.

2.6 Single-Crystal X-ray Diffraction (SCXRD)

Crystallographic data for complexes **2**, **2**·12H_2O, **5**, **11**, **18**, **19**, **23** and **24** were collected by the National Crystallography Service (NCS) at the University of Southampton.[3]

- For complexes **2**, **2**·12H_2O and **18**, a Rigaku FRE+ equipped with VHF Varimax confocal mirrors and an AFC12 goniometer and HG Saturn 724+ detector diffractometer was used; cell refinement, data collection, and data reduction for **2** and **2**·12H_2O were performed using CrysAllisPro 1.171.39.9g (Rigaku Oxford Diffraction, 2015), and for **18** using CrysAlisPro 1.171.39.34b (Rigaku Oxford Diffraction, 2017).
- For complex **5** a Rigaku FRE+ equipped with VHF Varimax confocal mirrors and an AFC10 goniometer and HG Saturn 724+ detector was used; cell refinement, data collection, and data reduction for **5** were performed using CrysAlisPro 1.171.38.43 (Rigaku Oxford Diffraction, 2015)
- For complexes **11**, **19** and **23** a Rigaku 007HF equipped with Varimax confocal mirrors and an AFC11 goniometer and HyPix 6000 detector was used. Cell refinement, data collection, and data reduction for **11** were performed using CrysAlisPRO 1.171.39.46b (Rigaku Oxford Diffraction, 2018), for **19** using CrysAlisPro 1.171.40.47a (Rigaku Oxford Diffraction, 2019) and for **23** using CrysAlisPro 1.171.40.18b (Rigaku Oxford Diffraction, 2018).
- For complex **24** a Rigaku FRE+ equipped with VHF Varimax confocal mirrors and an AFC12 goniometer and HyPix 6000 detector was used; cell refinement, data collection, and data reduction for **24** were performed using CrysAlisPro 1.171.39.34b (Rigaku Oxford Diffraction, 2017).

Crystallographic data for **4** were collected using a Nonius Kappa CCD diffractometer with an Oxford Cryosystems cryostream low temperature device. Data collection: COLLECT; cell refinement: SAINT v8.34A; data reduction: SAINT v8.34A.[4]

Crystallographic data for **6**, **7**, **8**, **9a**, **9b**, **12** – **17**, **20**, **21** and **22** were collected using a Bruker D8 VENTURE diffractometer equipped with a Photon II CMOS detector with an Oxford Cryosystems N-Helix device mounted on a dual Cu and Mo IμS 3.0 microfocus sealed tube generator. Data collection: APEX3 Ver. 2016.9-0 (Bruker-AXS, 2016); cell refinement: SAINT V8.37A (Bruker-AXS, 2016); data reduction: SHELXS97 (Sheldrick 2008).

All structures were solved using SHELXT and refined using SHELXL refinement within Olex2 software.[5, 6] The structural visualisation was performed with the programs Mercury[2] and Diamond[7] using the CIF of the crystal structures.

2.7 SQUID Magnetometry

Direct current (dc) and alternating current (ac) magnetic susceptibility data were collected on a Quantum Design MPMS-XL SQUID magnetometer equipped with a 5 T magnet operating in the 290 − 2 K range, for complexes **1**, **2**, **2**·12H_2O, **3** − **7**, **13** – **15** and **21** − **23**. All samples were embedded in eicosane, to prevent torquing. The magnetic data have been corrected for diamagnetism using the approximation that χ_{diam} = −(molecular weight/2)x10^{-6} cm^3 mol^{-1}.[8, 9] Additionally, the diamagnetic contribution of the sample holder and eicosane by measurements were also corrected.

In the cases of the air-sensitive complexes **13** and **15**, the samples were prepared in a glove-box under inert atmosphere and an air-sensitive holder was used (Fig. 2.1). The holder was made by a Wilmad® NMR tube 5 mm diameter (parameter: 600 MHz frequency and length: 7 in.) by the glassblowing service at the School of Chemistry, University of Glasgow, according to instructions found in 'Sample Mounting Considerations' (MPMS Application Note 1014-201) for air-sensitive samples by Quantum Design.[10] After the mount of the sample and the eicosane on the holder, a J. Young high-vacuum valve was attached to seal the sample in the glove-box; the sealed tube was removed from the glove-box and it was sealed using flame under vacuum, in order to remove the valve (Fig. 2.1right : air-sensitive holder with sample).

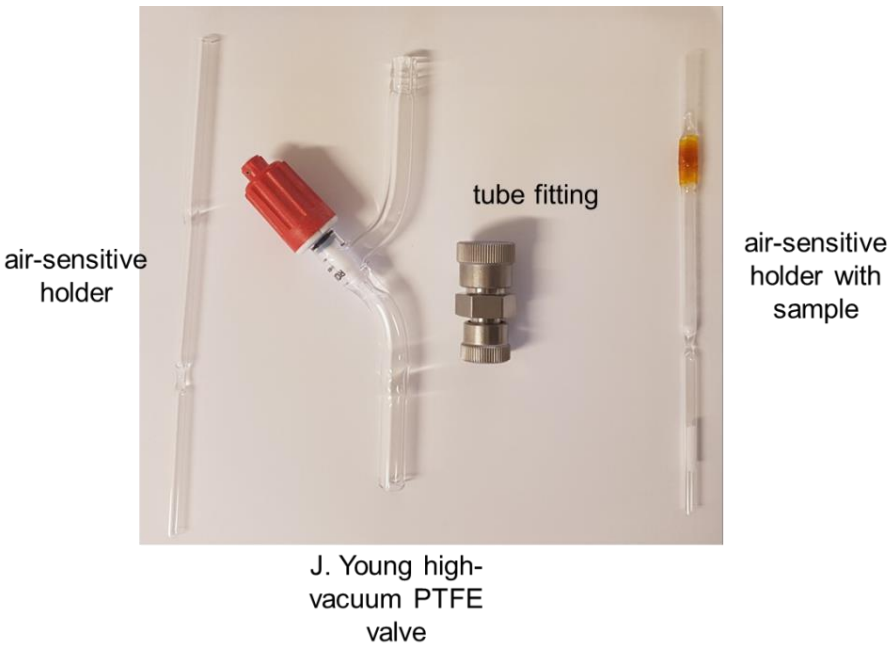

Figure 2.1 The apparatus used for the air-sensitive holder.

2.8 Solvothermal synthesis

According to solvothermal synthesis, the reaction takes place in a stainless steel autoclave (acid digestion vessel) (Fig. 2.2) which is subsequently heated in a specially designed furnace (Fig. 2.3). The reaction solution is placed in the Teflon liner and subsequently is placed in the stainless steel autoclave. The reaction conditions, *i.e.* the temperature rate used to achieve the desired temperature of the experiment, the duration of the experiment and the temperature cooling rate, can be adjusted by the temperature controller of the furnace.

Figure 2.2 Autoclave (acid digestion vessel) from Parr Instrument Company.[11, 12]

Figure 2.3 Oven with temperature controller (red circle) used for solvothermal synthesis.

2.9 Microwave synthesis

According to microwave synthesis, the reaction takes place in a sealed glass vessel (Fig. 2.4) which is subsequently heated in a microwave reactor (Fig. 2.5). The reaction conditions can be adjusted by programming a method including the following factors: the maximum amount of the microwave power that can be applied; the temperature control point; the pressure control point; the experiment duration; and the stirring function.

Figure 2.4 The glass vessel with the lid and the stir bar used for the microwave synthesis.

Figure 2.5 The microwave reactor. Microwave reactor model**:** Discover LabMate (model no. 908010), Matthews. NC, made in USA by CEM Corporation.

2.10 References

1. A. K. Hassan, L. A. Pardi, J. Krzystek, A. Sienkiewicz, P. Goy, M. Rohrer and L. C. Brunel, *Journal of Magnetic Resonance*, 2000, **142**, 300-312.
2. C. F. Macrae, P. R. Edgington, P. McCabe, E. Pidcock, G. P. Shields, R. Taylor, M. Towler and J. van de Streek, *Journal of Applied Crystallography*, 2006, **39**, 453-457.
3. S. J. Coles and P. A. Gale, *Chemical Science*, 2012, **3**, 683-689.
4. SAINT v8.34a, © 1997 - 2013, Bruker AXS Inc., Madison, WI
5. O. V. Dolomanov, L. J. Bourhis, R. J. Gildea, J. A. K. Howard and H. Puschmann, *Journal of Applied Crystallography*, 2009, **42**, 339-341.
6. G. Sheldrick, *Acta Crystallographica Section C*, 2015, **71**, 3-8.
7. Diamond - Crystal and Molecular Structure Visualization, Crystal Impact - Dr. H. Putz & Dr. K. Brandenburg GbR, Kreuzherrenstr. 102, 53227 Bonn, Germany http://www.crystalimpact.com/diamond
8. O. Kahn, *Molecular Magnetism*, VCH Publishers, New York, 1993.
9. D. W. Bruce, D. O'Hare and R. I. Walton, *Molecular Materials*, John Wiley & Sons, Ltd, Chichester, 2010.
10. https://www.qdusa.com/sitedocs/appNotes/mpms/1014-201.pdf
11. Parr Instrument Company https://www.parrinst.com/products/sample-preparation/acid-digestion/general-purpose-acid-digestion-vessel-model-4749-23-ml/
12. L. S. L. Santos, PhD, *Engineering of Metal Oxide Nanoparticles for Application in Electrochemical Devices*, Universidade Nova de Lisboa's Repository, 2015, http://hdl.handle.net/10362/15429

Chapter 3

Microwave−assisted synthesis: from a mononuclear {Co^{II}} complex to {Co^{II}_9} solvomorphs

Contents

3. Microwave−assisted synthesis: from a mononuclear {Co^{II}} complex to {Co^{II}_9} solvomorphs.

3.1 Introduction

As discussed previously in Chapter 1, polymetallic 3*d* and/or 4*f* complexes have attracted a great deal of interest due to their interesting properties and applications in scientific fields such as molecule-based magnets, magnetic refrigerants, water oxidation electrocatalysts and MRI contrast agents.[1-6] Therefore, the need to synthesise and characterise these complexes continues to grow. Polydentate ligands such as amino-polyalcohols (Fig. 3.1) have been widely used towards the synthesis of high nuclearity complexes. These are flexible ligands, which are able to coordinate in different modes, depending on the deprotonation level, and contain both N and O coordination sites, which could lead to the coordination of both 3*d* and 4*f* metal ions.[6, 7] The tripodal ligand bicine (H_3bic, *N,N*-Bis(2-hydroxyethyl)glycine) (Fig. 3.2) is a widely known buffer (one of Good's buffers)[8] and has been used for years as a pH regulator in the field of bioinorganic chemistry. However, due to its amino-alcohol and amino-acid groups it has been also used towards the synthesis of coordination complexes. At the start of this project (Cambridge Structural Database, CSD, of 2016), the majority of these coordination complexes were mononuclear incorporating Co^{II}, Ni^{II}, Cu^{II}, Zn^{II} and Gd^{III} metal ions,[9-15] while there were only three polynuclear complexes with Fe^{III} and one with $Co^{II/III}$ [16-18]; therefore, we were interested in investigating the coordination chemistry of bicine with Co^{II}. Furthermore, we decided to investigate the magnetic properties of a previously reported mononuclear Co^{II} complex with bicine in trigonal bipyramidal geometry (TBP)[15] (Co^{II} in TBP geometry could lead to interesting magnetic properties as discussed in Chapter 1).

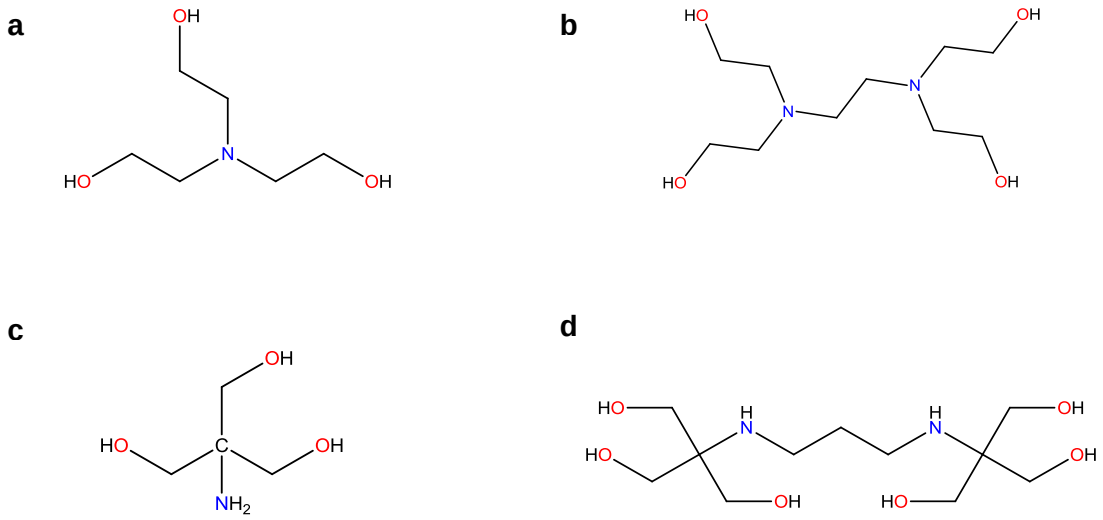

Figure 3.1 Illustration of some of the most commonly used amino-polyalcohols. *a)* Triethanolamine (= 2-[bis(2-hydroxyethyl)amino]ethanol), *b)* Ethylenediamine tetraethanol (= 2,2',2'',2'''-(ethane-1,2-diyldinitrilo)tetraethanol), *c)* Tris (= 2-amino-2-(hydroxymethyl)propane-1,3-diol) and *d)* Bis-Tris propane (= 2,2'-(propane-1,3-diyldiimino)bis[2-(hydroxymethyl)propane-1,3-diol]).

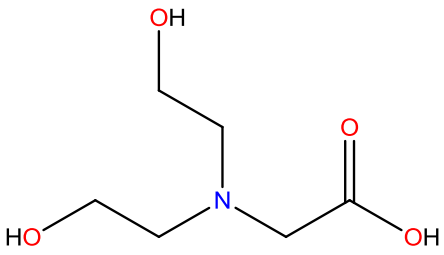

Figure 3.2 Illustration of the ligand bicine (H_3bic, *N,N*-Bis(2-hydroxyethyl)glycine).

Although the choice of ligand is important in order to obtain high nuclearity complexes, it is not the only prerequisite. The synthetic procedure, and more specifically the conditions of the reactions play an important role in the isolation of such complexes. Solvothermal heating is a commonly used synthetic approach in inorganic synthesis. According to this synthetic method, the reaction takes place in a sealed vessel which is subsequently heated in an oven; under these conditions the reaction can reach temperatures above the boiling point of the solvent, leading to high pressures. By achieving such high temperatures and pressures, solvents can exhibit enhanced diffusion of the chemical species (due to their reduced viscosity) and can show different solubilising properties (insoluble chemicals can become soluble under these conditions) in comparison to ambient conditions.[19, 20] Another synthetic method that is being employed more frequently

in inorganic synthesis, is microwave-assisted synthesis. In this case, the microwave radiation is used as a heating source, instead of conventional heating (microwave energy can be absorbed by dielectric materials and generate heat through different mechanisms). The main advantages of microwave−assisted synthesis are the reduced reaction times, increased yields and product selectivity.[21]

Herein, we report a new synthetic procedure for the previously reported $[Co^{II}(H_2bic)Cl]$ (**1**)[15], and a new nonanuclear complex $[Co^{II}_9(Hbic)_4(bic)_2Cl_4]$ (**2**) and its solvomorph $[Co^{II}_9(Hbic)_4(bic)_2Cl_4]\cdot 12H_2O$ (**2**$\cdot 12H_2O$). Complex **2** displays a metallic core different from any reported $\{Co^{II}_9\}$ complex, and contains a $\{Co^{II}_7\}$ disk−like core with two adjacent tetrahedral Co^{II} centres. The reaction between $CoCl_2\cdot 6H_2O$, bicine and NEt_3 in EtOH under solvothermal conditions, resulted in a mixture of the complexes **1**, **2** and **2**$\cdot 12H_2O$. However, the application of microwave heating resulted in the isolation of these three complexes separately. Magnetic characterisation for all complexes revealed that only **2** displays the onset of out-of-phase signals, while **1** and **2**$\cdot 12H_2O$ do not exhibit any out-of-phase signals.

3.2 Synthesis

Solvothermal conditions

Mixture of complexes: $[Co^{II}(H_2bic)Cl]$ (**1**), $[Co^{II}_9(Hbic)_4(bic)_2Cl_4]$ (**2**) and $[Co^{II}_9(Hbic)_4(bic)_2Cl_4]\cdot 12H_2O$ (**2**·$12H_2O$)

Into a solution of bicine (H_3bic, *N,N*-Bis(2-hydroxyethyl)glycine) (0.5 mmol, 82 mg) in EtOH (2 ml) was added a solution of $CoCl_2\cdot 6H_2O$ (1 mmol, 238 mg) in EtOH (5 ml) and the solution was stirred for 5 minutes at room temperature. Then, NEt_3 (0.13 mmol, 0.02 ml) was added and the solution stirred for another 15 minutes. The dark blue solution was placed in a Teflon lined autoclave and heated to 140 °C, at a rate of 5 °C/min. The temperature was held at 140 °C for 3 days and then the solution was allowed to cool to room temperature at a rate of 0.1 °C/min yielding three kinds of crystals: pink and blue block-like crystals (complexes **1** and **2**, respectively) and blue needle-like (complex **2**·$12H_2O$) crystals.

Microwave-mediated conditions

$[Co^{II}(H_2bic)Cl]$ (1) : A solution of $CoCl_2\cdot 6H_2O$ (1 mmol, 238 mg), bicine (0.5 mmol, 82 mg) and NEt_3 (0.13 mmol, 0.02 ml) in EtOH (7 ml) was placed in a in a glass tube sealed with a cap (suitable glass tube and cap designed for microwave reaction), which was then inserted into the cavity of a microwave reactor. The reaction mixture was held at 140 °C, power: 150 W and pressure: 300 PSI for a total of 15 min. Then the solution was allowed to cool naturally to room temperature to give a dark blue solution with pink crystalline precipitate which was collected by filtration and dried in air before characterising with powder X-ray diffraction and elemental analysis (~18% yield). Elemental analysis calcd(%) for $C_6H_{12.5}CoNO_{4.25}Cl$: C 27.61%, H 4.83%, N 5.37%, found: C 27.49%, H 4.69%, N 5.26%, which corresponds to $[Co^{II}(H_2bic)Cl]\cdot 0.25H_2O$ (**1**·$0.25H_2O$).

$[Co^{II}_9(Hbic)_4(bic)_2Cl_4]$ (2) : A solution of $CoCl_2\cdot 6H_2O$ (1 mmol, 238 mg), bicine (0.5 mmol, 82 mg) and NEt_3 (0.5 mmol, 0.075 ml) in EtOH (7 ml) was placed in a sealed glass tube, which was then inserted into the cavity of a microwave reactor. The reaction mixture was held at 140 °C, power: 150 W and pressure: 300 PSI for a total of 15 min. Then the solution was allowed to cool naturally to room temperature to give a dark blue solution with blue crystalline precipitate which was collected by filtration and dried under a nitrogen atmosphere before characterising with powder X-ray diffraction and elemental analysis (~17% yield). Elemental analysis calcd(%) for $C_{36}H_{64}Co_9N_6O_{24}Cl_4$: C 26.41%, H 3.94%, N 5.13%, found: C 26.27%, H 4.12%, N 4.91%.

[Co^{II}_9(Hbic)$_4$(bic)$_2$Cl$_4$]·12H$_2$O (2·12H$_2$O) : A solution of $CoCl_2·6H_2O$ (1 mmol, 238 mg), bicine (0.5 mmol, 82 mg) and NEt_3 (0.5 mmol, 0.075 ml) in EtOH (7 ml) was placed in a sealed glass tube, which was then inserted into the cavity of a microwave reactor. The reaction mixture was held at 140 °C, power: 150 W and pressure: 300 PSI for a total of 15 min. Then the solution was allowed to cool naturally to room temperature to give a dark blue solution with blue crystalline precipitate which was collected by filtration and dried in air before characterising with powder X-ray diffraction and elemental analysis (~17% yield). Elemental analysis calcd(%) for $C_{36}H_{86}Co_9N_6O_{35}Cl_4$: C 23.56%, H 4.72%, N 4.58%, found: C 24.06%, H 4.39%, N 4.52% which corresponds to [Co^{II}_9(Hbic)$_4$(bic)$_2$Cl$_4$]·11H$_2$O (one molecule of water is lost).

3.3 Results and discussion

The reaction of $CoCl_2·6H_2O$ with bicine and NEt_3 in EtOH under solvothermal conditions, resulted in a mixture of three kinds of crystals: pink and blue block-like crystals and blue needle-like crystals. Single-crystal X-ray diffraction (SCXRD) revealed that the unit cell of the pink block-like crystals corresponds to the previously reported [Co^{II}(H_2bic)Cl] (**1**)[15] (Fig. 3.3 left) and the blue block-like crystals correspond to a new nonanuclear Co-based complex, [Co^{II}_9(Hbic)$_4$(bic)$_2$Cl$_4$] (**2**) (Fig. 3.3 right). SCXRD for the blue needle-like crystals revealed a solvomorph of **2**, complex [Co^{II}_9(Hbic)$_4$(bic)$_2$Cl$_4$]·12H$_2$O (**2**·12H$_2$O). In order to examine if it is possible to isolate the three compounds separately we investigated further by making various changes to the synthetic procedure (*e.g.* the amount of the base, the cobalt salt, the reaction time and/or temperature used in the solvothermal reactions). However, solvothermal conditions always led to a mixture of crystals or crystalline precipitates. As mentioned above, one of the advantages of microwave heating is product selectivity; therefore, we investigated microwave heating instead. Under these conditions, in EtOH with a ligand to base ratio ~4:1 a pink crystalline powder is isolated, whereas when the ligand to base ratio is changed to 1:1, a blue crystalline powder is formed. Both products were collected by filtration and dried in air, and powder X-ray diffraction (PXRD) (Fig. 3.4) revealed that the pink and blue products corresponded to complexes **1** and **2**·12H$_2$O, respectively. Moreover, when the blue crystalline product is instead collected by filtration and dried under a nitrogen atmosphere (glove bag), complex **2** is obtained, as confirmed by powder X-ray diffraction (Fig. 3.4). Therefore, the use of microwave heating led to the separation of the mononuclear and the polynuclear complexes, and furthermore, depending on which drying process is applied, we are able to control which {Co^{II}_9} solvomorph is formed (Scheme 3.1).

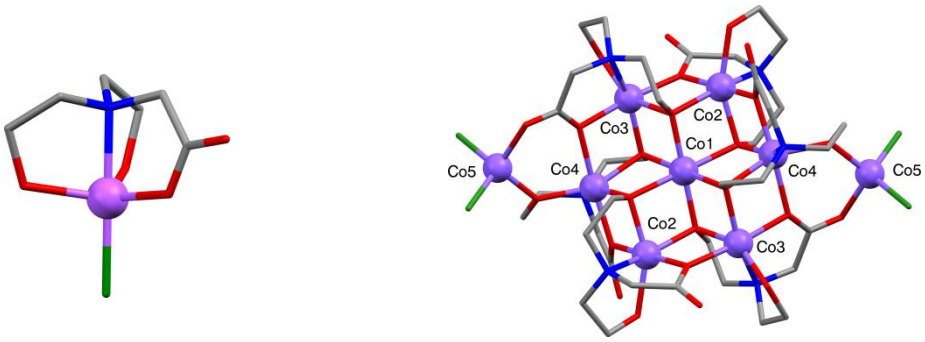

Figure 3.3 The molecular structure of **1** (*left*) and $[Co^{II}_9(Hbic)_4(bic)_2Cl_4]$ (*right*). Colour code: Co^{II}: violet, Cl: green, O: red, N: blue, C: grey. Hydrogen atoms are omitted for clarity.

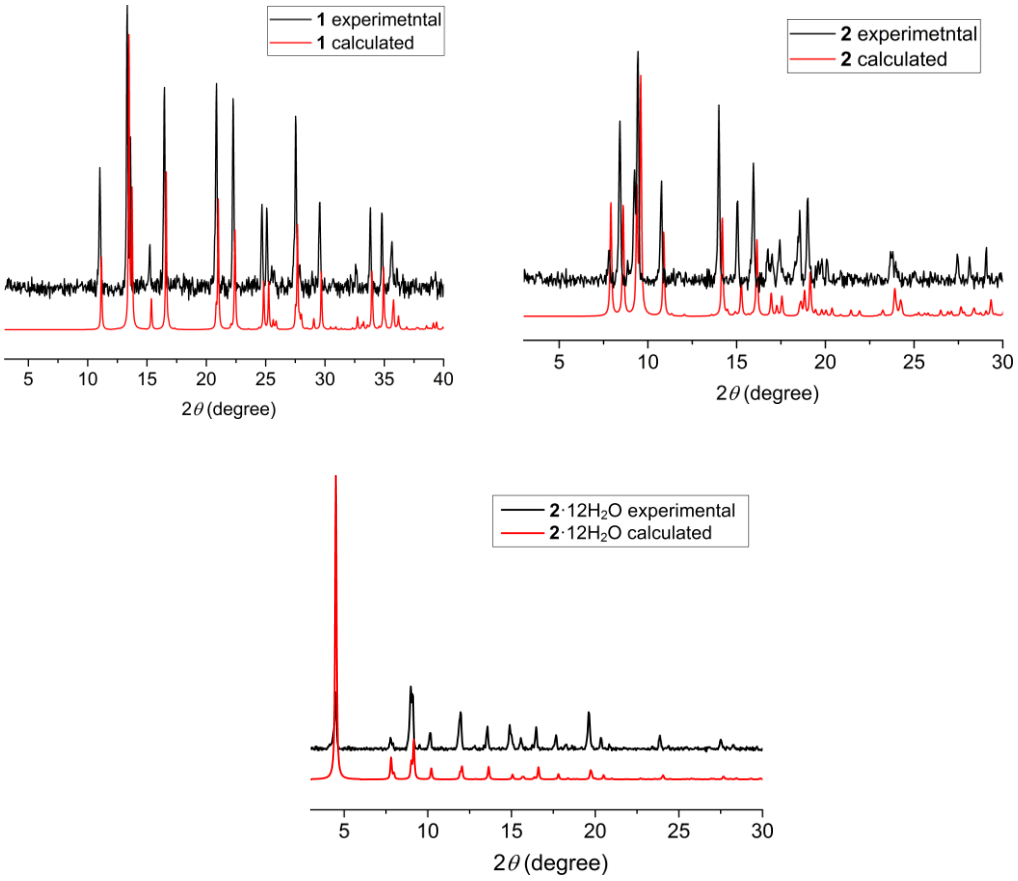

Figure 3.4 The PXRD patterns of **1** (3−40°), **2** (3−30°) and **2**·12H_2O (3−30°). The red lines represent the calculated PXRD pattern for each complex and the black lines the experimental ones. All the experimental PXRD patterns were measured at ambient temperature, while the calculated patterns are generated from the single-crystal data collected at 296 K for **1**, [15] and 100 K for **2** and **2**·12H_2O.

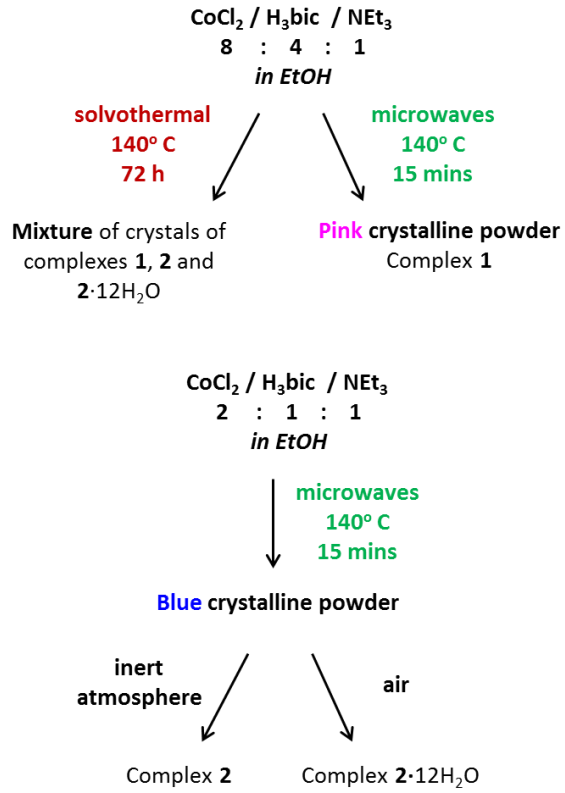

Scheme 3.1 The synthetic procedure followed to isolate complexes **1**, **2** and **2**·12H_2O.

Crystal structure analysis

Complex **1** crystallises in the orthorhombic *Pbca* space group,[15] while single-crystal X-ray diffraction for **2** and **2**·12H_2O revealed that the complexes crystallise in the monoclinic $P2_1/n$ and trigonal $R\bar{3}$ space groups, respectively. Selected crystallographic data for **2** and **2**·12H_2O can be found in Table 3.1.

The Co^{II} centre in complex **1** is five-coordinate and adopts a distorted trigonal bipyramidal (TBP) geometry, with one singly deprotonated bicine ligand (the nitrogen atom is in an axial position and three oxygen atoms are in equatorial positions) and one terminal Cl^- ligand in axial position (Fig. 3.3 left). Continuous shape measures (CShMs) calculated with the program SHAPE[22, 23] which provide an estimate of the distortion from the ideal TBP geometry for the Co^{II}, give a value of 1.42 (where 0 corresponds to the ideal polyhedron), confirming a significant distortion (Table A3.1 and Fig. A3.1 in the appendix). Bond Valence Sum (BVS) analysis was used to confirm the oxidation state of Co^{II}.[24, 25] Intermolecular hydrogen bonds occur between the hydroxyl groups and the carboxylate groups of neighbouring molecules, forming a two-dimensional network (Fig. 3.5) and the shortest intermolecular Co···Co' distances are ~4.8 Å.[15]

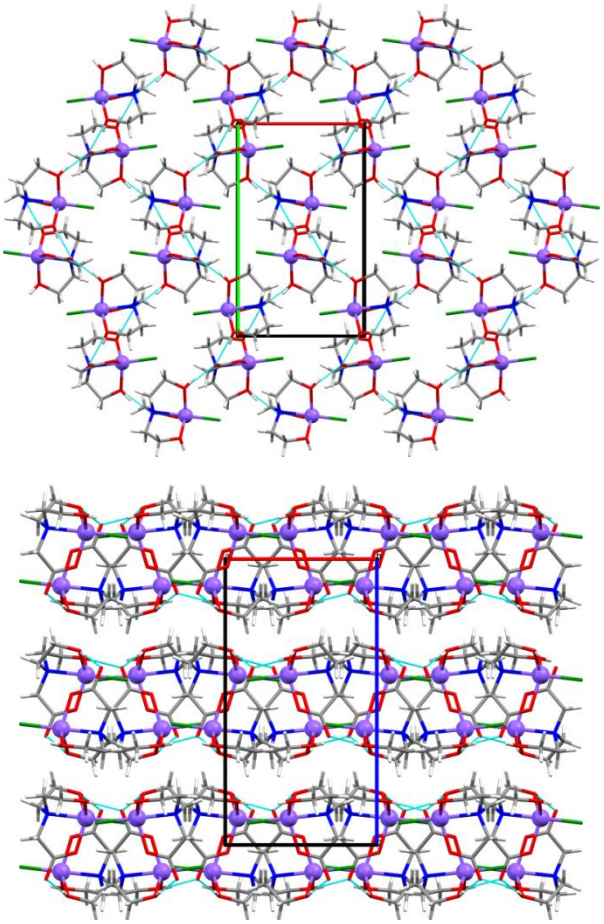

Figure 3.5 *Top)* The crystal packing of **1** along the crystallographic *c*-axis. *Bottom)* The crystal packing of **1** along the crystallographic *b*-axis. Colour code: Co^{II}: violet, Cl: green, O: red, N: blue, C: grey, H: white. Light blue lines: illustration of the 2D network formed by the H-bonds. (space group: *Pbca*)

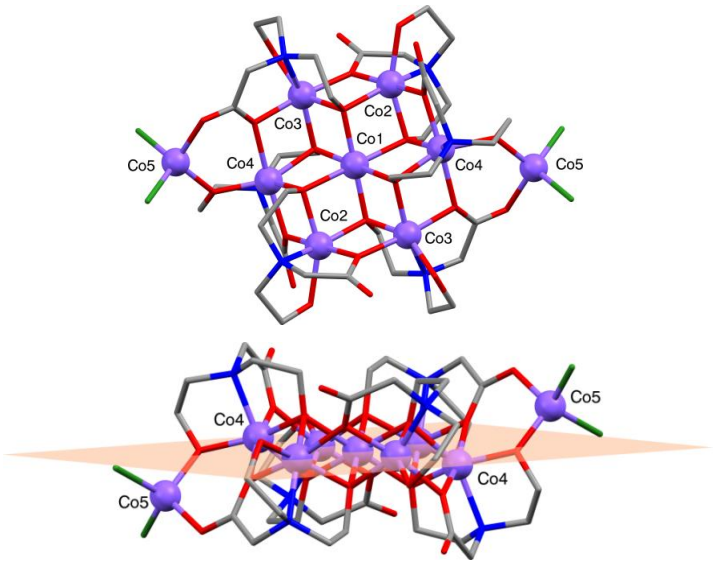

Figure 3.6 *Top)* The molecular structure of [Co^{II}_9(Hbic)$_4$(bic)$_2$Cl$_4$]. *Bottom)* The plane that five Co^{II} (Co1, Co2, Co2', Co3, Co3') centres define, with Co4, Co4', Co5 and Co5' located outside this plane. Colour code: Co^{II}: violet, Cl: green, O: red, N: blue, C: grey. Hydrogen atoms are omitted for clarity.

The new nonanuclear complex **2** adopts an unusual structural motif which consists of the well-known $\{Co^{II}_7\}$ disk-like core[26-29] with two additional tetrahedral Co^{II} centres (Fig. 3.6). The crystal packing of **2** and **2**·12H_2O is different (Fig. 3.7) due to the co-crystallised molecules of water. Due to a region of poorly defined and disordered molecules of solvent in **2**·12H_2O, only two molecules of water could be modelled. The routine SQUEEZE (in PLATON)[30] was used to identify the solvent voids and account for the electron density within them, calculated to contain 886 e^- per unit cell, corresponding to approximately 98 e^- per molecule. Approximately 10 molecules of water solvent correspond to ~98 e^-, therefore in total there are 12 molecules of co-crystallised water per complex. This is also consistent with the elemental analysis (see experimental procedure of **2**·12H_2O in Section 3.1).

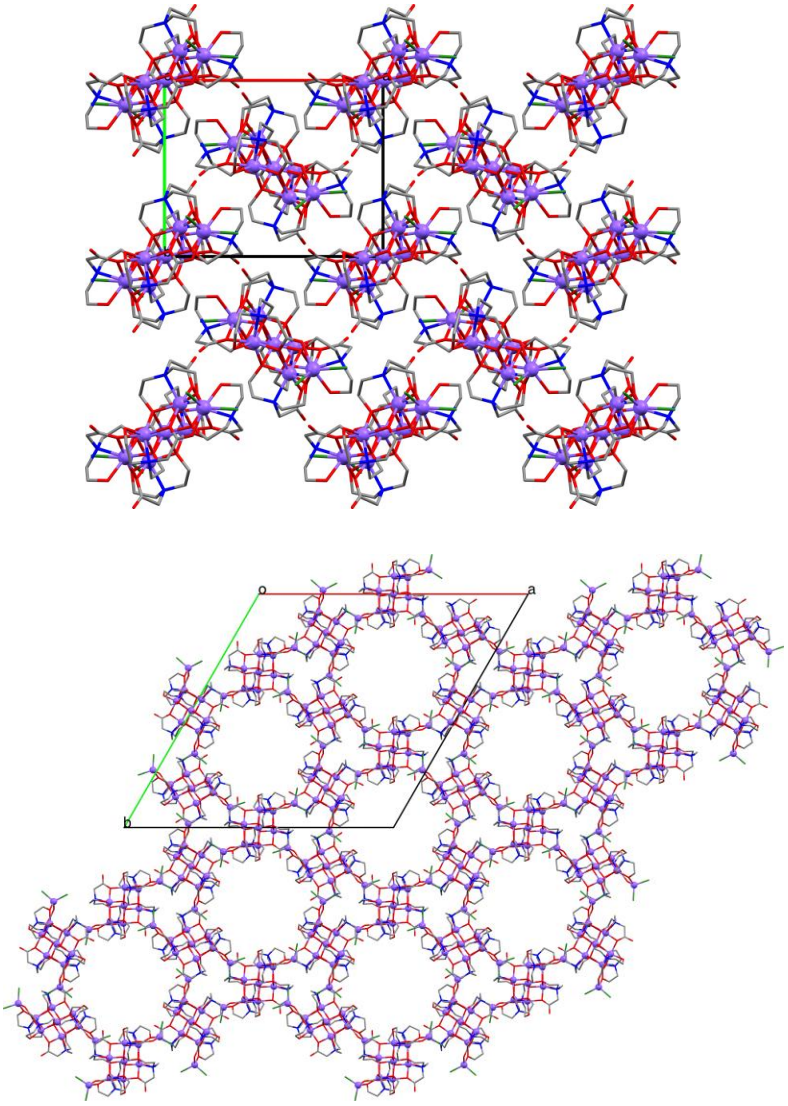

Figure 3.7 The crystal packing of **2** (*top*) ($P2_1/n$) and **2**·12H_2O (*bottom*) ($R\bar{3}$) along the crystallographic *c*-axis. The water molecules inside the channels of **2**·12H_2O are omitted for clarity. Colour code: Co^{II}: violet, Cl: green, O: red, N: blue, C: grey. Hydrogen atoms are omitted for clarity.

The asymmetric unit of **2** contains a half molecule of $[Co^{II}_9(Hbic)_4(bic)_2Cl_4]$ and the asymmetric unit of **2**·12H_2O contains a half molecule of $[Co^{II}_9(Hbic)_4(bic)_2Cl_4]$ and one molecule of water in the crystal lattice. As discussed above, only two molecules of water in the crystal lattice were able to be modelled. The routine SQUEEZE[30] was used to account for the electron density within the solvent voids, and calculated approximately another 10 molecules of water (in total 12 molecules of water per molecule). There are five crystallographically independent Co^{II} centres, with Co1 lying on the inversion centre, and all of them are bridged by two doubly and one triply deprotonated bicine ligands (Fig. 3.8), while two terminal Cl^- ligands complete the coordination sphere of Co5. Co1 – Co4 adopt distorted octahedral geometries, while Co5 adopts a slightly distorted tetrahedral geometry. Subtle differences are observed in the distortion of the geometries of the cobalt centres between the two solvomorphs, and CShMs values for all Co^{II} centres for **2** and **2**·12H_2O were calculated with the programme SHAPE[31, 32] (Tables A3.2 and A3.3 in the appendix). All cobalt centres in both solvomorphs are in the +2 oxidation state, as confirmed by BVS analysis.[24, 25] Five Co^{II} centres (Co1, Co2, Co3 and their centrosymmetric equivalents) define a plane while Co4 and Co5 and their centrosymmetric equivalents are located outside this plane (Fig. 3.8). Intramolecular interactions are present between the hydroxyl and carboxylate groups of **2** and **2**·12H_2O, and intermolecular interactions occur between the hydroxyl and carboxylate groups of neighbouring molecules with the molecules of solvent in the solvomorph **2**·12H_2O (Fig. A3.2 in the appendix). The shortest intermolecular Co···Co' distances are ~6.7 Å and ~6 Å in **2** and **2**·12H_2O, respectively.

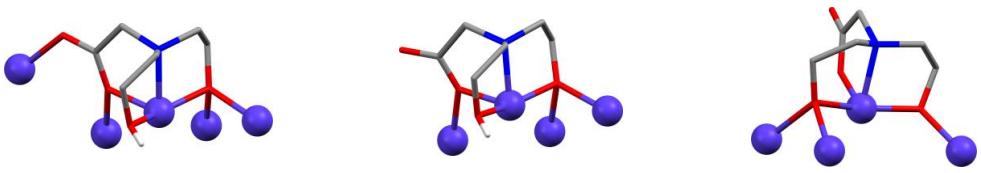

Figure 3.8 Illustration of the bridging modes of the doubly (a and b) and triply (c) deprotonated bicine ligands. Colour code: Co^{II}: violet, O: red, N: blue, C: grey, H: white. Hydrogen atoms are omitted for clarity except for the H atoms of the protonated hydroxyl groups.

Table 3.1. Data collection and crystallographic parameters for complexes **2** and **2**·12H_2O.

Chemical formula	$C_{36}H_{64}Cl_4Co_9N_6O_{24}$ (**2**)	$C_{36}H_{88}Cl_4Co_9N_6O_{36}$ (**2**·12H_2O)
M_r	1637.10	1853.29
Crystal system, space group	Monoclinic, $P2_1/n$	Trigonal, $R\bar{3}$
Temperature (K)	100	100
***a*, *b*, *c* (Å)**	14.7276 (4), 11.8295 (3), 15.6451 (5)	39.2116 (8), 39.2116 (8), 11.7240 (3)
α, β, γ (°)	90, 94.809, 90	90, 90, 120
***V* (Å^3)**	2716.10 (13)	15611.2 (8)
Z	2	9
Radiation type	Mo *K*α radiation	Mo *K*α radiation
μ (mm^{-1})	2.96	2.34
Crystal size (mm)	0.08 × 0.07 × 0.04	0.26 × 0.03 × 0.03
Diffractometer	Rigaku FRE+ equipped with VHF Varimax confocal mirrors and an AFC12 goniometer and HG Saturn 724+ detector diffractometer	Rigaku FRE+ equipped with VHF Varimax confocal mirrors and an AFC12 goniometer and HG Saturn 724+ detector diffractometer
No. of measured, independent and observed [$I > 2\sigma(I)$] reflections	34254, 6234, 5718	38042, 7930, 6410
R_{int}	0.028	0.061
$R[F^2 > 2\sigma(F^2)]$, $wR(F^2)$, GOF on F^2	0.023, 0.055, 1.03	0.054, 0.139, 1.00
No. of reflections	6234	7930
No. of parameters	364	368
No. of restraints	6	483
Δ>max, Δ>min (e Å^{-3})	1.25, −0.66	2.11, −1.63

Magnetic characterisation

Variable temperature direct current (dc) susceptibility data were collected for **1**, **2** and **2**·12H_2O in a field of 1000 Oe in the 290–2 K temperature range (Fig. 3.9 and 3.10). At 290 K the $\chi_M T$ value of **1** is 2.57 cm^3 mol^{-1} K, higher than the expected $\chi_M T$ = 1.88 cm^3 mol^{-1} K for a high-spin Co^{II} (*S* = 3/2 and *g* = 2), indicating a spin-orbit coupling contribution. Upon cooling, $\chi_M T$ decreases slowly until ~12 K, then increases slightly at 8 K (2.27 cm^3 mol^{-1} K) and drops again to a minimum at 2 K. This behaviour indicates the presence of magnetic anisotropy and weak ferromagnetic intermolecular interactions. Intermolecular interactions are not unusual in mononuclear systems[33-35], especially in the presence of hydrogen bonds and short Co···Co' distances of neighbouring molecules (~4.8 Å). Magnetisation *versus* field plots at 2, 4 and 6 K did not saturate, a further indication of the presence of magnetic anisotropy (Fig. 3.9 right). The dc magnetic susceptibility data and the magnetisation curves of **1** were fitted simultaneously using the programme PHI[36] (Fig. 3.9) as described by the following effective Hamiltonian equation[37] (Equation **1**):

$$\hat{H} = D[\hat{S}_z^2 - \tfrac{1}{3}S(S+1)] + E(\hat{S}_x^2 - \hat{S}_y^2) + \mu_B \vec{B} \cdot \overleftrightarrow{g} \cdot \hat{S} \qquad (\mathbf{1})$$

The first and second terms represent the axial and rhombic ZFS terms, parameterised by *D* and *E*, respectively, $\hat{S}$ is the spin operator with components $\hat{S}_i$ (*i* = *x, y, z*), and the final term denotes the Zeeman interaction with the local magnetic field, $\vec{B}$, parameterised through the Landé *g* tensor. Attempts to fit the data with an anisotropic *g* value were not successful, while using a positive *D* (easy-plane magnetic anisotropy) did not produce reasonable results, which is a strong indication that an easy-axis magnetic anisotropy (*D*<0) is present here. Previously reported theoretical and experimental investigations of high-spin Co^{II} complexes in TBP geometry and C_{3v} symmetry, demonstrated that the axial symmetry imposed by coordinating ligands leads to the stabilisation of easy-axis anisotropy.[38-40] Therefore, the assumption here that *D*<0 is not unreasonable since the use of a tripodal ligand can enforce C_3 symmetry. In order to consider the intermolecular interactions which are present at low temperatures (Fig.3.9), we attempted to fit the data including a ferromagnetic intermolecular term; however we were unable to obtain a satisfactory fit. The extracted parameters from the fitting of the data are: *g* = 2.25, *D* = −5.92 (±0.24) cm^{-1} and *E* = −1.32 (±0.09) cm^{-1}, with χ_{TIP} = 0.0006 cm^3 mol^{-1} (Temperature Independent Paramagnetic susceptibility) for a Co^{II} in TBP geometry.[41, 42]

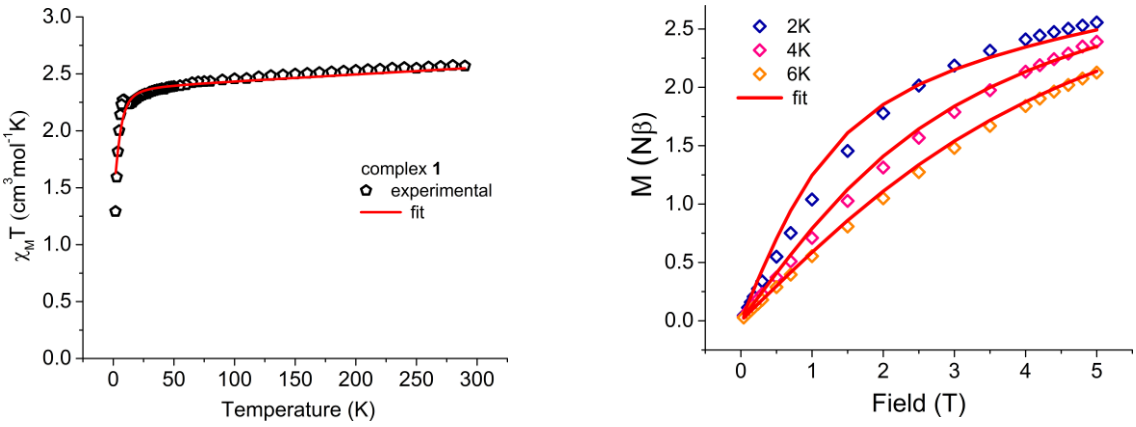

Figure 3.9 *Left)* χ_MT *versus* Temperature data for **1** in a field of 1000 Oe from 290–2 K. *Right)* Magnetisation *versus* Field data at temperatures 2, 4 and 6 K for **1**. The red solid lines represent the fit (see text for details).

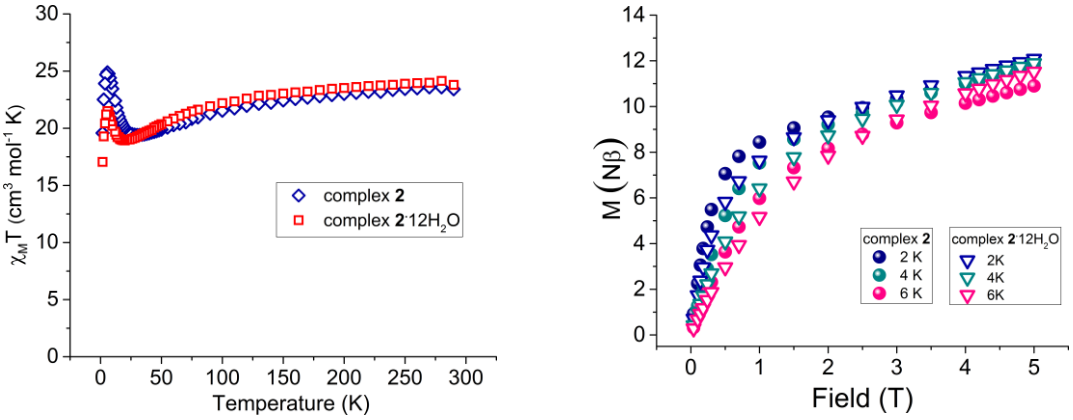

Figure 3.10 *Left)* χ_MT *versus* Temperature data for **2** (blue) and **2**·12H_2O (red) in a field of 1000 Oe from 290–2 K. *Right*) Magnetisation *versus* Field data at temperatures 2, 4 and 6 K for complexes **2** (spheres) and **2**·12H_2O (triangles).

The $\chi_M T$ values at room temperature for **2** and **2**·12H_2O are 23.4 and 23.8 cm^3 mol^{-1} K, respectively, which are higher than the theoretical spin-only value $\chi_M T$ = 16.9 cm^3 mol^{-1} K for nine non-interacting high-spin Co^{II} (S = 3/2 and g = 2), indicating a spin-orbit coupling contribution. $\chi_M T$ slowly decreases with the decrease of temperature until 26 and 19 K for **2** and **2**·12H_2O, due to the presence of spin-orbit coupling; then $\chi_M T$ increases sharply at 6 K for both complexes reaching the values of 26.2 and 21.5 cm^3 mol^{-1} K for **2** and **2**·12H_2O respectively, which can be attributed to the presence of ferromagnetic exchange interactions. Finally, $\chi_M T$ decreases for both complexes at low temperature, due to zero-field splitting (ZFS) and/or intermolecular antiferromagnetic interactions. It has been

previously shown that when the Co−$\widehat{O}$−Co angles are close to 90°, ferromagnetic interactions are promoted.[43-45] In the present complex the Co−$\widehat{O}$−Co angles between Co1 and the peripheral Co2−Co4, and the Co−$\widehat{O}$−Co angles between the peripheral Co2−Co4 centres are in the range ~94°−101°, therefore the ferromagnetic exchange interactions at lower temperatures is reasonable.[43-45] Magnetisation *versus* field plots at 2, 4 and 6 K did not saturate for both complexes, an indication of the presence of magnetic anisotropy (Fig. 3.10 right). This behaviour is in agreement with other polynuclear Co^{II}-based complexes.[44, 46-50] Using the program PHI we attempted to fit the data with seven Co^{II} centres in (distorted) octahedral geometry with S = 3/2, two Co^{II} centres in (slightly distorted) tetrahedral geometry with S = 3/2 and the approximation of one isotropic exchange interaction J, equal for all the bridges between the Co^{II} centres; however, the fit was not able to produce any values due to the complexity of the system. Therefore, we attempted to fit the data considering all octahedral Co^{II} centres to possess S = 1/2, a S = 3/2 for the two tetrahedral Co^{II} centres and one isotropic exchange interaction J. However, due to the huge discrepancy between the experimental data and the obtained fit (Fig. A3.3 in the appendix) no meaningful values were extracted. Further attempts to fit the data by adjusting the g and J parameters were unsuccessful (no reasonable results could be obtained), confirming the complexity of the system.

Alternating current (ac) susceptibility measurements were performed for all complexes in the temperature range 10−2 K, in a 3 Oe ac field and in the frequency range 1–1488 Hz, in order to examine if there is slow relaxation of the magnetisation. Complex **1** does not display any out-of-phase ac signal in zero or an applied dc field (Fig. A3.4 in the appendix). This could be attributed to the large E term (E/D ratio ~0.22) caused by the non-strict C_3 symmetry of the complex, the presence of hydrogen bonds between neighbouring molecules and/or the short intermolecular Co···Co' distances (~4.8 Å), all of which can facilitate a faster magnetic relaxation.[35, 40, 51-54]

Complex **2** displays only the onset of a weak χ'' signal (out-of-phase signal) in a zero dc field, while the application of a 2000 Oe dc field (Fig. 3.11) did not improve the intensity of the signal. Complex **2**·12H_2O does not display any out-of-phase signals in zero or an applied dc field (Fig. 3.12), which can be attributed to the QTM arising from the intermolecular interactions (intermolecular interactions occur between the hydroxyl and carboxylate groups of neighbouring molecules with the molecules of solvent and the intermolecular Co···Co' distances are shorter than in **2**). Moreover, the different magnetic behaviour between the two {Co^{II}_9} complexes could be ascribed to the subtle structural differences between the two complexes (slightly different distortion of the Co^{II} centres, Tables A3.2 and A3.3 in the appendix) and/or the absence of solvent molecules in the

crystal lattice of **2**. This behaviour is not unusual, as it has been previously reported that the absence or change of solvent can drastically affect the magnetic properties of a complex.[51-53] Although none of the other reported {Co^{II}_9} complexes exhibits any out-of-phase signals,[46, 55-63] similar out-of-phase signals as in complex **2** have been observed in {Co^{II}_7} disk-like structures.[44, 64-68] The majority of these complexes contain azido-bridges and only a couple of examples contain phenoxo, alkoxo and/or methoxo bridges. Due to the weak χ'' signal in **2**, we did not expect to see any improvement in the signal by performing an isothermal field sweep ac measurement; hence no further magnetic measurements were carried out.

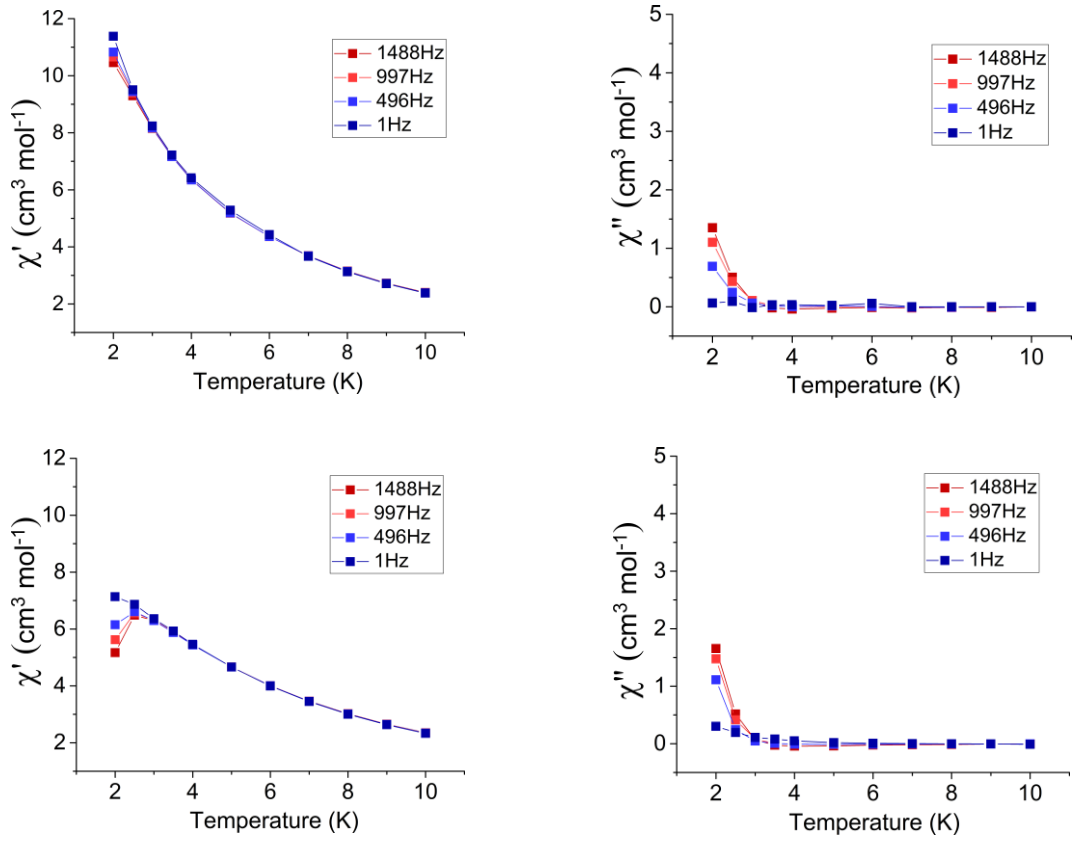

Figure 3.11 *Top)* Temperature dependence of the in-phase (*left*) and out-of-phase (*right*) magnetic susceptibility in zero dc field for complex **2** with ac frequencies of 1−1488 Hz. *Bottom)* Temperature dependence of the in-phase (*left*) and out-of-phase (*right*) magnetic susceptibility in a 2000 Oe dc field for complex **2** with ac frequencies of 1−1488 Hz.

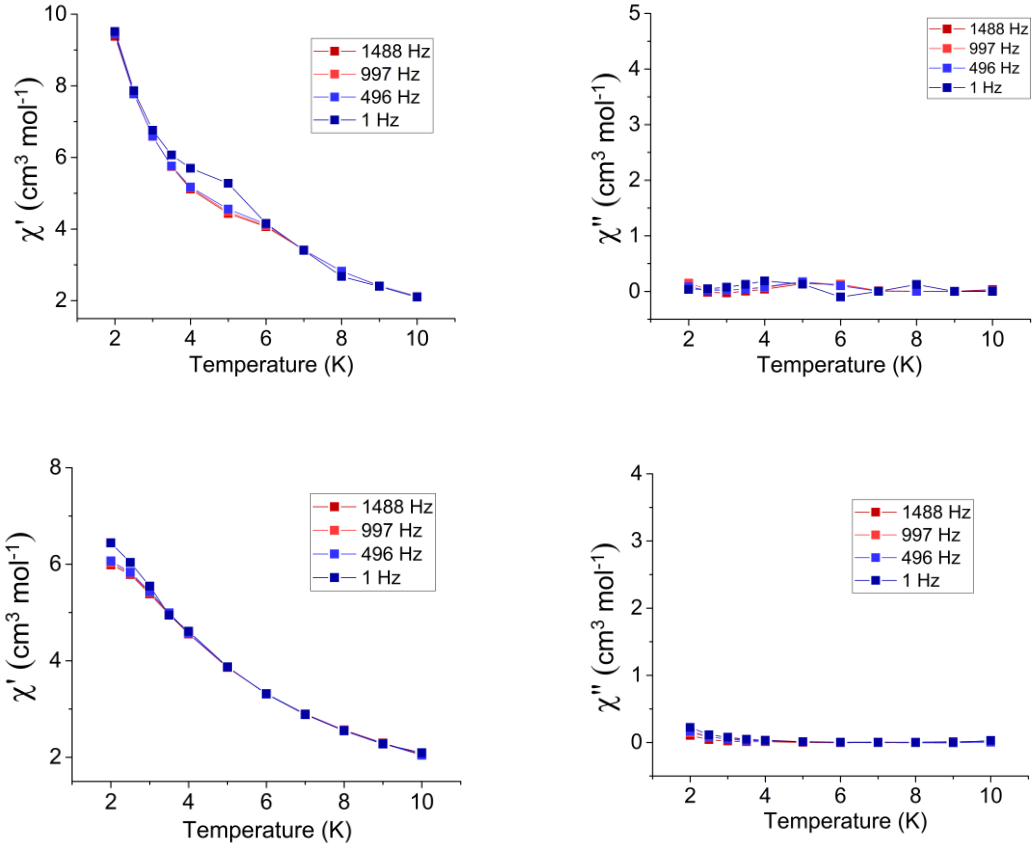

Figure 3.12 *Top)* Temperature dependence of the in-phase (*left*) and out-of-phase (*right*) magnetic susceptibility in zero dc field for complex **2**·12H_2O with ac frequencies of 1−1488 Hz. *Bottom)* Temperature dependence of the in-phase (*left*) and out-of-phase (*right*) magnetic susceptibility in a 2000 Oe dc field for complex **2**·12H_2O with ac frequencies of 1−1488 Hz.

3.4 Conclusions

In conclusion, we have investigated the coordination chemistry of the polydentate ligand bicine with Co^{II} and have presented a new, microwave-assisted synthetic procedure for the previously reported [$Co^{II}(H_2bic)Cl$] (**1**)[15]. Furthermore, we presented the synthesis and characterisation of a new nonanuclear complex [$Co^{II}_9(Hbic)_4(bic)_2Cl_4$] (**2**), which extends the well-known {Co^{II}_7} disk-like structure[26-29] with two adjacent tetrahedral Co^{II} centres, and its solvated analogue [$Co^{II}_9(Hbic)_4(bic)_2Cl_4$]·$12H_2O$ (**2**·$12H_2O$), by adjusting the synthetic procedure used for **1**. A CSD search (November 2018) showed that there are only a few examples of {Co^{II}_9} complexes and none of them adopt a similar topology as the complex presented here.[46, 55-63] Solvothermal conditions resulted in a mixture of the complexes **1**, **2** and **2**·$12H_2O$; however, by using microwave-assisted heating the selectivity is improved (see Scheme 3.1) and **1**, **2** and **2**·$12H_2O$ can be isolated separately. Therefore, we demonstrated that microwave−assisted synthesis can be a useful tool in the synthesis of polymetallic complexes using polydentate ligands where bench or solvothermal synthesis leads to a mixture of products and this approach could be applicable to a wide range of systems. Finally, magnetic studies for all complexes revealed that only complex **2** shows the onset of out-of-phase signals in a zero and an applied dc field of 2000 Oe, while complexes **1** and **2**·$12H_2O$ do not display any out-of-phase signals in zero or an applied dc field.

3.5 References

1. J. Ferrando-Soria, J. Vallejo, M. Castellano, J. Martínez-Lillo, E. Pardo, J. Cano, I. Castro, F. Lloret, R. Ruiz-García and M. Julve, *Coordination Chemistry Reviews*, 2017, **339**, 17-103.
2. Y.-Z. Zheng, G.-J. Zhou, Z. Zheng and R. E. P. Winpenny, *Chemical Society Reviews*, 2014, **43**, 1462-1475.
3. R. Brimblecombe, G. F. Swiegers, G. C. Dismukes and L. Spiccia, *Angewandte Chemie International Edition*, 2008, **47**, 7335-7338.
4. G. Maayan, N. Gluz and G. Christou, *Nature Catalysis*, 2018, **1**, 48-54.
5. G. Guthausen, J. R. Machado, B. Luy, A. Baniodeh, A. K. Powell, S. Krämer, F. Ranzinger, M. P. Herrling, S. Lackner and H. Horn, *Dalton Trans.*, 2015, **44**, 5032-5040.
6. M. Murrie, *Polyhedron*, 2018, **150**, 1-9.
7. J. W. Sharples and D. Collison, *Coordination Chemistry Reviews*, 2014, **260**, 1-20.
8. N. E. Good, G. D. Winget, W. Winter, T. N. Connolly, S. Izawa and R. M. M. Singh, *Biochemistry*, 1966, **5**, 467-477.
9. Y. Hiromitsu, N. Makoto, Y. Yasuhiko, I. Yoshie and T. Toshio, *Bulletin of the Chemical Society of Japan*, 1988, **61**, 2763-2766.
10. H. Yamaguchi, Y. Inomata and T. Takeuchi, *Inorganica Chimica Acta*, 1991, **181**, 31-36.
11. X.-f. He, L.-s. Long, X.-y. Le, X.-m. Chen, L.-n. Ji and Z.-y. Zhou, *Inorganica Chimica Acta*, 1999, **285**, 326-331.
12. H. Thakuria and G. Das, *Polyhedron*, 2007, **26**, 149-153.
13. K. M. Lo and S. W. Ng, *Acta Crystallographica Section E*, 2010, **66**, m1485.
14. J.-P. Zhao and F.-C. Liu, *Acta Crystallographica Section E*, 2010, **66**, m848.
15. Y. Zhou, X. Liu, Q. Wang, L. Wang and B. Song, *Acta Crystallographica Section E*, 2016, **72**, 1463-1467.
16. M. Murugesu, K. A. Abboud and G. Christou, *Dalton Transactions*, 2003, 4552-4556.
17. K. Graham, A. Darwish, A. Ferguson, S. Parsons and M. Murrie, *Polyhedron*, 2009, **28**, 1830-1833.
18. A. V. Funes, L. Carrella, L. Sorace, E. Rentschler and P. Alborés, *Dalton Transactions*, 2015, **44**, 2390-2400.
19. Rebecca H. Laye and Eric J. L. McInnes, *European Journal of Inorganic Chemistry*, 2004, 2811-2818.
20. S. Feng and L. Guanghua, in *Modern Inorganic Synthetic Chemistry*, eds. R. Xu, W. Pang and Q. Huo, Elsevier, Amsterdam, 2011, pp. 63-95.
21. J. Zhao and W. Yan, in *Modern Inorganic Synthetic Chemistry*, eds. R. Xu, W. Pang and Q. Huo, Elsevier, Amsterdam, 2011, pp. 173-195.
22. M. Pinsky and D. Avnir, *Inorganic Chemistry*, 1998, **37**, 5575-5582.
23. S. Alvarez and M. Llunell, *Journal of the Chemical Society, Dalton Transactions*, 2000, 3288-3303.
24. N. E. Brese and M. O'Keeffe, *Acta Crystallographica Section B*, 1991, **47**, 192-197.
25. I. D. Brown, Brockhouse Institute for Materials Research, McMaster University, Hamilton, Ontario Canada. idbrown@mcmaster.ca, https://www.iucr.org/__data/assets/file/0007/126574/bvparm2016.cif.
26. A. B. Canaj, L. E. Nodaraki, K. Ślepokura, M. Siczek, D. I. Tzimopoulos, T. Lis and C. J. Milios, *RSC Advances*, 2014, **4**, 23068-23077.
27. R. Modak, Y. Sikdar, A. E. Thuijs, G. Christou and S. Goswami, *Inorganic Chemistry*, 2016, **55**, 10192-10202.

28. R. Pattacini, P. Teo, J. Zhang, Y. Lan, A. K. Powell, J. Nehrkorn, O. Waldmann, T. S. A. Hor and P. Braunstein, *Dalton Trans.*, 2011, **40**, 10526-10534.
29. S.-H. Zhang, L.-F. Ma, H.-H. Zou, Y. G. Wang, H. Liang and M. H. Zeng, *Dalton Trans.*, 2011, **40**, 11402-11409.
30. A. Spek, *Acta Crystallographica Section D*, 2009, **65**, 148-155.
31. S. Alvarez, D. Avnir, M. Llunell and M. Pinsky, *New Journal of Chemistry*, 2002, **26**, 996-1009.
32. C. Jordi, A. Pere and A. Santiago, *Chemistry – A European Journal*, 2004, **10**, 190-207.
33. T. Jurca, A. Farghal, P.-H. Lin, I. Korobkov, M. Murugesu and D. S. Richeson, *Journal of the American Chemical Society*, 2011, **133**, 15814-15817.
34. F. Habib, O. R. Luca, V. Vieru, M. Shiddiq, I. Korobkov, S. I. Gorelsky, M. K. Takase, L. F. Chibotaru, S. Hill, R. H. Crabtree and M. Murugesu, *Angewandte Chemie International Edition*, 2013, **52**, 11290-11293.
35. W. Huang, T. Liu, D. Wu, J. Cheng, Z. W. Ouyang and C. Duan, *Dalton Transactions*, 2013, **42**, 15326-15331.
36. N. F. Chilton, R. P. Anderson, L. D. Turner, A. Soncini and K. S. Murray, *Journal of Computational Chemistry*, 2013, **34**, 1164-1175.
37. R. L. Carlin, *Magnetochemistry*, Springer-Verlag Berlin Heidelberg, 1986.
38. R. Ruamps, L. J. Batchelor, R. Guillot, G. Zakhia, A.-L. Barra, W. Wernsdorfer, N. Guihéry and T. Mallah, *Chem Sci*, 2014, **5**, 3418-3424.
39. T. J. Woods, M. F. Ballesteros-Rivas, S. Gómez-Coca, E. Ruiz and K. R. Dunbar, *Journal of the American Chemical Society*, 2016, **138**, 16407-16416.
40. D. Schweinfurth, J. Krzystek, M. Atanasov, J. Klein, S. Hohloch, J. Telser, S. Demeshko, F. Meyer, F. Neese and B. Sarkar, *Inorganic Chemistry*, 2017, **56**, 5253-5265.
41. R. Herchel and R. Boča, *Dalton Trans.*, 2005, 1352-1353.
42. J. S. Wood, *Journal of the Chemical Society A: Inorganic, Physical, Theoretical*, 1969, 1582-1586.
43. J. M. Clemente-Juan, E. Coronado, A. Forment-Aliaga, J. R. Galán-Mascarós, C. Giménez-Saiz and C. J. Gómez-García, *Inorganic Chemistry*, 2004, **43**, 2689-2694.
44. X.-T. Wang, B.-W. Wang, Z.-M. Wang, W. Zhang and S. Gao, *Inorganica Chimica Acta*, 2008, **361**, 3895-3902.
45. S. T. Meally, C. McDonald, P. Kealy, S. M. Taylor, E. K. Brechin and L. F. Jones, *Dalton Transactions*, 2012, **41**, 5610-5616.
46. G. S. Papaefstathiou, A. K. Boudalis, T. C. Stamatatos, C. J. Milios, C. G. Efthymiou, C. P. Raptopoulou, A. Terzis, V. Psycharis, Y. Sanakis, R. Vicente, A. Escuer, J.-P. Tuchagues and S. P. Perlepes, *Polyhedron*, 2007, **26**, 2089-2094.
47. L.-Q. Wei, B.-W. Li, S. Hu and M.-H. Zeng, *CrystEngComm*, 2011, **13**, 510-516.
48. S.-H. Zhang, R.-X. Zhao, G. Li, H.-Y. Zhang, C.-L. Zhang and G. Muller, *RSC Advances*, 2014, **4**, 54837-54846.
49. T. Singha Mahapatra, D. Basak, S. Chand, J. Lengyel, M. Shatruk, V. Bertolasi and D. Ray, *Dalton Trans.*, 2016, **45**, 13576-13589.
50. S.-H. Zhang, Y. Song, H. Liang and M.-H. Zeng, *CrystEngComm*, 2009, **11**, 865-872.
51. J.-Y. Ge, L. Cui, J. Li, F. Yu, Y. Song, Y.-Q. Zhang, J.-L. Zuo and M. Kurmoo, *Inorganic Chemistry*, 2017, **56**, 336-343.
52. C.-M. Liu, D.-Q. Zhang and D.-B. Zhu, *Scientific Reports*, 2017, **7**, 15483.
53. W.-Y. Zhang, Y.-Q. Zhang, S.-D. Jiang, W.-B. Sun, H.-F. Li, B.-W. Wang, P. Chen, P.-F. Yan and S. Gao, *Inorg. Chem. Front.*, 2018, **5**, 1575-1586.

54. S. Vaidya, S. Tewary, S. K. Singh, S. K. Langley, K. S. Murray, Y. Lan, W. Wernsdorfer, G. Rajaraman and M. Shanmugam, *Inorganic Chemistry*, 2016, **55**, 9564-9578.
55. A. Tsohos, S. Dionyssopoulou, C. P. Raptopoulou, A. Terzis, E. G. Bakalbassis and S. P. Perlepes, *Angewandte Chemie International Edition*, 1999, **38**, 983-985.
56. E. Fursova, O. Kuznetsova, V. Ovcharenko, G. Romanenko, V. Ikorskii, I. Eremenko and A. Sidorov, *Polyhedron*, 2007, **26**, 2079-2088.
57. L. N. Dawe, K. V. Shuvaev and L. K. Thompson, *Inorganic Chemistry*, 2009, **48**, 3323-3341.
58. S. K. Langley, M. Helliwell, S. J. Teat and R. E. P. Winpenny, *Dalton Trans.*, 2012, **41**, 12807-12817.
59. W. Shentang, B. Yanfeng, H. Xinxin, Z. Xiaofei and L. Wuping, *Zeitschrift fur Anorganische und Allgemeine Chemie*, 2017, **643**, 160-165.
60. E. K. Brechin, S. G. Harris, S. Parsons and R. E. P. Winpenny, *Angewandte Chemie International Edition in English*, 1997, **36**, 1967-1969.
61. S. Biswas, M. Tonigold, M. Speldrich, P. Kögerler and D. Volkmer, *European Journal of Inorganic Chemistry*, 2009, **2009**, 3094-3101.
62. T. C. Stamatatos, C. P. Raptopoulou, S. P. Perlepes and A. K. Boudalis, *Polyhedron*, 2011, **30**, 3026-3033.
63. D. Sahoo, R. Suriyanarayanan and V. Chandrasekhar, *Crystal Growth & Design*, 2014, **14**, 2725-2728.
64. Y.-Z. Zhang, W. Wernsdorfer, F. Pan, Z.-M. Wang and S. Gao, *Chemical Communications*, 2006, 3302-3304.
65. Y.-L. Zhou, M.-H. Zeng, L.-Q. Wei, B.-W. Li and M. Kurmoo, *Chemistry of Materials*, 2010, **22**, 4295-4303.
66. D. I. Alexandropoulos, L. Cunha-Silva, A. Escuer and T. C. Stamatatos, *Chemistry – A European Journal*, 2014, **20**, 13860-13864.
67. T. Singha Mahapatra, D. Basak, S. Chand, J. Lengyel, M. Shatruk, V. Bertolasi and D. Ray, *Dalton Transactions*, 2016, **45**, 13576-13589.
68. H. Zhang, J. Zhang, R. Liu, Y. Li, W. Liu and W. Li, *European Journal of Inorganic Chemistry*, 2016, **2016**, 4134-4143.

Chapter 4

Slow magnetic relaxation in $\{Co^{II}Co^{III}_2\}$ complexes containing high magnetic anisotropy trigonal bipyramidal Co^{II} centres

Conetnts

4. Slow magnetic relaxation in {$Co^{II}Co^{III}_2$} complexes containing high magnetic anisotropy trigonal bipyramidal Co^{II} centres

4.1 Introduction

The pursuit of high magnetic anisotropy in polymetallic complexes, in order to achieve exceptional magnetic properties, is one of the main challenges for many research groups studying single-molecule magnets. The presence of both high magnetic anisotropy and a high spin ground state in polynuclear complexes is difficult to achieve. As discussed in Chapter 1, studies showed that the increase of the total spin did not translate into high energy barriers;[1-5] additionally O. Waldman demonstrated that the magnetic anisotropy was inversely proportional to S^2.[6] Therefore, researchers have focused on 3*d* and 4*f* single-ion magnets (SIMs) in order to control the magnetic anisotropy. However, in the case of 3*d* SIMs the main obstacle is the low spin of the metal ion, which translates to a small m_s ground state. Hence, the incorporation of highly anisotropic 3*d* centres (*e.g.* Co^{II}) in clusters containing transition metal ions with high spin ground state (*e.g.* Cr^{III}, Mn^{II}, Fe^{III}) is a great approach towards the synthesis of polymetallic complexes combining both of the desired properties. It has been reported recently by E. Garlatti *et al.* how the magnetic anisotropy of octahedral Co^{II} is transferred to the overall magnetic anisotropy of a polymetallic {Cr_7Co} system. In their work they demonstrated how the combination of high-spin ions strongly coupled to a few highly-anisotropic ions like Co^{II} represents a promising route for building scalable quantum information architectures.[7]

Herein, we describe three {$Co^{II}Co^{III}_2$} complexes with a high anisotropy Co^{II} in trigonal bipyramidal (TBP) geometry incorporating the ligands pyrazole (= Hpz), dibenzoylmethane (= HDBM) and acetylacetone (= Hacac). We report a new synthetic route for the previously reported [$Co^{II}Co^{III}_2$(μ_3-OH)(μ-pz)$_4$(DBM)$_3$]·2THF (**3**·2THF) [8], a new solvate of **3**·2THF, complex [$Co^{II}Co^{III}_2$(μ_3-OH)(μ-pz)$_4$(DBM)$_3$]·2MeCN (**4**·2MeCN) and a new analogue with the same triangular metallic core as in **3**·2THF and **4**·2MeCN, complex [$Co^{II}Co^{III}_2$(μ_3-OH)(μ-pz)$_4$(acac)$_3$] (**5**). All complexes were magnetically characterised with dc and ac magnetic susceptibility measurements, and slow relaxation of the magnetisation at low temperature was observed for complexes **3**·2THF and **4**·2MeCN, while complex **5** shows only the onset of the out-of-phase ac signals. Complexes **3**·2THF and **4**·2MeCN are the only reported Co^{II}/Co^{III} complexes, to our knowledge, with one single Co^{II} centre in TBP geometry that exhibit slow magnetic relaxation (CSD search, database of 2017).[9-16]

4.2 Synthesis

[$Co^{II}Co^{III}_2$(μ_3-OH)(μ-pz)$_4$(DBM)$_3$]·2THF (**3·2THF**) : $CoCl_2 \cdot 6H_2O$ (0.3 mmol, 71 mg) was added to a solution of Hpz (0.4 mmol, 27 mg) and DBMH (0.3 mmol, 67 mg) in THF (14 ml) in the presence of NEt_3 (2 mmol, 0.3 ml). The solution was placed in a Teflon lined autoclave and heated to 100 °C over a period of 30 minutes. The temperature was held at 100 °C for 12 h and then the solution was allowed to cool to room temperature at 0.1 ^oC/min rate. Liquid diffusion of the solution with hexane resulted in red block-like crystals after 7 days (~20% yield). Elemental analysis calcd(%) for $C_{65}H_{63}Co_3N_8O_{9.5}$ (**3**·2THF·0.5H_2O): C 60.75%, H 4.94%, N 8.72%, found C 60.61%, H 4.88%, N 8.83%.

[$Co^{II}Co^{III}_2$(μ_3-OH)(μ-pz)$_4$(DBM)$_3$]·2MeCN (**4·2MeCN**) : $CoCl_2 \cdot 6H_2O$ (0.1 mmol, 24 mg) was added to a solution of Hpz (0.3 mmol, 20 mg) and DBMH (0.3 mmol, 67 mg) in 16 ml MeOH/MeCN (1:1) in the presence of NEt_3 (2 mmol, 0.3 ml). The solution was stirred for 1 hour at room temperature, and left to slowly evaporate to give red block-like crystals after 4 days (~15% yield). Elemental analysis calcd(%) (calculated with two MeCN solvent molecules being lost) for $C_{57}H_{46}Co_3N_8O_7$ (**4**): C 60.49%, H 4.09%, N 9.9%, found C 60.12%, H 4.10%, N 9.73%.

[$Co^{II}Co^{III}_2$(μ_3-OH)(μ-pz)$_4$(acac)$_3$] (**5**) : $Co(NO_3)_2 \cdot 6H_2O$ (0.5 mmol, 145 mg) was added to a solution of Hpz (0.5 mmol, 34 mg) and Hacac (0.5 mmol, 0.05 ml) in 10 ml MeOH/MeCN (1:1) in the presence of $NMe_4OH \cdot 5H_2O$ (1 mmol, 181 mg). The solution was placed in a Teflon lined autoclave and heated to 100 °C over a period of 30 minutes. The temperature was held at 100 °C for 12 h and then the solution was allowed to cool to room temperature at 0.1 ^oC/min rate. The solution was loosely closed with a lid and was left at room temperature to slowly evaporate to give red block-like crystals after ~2 months (~5% yield). Elemental analysis calcd(%) for $C_{27}H_{34}Co_3N_8O_7$ (**5**): C 42.70%, H 4.51%, N 14.75%. Due to the extremely low yield of the reaction and the destructive nature of the microanalysis method, we were not able to perform a CHN analysis. In order to be able to perform magnetic measurements the whole quantity of the sample (~20 mg) was required and therefore the microanalysis could not be carried out for this sample.

4.3 Results and discussion

As mentioned previously, the structure of complex $[Co^{II}Co^{III}_2(\mu_3\text{-OH})(\mu\text{-pz})_4(DBM)_3]\cdot 2THF$ (**3**·2THF)[8] (Fig. 4.1 left) has been already reported, however no dynamic ac magnetic studies were performed for this complex; therefore our first step was to refine the synthetic procedure in order to study the magnetic properties. According to the synthesis reported by M. Łukasiewicz *et al.*, an aqueous solution of cobalt(II) nitrate was added into a solution of HDBM and Hpz in THF. Dichloromethane (= DCM) was added to the mixture in order to extract the organic phase, followed by the addition of 1 M aq. NaOH. After DCM was removed, the remained solid residue was re-dissolved in THF and crystals were obtained from a THF/hexane mixture. Various changes in the above synthesis (*e.g.* change of solvent, base, cobalt salt and/or reaction conditions) led to the refined reaction of $CoCl_2\cdot 6H_2O$ with Hpz and DBMH, in THF and in the presence of NEt_3, under solvothermal conditions (for full experimental procedure see Section 4.2). The resulting solution was layered with liquid hexane resulting in red block-like crystals, and single-crystal X-ray diffraction showed that the unit cell corresponds to $[Co^{II}Co^{III}_2(\mu_3\text{-OH})(\mu\text{-pz})_4(DBM)_3]\cdot 2THF$. During our attempts to improve the synthetic procedure, we also managed to isolate a new solvate of **3**·2THF, complex $[Co^{II}Co^{III}_2(\mu_3\text{-OH})(\mu\text{-pz})_4(DBM)_3]\cdot 2MeCN$ (**4**·2MeCN) (Fig. 4.1 right). Complex **4**·2MeCN is synthesised from the reaction of $CoCl_2\cdot 6H_2O$ with Hpz and HDBM, in a mixture of MeOH/MeCN and in the presence of NEt_3 under ambient conditions (for full experimental procedure see Section 4.2). Complexes **3**·2THF and **4**·2MeCN are based on the same triangular motif with slight differences in the solvents employed.

Previous studies on mononuclear Co^{II}–based complexes in TBP geometry, have demonstrated that the change of either the nature of the axial ligand or the substituted groups on the overall ligand, can affect the geometry and therefore the magnetic properties of the complexes.[17-24] This prompted us to examine if it is possible to isolate another analogue with a different ligand than HDBM, the ligand acetylacetone. Acetylacetone is a less bulky ligand than HDBM and could lead to a change in the geometry around the cobalt centres. Indeed we were able to isolate another analogue of **3** with the same triangular motif, complex $[Co^{II}Co^{III}_2(\mu_3\text{-OH})(\mu\text{-pz})_4(acac)_3]$ (**5**) (Fig. 4.2); however, in this case no molecules of solvent are present in the crystal lattice. Attempts to isolate other analogues with different ligands, such as 1-benzoylacetone (= 1-phenyl-1,3-butanedione), hexafluoroacetylacetone (= 1,1,1,5,5,5-hexafluoro-2,4-pentanedione) and/or 3,5-dimethylpyrazole were not successful (Fig. 4.3).

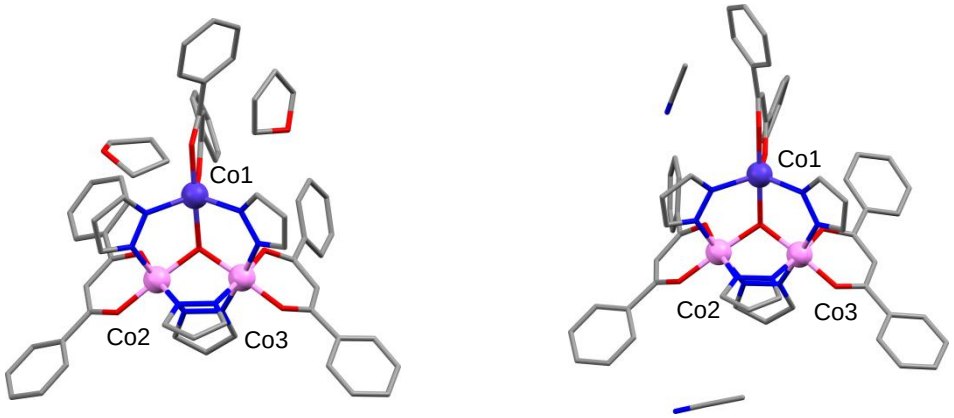

Figure 4.1 The molecular structure of **3**·2THF (*left*) and the molecular structure of **4**·2MeCN (*right*). Colour code: Co^{II}: violet, Co^{III}: pink, O: red, N: blue, C: grey. Hydrogen atoms are omitted for clarity.

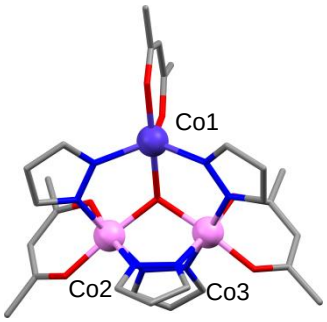

Figure 4.2 The molecular structure of **5**. Colour code: Co^{II}: violet, Co^{III}: pink, O: red, N: blue, C: grey. Hydrogen atoms are omitted for clarity.

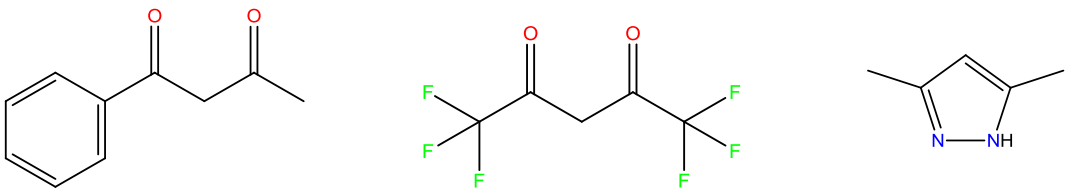

Figure 4.3 Illustration of the ligands 1-benzoylacetone, hexafluoroacetylacetone and 3,5-dimethylpyrazole, from left to right.

Crystal structure analysis

Complexes **3**·2THF[8] and **4**·2MeCN crystallise in the triclinic $P\bar{1}$ space group and both can be described as mixed-valence isosceles triangles of Co^{II}/Co^{III} ions. Since the molecular structures of **3** and **4** are very similar, only the structure of **4** will be described. Selected crystallographic data for **4**·2MeCN can be found in Table 4.1.

All cobalt centres are connected by a μ_3-OH bridge, while Co^{II} (Co1) is further bridged with each Co^{III} (Co2 and Co3) through one pyrazolate ligand, and Co2 and Co3 are also bridged through two pyrazolate ligands. One singly deprotonated DBM^- ligand completes the coordination sphere of each cobalt centre. Co1 is five-coordinate adopting a slightly distorted TBP geometry, while the two diamagnetic Co2 and Co3 adopt an octahedral geometry (Fig. 4.4). The oxidation states of Co^{II} and Co^{III} of both complexes were confirmed using Bond Valence Sum (BVS) analysis.[25, 26] Continuous shape measures (CShMs)[27, 28] give the values of 0.27 and 0.33 for the Co^{II} in TBP (where 0 corresponds to the ideal polyhedron), for **3** and **4** respectively, confirming a small distortion (Fig. A4.1 and Table A4.1 in the appendix). The asymmetric unit of **3**·2THF contains a molecule of [$Co^{II}Co^{III}_2$(μ_3-OH)(μ-pz)$_4$(DBM)$_3$] and two molecules of THF solvent in the crystal lattice, while the asymmetric unit of **4**·2MeCN contains a molecule of [$Co^{II}Co^{III}_2$(μ_3-OH)(μ-pz)$_4$(DBM)$_3$] and two molecules of MeCN solvent in the crystal lattice. The crystal packing is similar for both complexes (Fig. 4.5) and intermolecular interactions are present in **3**·2THF and **4**·2MeCN through hydrogen-π and π-π interactions between the phenyl and pyrazolate rings of neighbouring molecules (Fig. A4.2 in the appendix). The shortest intermolecular Co1···Co1' distances are ~9.3 Å in both complexes.

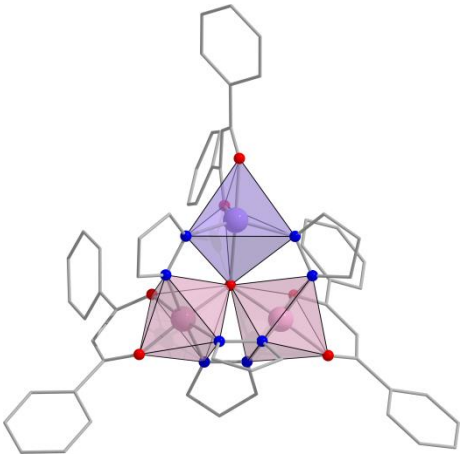

Figure 4.4 The molecular structure of [$Co^{II}Co^{III}_2$(μ_3-OH)(μ-pz)$_4$(DBM)$_3$]. Colour code: Co^{II}: violet (the violet polyhedron represents the TBP geometry), Co^{III}: pink (the pink polyhedra represent the octahedral geometry), O: red, N: blue, C: grey. Hydrogen atoms are omitted for clarity.

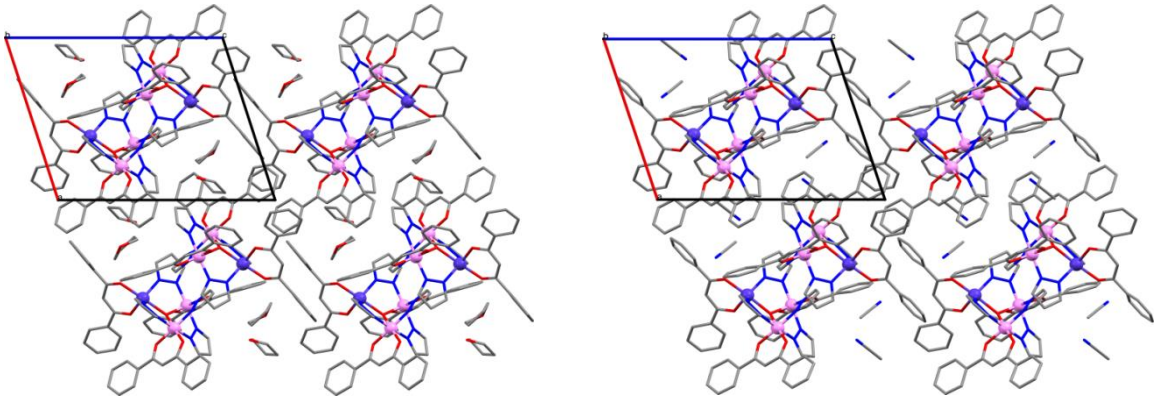

Figure 4.5 The crystal packing of **3**·2THF (*left*) ($P\bar{1}$) and **4**·2MeCN (*right*) ($P\bar{1}$) along the crystallographic *b*-axis. Colour code: Co^{II}: violet, Co^{III}: pink, O: red, N: blue, C: grey. Hydrogen atoms are omitted for clarity.

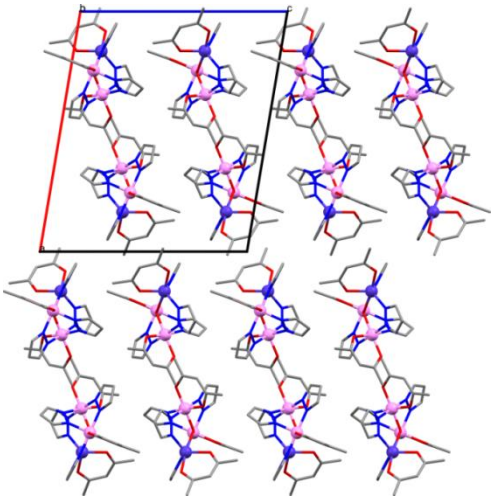

Figure 4.6 The crystal packing of **5** ($P2_1/c$) along the crystallographic *b*-axis. Colour code: Co^{II}: violet, Co^{III}: pink, O: red, N: blue, C: grey. Hydrogen atoms are omitted for clarity.

Complex **5** crystallises in the monoclinic $P2_1/c$ space group and is a mixed-valence isosceles triangle of Co^{II}/Co^{III} ions, as seen for complexes **3** and **4**. Selected crystallographic data for **5** can be found in Table 4.1. All cobalt centres are connected by a μ_3-OH bridge, while Co^{II} (Co1) is further bridged with each Co^{III} (Co2 and Co3) through one pyrazolate ligand, and Co2 and Co3 are also bridged through two pyrazolate ligands. One singly deprotonated $acac^-$ ligand completes the coordination sphere for each cobalt centre. Co1 is five-coordinate adopting a slightly distorted TBP geometry, while the two diamagnetic Co2 and Co3 adopt an octahedral geometry. The oxidation states of Co^{II} and Co^{III} of both complexes were confirmed using Bond Valence Sum (BVS) analysis.[25, 26] Continuous shape measures (CShMs)[27, 28] give a value of 0.54 for the Co^{II} in TBP, slightly

higher than in **3** and **4** (Fig. A4.1 and Table A4.1 in the appendix). The asymmetric unit of **5** consists of a molecule of $[Co^{II}Co^{III}_2(\mu_3\text{-OH})(\mu\text{-pz})_4(acac)_3]$ and the crystal packing is different from **3** and **4** (Fig. 4.6). Intermolecular interactions are present through hydrogen-π interactions between the hydrogens of the $acac^-$ ligands and the pyrazolate rings of neighbouring molecules (Fig. A4.3 in the appendix). The shortest intermolecular Co1···Co1' distance is ~7 Å.

Table 4.1. Data collection and crystallographic parameters for complexes **4**·2MeCN and **5**.

Chemical formula	$C_{57}H_{46}Co_3N_8O_7\cdot2(C_2H_3N)$ **4**·2MeCN	$C_{27}H_{34}Co_3N_8O_7$ **5**
M_r	1213.91	759.41
Crystal system, space group	Triclinic, $P\bar{1}$	Monoclinic, $P2_1/c$
Temperature (K)	100	100
***a*, *b*, *c* (Å)**	13.25 (1), 14.173 (11), 16.426 (13)	19.1735 (4), 10.4861 (2), 16.2980 (4)
***α*, *β*, *γ* (°)**	85.880 (19), 71.750 (19), 72.444 (18)	β = 99.552 (2)
***V* (Å^3)**	2792 (4)	3231.37 (12)
Z	2	4
Radiation type	Mo *K*α	Mo *K*α
***μ* (mm^{-1})**	0.95	1.58
Crystal size (mm)	0.34 × 0.1 × 0.06	0.18 × 0.07 × 0.02
Diffractometer	KappaCCD	Rigaku FRE+ equipped with VHF Varimax confocal mirrors and an AFC10 goniometer and HG Saturn 724+ detector
No. of measured, independent and observed [$I > 2\sigma(I)$] reflections	15656, 9616, 6683	40709, 7398, 6188
R_{int}	0.043	0.039
$R[F^2 > 2\sigma(F^2)]$, $wR(F^2)$, GOF on F^2	0.047, 0.111, 1.06	0.032, 0.076, 1.01
No. of reflections	9616	7398
No. of parameters	736	416
No. of restraints	1	-
Δ>max, Δ>min (e Å^{-3})	0.59, -0.50	0.63, -0.39

Powder X-ray diffraction analysis

The experimental powder X-ray diffraction (PXRD) patterns of complexes **3**·2THF and **5** (Fig. 4.7) are consistent with the calculated ones from the single crystal structures of **3**·2THF and **5**, respectively; therefore, we can conclude that the samples are phase pure. The slight shift in 2θ values of the peaks is due to the temperature difference between the experimental PXRD patterns, measured at room temperature, while the calculated patterns are generated from the single-crystal data collected at 100 K.

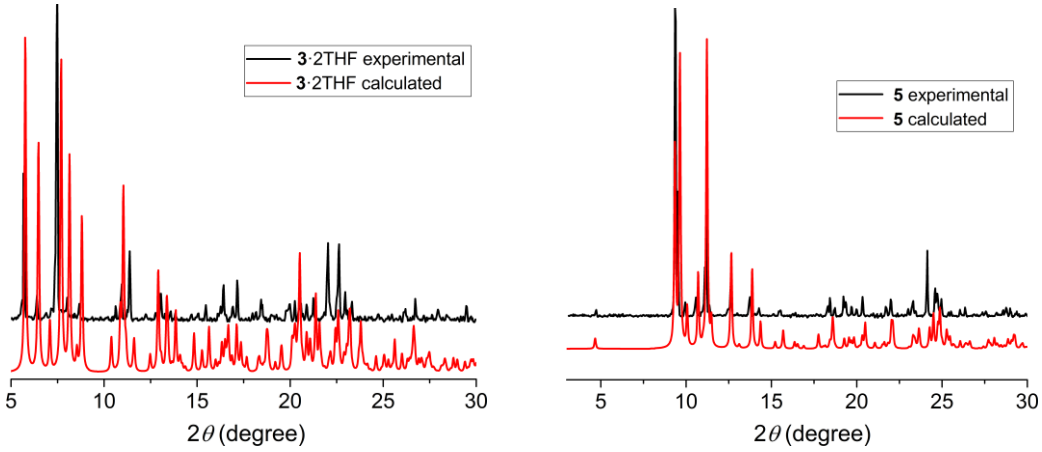

Figure 4.7 *Left)* The PXRD pattern (5−30°) of complex **3**·2THF. *Right)* The PXRD pattern (3−30°) of complex **5**. The red lines represent the calculated PXRD patterns for **3**·2THF and **5** and the black lines the experimental ones. The experimental PXRD patterns were measured at room temperature, while the calculated pattern is generated from the single-crystal data collected at 100 K.[8]

However, looking at the experimental PXRD pattern of complex **4** in Figure 4.8 (left), it is clear that there is a deviation from the pattern calculated from the single crystal structure; this could be attributed to the loss of solvent, during the grinding process, as seen in the elemental analysis (see Section 4.2). In order to examine if the desolvation is the reason for the deviation of the experimental pattern from the calculated pattern, the sample was prepared in a different way, by avoiding grinding the sample to powder. The new PXRD pattern (Fig. 4.8 right) is now closer to the calculated one, which suggests that desolvation causes the deviation in the ground sample. This desolvation could cause a slight change of the crystal packing and therefore a slight change of the local environment around the cobalt centres, resulting in small changes to the *g*, *D* and *E* parameters (see below magnetic characterisation). The difference in the intensities of the peaks could also be attributed to the desolvation, while the slight shift in 2θ values of the peaks is due to the

temperature difference between the experimental PXRD pattern, measured at room temperature, and the calculated pattern which is generated from the single-crystal data collected at 100 K.

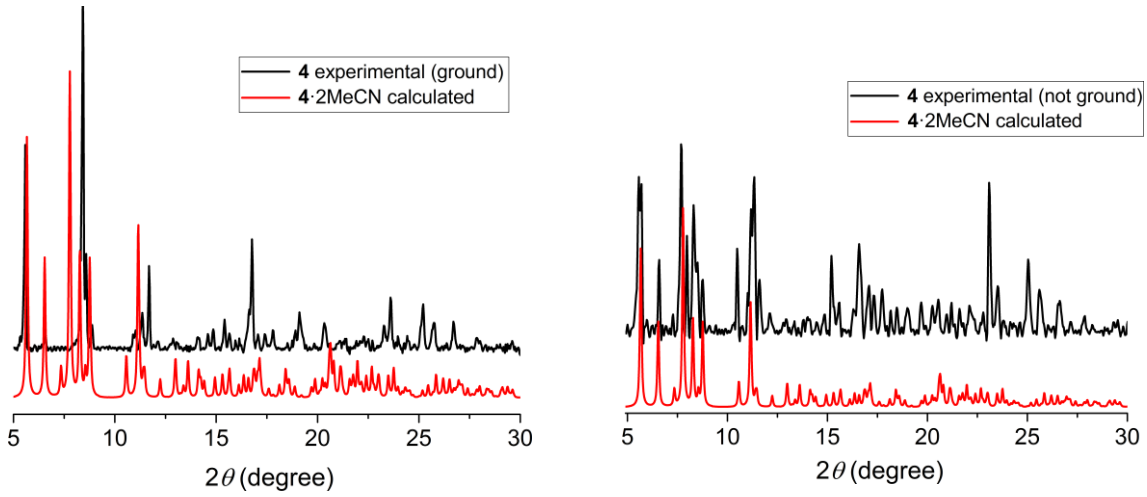

Figure 4.8 *Left)* The PXRD pattern (5−30°) of the desolvated complex (ground). *Right)* The PXRD pattern (5−30°) of the solvated complex (not ground). The red line represents the calculated PXRD pattern for the solvated complex **4**·2MeCN and the black lines the experimental ones. The experimental PXRD patterns were measured at room temperature, while the calculated pattern is generated from the single-crystal data collected at 100 K.

Magnetic characterisation

Variable temperature dc susceptibility measurements were carried out for **3**·2THF, **4** and **5** in a field of 1000 Oe in the 290–2 K temperature range (Fig. 4.9). At 290 K the $\chi_M T$ values are 2.51, 2.47 and 2.47 $cm^3\ mol^{-1}$ K, for **3**·2THF, **4** and **5** respectively**.** These values are higher than the expected $\chi_M T$ = 1.88 $cm^3\ mol^{-1}$ K for a high-spin Co^{II} (S = 3/2 and g = 2), indicating a spin-orbit coupling contribution. As the temperature decreases, $\chi_M T$ drops gradually until ~50 K and then decreases rapidly below that, to reach 1.45 (**3**·2THF), 1.40 (**4**) and 1.45 (**5**) $cm^3\ mol^{-1}$ K at 2 K, indicating zero-field splitting of the ground state. Additionally, magnetisation versus field plots at 2, 4 and 6 K (Fig. A4.4 in the appendix) did not saturate at the highest available field of 5 T, a further indication of the presence of magnetic anisotropy.

High-field/frequency EPR (HFEPR) studies were performed only for complex **4**, due to limited time being available at the National High Magnetic Field Laboratory (NHMFL). The HFEPR studies on **4** (Fig. A4.5 and A4.6 in the appendix) suggest the presence of two discrete species within the microcrystalline powder sample in an ~ 50 : 50 ratio, having

distinct ZFS parameters (for the full HFEPR analysis see Chapter 4 in the appendix). This is in agreement with the elemental and PXRD analysis (as discussed above), which show that the lattice solvent is easily lost. Analysis of the EPR data gives the parameters for the two species as: $g_x = g_y = 2.18$, $g_z = 2.07$ with an E/D ratio ~0.13, and $g_x = g_y = 2.23$, $g_z = 2.08$ with an E/D ratio ~0.17. Using the average of these two sets, $g_x = g_y = 2.205$, $g_z = 2.075$, the dc magnetic susceptibility data and the magnetisation curves of complex **4** were fitted simultaneously using the program PHI[29] (Fig. 4.10), as described by the following effective Hamiltonian equation (4.1)[30]:

$$\hat{H} = D[\hat{S}_z^2 - \tfrac{1}{3}S(S+1)] + E(\hat{S}_x^2 - \hat{S}_y^2) + \mu_B \vec{B} \cdot \overleftrightarrow{g} \cdot \hat{S} \qquad (4.1)$$

The first and second terms represent the axial and rhombic ZFS terms, parameterised by D and E, respectively, $\hat{S}$ is the spin operator with components $\hat{S}_i$ ($i = x, y, z$), and the final term denotes the Zeeman interaction with the local magnetic field, $\vec{B}$, parameterised through the Landé g tensor. Fixing the values of $g_x = g_y = 2.205$ and $g_z = 2.075$, and χ_{TIP} = 0.0009 $cm^3\ mol^{-1}$, where χ_{TIP} stands for the contribution of temperature-independent paramagnetism arising from two Co^{III} and one TBP Co^{II},[31, 32] we were able to extract the ZFS parameters D = +23.85 (±0.17) cm^{-1} and E = +4.04 (±0.09) cm^{-1}. The E/D ratio extracted from the fitting of the magnetic data is ~0.17, consistent with the EPR studies.

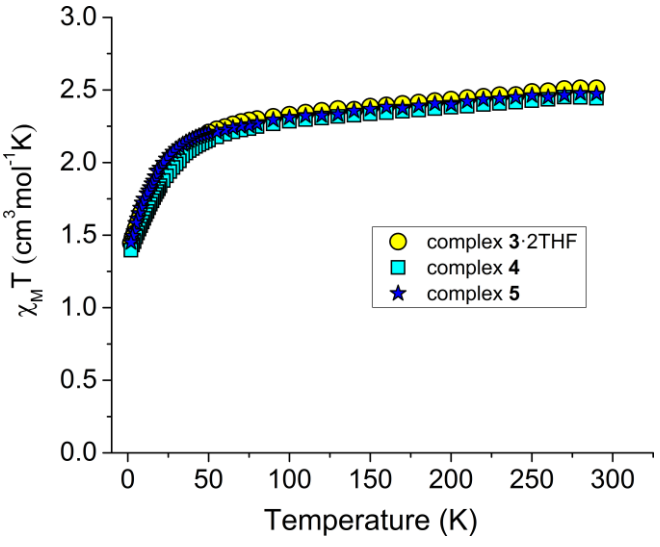

Figure 4.9 χ_MT *versus* Temperature data for complexes **3**·2THF (yellow), **4** (light blue) and **5** (blue) in a field of 1000 Oe from 290–2 K.

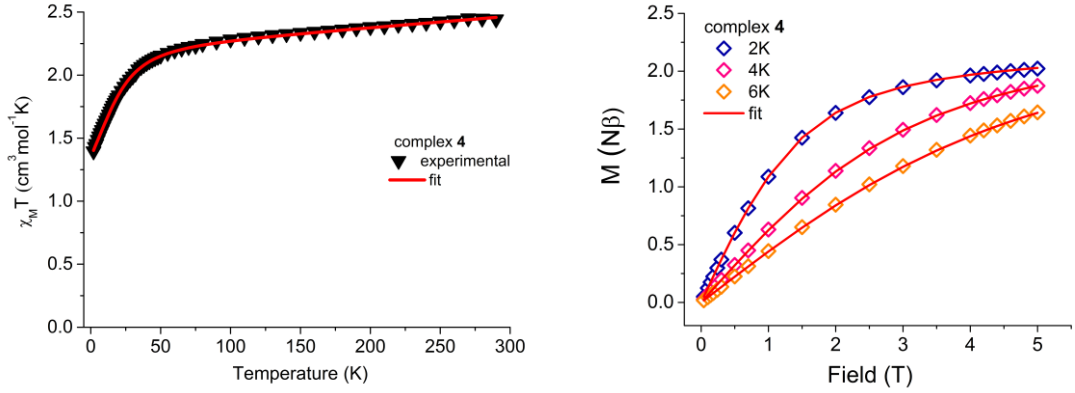

Figure 4.10 *Left)* χ_MT *versus* Temperature data for **4** in a field of 1000 Oe from 290–2 K. *Right)* Magnetisation *versus* Field data at temperatures 2, 4, and 6 K for **4**. The red solid lines represent the fit with the program PHI[29].

Furthermore, the dc magnetic susceptibility data and the magnetisation curves were fitted simultaneously for complexes **3**·2THF and **5** using the program PHI[29] (Fig. 4.11), as described by equation 4.1. In the cases of **3**·2THF and **5** no HFEPR studies were performed (due to limited time at the NHMFL), therefore all values g_x, g_y, g_z, D and E were extracted from the fit. Again χ_{TIP} was necessary in order to obtain a satisfactory fit for both complexes; χ_{TIP} = 0.0008 cm^3 mol^{-1} for **3**·2THF and χ_{TIP} = 0.0007 cm^3 mol^{-1} for **5**.[31, 32] The extracted values for **3**·2THF are $g_x = g_y$ = 2.24, g_z = 2.10, D = +22.46 (±0.08) cm^{-1} and E = +2.53 (±0.05) cm^{-1} (E/D ratio ~0.11) and for **5** are $g_x = g_y$ = 2.20, g_z = 2.17, D = +16.53 (±0.17) cm^{-1} and E = +2.40 (±0.08) cm^{-1} (E/D ratio ~0.15) (Table 4.2). Negative D and E parameters were also used to fit the data for both complexes; however, the values produced were not sensible (*i.e.* E/D > 0.33 with considerable uncertainties). Moreover, considering that the local environment of Co1 in all complexes remains the same, with slightly different distortion of the TBP geometry, these results are sensible and the sign of D is consistent with the HFEPR studies for complex **4**.

The relatively high values of the transverse anisotropy in all complexes indicate significant mixing of the $m_S = \pm^3/_2$ and $\pm^1/_2$ levels, and can be attributed to the small deviation from the ideal TBP geometry and/or the different nature of the ligands in the equatorial positions.[17, 18, 33-35] Although theoretical calculations have shown that a large positive D value is expected for Co^{II} in TBP geometry,[36] the majority of the complexes that have been reported possess a negative D. However, positive values for the D term for Co^{II} complexes in TBP geometry are being reported increasingly, with the values being in the range 5 – 30 cm^{-1} [18, 20, 23, 24, 33, 35, 37, 38] and only a few reaching 40 – 70 cm^{-1};[17, 19, 39] therefore complexes **3**·2THF, **4** and **5** possess relatively high positive D values.

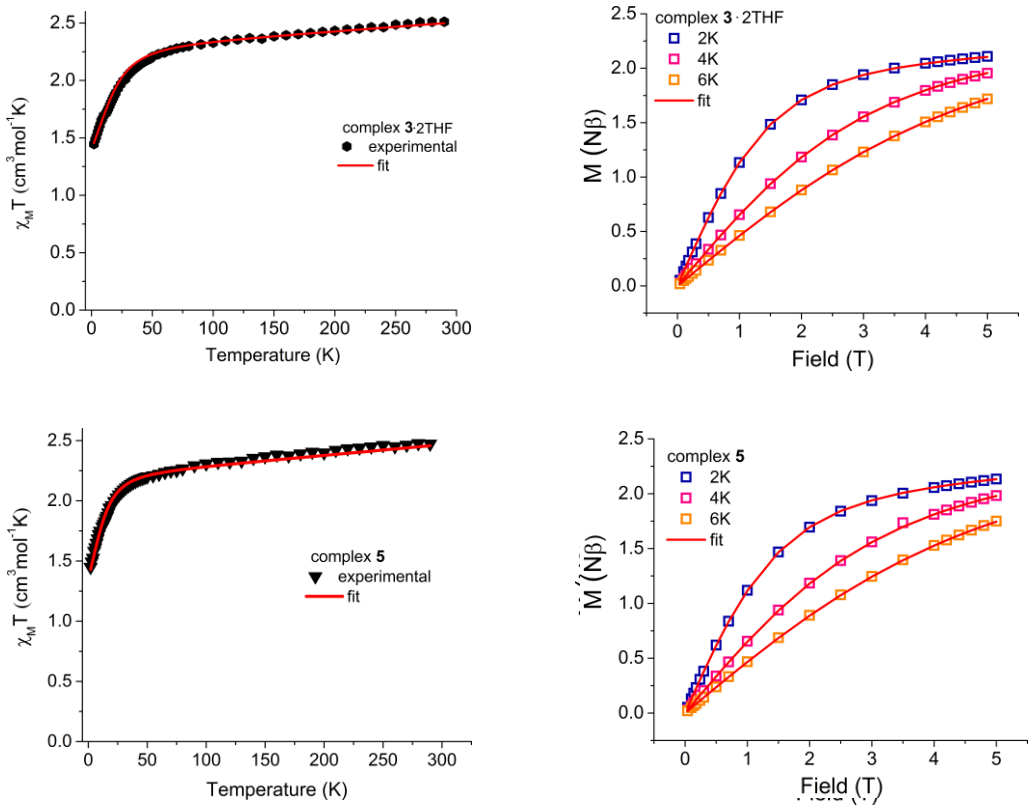

Figure 4.11 *Left)* χ_MT *versus* Temperature data for **3**·2THF (top) and **5** (bottom) in a field of 1000 Oe from 290–2 K. *Right)* Magnetisation versus Field plots at temperatures 2, 4, and 6 K for **3**·2THF (top) and **5** (bottom). The red solid lines represent the fit with program PHI[29].

Table 4.2 Experimental ZFS parameters and *g* values extracted with PHI for complexes **3**·2THF, **4** and **5**.

Complex	$g_x = g_y$	g_z	D (cm^{-1})	E (cm^{-1})
3·2THF	2.24	2.10	+22.46	+2.53
4	2.205 [a]	2.075 [a]	+23.85	+4.04
5	2.20	2.17	+16.53	+2.40

[a] These values were obtained from the HFEPR studies.

Ac susceptibility measurements were carried out for all three complexes. In zero applied dc field none of the complexes display any out-of-phase ac signals, due to efficient zero-field quantum tunnelling. However, by using an applied dc field to suppress tunnelling, all compounds display slow magnetic relaxation at low temperature. Variable dc fields (500 – 5000 Oe) were applied to **3**·2THF, **4** and **5** at 2 K (Fig. A4.7 in the appendix) in order to obtain the optimum dc field, at which the characteristic relaxation time of the

magnetisation (τ) possesses the largest value. Complex **5** shows only the onset out-of-phase ac signals and no clear maxima are observed in the ac susceptibility signals under different applied dc fields at 2 K; therefore no further measurements were performed for this complex. The characteristic relaxation times for each field were calculated using CC-FIT,[40, 41] and the τ_{max} value was obtained at 1500 and 1000 Oe for **3**·2THF and **4**, respectively (Fig. A4.8 in the appendix). The frequency dependence of the in-phase and out-of-phase magnetic susceptibility was measured for both complexes under the optimum dc field, for the range of temperatures 1.8 – 8 K (Fig. 4.12). Additionally, for complex **3**·2THF the frequency dependence of the magnetic susceptibility was also measured under 1000 Oe for the sake of comparison with complex **4** (Fig. 4.13). No obvious difference is observed in the frequency dependent ac signals of **3**·2THF with the change of field from 1500 to 1000 Oe, except that the intensities of the χ'' signals in 1000 Oe are somewhat lower than in 1500 Oe.

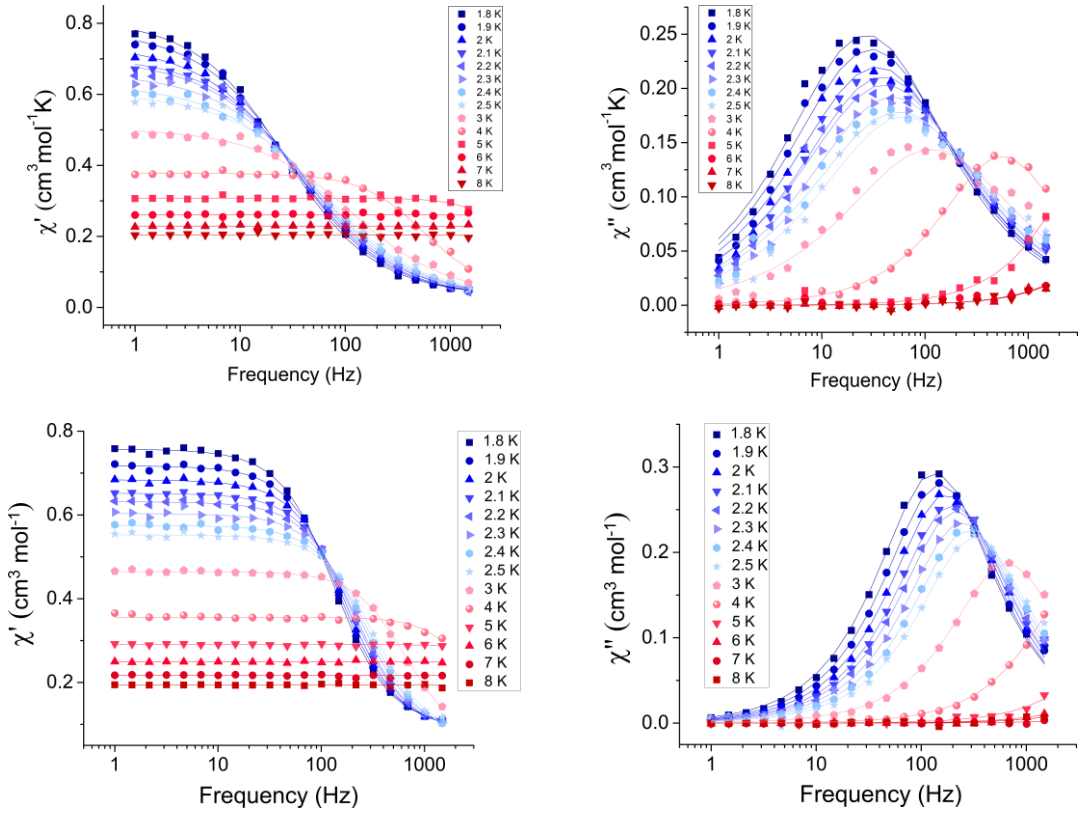

Figure 4.12 Frequency dependent in-phase (*left*) and out-of-phase (*right*) susceptibility signals for complexes **3**·2THF (*top*) and **4** (*bottom*) in 1500 and 1000 Oe dc applied magnetic field, respectively. The solid lines correspond to the fit (CC-FIT).[40, 41]

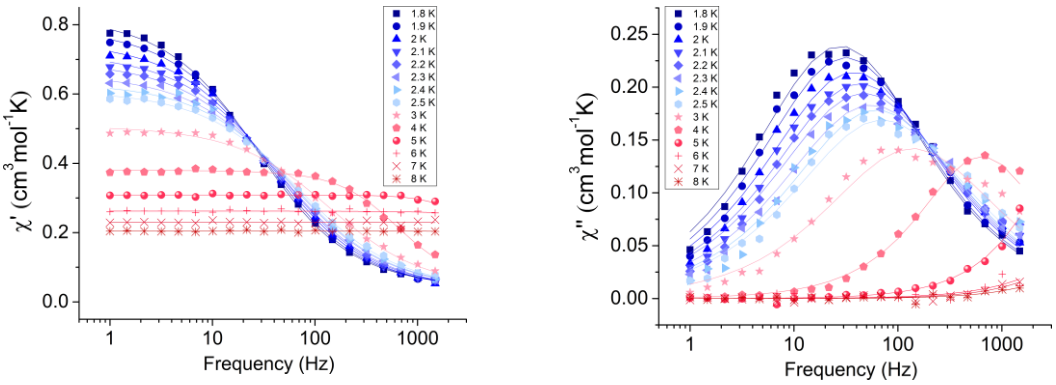

Figure 4.13 Frequency dependent in-phase (*left*) and out-of-phase (*right*) susceptibility signals for complex **3**·2THF in 1000 Oe dc applied magnetic field. The solid lines correspond to the fit (CC-FIT).[40, 41]

The fitting of the Cole–Cole plots (out-of-phase *versus* in-phase signals) for **3**·2THF and **4** was performed using CC-FIT[40, 41] (Fig. 4.14). The resulting values of the Cole–Cole parameter α were in the range 0.1 – 0.3 for **3**·2THF for both fields, indicative of a larger distribution of relaxation times, whereas for **4** the α values were in the range of 0.02 – 0.08, indicative of a relatively narrow distribution of relaxation times (Tables A4.2 and A4.3 in the appendix). The τ values were used to construct an Arrhenius plot for the temperatures 1.8 – 5 K for both complexes, from which the relaxation parameters of $\Delta E/k_B$ (energy barrier) and τ_0 (pre-exponential factor) at higher temperatures were extracted (Fig. A4.9 in the appendix). Fitting within the linear region (Orbach relaxation mechanism) the values $\Delta E/k_B$ = 26.19 (±1.7) K and τ_0 = 2.66 x 10^{-7} s for complex **3**·2THF (1500 Oe) and $\Delta E/k_B$ = 23.18 (± 2.2) K and τ_0 = 1.14 x 10^{-7} s for complex **4** were extracted. However, the values of $\Delta E/k_B$ are smaller than the calculated energy difference between the ground and first exited state of ~46 cm^{-1} (~66 K) and ~50 cm^{-1} (~72 K) for **3**·2THF and **4** respectively ($\Delta E_{theor} = 2\sqrt{D^2 + 3E^2}$), a clear indication that other relaxation processes need to be considered. Using Equation 4.2, we attempted to fit the τ versus T data but we were not able to extract reasonable values for either of the complexes. The terms are the direct, tunnelling, Raman and Orbach contributions, in that order.[35, 42]

$$\tau^{-1} = AH^mT + \frac{B_1}{1+B_2H^2} + CT^n + \tau_0^{-1}\exp(\frac{-\Delta E}{k_BT}) \quad (4.2)$$

$$\tau^{-1} = B + CT^n \quad (4.3)$$

In order to avoid over-parameterisation we attempted to fit the τ versus Field (H) data for **3**·2THF and **4** using only the terms for direct and tunnelling processes (which are dependent on field) to extract the parameters *A*, B_1, and B_2. However, all efforts were unsuccessful, an indication that there is a more complicated dependence of τ with the

field. Therefore, using only the tunnelling (expressed as the parameter *B*) and Raman contributions (see Equation 4.3) we were able to fit the τ^{-1} versus T plot (Fig. 4.14) affording the values B = 246 s^{-1}, C = 0.013 K^{-n} s^{-1} and n = 9 for **3**·2THF, and B = 926 s^{-1}, C = 2.3 K^{-n} s^{-1} and n = 6.6 for **4**. The exponent factor n in the Raman process should be equal to 9 for Kramers ions, or 5 in the presence of low-lying states. However, lower values for n have been reported in cases where acoustic and optical phonons are involved.[35, 42-45]

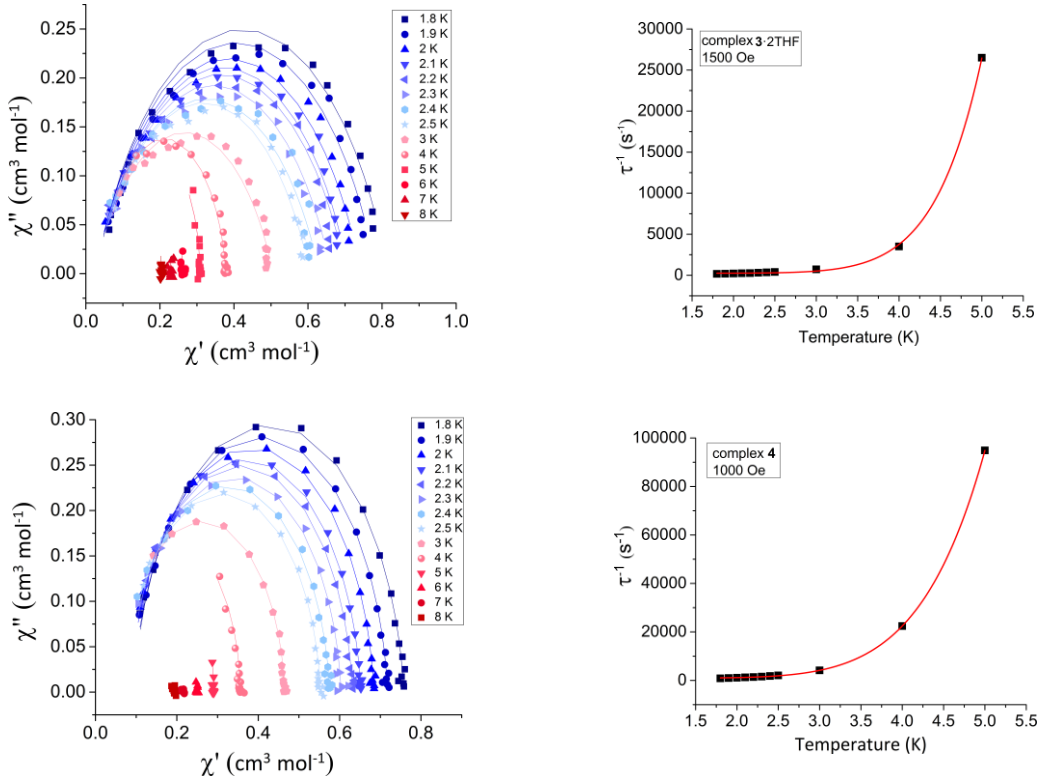

Figure 4.14 *Left)* Cole–Cole plots of the ac magnetic susceptibility of **3**·2THF (*top*) and **4** (*bottom*) at 1500 and 1000 Oe, respectively. The solid lines correspond to the fit (CC-FIT).[40, 41] *Right)* The plot of τ^{-1} vs T for **3**·2THF (*top*) and **4** (*bottom*) in the temperature range 1.8 – 5 K. The red solid lines correspond to the fit using eqn (4.3).

Magneto-structural correlation

The paramagnetic Co1 centre in all three complexes adopts a slightly distorted TBP geometry, with SHAPE[27, 28] values 0.27, 0.33 and 0.54 for **3**·2THF and **4** and **5**, respectively (0 is the ideal TBP geometry). Selected bond lengths and angles for the Co1 centre of all complexes can be found in Tables A4.4 – A4.9 in the appendix. If we consider only the first coordination environment of Co1 and compare the magnetic properties of all complexes, then we can assume that even a minor difference in the geometry (with the

ligand atoms remaining the same in all cases) can cause a different magnetic behaviour between the complexes. The *D* parameters for complexes **3**·2THF, **4** and **5** are +22.46, +23.86 and +16.53 cm^{-1}, respectively, and the *E* parameters are +2.53, +4.04, +2.40 cm^{-1} for **3**·2THF, **4** and **5** respectively (Table 4.2). We can observe that the rhombicity, expressed as the |*E*/*D*| ratio, is smaller for **3**·2THF (~0.11), than for **4** (~0.17) and **5** (~0.15). This is consistent with the increase of the distortion of the TBP geometry.[20] However, HFEPR studies are needed in order to determine the g_x, g_y and g_z values and extract more accurate *D* and *E* values for complexes **3**·2THF and **5**. Additionally, to further understand the different behaviour among the three complexes, theoretical calculations using the experimental geometries also needed.[18, 46]

However, the first coordination environment is insufficient when we attempt to compare the dynamic magnetic properties of the three complexes. Previously reported examples have shown that the presence, change or absence of solvent in the crystal lattice, and/or the intermolecular interactions (*i.e.* short distances of the neighbouring paramagnetic ions and/or hydrogen bonds) can drastically affect the magnetic properties. [47-51] In the cases of **3**·2THF and **4** the frequency dependent ac signals show a slight difference between them, whereas for complex **5** only the onset out-of-phase signals are observed. The absence of clear maxima in **5** could be ascribed to the higher TBP distortion, in comparison with **3**·2THF and **4**, and/or the short intermolecular Co1···Co1' distances ~7 Å (dipolar interactions for cobalt complexes are expected to be suppressed for distances larger than ~8 Å).[24] The slight change in the dynamic magnetic properties of **4** in comparison with **3**·2THF could be ascribed to the absence of solvent in the measured sample (see Powder X-ray diffraction analysis) and/or the slightly higher distortion of the TBP geometry in complex **4**. Finally, although the mechanisms of the relaxation of the magnetisation in the two complexes are the same (QTM and Raman), the contribution from QTM in **4** is somewhat larger (B = 926 s^{-1}) than in **3**·2THF (B = 246 s^{-1}). This could be attributed to the larger *E* term in **4**, which can facilitate a faster magnetic relaxation.[20] However, without theoretical calculations we cannot come to a strong conclusion.

4.4 Conclusions

The synthesis and magnetic characterisation of three Co^{II}/Co^{III} complexes were reported here; $[Co^{II}Co^{III}_2(\mu_3\text{-OH})(\mu\text{-pz})_4(DBM)_3]\cdot 2THF$ (**3**·2THF)[8], $[Co^{II}Co^{III}_2(\mu_3\text{-OH})(\mu\text{-pz})_4(DBM)_3]\cdot 2MeCN$ (**4**·2MeCN) and $[Co^{II}Co^{III}_2(\mu_3\text{-OH})(\mu\text{-pz})_4(acac)_3]$ (**5**) (Hpz = pyrazole, HDBM = dibenzoylmethane, Hacac = acetylacetone). Complex **4**·2MeCN is a new solvate of the previously reported **3**·2THF, while complex **5** is a new analogue based on the same triangular motif (the Co^{II} adopts a slightly distorted trigonal bipyramidal geometry while the two Co^{III} centres adopt an octahedral geometry) as in **3**·2THF and **4**·2MeCN. Dc magnetic susceptibility studies were carried out for all complexes, and in order to obtain the zero-field splitting parameters for **4** we used high-field/frequency EPR measurements to extract the *g* factors. Simultaneous fit of the dc magnetic susceptibility data and the magnetisation curves of complex **4** afforded the values D = +23.85 cm^{-1} and E = +4.04 cm^{-1} (E/D ~0.17), which are in accord with the EPR studies. Furthermore, the fit of the dc data for complexes **3**·2THF and **5** produced reasonable results with the values of D = +22.46 cm^{-1} and E = +2.53 cm^{-1} (E/D ~0.11) for **3**·2THF and D = +16.53 cm^{-1} and E = +2.40 cm^{-1} (E/D ~0.15) for **5**. The dynamic ac studies evidence slow magnetic relaxation for **3**·2THF and **4** at low temperature, whereas complex **5** exhibits the onset of the out-of-phase signals with no clear maxima of the peaks. Finally, complexes **3**·2THF and **4** are the only reported examples of a mixed-valence Co^{II}/Co^{III} polynuclear complex containing a single trigonal bipyramidal Co^{II} centre that gives rise to slow magnetic relaxation,[9-16] which in these cases arise from a large, easy-plane magnetic anisotropy. In general, molecules that exhibit a large spin ground state that is characterised by a large, easy-plane anisotropy are of interest for quantum information processing.[7, 52] Therefore, the next step is to develop a route to incorporate high magnetic anisotropy trigonal bipyramidal Co^{II} centres into exchange-coupled polymetallic systems that contain multiple paramagnetic centres.

4.5 References

1. A. J. Tasiopoulos, A. Vinslava, W. Wernsdorfer, K. A. Abboud and G. Christou, *Angewandte Chemie International Edition*, 2004, **43**, 2117-2121.
2. A. M. Ako, I. J. Hewitt, V. Mereacre, R. Clérac, W. Wernsdorfer, C. E. Anson and A. K. Powell, *Angewandte Chemie International Edition*, 2006, **45**, 4926-4929.
3. J. C. Goodwin, R. Sessoli, D. Gatteschi, W. Wernsdorfer, A. K. Powell and S. L. Heath, *Journal of the Chemical Society, Dalton Transactions*, 2000, 1835-1840.
4. E. C. Sañudo, W. Wernsdorfer, K. A. Abboud and G. Christou, *Inorganic Chemistry*, 2004, **43**, 4137-4144.
5. F. Neese and D. A. Pantazis, *Faraday Discussions*, 2011, **148**, 229-238.
6. O. Waldmann, *Inorganic Chemistry*, 2007, **46**, 10035-10037.
7. E. Garlatti, T. Guidi, A. Chiesa, S. Ansbro, M. L. Baker, J. Ollivier, H. Mutka, G. A. Timco, I. Vitorica-Yrezabal, E. Pavarini, P. Santini, G. Amoretti, R. E. P. Winpenny and S. Carretta, *Chemical Science*, 2018, **9**, 3555-3562.
8. M. Łukasiewicz, Z. Ciunik, J. Mazurek, J. Sobczak, A. Staroń, S. Wołowiec and Józef J. Zio´łkowski, *European Journal of Inorganic Chemistry*, 2001, 1575-1579.
9. V. Chandrasekhar, A. Dey, A. J. Mota and E. Colacio, *Inorganic Chemistry*, 2013, **52**, 4554-4561.
10. D. Wu, X. Zhang, P. Huang, W. Huang, M. Ruan and Z. W. Ouyang, *Inorganic Chemistry*, 2013, **52**, 10976-10982.
11. Y.-Y. Zhu, C. Cui, Y.-Q. Zhang, J.-H. Jia, X. Guo, C. Gao, K. Qian, S.-D. Jiang, B.-W. Wang, Z.-M. Wang and S. Gao, *Chemical Science*, 2013, **4**, 1802-1806.
12. E. A. Buvaylo, V. N. Kokozay, O. Y. Vassilyeva, B. W. Skelton, A. Ozarowski, J. Titiš, B. Vranovičová and R. Boča, *Inorganic Chemistry*, 2017, **56**, 6999-7009.
13. S. Mandal, S. Mondal, C. Rajnák, J. Titiš, R. Boča and S. Mohanta, *Dalton Transactions*, 2017, **46**, 13135-13144.
14. S. Manna, A. Bhunia, S. Mistri, J. Vallejo, E. Zangrando, H. Puschmann, J. Cano and S. C. Manna, *European Journal of Inorganic Chemistry*, 2017, **2017**, 2585-2594.
15. R. Mitsuhashi, K. S. Pedersen, T. Ueda, T. Suzuki, J. Bendix and M. Mikuriya, *Chemical Communications*, 2018, **54**, 8869-8872.
16. A. V. Funes, L. Carrella, L. Sorace, E. Rentschler and P. Alborés, *Dalton Transactions*, 2015, **44**, 2390-2400.
17. C. Rajnák, J. Titiš, I. Šalitroš, R. Boča, O. Fuhr and M. Ruben, *Polyhedron*, 2013, **65**, 122-128.
18. T. J. Woods, M. F. Ballesteros-Rivas, S. Gómez-Coca, E. Ruiz and K. R. Dunbar, *Journal of the American Chemical Society*, 2016, **138**, 16407-16416.
19. C. Rajnák, J. Titiš, J. Miklovič, G. E. Kostakis, O. Fuhr, M. Ruben and R. Boča, *Polyhedron*, 2017, **126**, 174-183.
20. D. Schweinfurth, J. Krzystek, M. Atanasov, J. Klein, S. Hohloch, J. Telser, S. Demeshko, F. Meyer, F. Neese and B. Sarkar, *Inorganic Chemistry*, 2017, **56**, 5253-5265.

21. A. K. Mondal, J. Jover, E. Ruiz and S. Konar, *Chemistry – A European Journal*, 2017, **23**, 12550-12558.
22. F. Shao, B. Cahier, E. Rivière, R. Guillot, N. Guihéry, V. E. Campbell and T. Mallah, *Inorganic Chemistry*, 2017, **56**, 1104-1111.
23. S. S. Massoud, R. C. Fischer, F. A. Mautner, M. M. Parfait, R. Herchel and Z. Trávníček, *Inorganica Chimica Acta*, 2018, **471**, 630-639.
24. K. A. Schulte, K. R. Vignesh and K. R. Dunbar, *Chemical Science*, 2018, **9**, 9018-9026.
25. N. E. Brese and M. O'Keeffe, *Acta Crystallographica Section B*, 1991, **47**, 192-197.
26. I. D. Brown, Brockhouse Institute for Materials Research, McMaster University, Hamilton, Ontario Canada. idbrown@mcmaster.ca, https://www.iucr.org/__data/assets/file/0007/126574/bvparm2016.cif.
27. M. Pinsky and D. Avnir, *Inorganic Chemistry*, 1998, **37**, 5575-5582.
28. S. Alvarez and M. Llunell, *Journal of the Chemical Society, Dalton Transactions*, 2000, 3288-3303.
29. N. F. Chilton, R. P. Anderson, L. D. Turner, A. Soncini and K. S. Murray, *Journal of Computational Chemistry*, 2013, **34**, 1164-1175.
30. R. L. Carlin, *Magnetochemistry*, Springer-Verlag Berlin Heidelberg, 1986.
31. R. Herchel and R. Boča, *Dalton Trans.*, 2005, 1352-1353.
32. J. S. Wood, *Journal of the Chemical Society A: Inorganic, Physical, Theoretical*, 1969, 1582-1586.
33. N. Nedelko, A. Kornowicz, I. Justyniak, P. Aleshkevych, D. Prochowicz, P. Krupiński, O. Dorosh, A. Ślawska-Waniewska and J. Lewiński, *Inorganic Chemistry*, 2014, **53**, 12870-12876.
34. F. Shao, B. Cahier, N. Guihéry, E. Rivière, R. Guillot, A.-L. Barra, Y. Lan, W. Wernsdorfer, V. E. Campbell and T. Mallah, *Chemical Communications*, 2015, **51**, 16475-16478.
35. A. K. Mondal, T. Goswami, A. Misra and S. Konar, *Inorganic Chemistry*, 2017, **56**, 6870-6878.
36. S. Gomez-Coca, E. Cremades, N. Aliaga-Alcalde and E. Ruiz, *Journal of the American Chemical Society*, 2013, **135**, 7010-7018.
37. B. Cahier, M. Perfetti, G. Zakhia, D. Naoufal, F. El-Khatib, R. Guillot, E. Rivière, R. Sessoli, A.-L. Barra, N. Guihéry and T. Mallah, *Chemistry – A European Journal*, 2017, **23**, 3648-3657.
38. J. Vallejo, E. Pardo, M. Viciano-Chumillas, I. Castro, P. Amorós, M. Déniz, C. Ruiz-Pérez, C. Yuste-Vivas, J. Krzystek, M. Julve, F. Lloret and J. Cano, *Chemical Science*, 2017, **8**, 3694-3702.
39. A. Świtlicka, B. Machura, M. Penkala, A. Bieńko, D. C. Bieńko, J. Titiš, C. Rajnák, R. Boča, A. Ozarowski and M. Ozerov, *Inorganic Chemistry*, 2018, **57**, 12740-12755.
40. CC-FIT Copyright © 2014 Nicholas F. Chilton.
41. Y.-N. Guo, G.-F. Xu, Y. Guo and J. Tang, *Dalton Transactions*, 2011, **40**, 9953-9963.
42. Y.-Z. Zhang, S. Gómez-Coca, A. J. Brown, M. R. Saber, X. Zhang and K. R. Dunbar, *Chemical Science*, 2016, **7**, 6519-6527.

43. E. Colacio, J. Ruiz, E. Ruiz, E. Cremades, J. Krzystek, S. Carretta, J. Cano, T. Guidi, W. Wernsdorfer and E. K. Brechin, *Angewandte Chemie International Edition*, 2013, **52**, 9130-9134.
44. L. Chen, S.-Y. Chen, Y.-C. Sun, Y.-M. Guo, L. Yu, X.-T. Chen, Z. Wang, Z. W. Ouyang, Y. Song and Z.-L. Xue, *Dalton Transactions*, 2015, **44**, 11482-11490.
45. D. Shao, S.-L. Zhang, L. Shi, Y.-Q. Zhang and X.-Y. Wang, *Inorganic Chemistry*, 2016, **55**, 10859-10869.
46. R. Ruamps, L. J. Batchelor, R. Guillot, G. Zakhia, A.-L. Barra, W. Wernsdorfer, N. Guihéry and T. Mallah, *Chem Sci*, 2014, **5**, 3418-3424.
47. J.-Y. Ge, L. Cui, J. Li, F. Yu, Y. Song, Y.-Q. Zhang, J.-L. Zuo and M. Kurmoo, *Inorganic Chemistry*, 2017, **56**, 336-343.
48. C.-M. Liu, D.-Q. Zhang and D.-B. Zhu, *Scientific Reports*, 2017, **7**, 15483.
49. W.-Y. Zhang, Y.-Q. Zhang, S.-D. Jiang, W.-B. Sun, H.-F. Li, B.-W. Wang, P. Chen, P.-F. Yan and S. Gao, *Inorg. Chem. Front.*, 2018, **5**, 1575-1586.
50. W. Huang, T. Liu, D. Wu, J. Cheng, Z. W. Ouyang and C. Duan, *Dalton Transactions*, 2013, **42**, 15326-15331.
51. S. Vaidya, S. Tewary, S. K. Singh, S. K. Langley, K. S. Murray, Y. Lan, W. Wernsdorfer, G. Rajaraman and M. Shanmugam, *Inorganic Chemistry*, 2016, **55**, 9564-9578.
52. J. Ferrando-Soria, E. Moreno Pineda, A. Chiesa, A. Fernandez, S. A. Magee, S. Carretta, P. Santini, I. J. Vitorica-Yrezabal, F. Tuna, G. A. Timco, E. J. L. McInnes and R. E. P. Winpenny, *Nature Communications*, 2016, **7**, 11377.

Chapter 5

Tuning the nuclearity in a family of cyclic cobalt phosphonate complexes: $\{Co^{II}_9\}$, $\{Co^{II}_8\}$, $\{Co^{II}_6\}$, $\{Co^{II}_3\}$ and $\{Co^{II}_2\}$

Contents

5. Tuning the nuclearity in a family of cyclic cobalt phosphonate complexes: $\{Co^{II}_9\}$, $\{Co^{II}_8\}$, $\{Co^{II}_6\}$, $\{Co^{II}_3\}$ and $\{Co^{II}_2\}$.

5.1 Introduction

As previously discussed in Chapter 4, the employment of 3,5-dimethylpyrazole (= Hdmpz) with the co-ligands dibenzoylmethane (= HDBM) and acetylacetone (= Hacac) towards the synthesis of $\{Co^{II}Co^{III}_2\}$ complexes with the same triangular motif as in **3**·2THF, **4**·2MeCN and **5**, was not successful. Hence, we were interested in employing other co-ligands along with Hdmpz, such as phosphonate ligands $[RPO_3]^{2-}$. Phosphonates, which are derived from the corresponding phosphonic acids RPO_3H_2, show a variety of coordination modes and can in principle bind to a maximum of nine metal ions; therefore they are ideal for polynuclear complexes[1] and 1D, 2D or 3D coordination polymers.[2] Phosphonate metal complexes and coordination polymers attract great attention due to their numerous applications in catalysis[3, 4], photochemistry[5], biotechnology[6, 7] and molecular magnetism[8-11]. Due to their tendency to form coordination polymers three main strategies are usually followed towards the synthesis of low dimensional structures.[1] The first is the introduction of ancillary ligands that can coordinate to the metal ions, preventing further expansion of the molecule through the phosphonate groups.[12-14] Moreover, the use of sterically hindered phosphonic acids can also prevent the expansion of the molecule and reduce/control the nuclearity.[15-18] Finally, preformed metal-organic complexes can be used as building blocks in combination with the phosphonate ligands, and help to gain some control over the final product.[19-21]

Homometallic and heterometallic Co-based complexes with phosphonate ligands are well studied in the literature and can exhibit high nuclearities.[1] In most of the cases cobalt is found in the +2 oxidation state and a variety of co-ligands have been used in conjunction with the phosphonate ligands.[22-26] More specifically, the pyrazole ligand and various substituted pyrazolate ligands have been employed in the synthesis of phosphonate complexes with 3*d* metals.[12, 27-32] However, cobalt-based complexes are scarce[33-35]; to our knowledge there are only four examples of Co-based complexes with pyrazolate or substituted pyrazolate ligands in conjunction with phosphonates (CSD search, database of 2018). V. Chandrasekhar *et al.* have reported two $\{Co^{II}_2\}$ complexes incorporating the ligands Hdmpz and trichlorophosphonic acid (= $Cl_3PO_3H_2$) with molecular formulae $[\{Co^{II}_2(Hdmpz)_4(Cl_3CPO_3)_2\}\{Co^{II}(Hdmpz)_2Cl_2\}_2]\cdot 2C_6H_5CH_3$ (**I**·$2C_6H_5CH_3$) and $[HNEt_3]_2[Co^{II}_2(Hdmpz)_2Cl_2(Cl_3CPO_3)_2]$ (**II**) (Fig. 5.1).[33] Using the same ligands, Hdmpz and $Cl_3CPO_3H_2$, D. Sahoo *et al.* reported a cyclic $\{Co^{II}_9\}$ complex with molecular formula $[Co^{II}_9(Cl_3CPO_3)_3(dmpz)_{12}(Hdmpz)_6]\cdot 7C_6H_5CH_3$ (**III**·$7C_6H_5CH_3$) (Fig. 5.2).[34] Another $\{Co^{II}_2\}$

complex, similar to complex **I**·2$C_6H_5CH_3$, was reported by S. K. Gupta *et al.* utilising the ligands Hdmpz and 2,6-di-iso-propylphenylphosphate (= $dippH_2$), $[Co^{II}_2(dipp)_2(dmpz)_4]$·2MeOH (**IV**·2MeOH) (Fig. 5.2).[35] Only complex **IV**·2MeOH was magnetically characterised and the dc magnetic susceptibility data revealed dominant antiferromagnetic interactions until ~5 K, while at lower temperatures the rise of $\chi_M T$ was attributed to a magnetic impurity.[35]

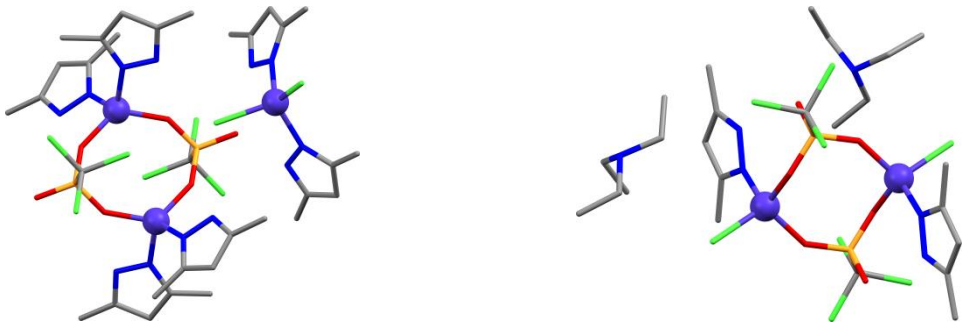

Figure 5.1 The molecular structures of complexes **I** (*left*) and **II** (*right*).[33] Colour code: Co^{II}: violet, O: red, N: blue, C: grey, Cl: green, P: orange. Hydrogen atoms are omitted for clarity.

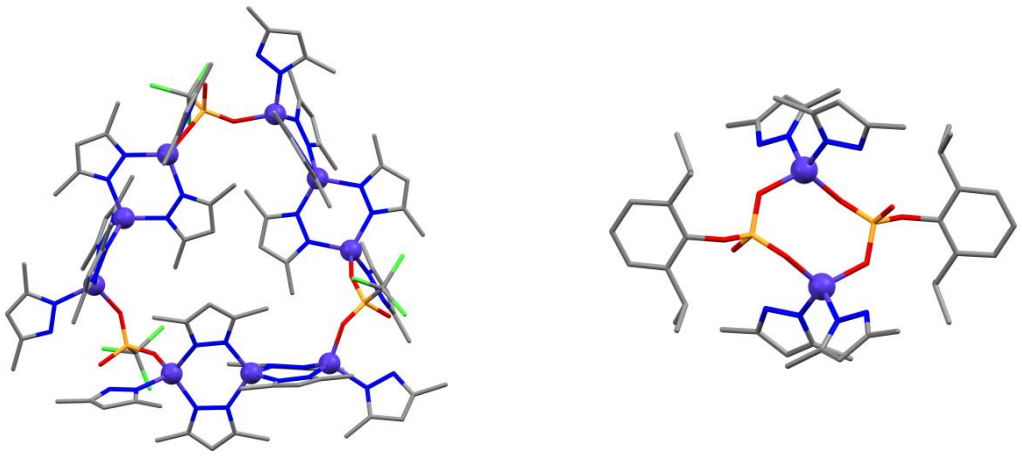

Figure 5.2 The molecular structures of complexes **III** (*left*) and **IV** (*right*).[34, 35] Colour code: Co^{II}: violet, O: red, N: blue, C: grey, Cl: green, P: orange. Hydrogen atoms are omitted for clarity.

Considering the small number of complexes reported, we investigated the chemistry of Co^{II} with 3,5-dimethylpyrazole (= Hdmpz) and the co-ligands *tert*-butylphosphonic acid (= *t*$BuPO_3H_2$), ethylphosphonic acid (= $EtPO_3H_2$), phenylphosphonic acid (= $PhPO_3H_2$) and *n*-butylphosphonic acid (= *n*$BuPO_3H_2$). As a result we have successfully isolated five new Co^{II} complexes: **7**, **8**·xMeCN·yH_2O, **9a**·xDCM·yH_2O (and its solvated analogue

9b·0.75(Hdmpz)·2.25DCE·H_2O), **11**·DCM and **12**, and a new solvate analogue of complex **III**·7$C_6H_5CH_3$ (**6**·xMeCN·yH_2O). These complexes are:

- $[Co^{II}_9(t\text{BuPO}_3)_3(\text{dmpz})_{12}(\text{Hdmpz})_6]$·xMeCN·y$H_2O$ (**6**·xMeCN·yH_2O),
- $[Co^{II}_3(t\text{BuPO}_3)_2(\text{Hdmpz})_4\text{Br}_2]$ (**7**),
- $[Co^{II}_8(\text{EtPO}_3)_3(\text{dmpz})_{10}(\text{Hdmpz})_6]$·xMeCN·y$H_2O$ (**8**·xMeCN·yH_2O or **8**(MeCN)),
- $[\text{HNEt}_3][Co^{II}_8(\text{EtPO}_3)_3(\text{dmpz})_{10}(\text{Hdmpz})_6][\text{ClO}_4]$·xDCM·y$H_2O$ (**9a**·xDCM·yH_2O or **9a**(DCM)),
- $[\text{HNEt}_3][Co^{II}_8(\text{EtPO}_3)_3(\text{dmpz})_{10}(\text{Hdmpz})_6][\text{ClO}_4]$·0.75(Hdmpz)·2.25DCE·$H_2O$ (**9b**·0.75(Hdmpz)·2.25DCE·H_2O or **9b**(DCE)),
- $[Co^{II}_3(\text{dmpz})_4(\text{Hdmpz})_2\text{Cl}_2]$ (**10**),
- $[\text{HNEt}_3][Co^{II}_6(\text{PhPO}_3)_3(\text{dmpz})_6(\text{Hdmpz})_6][\text{ClO}_4]$·DCM (**11**·DCM) and
- $[\text{HNEt}_4]_2[Co^{II}_2(\text{dmpz})_2\text{Cl}_4]$ (**12**).

Due to limited time available on the SQUID magnetometer and/or the need to refine the synthetic procedures (*e.g.* low yields, impurities etc.) for some of the complexes, only complexes **6** and **7** were magnetically characterised. Full magnetic characterisation for **6** and **7** revealed antiferromagnetic exchange interactions, with complex **7** being in the weak exchange limit. Complex **6** shows only the onset of the out-of-phase ac signals, while no ac signals were observed for complex **7**.

5.2 Synthesis

Ligands: **Hdmpz** = 3,5-dimethylpyrazole, ***t*BuPO$_3$H$_2$** = *tert*-butylphosphonic acid, **EtPO$_3$H$_2$** = ethylphosphonic acid, **PhPO$_3$H$_2$** = phenylphosphonic acid, ***n*BuPO$_3$H$_2$** = *n*-butylphosphonic acid

Solvents: **MeCN** = acetonitrile, **DCM** = dichloromethane, **DCE** = 1,2-dichloroethane

[Co$^{II}_9$(*t*BuPO$_3$)$_3$(dmpz)$_{12}$(Hdmpz)$_6$]·xMeCN·yH$_2$O (6·xMeCN·yH$_2$O) : $CoBr_2$ (0.3 mmol, 65 mg) was added to a solution of Hdmpz (0.6 mmol, 58 mg) and *t*BuPO$_3$H$_2$ (0.1 mmol, 14 mg) in MeCN (20 ml) in the presence of NEt_3 (1 mmol, 0.15 ml). The solution was placed in a Teflon lined autoclave and heated to 140 °C over a period of 25 minutes. The temperature was held at 140 °C for 72 h and then the solution was allowed to cool to room temperature at 0.1 ^{o}C/min rate. The resulting purple solution was left to slowly evaporate at room temperature to give purple block-like crystals after 1 day (~26% yield). Elemental analysis calcd(%) for $Co_9C_{102}H_{159}N_{36}O_9P_3$ ([Co$^{II}_9$(*t*BuPO$_3$)$_3$(dmpz)$_{12}$(Hdmpz)$_6$] (**6**)): C 46.11%, H 6.03%, N 18.98%, found C 45.82%, H 5.76%, N 18.58%.

[Co$^{II}_3$(*t*BuPO$_3$)$_2$(Hdmpz)$_4$Br$_2$] (7) : $CoBr_2$ (0.3 mmol, 65 mg) was added to a solution of Hdmpz (0.6 mmol, 58 mg) and *t*BuPO$_3$H$_2$ (0.1 mmol, 14 mg) in MeCN (20 ml) in the presence of NEt_3 (1 mmol, 0.15 ml). The solution was heated under reflux at 95 °C for 24 h and was allowed to cool to room temperature slowly. The resulting blue solution was left to slowly evaporate at room temperature to give blue rhombus-like crystals after 2 days (~29% yield). Elemental analysis calcd(%) for $Co_3C_{28}H_{50}Br_2N_8O_6P_2$ (**7**): C 33.86%, H 5.07%, N 11.28%, found C 33.59%, H 4.95%, N 10.95%.

[Co$^{II}_8$(EtPO$_3$)$_3$(dmpz)$_{10}$(Hdmpz)$_6$]·xMeCN·yH$_2$O (8·xMeCN·yH$_2$O or 8(MeCN)) : Hdmpz (0.6 mmol, 58 mg) and $EtPO_3H_2$ (0.1 mmol, 11 mg) in MeCN (15 ml) was added to a solution of $Co(BF_4)_2{\cdot}xH_2O$ (0.3 mmol, 70 mg) in MeCN (25 ml) in the presence of NEt_3 (1 mmol, 0.15 ml) and the mixture was stirred at room temperature for ~20 h. The resulting purple solution was left to slowly evaporate at room temperature to give purple block-like crystals after 1 week (~10% yield). We were not able to obtain a satisfactory elemental analysis, possibly due to impurities.

[HNEt$_3$][Co$^{II}_8$(EtPO$_3$)$_3$(dmpz)$_{10}$(Hdmpz)$_6$][ClO$_4$]·xDCM·yH$_2$O (9a·xDCM·yH$_2$O or 9a(DCM)) : Hdmpz (0.6 mmol, 58 mg) and $EtPO_3H_2$ (0.1 mmol, 11 mg) in DCM (15 ml) was added to a solution of $Co(ClO_4)_2{\cdot}6H_2O$ (0.3 mmol, 116 mg) in DCM (25 ml) in the presence of NEt_3 (1 mmol, 0.15 ml) and the mixture was stirred at room temperature for ~20 h. The resulting purple solution was layered with liquid hexane to give purple block-

like crystals after 1 week (~8% yield). We were not able to obtain a satisfactory elemental analysis, possibly due to impurities.

$[HNEt_3][Co^{II}_8(EtPO_3)_3(dmpz)_{10}(Hdmpz)_6][ClO_4]\cdot 0.75(Hdmpz)\cdot 2.25DCE\cdot H_2O$ ($9b\cdot 0.75(Hdmpz)\cdot 2.25DCE\cdot H_2O$ or 9b(DCE)) : Hdmpz (0.6 mmol, 58 mg) and $EtPO_3H_2$ (0.1 mmol, 11 mg) in DCE (15 ml) was added to a solution of $Co(ClO_4)_2\cdot 6H_2O$ (0.3 mmol, 116 mg) in DCE (25 ml) in the presence of NEt_3 (1 mmol, 0.15 ml) and the mixture (purple solution) was stirred at room temperature for ~20 h. Purple block-like crystals were obtained from slow evaporation and from liquid layering of the solution with hexane after 1 week (~14% yield). We were not able to obtain a satisfactory elemental analysis, possibly due to impurities.

$[Co^{II}_3(dmpz)_4(Hdmpz)_2Cl_2]$ (10) : Hdmpz (0.6 mmol, 58 mg) and $EtPO_3H_2$ (0.1 mmol, 11 mg) in DCM (15 ml) was added to a solution of $CoCl_2\cdot 6H_2O$ (0.3 mmol, 71 mg) in DCM (25 ml) in the presence of NEt_3 (1 mmol, 0.15 ml) and the mixture was stirred at room temperature for ~20 h. The resulting blue solution was left to slowly evaporate at room temperature to give blue needle-like crystals after 4 days (~12% yield). Elemental analysis calcd(%) for $Co_3C_{30}H_{44}Cl_2N_{12}$ (**11**$\cdot 3.6H_2O$): C 43.92%, H 5.41%, N 20.49%, found C 43.66%, H 5.21%, N 20.12%.

$[HNEt_3][Co^{II}_6(PhPO_3)_3(dmpz)_6(Hdmpz)_6][ClO_4]\cdot$DCM (11·DCM) : Hdmpz (0.6 mmol, 58 mg) and $PhPO_3H_2$ (0.1 mmol, 16 mg) in DCM (15 ml) was added to a solution of $Co(ClO_4)_2\cdot 6H_2O$ (0.3 mmol, 116 mg) in DCM (25 ml) in the presence of NEt_3 (1 mmol, 0.15 ml) and the mixture was stirred at room temperature for ~20 h. The resulting purple solution was layered with liquid hexane to give blue plate-like crystals after 2 weeks (~7% % yield). Elemental analysis calcd(%) for $Co_6C_{84}H_{127}ClN_{25}O_{16}P_3$ (**11**$\cdot 3H_2O$): C 45.34%, H 5.75%, N 15.74%, found C 45.01%, H 5.75%, N 15.75%.

$[NEt_4]_2[Co^{II}_2(dmpz)_2Cl_4]$ (12) : Hdmpz (0.6 mmol, 58 mg) and *n*$BuPO_3H_2$ (0.1 mmol, 14 mg) in DCM (15 ml) was added to a solution of $CoCl_2\cdot 6H_2O$ (0.3 mmol, 78 mg) in DCM (25 ml) in the presence of NEt_3 (1 mmol, 0.15 ml) and the mixture was stirred at room temperature for ~20 h. The resulting purple solution was layered with liquid hexane to give blue plate-like crystals after 5 days (~5% yield). Complex **10** was not further investigated (*vide infra*) and therefore no elemental analysis was obtained for this complex.

5.3 Results and discussion

Previous research has shown how the substituted group of the phosphonate ligand, $[RPO_3]^{2-}$, can affect the nuclearity of a complex[26, 36-38]; considering that, the choice of the ligands *tert*-butylphosphonic acid (= *t*BuPO$_3$H$_2$), ethylphosphonic acid (= EtPO$_3$H$_2$), phenylphosphonic acid (= PhPO$_3$H$_2$) and *n*-butylphosphonic acid (= *n*BuPO$_3$H$_2$) (Fig. 5.3) in this work was based on the bulkiness and the aromaticity of the R group. The structure of the *tert*-butylphosphonic acid is very similar to the aforementioned trichlorophosphonic acid (= Cl$_3$PO$_3$H$_2$), however the acidity of Cl$_3$PO$_3$H$_2$ is higher than that of *t*BuPO$_3$H$_2$ (pK_a^1 = 1.63 and pK_a^2 = 4.81 for Cl$_3$PO$_3$H$_2$, whereas pK_a^1 = 2.79 and pK_a^2 = 8.88 for *t*BuPO$_3$H$_2$).[1] The ethylphosphonic acid is less bulky than the *t*BuPO$_3$H$_2$ ligand, while the *n*-butylphosphonic acid possesses a hydrophobic tail. Finally, the aromatic ring of the phenylphosphonic acid could impose *π*-*π* or hydrogen-*π* interactions which could lead to the stabilisation of a product during the crystallisation process. Scheme 5.1 shows a summary of the different synthetic procedures and the final products for each phosphonic acid (complexes **10** and **12** which do not include a phosphonic acid are omitted).

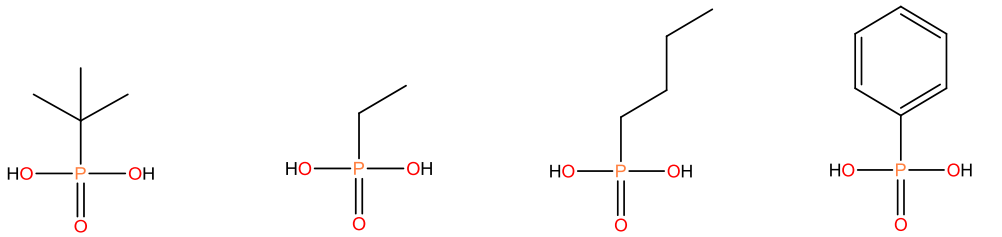

Figure 5.3 Illustration of the different phosphonic acids employed in this work.

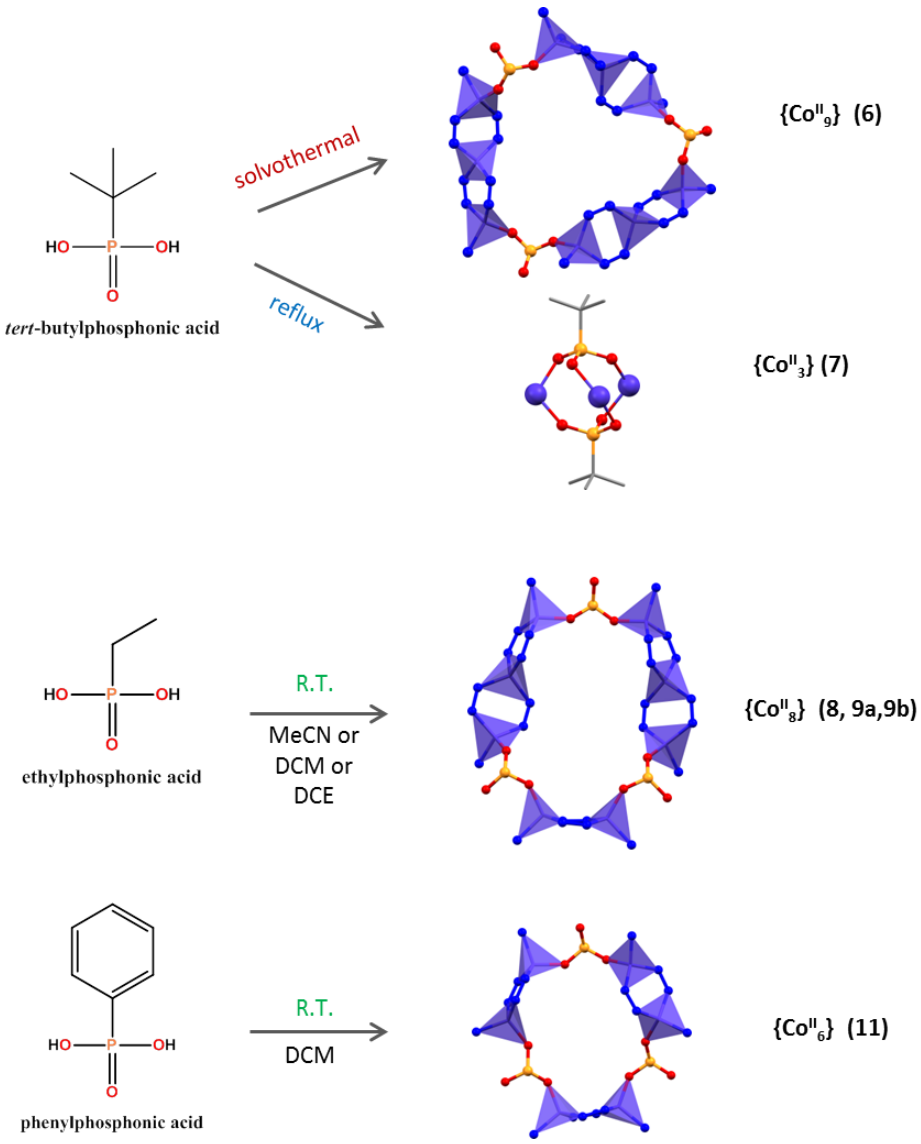

Scheme 5.1 Illustration of the different metallic cores isolated by utilising different phosphonate ligands and the different synthetic procedures (solvothermal, reflux and at room temperature). The purple polyhedra represent the tetrahedral geometry of the metal centres. Colour code: Co^{II}: violet, O: red, N: blue, P: orange. Hydrogen and carbon atoms are omitted for clarity.

5.3.1 *tert*-Butylphosphonic acid

We investigated a variety of cobalt salts and solvents in conjunction with the ligands Hdmpz and tBuPO$_3$H$_2$, under various conditions such as solvothermal, reflux and ambient conditions (room temperature). The optimised reaction of $CoBr_2$ with Hdmpz, tBuPO$_3$H$_2$ and NEt_3 (in 3:6:1:10 ratio), in MeCN and under solvothermal conditions, yielded a nonanuclear cyclic Co^{II} complex, $[Co^{II}_9(t\text{BuPO}_3)_3(\text{dmpz})_{12}(\text{Hdmpz})_6]\cdot x\text{MeCN}\cdot y\text{H}_2\text{O}$ (**6**·x$\text{MeCN}\cdot y\text{H}_2\text{O}$) (Fig. 5.4), which is a new solvate analogue of complex **III**·7$C_6H_5CH_3$.

The structure was determined by single-crystal X-ray diffraction (SCXRD). A variety of solvothermal reactions were carried out, changing the temperature and/or the experiment duration, in order to examine if there is any effect on the final product; however, no changes were observed, except the slight decrease of the yield for shorter experiment times. The optimum solvothermal conditions with the highest yield were found at 140 °C for 72 h. The reaction was also performed under milder conditions, in the same ratio, in order to examine if that would affect the final product. Indeed using heating under reflux for 24 h at 95 °C, a new trinuclear Co^{II} complex, $[Co^{II}_3(t\text{BuPO}_3)_2(\text{Hdmpz})_4\text{Br}_2]$ (**7**) (Fig. 5.4) was isolated. Furthermore, the reaction of $Co(ClO_4)_2{\cdot}6H_2O$ with Hdmpz, $t\text{BuPO}_3H_2$ and NEt_3 (in 3:6:1:10 ratio), in dichloromethane (= DCM) at ambient conditions, yielded another new solvate of complex **III**$\cdot 7C_6H_5CH_3$, $[Co^{II}_9(t\text{BuPO}_3)_3(\text{dmpz})_{12}(\text{Hdmpz})_6]{\cdot}x\text{DCM}{\cdot}yH_2O$ (Figure A5.1 in the appendix), as confirmed by SCXRD. However, due to the very low yield of the reaction (<5%), no further studies were carried out for this complex.

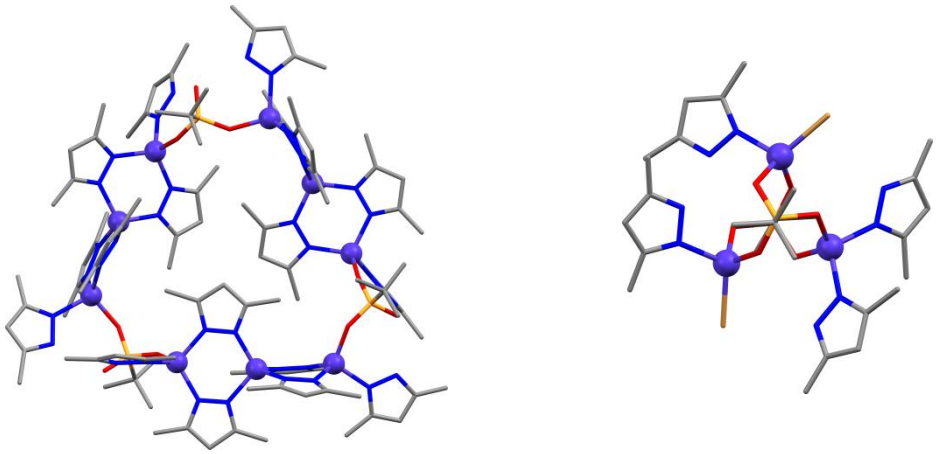

Figure 5.4 The molecular structures of complexes $[Co^{II}_9(t\text{BuPO}_3)_3(\text{dmpz})_{12}(\text{Hdmpz})_6]$ (**6**) (*left*) and $[Co^{II}_3(t\text{BuPO}_3)_2(\text{Hdmpz})_4\text{Br}_2]$ **7** (*right*). Colour code: Co^{II}: violet, O: red, N: blue, C: grey, P: orange, Br: light brown. Hydrogen atoms are omitted for clarity.

Crystal structure analysis and Powder X-ray Diffraction (PXRD)

Complex $[Co^{II}_9(t\text{BuPO}_3)_3(\text{dmpz})_{12}(\text{Hdmpz})_6]{\cdot}x\text{MeCN}{\cdot}yH_2O$ (**6**$\cdot x\text{MeCN}\cdot yH_2O$) crystallises in the triclinic $P\bar{1}$ space group and is a nonanuclear cyclic Co^{II} complex (Table A5.6 in the appendix). Due to a region of poorly defined and disordered molecules of solvent the routine SQUEEZE (in PLATON)[39] was used to identify the solvent voids and account for the electron density within them. The solvent voids were calculated to contain 363 e^- per unit cell, corresponding to approximately 181.5 e^- per molecule. A combination of molecules of solvent could be present in the crystal lattice and therefore it was not

possible to determine the number of MeCN and/or H_2O molecules that are co-crystallised. Moreover, the elemental analysis suggests that no molecules of solvent are present, hence no firm conclusion can be reached. The experimental PXRD pattern is shown in Figure 5.5, and it is clear that there is a deviation from the pattern calculated from the single-crystal structure. This could be attributed to the loss of solvent, which is consistent with the elemental analysis suggesting that no molecules of solvent are present (see Section 5.2).

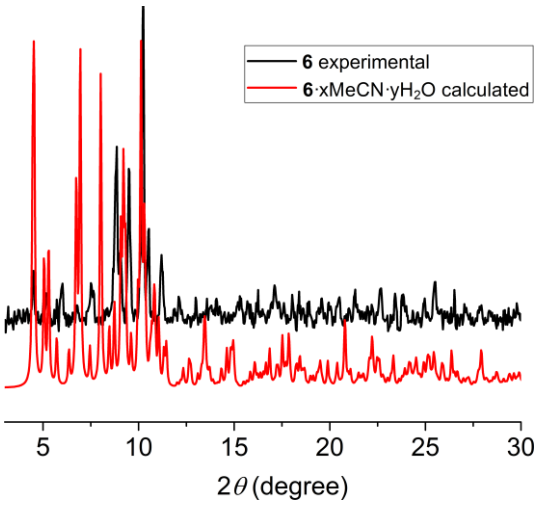

Figure 5.5 The PXRD pattern (3−30°) of the desolvated complex $[Co^{II}_9(tBuPO_3)_3(dmpz)_{12}(Hdmpz)_6]$ (**6**). The red line represents the calculated PXRD pattern for complex **6**·xMeCN·yH_2O and the black line the experimental one. The experimental PXRD pattern was measured at room temperature, while the calculated pattern is generated from the single-crystal data collected at 150 K.

The asymmetric unit consists of a full molecule of $[Co^{II}_9(tBuPO_3)_3(dmpz)_{12}(Hdmpz)_6]$ (Fig. 5.6). The molecular structure of **6** consists of three $\{Co^{II}_3\}$ subunits (Fig.5.7) which are connected with each other by three doubly deprotonated $tBuPO_3^{2-}$ ligands forming a cyclic $\{Co^{II}_9\}$ complex (Fig. 5.8). Note that the cyclic $\{Co^{II}_9\}$ complex is not planar; a plane is defined by the three P atoms of the phosphonate ligands, while the Co^{II} centres are located above and below that plane at distances in the range ~0.12−2 Å (Fig. 5.6 right). Each subunit contains three four-coordinate cobalt centres bridged by four deprotonated $dmpz^-$ ligands; the coordination sphere of each edge Co^{II} centre is completed by one N atom from a Hdmpz ligand and one O atom from the phosphonate ligand. The oxidation states of all Co^{II} centres were confirmed using Bond Valence Sum (BVS) analysis.[40, 41] All Co^{II} centres adopt a slightly distorted tetrahedral geometry, and continuous shape measures (CShMs)[42, 43] were used to determine the distortion around each metal ion (Table A5.1 in the appendix). The CShMs values are in the range of 0.063−0.433, where

0 corresponds to the ideal tetrahedron. The crystal packing of the structure is shown in Figure 5.9 and intramolecular hydrogen-π interactions are present between the dmpz$^-$ rings and the hydrogen atoms of the methyl groups of the dmpz$^-$ ligands (Fig. A5.2 in the appendix), while the shortest intermolecular Co···Co' distance is ~8.1 Å.

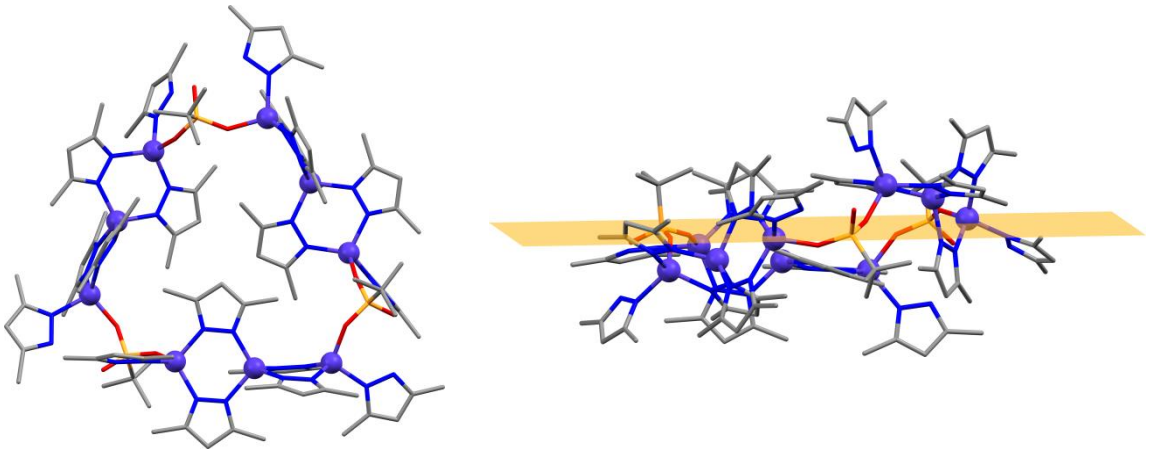

Figure 5.6 The molecular structure of complex **6**. The plane is defined by the three P atoms of the phosphonate ligands. Colour code: Co^{II}: violet, O: red, N: blue, C: grey, P: orange. Hydrogen atoms are omitted for clarity.

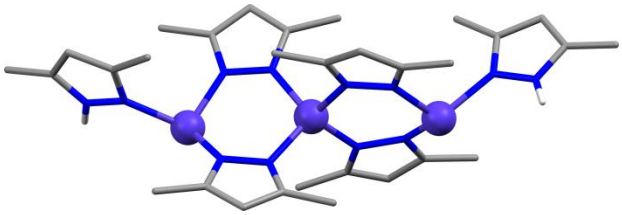

Figure 5.7 Illustration of the $\{Co^{II}_3\}$ subunit. Colour code: Co^{II}: violet, N: blue, C: grey, H: white. Hydrogen atoms are omitted except for the hydrogens of the protonated Hdmpz ligands.

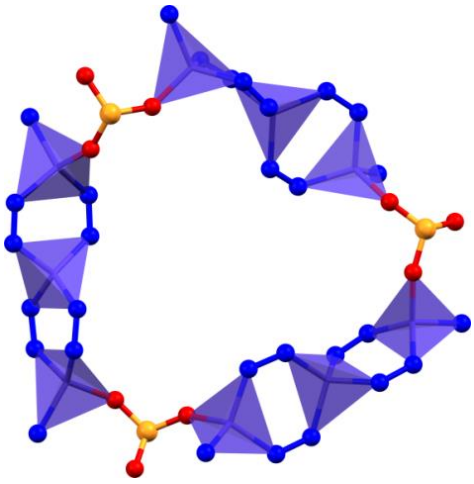

Figure 5.8 Illustration of the cyclic metallic core of complex **6**. The purple polyhedra represent the tetrahedral geometry of the metal centres. Colour code: Co^{II}: violet, O: red, N: blue, P: orange. Hydrogen and carbon atoms are omitted for clarity.

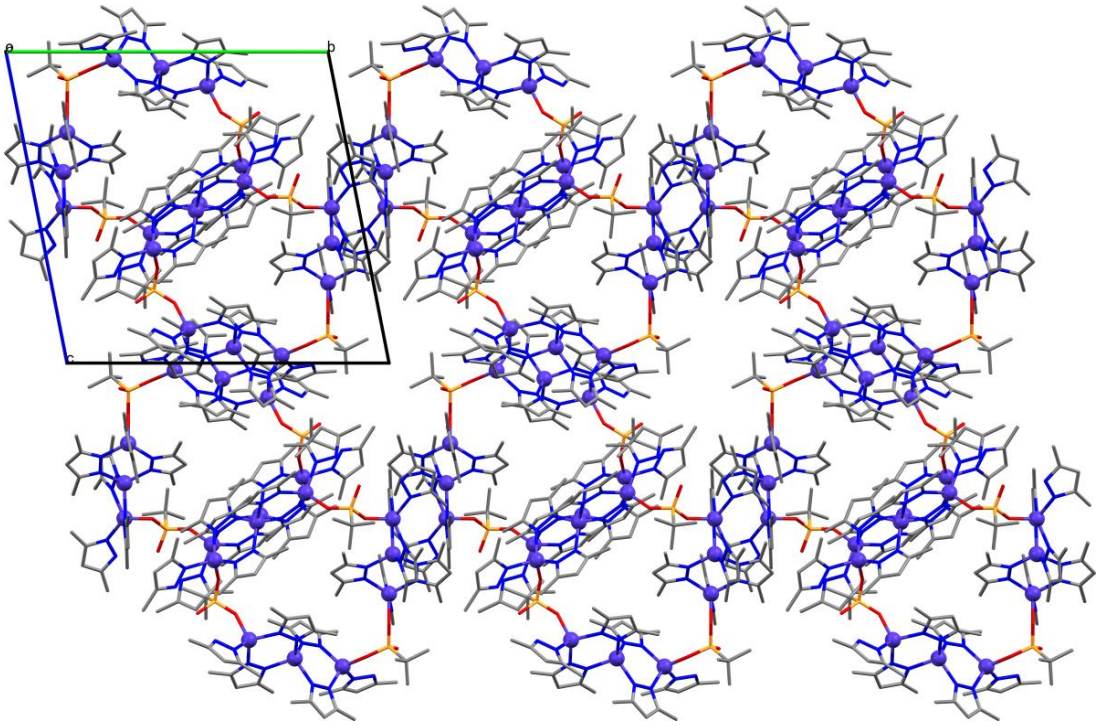

Figure 5.9 The crystal packing of **6** ($P\bar{1}$) along the crystallographic *a*-axis. Colour code: Co^{II}: violet, O: red, N: blue, P: orange, C: grey. Hydrogen atoms are omitted for clarity.

Complex $[Co^{II}_3(t\text{BuPO}_3)_2(\text{Hdmpz})_4\text{Br}_2]$ (**7**) is a new trinuclear Co^{II} complex which crystallises in the triclinic $P\bar{1}$ space group (Table A5.6 in the appendix). In contrast to complex **6**, the Co^{II} centres in **7** are only bridged by two doubly deprotonated $t\text{BuPO}_3^{2-}$ ligands forming a propeller-like structure (Fig. 5.10). All Co^{II} centres are four-coordinate and the coordination sphere of Co1 is completed by two Hdmpz ligands, while one terminal Br^- and one Hdmpz ligand complete the coordination sphere of each Co2 and Co3.

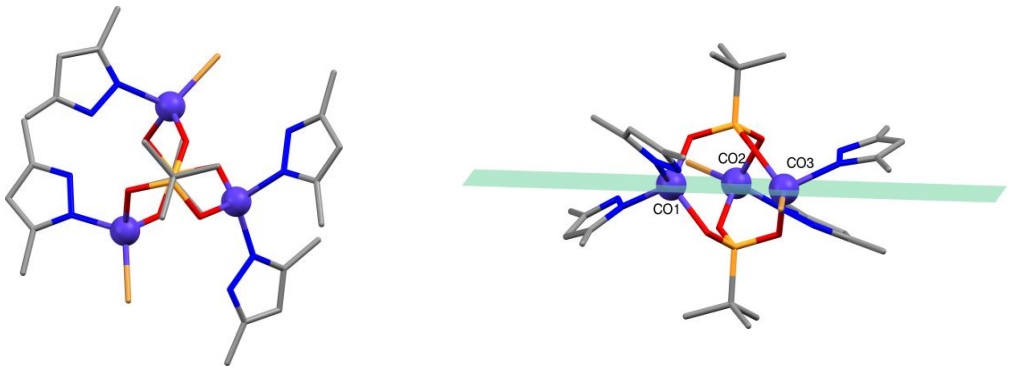

Figure 5.10 The molecular structure of complex **7**. The green plane is defined by the three Co^{II} centres. Colour code: Co^{II}: violet, O: red, N: blue, P: orange, C: grey, Br: light brown. Hydrogen atoms are omitted for clarity.

The oxidation states of all Co^{II} centres were confirmed by BVS analysis[40, 41], while continuous shape measures (CShMs)[42, 43] were used to determine the distortion of the tetrahedral geometry of each metal ion (Table A5.2 in the appendix). The CShMs values extracted are 0.54, 1.71 and 1.64 for Co1, Co2 and Co3, respectively (where 0 corresponds to the ideal geometry). The intramolecular Co···Co distances are ~3.8 Å for Co1···Co2 and Co1···Co3, and ~4.4 Å for Co2···Co3, while the shortest intermolecular Co···Co' distance is ~7.3 Å. Intramolecular hydrogen bonds are present between the Hdmpz and the phosphonate ligands. The crystal packing of the structure is shown in Figure 5.11. Although this structural motif is quite unusual, it has been previously reported with Zn^{II} and Mn^{II}, incorporating the *t*$BuPO_3H_2$ ligand along with Hdmpz in the case of Zn^{II} [44], and 2,6-bis(pyrazol-3-yl)pyridine in the case of Mn^{II} [13].

The experimental PXRD pattern of complex **7** (Fig. 5.12) is consistent with the calculated one from the single-crystal structure; therefore, we can conclude that the sample is phase pure. This is also consistent with the elemental analysis (see Section 5.2).

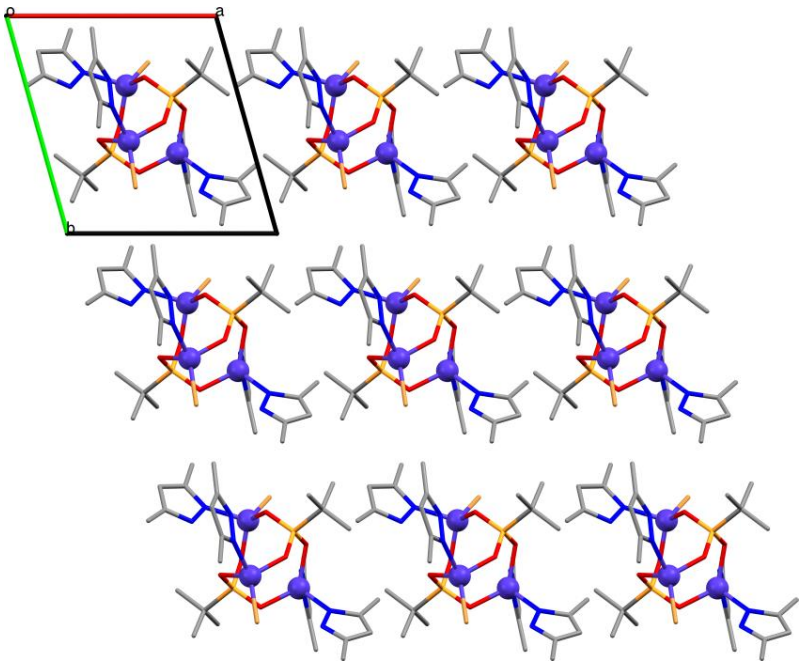

Figure 5.11 The crystal packing of **7** ($P\bar{1}$) along the crystallographic *c*-axis. Colour code: Co^{II}: violet, O: red, N: blue, P: orange, C: grey, Br: light brown. Hydrogen atoms are omitted for clarity.

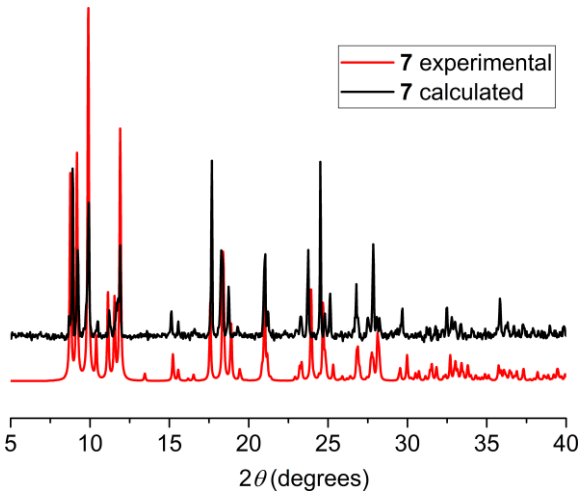

Figure 5.12 The PXRD pattern (5−40°) of complex **7**. The red line represents the calculated PXRD pattern for complex **7** and the black line the experimental one. The experimental PXRD pattern was measured at room temperature and the calculated pattern is generated from the single-crystal data collected at 150 K.

5.3.2 Ethylphosphonic acid

Our next step was to employ the less bulky ethylphosphonic acid (= $EtPO_3H_2$), in order to examine if there is any effect on the nuclearity. As described previously in Section 5.3.1, a variety of synthetic routes was examined, including heating under reflux, solvothermal and ambient conditions. The reaction of $Co(BF_4)_2{\cdot}xH_2O$ with Hdmpz, $EtPO_3H_2$ and NEt_3 (in 3:6:1:10 ratio), in MeCN and under ambient conditions led to a new octanuclear cyclic Co^{II} complex, $[Co^{II}_8(EtPO_3)_3(dmpz)_{10}(Hdmpz)_6]{\cdot}xMeCN{\cdot}yH_2O$ (**8**·xMeCN·yH_2O), hereafter abbreviated as **8**(MeCN). Moreover, the change of solvent from MeCN to dichloromethane (= DCM) and by using $Co(ClO_4)_2{\cdot}6H_2O$ instead of $Co(BF_4)_2{\cdot}xH_2O$, at ambient conditions and in the same ratio, afforded a new analogue of complex **8**(MeCN), complex $[HNEt_3][Co^{II}_8(EtPO_3)_3(dmpz)_{10}(Hdmpz)_6][ClO_4]{\cdot}xDCM{\cdot}yH_2O$ (**9a**·xDCM·yH_2O). The $\{Co^{II}_8\}$ metallic core remains the same as in complex **8**, however one molecule of protonated triethylamine and a molecule of ClO_4^- are co-crystallised in the lattice, along with solvent molecules of DCM and H_2O. We also performed the same reaction as for complex **8**(MeCN) but instead of ambient temperature we used solvothermal conditions and heating under reflux; however no result suitable for single-crystal X-ray diffraction was obtained. Solvothermal and reflux conditions were avoided in the case of perchlorates due to their potentially explosive nature.

Crystal structure analysis and Powder X-ray Diffraction (PXRD)

Complex $[Co^{II}_8(EtPO_3)_3(dmpz)_{10}(Hdmpz)_6]\cdot xMeCN\cdot yH_2O$ (**8**(MeCN)) crystallises in the triclinic $P\bar{1}$ space group (Table A5.7 in the appendix) and is a new octanuclear cyclic Co^{II} complex (Fig. 5.13). Due to a region of poorly defined and disordered molecules of solvent, only four molecules of MeCN could be modelled. The routine SQUEEZE (in PLATON)[39] was used to identify the solvent voids and account for the electron density within them, calculated to contain 98 e^- per unit cell, corresponding to approximately 49 e^- per molecule. A combination of molecules of solvent could be present in the crystal lattice and therefore it was not possible to determine the number of MeCN and/or H_2O molecules that are co-crystallised. Moreover, the elemental analysis was not satisfactory, possibly due to the presence of impurities. Note that in order to avoid impurities from the starting materials the sample was washed with hexane and diethyl-ether; however we were still not able to obtain a pure sample. The experimental PXRD pattern is shown in Figure 5.14, and it is clear that there is a deviation from the pattern calculated from the single-crystal structure. This could be attributed to the presence of impurities and/or loss of solvent.

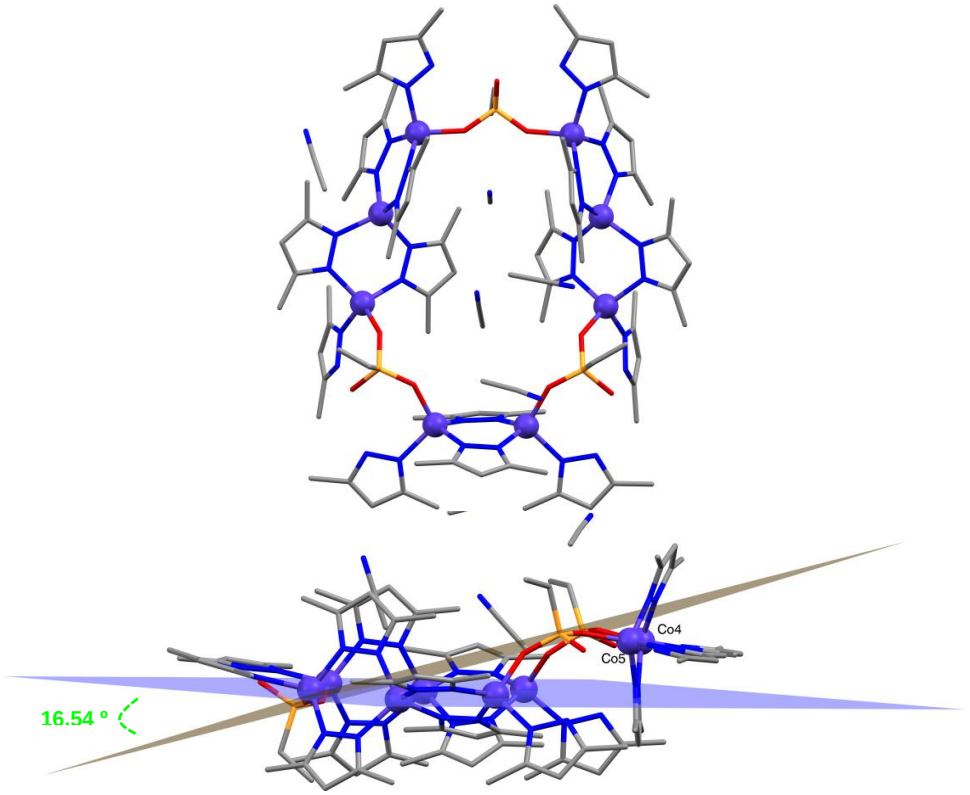

Figure 5.13 The molecular structure of complex **8**(MeCN) (*top*). The grey plane is defined by the three P atoms of the phosphonate ligands and the purple plane is defined by the Co1−Co3 and Co6−Co8 centres (*bottom*). Colour code: Co^{II}: violet, O: red, N: blue, C: grey, P: orange. Hydrogen atoms are omitted for clarity.

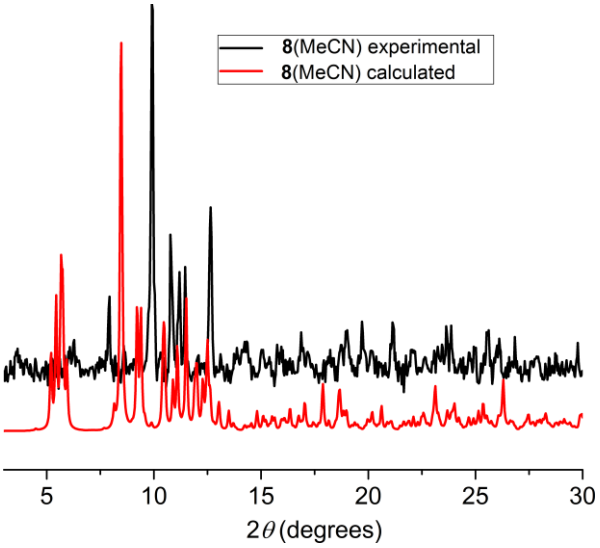

Figure 5.14 The experimental PXRD pattern (3−30°) of **8**(MeCN). The red line represents the calculated PXRD pattern for complex **8**(MeCN) and the black line the experimental one. The experimental PXRD pattern was measured at room temperature, while the calculated pattern is generated from the single-crystal data collected at 150 K.

The asymmetric unit consists of a full molecule of $[Co^{II}_8(EtPO_3)_3(dmpz)_{10}(Hdmpz)_6]$ and molecules of MeCN and/or H_2O. The molecular structure of **8** consists of one $\{Co^{II}_2\}$ and two $\{Co^{II}_3\}$ subunits (Fig. 5.15) which are connected with each other by three doubly deprotonated $EtPO_3^{2-}$ ligands forming a cyclic $\{Co^{II}_8\}$ complex (Fig. 5.16). As also seen in complex **6** the cyclic $\{Co^{II}_8\}$ complex is not planar; a plane is defined by the three P atoms of the phosphonate ligands, while the Co1−Co3 and Co6−Co8 centres define another plane, with Co4 and Co5 located outside this plane (~2 Å). Each $\{Co^{II}_3\}$ subunit contains three four-coordinate cobalt centres bridged by four deprotonated $dmpz^-$ ligands, while the $\{Co^{II}_2\}$ subunit contains two four-coordinate cobalt centres bridged by two $dmpz^-$ ligands; the coordination sphere of each edge Co^{II} centre (in each subunit) is completed by one N atom from a Hdmpz ligand and one O atom from the phosphonate ligand. The oxidation states of all Co^{II} centres were confirmed using BVS analysis.[40, 41] All Co^{II} centres adopt a slightly distorted tetrahedral geometry, and continuous shape measures (CShMs) [42, 43] were used to determine the distortion around each metal ion (Table A5.3 in the appendix). The CShMs values are in the range 0.055−0.511, where 0 corresponds to the ideal tetrahedron. The crystal packing of the structure is shown in Figure 5.17 and intermolecular hydrogen-π interactions are present between the $dmpz^-$ rings and the hydrogen atoms of the MeCN solvent (Fig. A5.3 in the appendix), while the shortest intermolecular Co···Co' distance is ~8.5 Å.

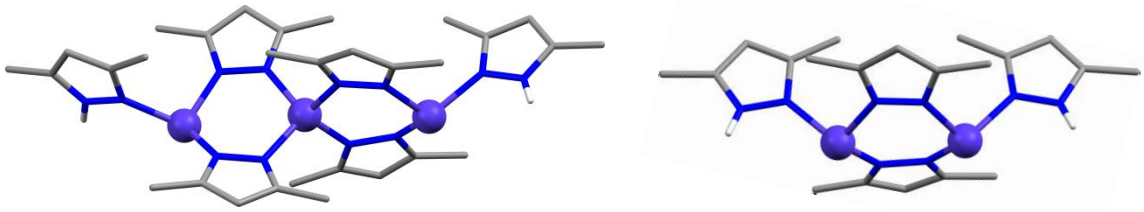

Figure 5.15 Illustration of the $\{Co^{II}_3\}$ and $\{Co^{II}_2\}$ subunits. Colour code: Co^{II}: violet, N: blue, C: grey, H: white. Hydrogen atoms are omitted for clarity, except from the hydrogens of the protonated Hdmpz ligands.

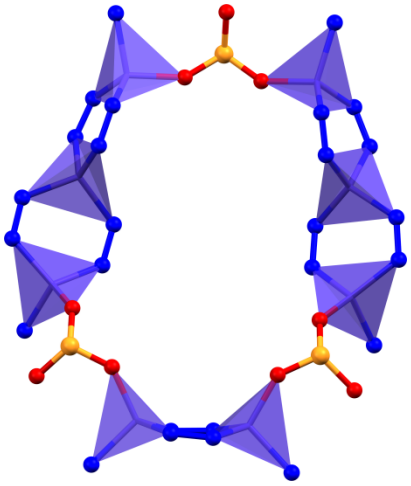

Figure 5.16 Illustration of the cyclic metallic core of complex **8**. The purple polyhedra represent the tetrahedral geometry of the metal centres. Colour code: Co^{II}: violet, O: red, N: blue, P: orange. Hydrogen and carbon atoms are omitted for clarity.

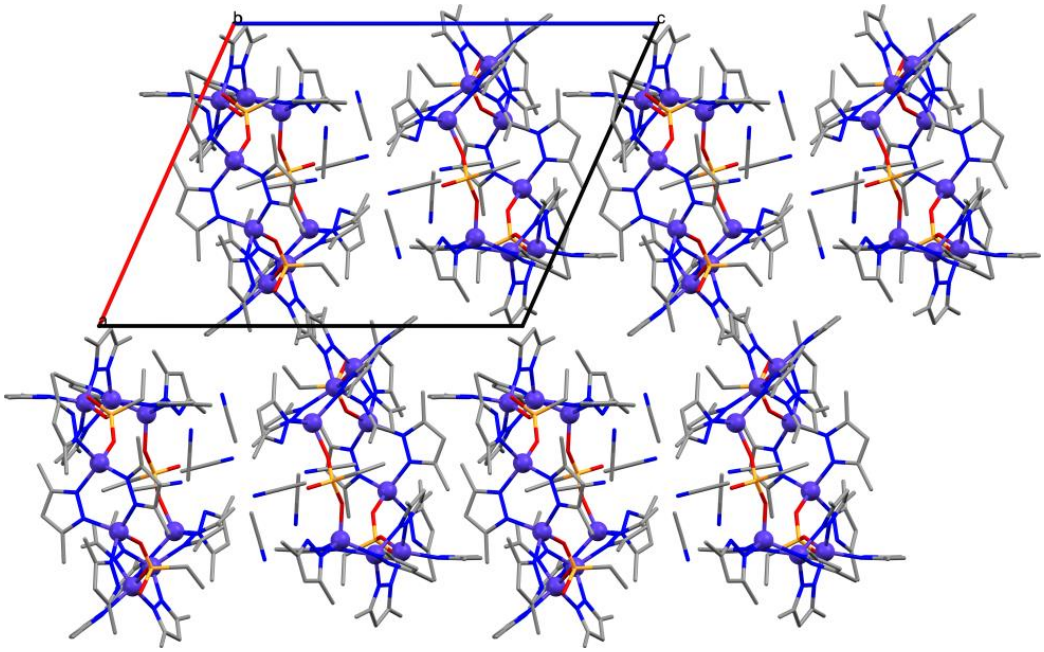

Figure 5.17 The crystal packing of **8**(MeCN) ($P\bar{1}$) along the crystallographic *b*-axis. Colour code: Co^{II}: violet, O: red, N: blue, P: orange, C: grey. Hydrogen atoms are omitted for clarity.

Complex $[HNEt_3][Co^{II}_8(EtPO_3)_3(dmpz)_{10}(Hdmpz)_6][ClO_4]\cdot xDCM\cdot yH_2O$ (**9a**·xDCM·yH_2O) (Fig. 5.18 and 5.19), hereafter abbreviated as **9a**(DCM), crystallises in the triclinic $P\bar{1}$ space group (Table A5.7 in the appendix) and is a new analogue of complex **8**(MeCN). Due to a region of poorly defined and disordered molecules of solvent, only half a molecule of DCM and half a molecule of H_2O could be modelled. The routine SQUEEZE (in PLATON)[39] was used to identify the solvent voids and account for the electron density within them, calculated to contain 260 e^- per unit cell, corresponding to approximately 130 e^- per molecule. A combination of molecules of solvent could be present in the crystal lattice and therefore it was not possible to determine the number of DCM and/or H_2O molecules that are co-crystallised. Moreover, the elemental analysis was not satisfactory, possibly due to the presence of impurities. Again, in order to avoid impurities from the starting materials the sample was washed with hexane and diethyl-ether; however we were still not able to obtain a pure sample. Moreover, there is a deviation between the experimental PXRD pattern and the pattern calculated from the single-crystal structure (Fig. A5.4 in the appendix). This could be attributed to the presence of impurities and/or loss of solvent.

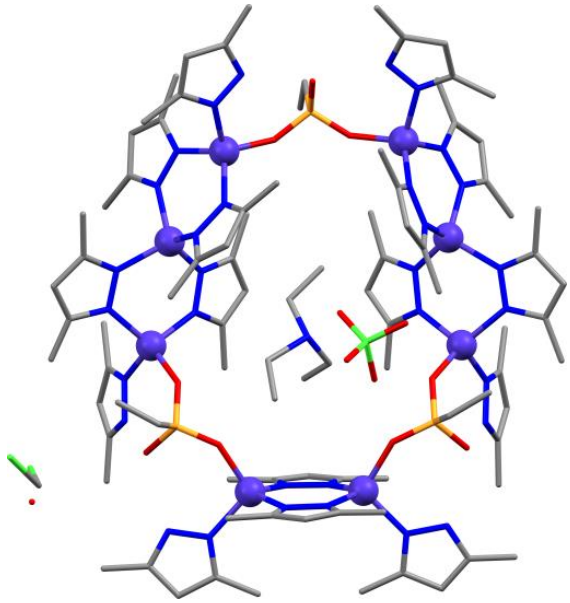

Figure 5.18 The molecular structure of complex **9a**(DCM), including the modelled molecules of solvent (0.5DCM and 0.5H_2O). Colour code: Co^{II}: violet, O: red, N: blue, C: grey, P: orange, Cl: green. Hydrogen atoms are omitted for clarity.

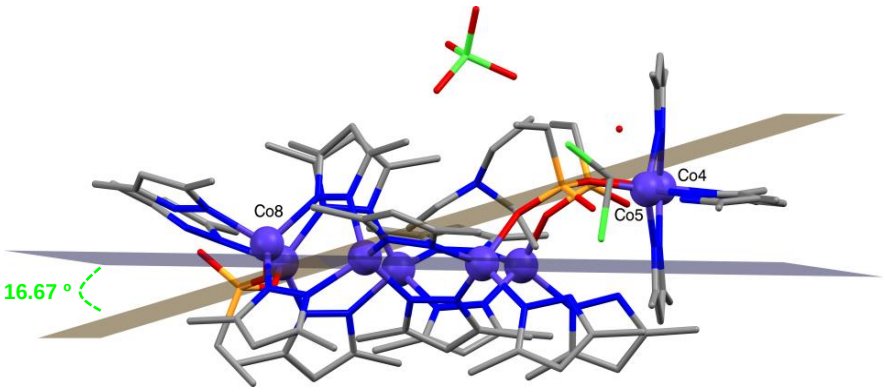

Figure 5.19 The molecular structure of complex **9a**(DCM), including the modelled molecules of solvent (0.5DCM and 0.5H_2O). The grey plane is defined by the three P atoms of the phosphonate ligands and the purple plane is defined by the Co1, Co2, Co3, Co6 and Co7 centres.

The asymmetric unit contains a full molecule of $[Co^{II}_8(EtPO_3)_3(dmpz)_{10}(Hdmpz)_6]$, one protonated molecule of triethylamine and one molecule of ClO_4^- co-crystallised in the lattice. As discussed above there are also molecules of solvent crystallised in the lattice (approximately 130 e^- per molecule), however the exact number of DCM and/or H_2O molecules could not be defined. The molecular structure of **9a**(DCM) is similar to that of complex **8**, therefore it will not be described extensively. As seen in complex **8**(MeCN) the cyclic $\{Co^{II}_8\}$ complex is not planar (Fig. 5.19). A plane is defined by the three P atoms of the phosphonate ligands, while the Co1, Co2, Co3, Co6, and Co7 centres define another plane, with Co4, Co5 and Co8 located outside this plane at ~2.2, ~2.1 and ~0.5 Å, respectively. In comparison with **8**, where the Co1−Co3 and Co6−Co8 centres define a plane, with Co4 and Co5 located outside this plane (~2 Å), complex **9a**(DCM) could be described as more distorted since there are less Co centres in the same plane. All cobalt ions are four-coordinate adopting a distorted tetrahedral geometry. Continuous shape measures (CShMs)[41, 42] were used to determine the distortion around each metal ion (Table A5.4 in the appendix). The CShMs values are in the range of 0.061−0.291, where 0 corresponds to the ideal tetrahedron. The oxidation states of all Co^{II} centres were confirmed using BVS analysis.[40, 41] The crystal packing of the structure is shown in Figure 5.20. Intermolecular hydrogen-π interactions are present between the $dmpz^-$ rings and the hydrogen atoms of the $[HNEt_3]^+$ cation, and between the $dmpz^-$ rings and the hydrogen atoms from the methyl groups of $dmpz^-$ of neighbouring molecules (Fig. A5. in the appendix). The shortest intermolecular Co···Co' distance is ~8.5 Å.

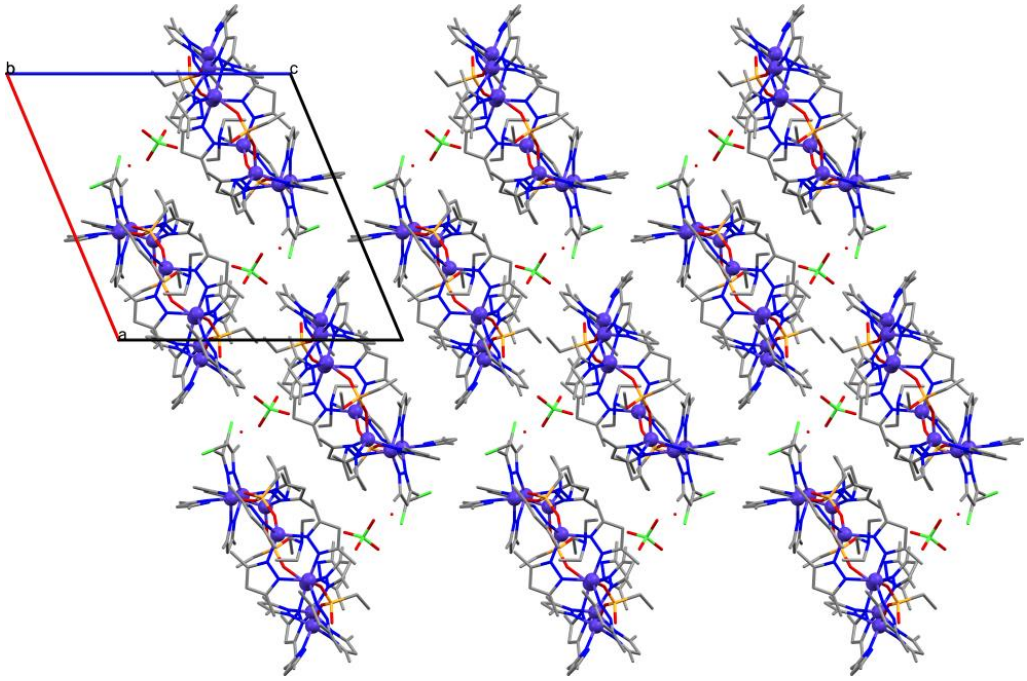

Figure 5.20 The crystal packing of **9a**(DCM) ($P\bar{1}$), including the modelled molecules of solvent (0.5DCM and 0.5H_2O), along the crystallographic *b*-axis. Colour code: Co^{II}: violet, O: red, N: blue, P: orange, C: grey, Cl: green. Hydrogen atoms are omitted for clarity.

As discussed previously, both complexes **8**(MeCN) and **9a**(DCM) contain a large number of co-crystallised solvent molecules. Moreover, elemental analysis and PXRD analysis for both complexes was not satisfactory suggesting the presence of impurities and/or the loss of solvent. In our attempt to isolate a pure $\{Co^{II}_8\}$ analogue, we replaced the solvent DCM with 1,2-dichloroethane (= DCE). DCE has a similar polarity index (= 3.5) as DCM (= 3.1), however its boiling point is almost double than that of DCM, 84 ºC versus 41 ºC, hence the possibility that the desolvation of the sample could be reduced by using the solvent DCE. The reaction of $Co(ClO_4)_2{\cdot}6H_2O$ with Hdmpz, $EtPO_3H_2$ and NEt_3 (in 3:6:1:10 ratio), in DCE and under ambient conditions led to a new solvate analogue of complex **9a**(DCM), complex $[HNEt_3][Co^{II}_8(EtPO_3)_3(dmpz)_{10}(Hdmpz)_6][ClO_4]$ ·0.75(Hdmpz)·2.25DCE·H_2O (**9**·0.75(Hdmpz)·2.25DCE·H_2O), hereafter referred to as **9b**(DCE). The metallic core and the co-crystallised molecules of $[HNEt_3]^+$ and ClO_4^- remain the same, while molecules of DCE and Hdmpz are also present in the crystal lattice.

Complex **9b**(DCE) crystallises in the triclinic $P\bar{1}$ space group (Table A5.7 in the appendix) and is a new solvate analogue of complex **9a**(DCM) (Fig. 5.21). The crystal lattice contains two molecules of water with chemical occupancy 0.25 and one with 0.5, therefore one H_2O molecule in total. Moreover, there are two DCE molecules co-crystallised, and the molecules Hdmpz and DCE with chemical occupancies 0.75 and 0.25, respectively.

The molecular structure is similar to that found in **9a**(DCM) (Fig. A5.7 in the appendix), with slight differences in the distortion of the geometries of the Co centres and the crystal packing due to the change of solvent; hence the structure will not be described extensively.

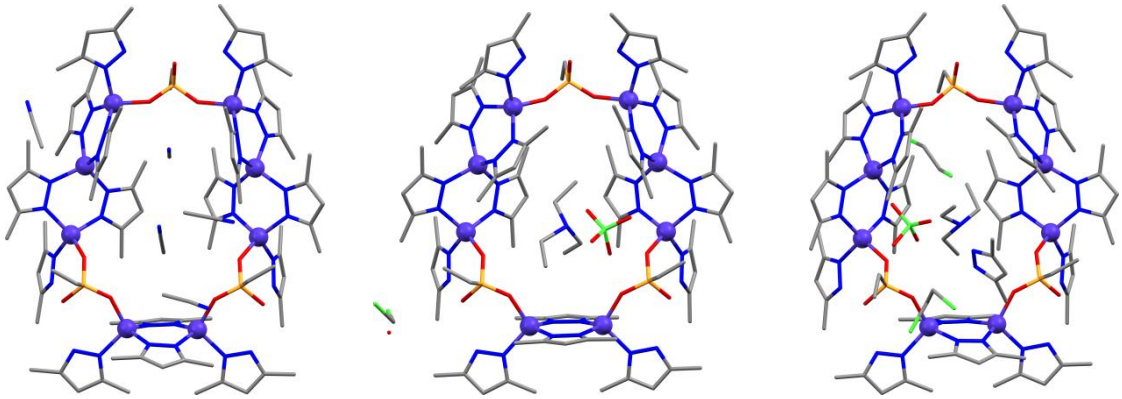

Figure 5.21 The molecular structures of complexes **8**(MeCN), **9a**(DCM) and **9b**(DCE) from left to right. Colour code: Co^{II}: violet, O: red, N: blue, P: orange, C: grey, Cl: green. Hydrogen atoms are omitted for clarity.

CShMs[41, 42] were used to determine the distortion of the tetrahedral geometry around each metal ion (Table A5.4 in the appendix). The CShMs values are in the range 0.089−0.510, where 0 corresponds to the ideal tetrahedron. The oxidation states of all Co^{II} centres were confirmed using BVS analysis.[40, 41] A plane is defined by the three P atoms of the phosphonate ligands, while the Co1−Co3 and Co6−Co8 centres define another plane, with Co4 and Co5 located outside this plane at ~2.1 and ~2.3 Å, respectively (Fig. 5.22) (as previously seen for complex **8**(MeCN)). The crystal packing of **9b**(DCE) is shown in Figure 5.23; intermolecular hydrogen-π interactions are present between the $dmpz^-$ rings and the hydrogen atoms of the $[HNEt_3]^+$ cation, and between the $dmpz^-$ rings and the hydrogen atoms of $dmpz^-$ ligands from neighbouring molecules (Fig. A5.8 in the appendix). The shortest intermolecular Co···Co' distance is ~7.7 Å.

Finally, in order to examine if the sample is phase pure, powder X-ray diffraction was carried out along with elemental analysis. Unfortunately, the elemental analysis was not satisfactory possibly due to impurities, despite the fact that the sample was washed with hexane and diethyl-ether in order to avoid impurities from the starting materials. In addition, there is a deviation between the experimental PXRD pattern and the one

calculated from the single-crystal structure (Fig. 5.24), suggesting that the bulk sample is possibly not pure.

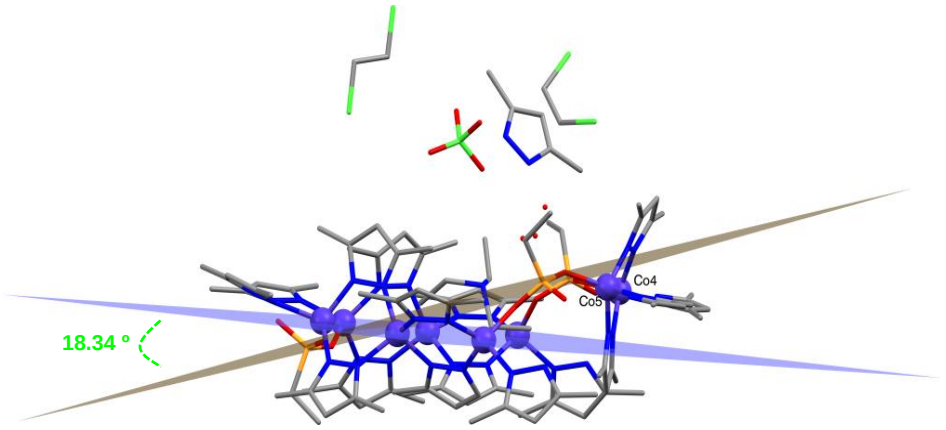

Figure 5.22 The molecular structure of complex **9b**(DCE). The grey plane is defined by the three P atoms of the phosphonate ligands and the purple plane is defined by the Co1−Co3 and Co6−Co8 centres (as previously seen for complex **8**(MeCN) Fig. 5.13). Colour code: Co^{II}: violet, O: red, N: blue, P: orange, C: grey, Cl: green. Hydrogen atoms are omitted for clarity.

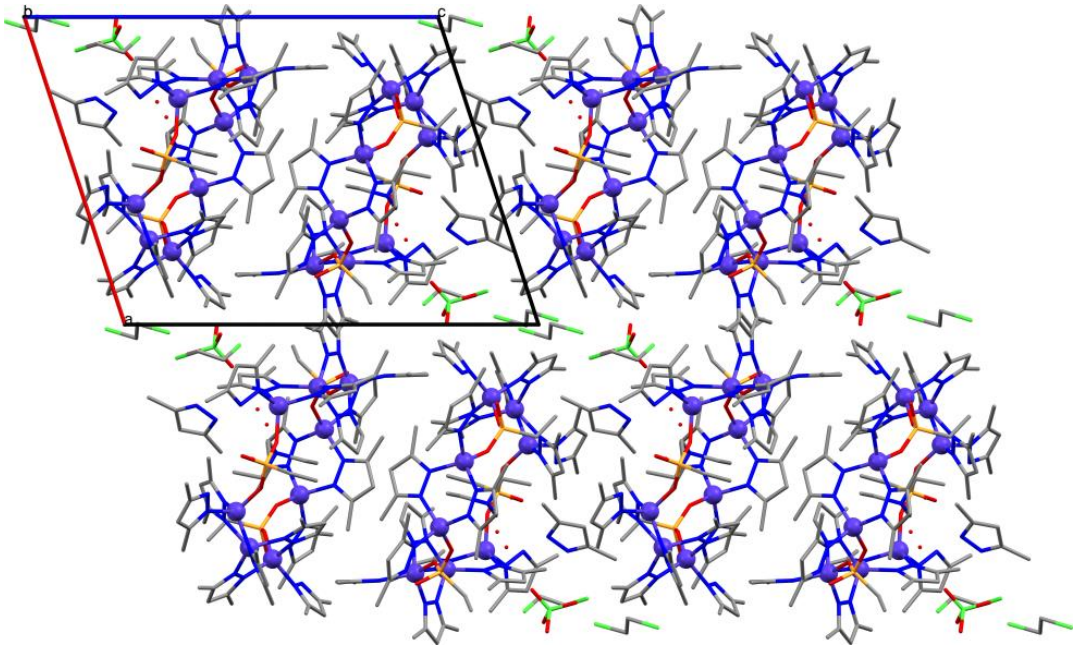

Figure 5.23 The crystal packing of **9b**(DCE) ($P\bar{1}$) along the crystallographic *b*-axis. Colour code: Co^{II}: violet, O: red, N: blue, P: orange, C: grey, Cl: green. Hydrogen atoms are omitted for clarity.

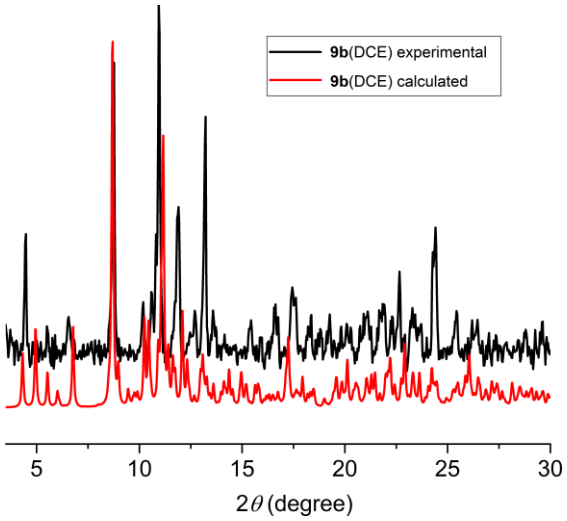

Figure 5.24 The experimental PXRD pattern (3−30°) of **9b**(DCE). The red line represents the calculated PXRD pattern for complex **9b**(DCE) and the black line the experimental one. The experimental PXRD pattern was measured at room temperature, while the calculated pattern is generated from the single-crystal data collected at 150 K.

At this stage it is worth mentioning that changing the cobalt salt from $Co(ClO_4)_2 \cdot 6H_2O$ to $CoCl_2 \cdot 6H_2O$ can also affect the final product. We followed the same synthetic route as for complex **9a**(DCM), however we used $CoCl_2 \cdot 6H_2O$ instead of $Co(ClO_4)_2 \cdot 6H_2O$. As a result we managed to isolate the previously reported $[Co^{II}_3(dmpz)_4(Hdmpz)_2Cl_2]$ (**10**)[45] (Fig. 5.25, and Figures A5.9 and A5.10 in the appendix). This trinuclear complex adopts the same metallic core as the $\{Co^{II}_3\}$ subunit of the complexes mentioned above. All Co^{II} centres are four-coordinate and one terminal Cl^- ligand completes the coordination sphere of each edge Co^{II} centre, instead of a phosphonate ligand as seen in the $\{Co^{II}_9\}$ and $\{Co^{II}_8\}$ complexes. The terminal Cl^- could cause the inhibition of further assembly through the phosphonate bridges. This structure has been previously reported, therefore there will not be any further discussion about this complex.

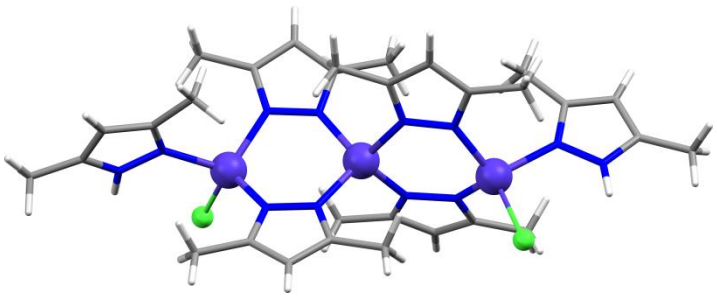

Figure 5.25 The molecular structure of complex **10**. Colour code: Co^{II}: violet, N: blue, C: grey, Cl: green, H: white.[45]

5.3.3 Phenylphosphonic acid and *n*-butylphosphonic acid

The phenylphosphonate ligand possesses a bulky aromatic ring, which could impose *π*-*π* or hydrogen-*π* interactions and help to the stabilisation of a product during the crystallisation process; therefore the use of this bulkier ligand could lead to the isolation of a different final product. Indeed, the reaction of $Co(ClO_4)_2 \cdot 6H_2O$ with Hdmpz, $PhPO_3H_2$ and NEt_3 (in 3:6:1:10 ratio), in DCM and under ambient conditions led to a new hexanuclear cyclic Co^{II} complex, $[HNEt_3][Co^{II}_6(PhPO_3)_3(dmpz)_6(Hdmpz)_6][ClO_4] \cdot DCM$ (**11**·DCM) (Fig. 5.26 left). Further studies on this reaction system were carried out, and various conditions and staring materials were examined as previously seen in the synthetic routes of the $\{Co^{II}_9\}$ and $\{Co^{II}_8\}$ complexes; however we only obtained some preliminary results which will not be mentioned in this thesis.

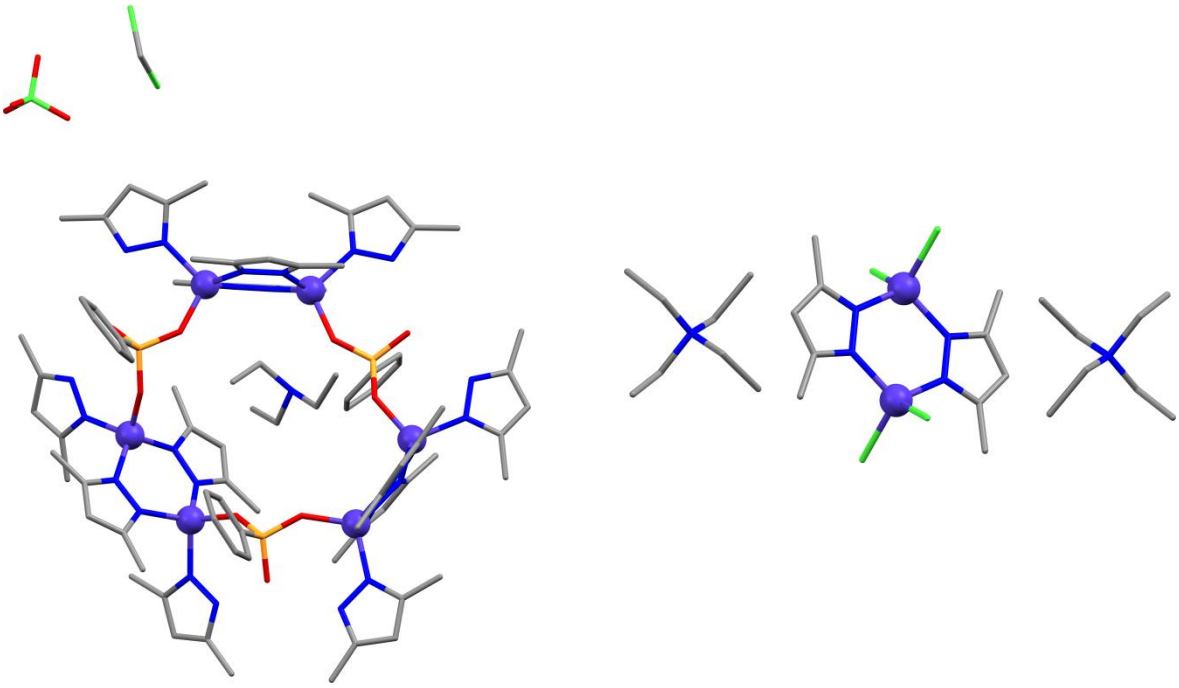

Figure 5.26 *Left)* The molecular structure of complex **11**·DCM. *Right)* The molecular structure of complex **12**. Colour code: Co^{II}: violet, N: blue, O: red, P: orange, C: grey, Cl: green. Hydrogen atoms are omitted for clarity.

Furthermore, we did not manage to obtain any crystals suitable for single-crystal X-ray diffraction incorporating the *n*-butylphosphonate ligand. However, the reaction of $CoCl_2 \cdot 6H_2O$ with Hdmpz, $n BuPO_3H_2$ and NEt_3 (in 3:6:1:10 ratio), in DCM and under ambient conditions resulted in the dinuclear complex $[NEt_4]_2[Co^{II}_2(dmpz)_2Cl_4]$ (**12**) (Fig. 5.26 right) containing only the ligand Hdmpz. This metallic core has been previously reported, incorporating the ligands Hdmpz, substituted Hdmpz or 3,5-diisopropylpyrazole, with different terminal groups than Cl^-.[45-48] Although the base triethylamine was used in

the synthesis of complex **12**, two molecules of the tetraethylamonium cation are found in the crystal lattice. This is not an unusual transformation of NEt_3 in the presence of DCM; the reactivity of di- or trialkylamines with DCM under mild reaction conditions has been previously reported.[49] More specifically the use of NEt_3 along with solvent DCM in conjunction with transition metals can lead to a variety of products, such as $[Et_4N]^+$, $[Et_2NH_2]^+$ or chloro-alkyl derivatives.[50-53]

Crystal structure analysis and Powder X-ray Diffraction (PXRD)

Complex $[HNEt_3][Co^{II}_6(PhPO_3)_3(dmpz)_6(Hdmpz)_6][ClO_4]$·DCM (**11**·DCM) crystallises in the monoclinic *P2₁/n* space group (Table A5.8 in the appendix) and is a new hexanuclear cyclic Co^{II} complex. The asymmetric unit consists of a full molecule of $[Co^{II}_6(PhPO_3)_3(dmpz)_6(Hdmpz)_6]$, one $[HNEt_3]^+$, one ClO_4^- and one molecule of DCM solvent present in the crystal lattice. The molecular structure of **11** consists of three $\{Co^{II}_2\}$ subunits which are connected with each other by three doubly deprotonated $PhPO_3^{2-}$ ligands forming a cyclic $\{Co^{II}_6\}$ complex (Fig. 5.27). Again, the cyclic $\{Co^{II}_6\}$ complex is not planar, as seen in the $\{Co^{II}_9\}$ and $\{Co^{II}_8\}$ complexes; a plane is defined by the three P atoms of the phosphonate ligands, while the Co1−Co4 centres define another plane, with Co5 and Co6 located outside this plane (~2.1 Å) (Fig. 5.28). Each $\{Co^{II}_2\}$ subunit contains two four-coordinate cobalt centres bridged by two $dmpz^-$ ligands (as also seen in $\{Co^{II}_8\}$); the coordination sphere of the edge Co^{II} centres (in each subunit) is completed by one N atom from an Hdmpz ligand and one O atom from the phosphonate ligand. The oxidation states of all Co^{II} centres were confirmed using BVS analysis[40, 41] and CShMs[41, 42] were used to determine the distortion of the tetrahedral geometry around each metal ion (Table A5.5 in the appendix) and the values are in the range 0.099−0.265 (where 0 corresponds to the ideal tetrahedron). The crystal packing of the structure is shown in Figure 5.29 and intermolecular hydrogen-π interactions are present between the $dmpz^-$ rings and the hydrogen atoms of the $[HNEt_3]^+$ cation, while intramolecular hydrogen-π interactions are present between the phenyl rings and the hydrogen atoms from the $dmpz^-$ ligands (Fig. A5.11 in the appendix). The shortest intermolecular Co···Co' distance is ~8.2 Å.

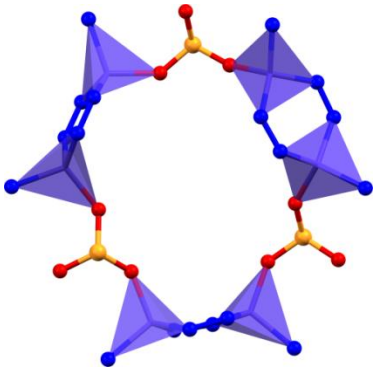

Figure 5.27 Illustration of the cyclic metallic core of complex **11**·DCM. The purple polyhedra represent the tetrahedral geometry of the metal centres. Colour code: Co^{II}: violet, O: red, N: blue, P: orange. Hydrogen and carbon atoms are omitted for clarity.

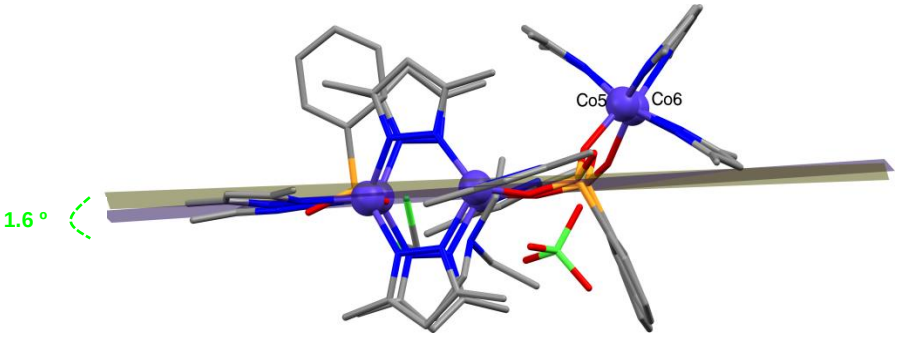

Figure 5.28 The molecular structure of complex **11**·DCM. The grey plane is defined by the three P atoms of the phosphonate ligands and the purple plane is defined by Co1−Co4. Colour code: Co^{II}: violet, O: red, N: blue, P: orange, C: grey, Cl: green. Hydrogen atoms are omitted for clarity.

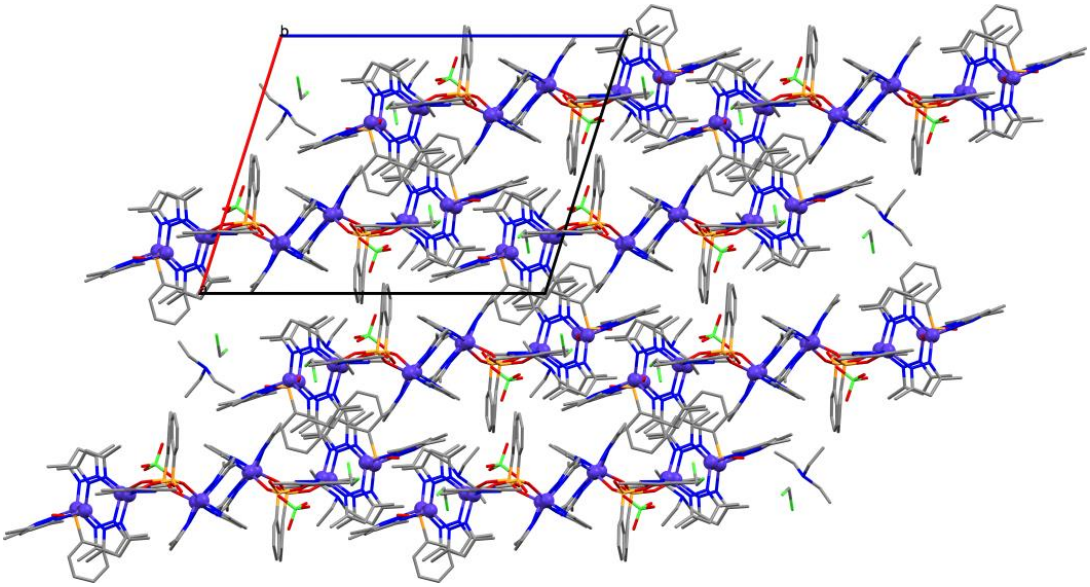

Figure 5.29 The crystal packing of **11**·DCM ($P2_1/n$) along the crystallographic *b*-axis. Colour code: Co^{II}: violet, O: red, N: blue, P: orange, C: grey, Cl: green. Hydrogen atoms are omitted for clarity.

Powder X-ray diffraction was carried out along with elemental analysis in order to examine if the sample is phase pure. The experimental elemental analysis suggests that there is no DCM present in the sample, however there are ~3 molecules of water (see Section 5.2). Moreover, there is a deviation of the experimental PXRD pattern and the calculated one from the single-crystal structure (Fig. 5.30), which could be attributed to the loss of solvent and the presence of water molecules in the sample.

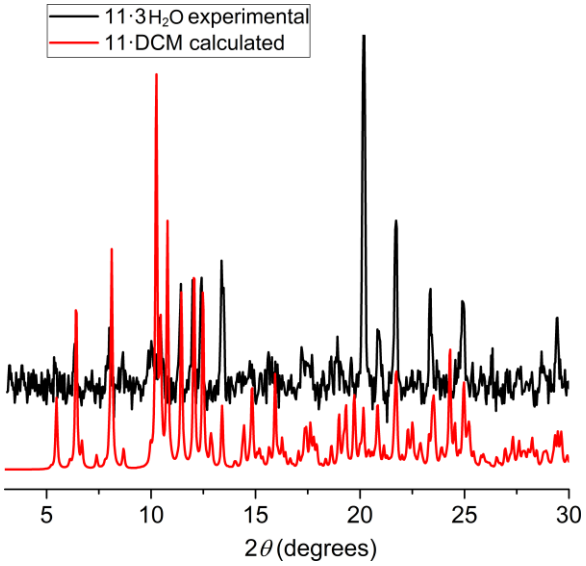

Figure 5.30 The experimental PXRD pattern (3−30°) of **11**·3H_2O. The red line represents the calculated PXRD pattern for complex **11**·DCM and the black line the experimental one. The experimental PXRD pattern was measured at room temperature, while the calculated pattern is generated from the single-crystal data collected at 100 K.

Complex $[NEt_4]_2[Co^{II}_2(dmpz)_2Cl_4]$ (**12**) crystallises in the monoclinic *P2₁/c* space group (Table A5.8 in the appendix) and is a dinuclear Co^{II} complex (Fig. 5.31). As mentioned above the metallic core has been previously reported, incorporating slightly different ligands.[45-48] The asymmetric unit contains half a molecule of $[Co^{II}_2(dmpz)_2Cl_4]^{2-}$ and one $[NEt_4]^+$ molecule. The two Co^{II} centres are bridged by two $dmpz^-$ ligands while two terminal Cl^- ligands complete the coordination sphere of each metal ion. Continuous shape measures (CShMs)[41, 42] were used to determine the distortion of the tetrahedral geometry around the Co^{II} centre (which is the same for its centrosymmetric equivalent) and gave the value of 0.38, where 0 corresponds to the ideal tetrahedron. The crystal packing of the structure is shown in Figure 5.32 and intermolecular hydrogen-*π* interactions are present between the $dmpz^-$ rings and the hydrogen atoms of the $[NEt_4]^+$ molecules (Fig. A5.12 in the appendix). The shortest intermolecular Co···Co' distance is ~8.2 Å.

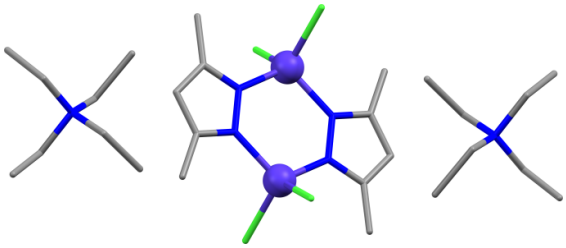

Figure 5.31 The molecular structure of complex **12**. Colour code: Co^{II}: violet, N: blue, O: red, P: orange, C: grey, Cl: green. Hydrogen atoms are omitted for clarity.

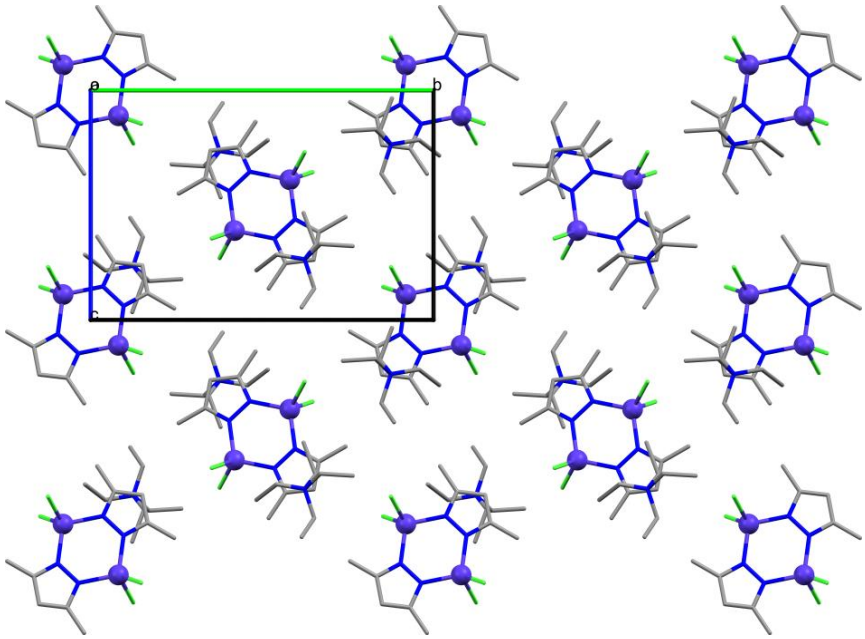

Figure 5.32 The crystal packing of **12** ($P2_1/c$) along the crystallographic *a*-axis. Colour code: Co^{II}: violet, N: blue, C: grey, Cl: green. Hydrogen atoms are omitted for clarity.

Discussion

In summary, we managed to isolate various new complexes with four different metallic cores utilising the substituted phosphonic acids: *tert*-butylphosphonic acid, ethylphosphonic acid and phenylphosphonic acid along with 3,5-dimethylpyrazole. Using *tert*-butylphosphonic acid under solvothemral and reflux heating, the nonanuclear complex $[Co^{II}_9(t\text{BuPO}_3)_3(\text{dmpz})_{12}(\text{Hdmpz})_6]\cdot x\text{MeCN}\cdot y\text{H}_2\text{O}$ (**6**·xMeCN·yH$_2$O) and the trinuclear complex $[Co^{II}_3(t\text{BuPO}_3)_2(\text{Hdmpz})_4\text{Br}_2]$ (**7**) were isolated, respectively (Scheme 5.2).

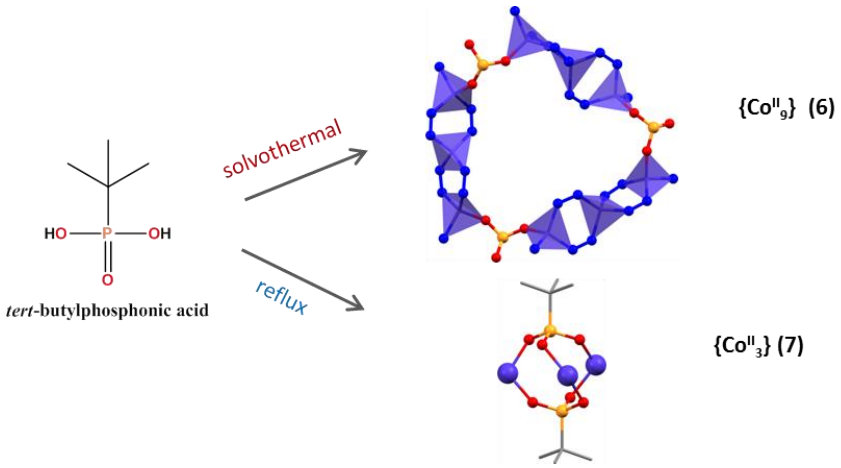

Scheme 5.2 Illustration of the different metallic cores isolated by utilising the *tert*-butylphosphonic acid using different synthetic procedures (solvothermal and reflux). The purple polyhedra represent the tetrahedral geometry of the metal centres. Colour code: Co^{II}: violet, O: red, N: blue, P: orange. Hydrogen and carbon atoms are omitted for clarity.

The use of ethylphosphonic acid under ambient conditions and a variety of solvents, led to the isolation of two octanuclear complexes with the same $\{Co^{II}_8\}$ metallic core (Scheme 5.3 top): $[Co^{II}_8(EtPO_3)_3(dmpz)_{10}(Hdmpz)_6]\cdot xMeCN\cdot yH_2O$ (**8**(MeCN)) and $[HNEt_3][Co^{II}_8(EtPO_3)_3(dmpz)_{10}(Hdmpz)_6][ClO_4]\cdot xDCM\cdot yH_2O$ (**9a**(DCM)), and its solvate analogue $[HNEt_3][Co^{II}_8(EtPO_3)_3(dmpz)_{10}(Hdmpz)_6][ClO_4]\cdot 0.75(Hdmpz)\cdot 2.25DCE\cdot H_2O$ (**9b**(DCE)). The replacement of the ethylphosphonic acid with phenylphosphonic acid and under ambient conditions led to the hexanuclear complex $[HNEt_3][Co^{II}_6(PhPO_3)_3(dmpz)_6(Hdmpz)_6][ClO_4]\cdot DCM$ (**11**·DCM) (Scheme 5.3 bottom). In each of these cyclic complexes there are $\{Co^{II}_3\}$ and/or $\{Co^{II}_2\}$ subunits, which could be considered as the building blocks connected by the phosphonate bridges. Furthermore, we were able to isolate the complexes $[Co^{II}_3(dmpz)_4(Hdmpz)_2Cl_2]$ (**10**) and $[NEt_4]_2[Co^{II}_2(dmpz)_2Cl_4]$ (**12**), which have the same metallic cores as the $\{Co^{II}_3\}$ and $\{Co^{II}_2\}$ subunits, respectively. Depending on the R group of the phosphonate ligand and the reaction conditions we can gain some control over the nuclearity of the final product. We are even able to inhibit the molecular assembly with the introduction of terminal ligands such as Cl^- or Br^-. The $\{Co^{II}_3\}$ and $\{Co^{II}_2\}$ complexes could also be used in the future as building blocks in order to achieve even higher nuclearities.

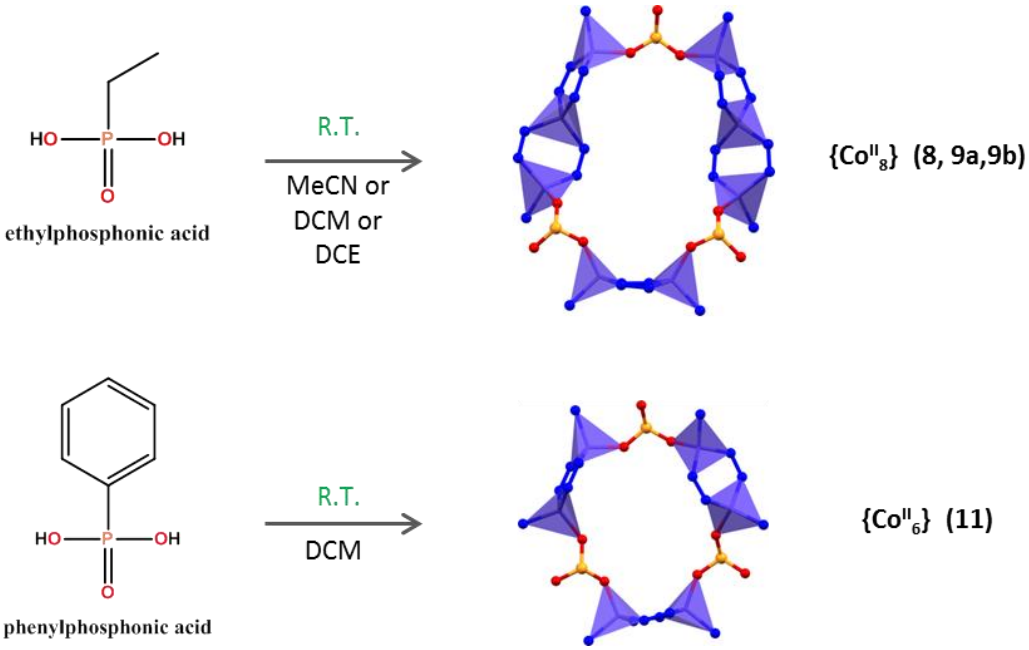

Scheme 5.3 Illustration of the different metallic cores isolated by utilising ethylphosphonic acid (*top*) and phenylphosphonic acid (*bottom*) under ambient conditions (room temperature). The purple polyhedra represent the tetrahedral geometry of the metal centres. Colour code: Co^{II}: violet, O: red, N: blue, P: orange. Hydrogen and carbon atoms are omitted for clarity.

Finally, an interesting feature of complexes **9a**(DCM), **9b**(DCE) and **11**·DCM, is that despite the fact that the molecules are neutral, a pair of $[HNEt_3]^+$ and ClO_4^- ions is co-crystallised in the lattice. A CSD search (database of February 2019) revealed that only a few such structures are reported with a neutral molecule and this pair.[54-65] Complex **8**(MeCN) presents the same metallic core as **9a**(DCM) and **9b**(DCE), however it does not contain the $[HNEt_3]^+/ClO_4^-$ pair; therefore we can assume that the presence of the ions in the crystal lattice is not necessary for the crystallisation of the product. Moreover, the yields of the complexes **8**(MeCN) (~10%), **9a**(DCM) (~8%) and **9b**(DCE) (~14%) vary among the complexes without following any trend, and therefore we cannot conclude if the co-crystallisation of the pair plays an important role in this matter.

5.3.4 Magnetic characterisation

Variable temperature direct current (dc) susceptibility data were collected for complexes **6** and **7** in a field of 1000 Oe in the 290–2 K temperature range (Fig. 5.33 and 5.34). The $\chi_M T$ value at room temperature for **6** is 21.33 cm^3 mol^{-1} K, which is higher than the

theoretical spin-only value $\chi_M T$ = 16.9 cm^3 mol^{-1} K for nine non-interacting high-spin Co^{II} (S = 3/2 and g = 2); this indicates a spin-orbit coupling contribution (arising from the mixing of orbitally degenerate excited states) as can be expected for tetrahedrally coordinated Co^{II} ions.[66, 67] $\chi_M T$ gradually decreases (Fig. 5.33) with the decrease of temperature until ~70 K and then decreases rapidly to reach 4.5 cm^3 mol^{-1} K at 2 K, which can be attributed to the presence of dominant antiferromagnetic exchange interactions. Magnetisation versus field plots at 2, 4 and 6 K did not saturate, an indication of the presence of magnetic anisotropy (Fig. 5.33). This behaviour is in agreement with other pyrazolate bridged Co^{II} complexes, where dominant antiferromagnetic exchange interactions are usually observed.[45, 48, 68-71] Moreover, complexes containing bridging phosphonate ligands also exhibit weak antiferromagnetic interactions.[13, 35, 72, 73] Using the program PHI we attempted to fit the data with nine Co^{II} centres in tetrahedral geometry with S = 3/2 and the approximation of one exchange interaction J; however, the fit was not able to produce any values due to the complexity of the system and the presence of nine Co metal centres.

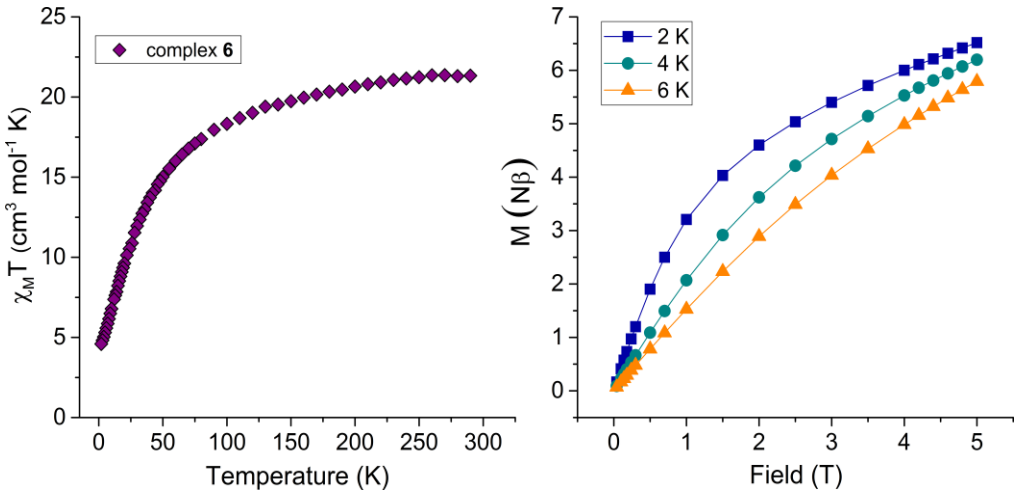

Figure 5.33 *Left)* χ_MT *versus* Temperature data for **6** in a field of 1000 Oe from 290 – 2 K. *Right*) Magnetisation *versus* Field data at temperatures 2, 4 and 6 K for complex **6**. The solid lines are a guide to the eye.

The $\chi_M T$ value at room temperature for **7** is 7.85 cm^3 mol^{-1} K, which is higher than the theoretical spin-only value $\chi_M T$ = 5.63 cm^3 mol^{-1} K for three non-interacting high-spin Co^{II} (S = 3/2 and g = 2), indicating an orbital contribution (arising from the mixing of orbitally degenerate excited states) as can be expected for tetrahedrally coordinated Co^{II} ions.[66, 67] $\chi_M T$ slowly decreases (Fig. 5.34) with the decrease of temperature until ~40 K and then

decreases rapidly to reach 1.82 cm^3 mol^{-1} K at 2 K, which can be attributed to the presence of dominant antiferromagnetic exchange interactions. Magnetisation versus field plots at 2, 4 and 6 K did not saturate, an indication of the presence of magnetic anisotropy (Fig. 5.34).

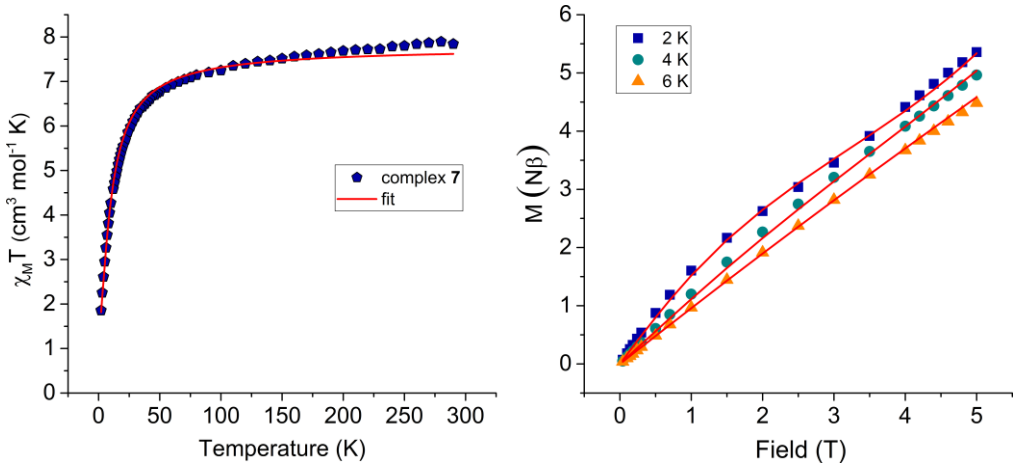

Figure 5.34 *Left)* χ_MT *versus* Temperature data for **7** in a field of 1000 Oe from 290–2 K. *Right)* Magnetisation *versus* Field data at temperatures 2, 4 and 6 K for **7**. The red solid lines represent the fit (see text for details).

The dc magnetic susceptibility data and the magnetisation curves of **7** were fitted simultaneously using the programme PHI[74] (Fig. 5.34) as described by the following effective Hamiltonian equation[75] (Equation **1**):

$$\hat{H} = -2J\left(\hat{S}_1 \cdot \hat{S}_2 + \hat{S}_2 \cdot \hat{S}_3 + \hat{S}_3 \cdot \hat{S}_1\right) + D\sum_{i=1}^{3}\left(\hat{S}_{iz}^2 - \frac{1}{3}S_i(S_i+1)\right) + \sum_{i=1}^{3}\mu_B \vec{B} \cdot \overleftrightarrow{g} \cdot \hat{S}_i \quad (\mathbf{1})$$

The above Hamiltonian takes into account the coupling between the Co^{II} ions (J) (see model in Fig. 5.35), the axial ZFS for each Co^{II} ion (D, which is assumed to be equal for all cobalt centres, $D = D_1 = D_2 = D_3$, in order to avoid overparameterisation) and the Zeeman interaction, in that order. The rhombic ZFS term (E) was not introduced in the equation to avoid overparameterisation. The extracted parameters from the fitting of the data are: J = −0.85 (±0.005) cm^{-1}, g = 2.35, D = −1.57 (±0.027) cm^{-1}. Although the susceptibility data could be fitted with a positive D (easy-plane magnetic anisotropy) and produced satisfactory fits, the magnetisation was sensitive to the change of the sign of D, yielding low quality fits. This is a strong indication that an easy-axis magnetic anisotropy (D < 0) is present here. The small J value is reasonable, as weak antiferromagnetic exchange interactions are expected for phosphonate bridges.[13, 35, 72, 73] Moreover, the obtained

parameters *J* and *D* have a ratio *J*/*D* smaller than 1 which suggests that **7** is in the weak exchange limit, where the spin-orbit contribution is larger than the exchange interaction.[76] This is consistent with previously reported complexes with high anisotropy 3*d* metal ions and weak exchange interactions, where a similar *M* vs H plot as for **7** can be observed.[77-81]

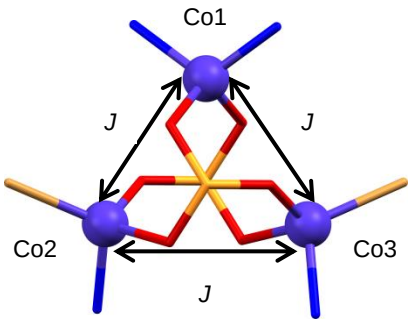

Figure 5.35 The magnetic model used for the fit of complex **7** with eq.1. Colour code: Co^{II}: violet, O: red, N: blue, P: orange. Hydrogen and carbon atoms are omitted for clarity.

Alternating current (ac) susceptibility measurements were performed for both complexes in the temperature range 10−2 K, in a 3 Oe ac field and in the frequency range 1–1488 Hz, in order to examine if there is slow magnetic relaxation. Complex **6** displays only the onset of a weak χ'' signal in a zero dc field, while the application of a 2000 Oe dc field (Fig. 5.36) did not improve the intensity of the signal. As previously discussed in Chapter 3, none of the other reported $\{Co^{II}_9\}$ complexes exhibit any out-of-phase signals.[34, 82-90] Due to the weak χ'' signal in **6**, we did not expect to see any improvement in the signal by performing an isothermal field sweep ac measurement; hence no further magnetic measurements were carried out.

Complex **7** does not display any out-of-phase ac signal in zero or an applied dc field (Fig. 5.37). This could be attributed to fast magnetic relaxation, due to the QTM arising from intermolecular dipolar interactions; the shortest intermolecular Co···Co' distance is ~7.3 Å (dipolar interactions for cobalt complexes are expected to be suppressed for distances larger than ~8 Å).[91] The absence of slow magnetic relaxation could be also attributed to the small value of the axial ZFS parameter and the near to zero $\chi_M T$ value at low temperature.

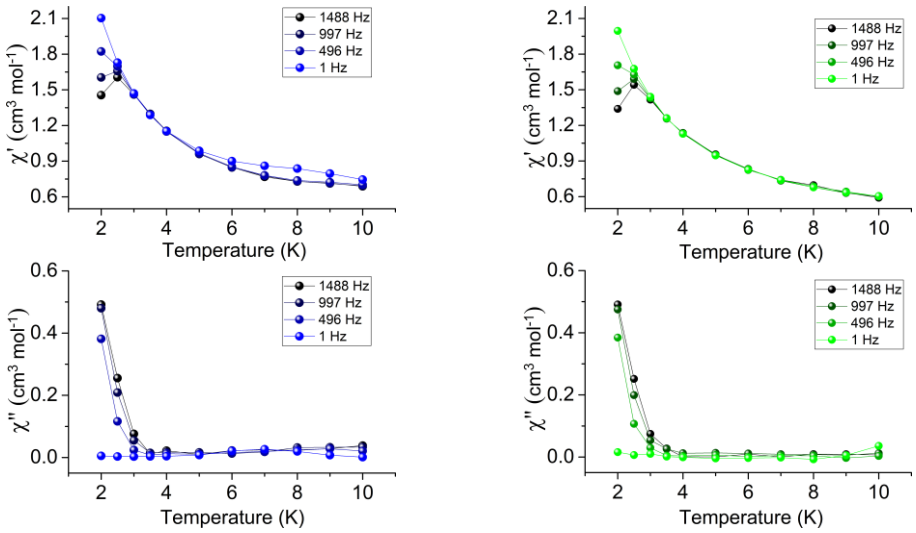

Figure 5.36 Temperature dependence of the in-phase (*top*) and the out-of-phase (*bottom*) ac susceptibility signals in 0 (*left*) and 2000 (*right*) Oe dc field, in the frequency range 1 – 1488 Hz, for complex **6**. The solid lines are a guide to the eye.

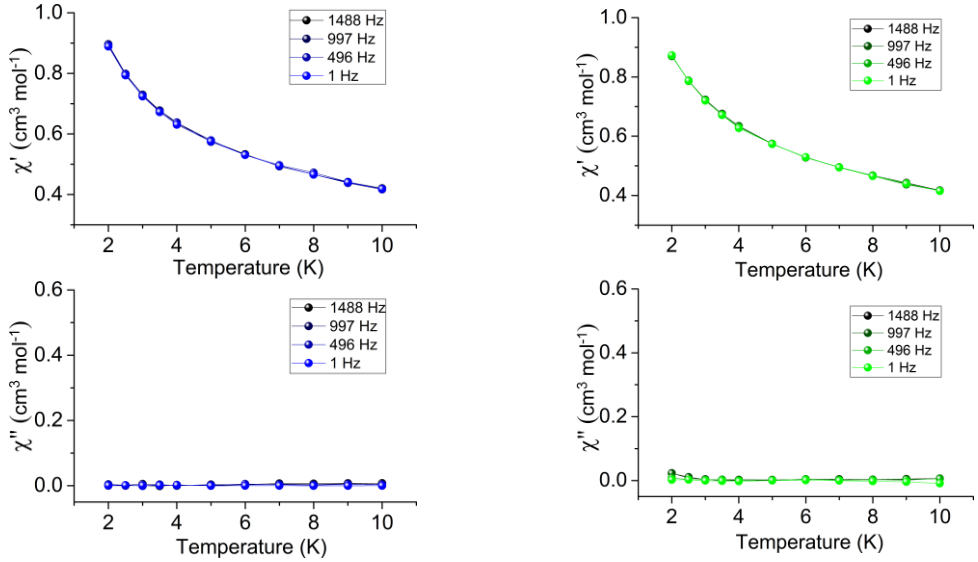

Figure 5.37 Temperature dependence of the in-phase (*top*) and the out-of-phase (*bottom*) ac susceptibility signals in 0 (*left*) and 2000 (*right*) Oe dc field, in the frequency range 1 – 1488 Hz, for complex **7**. The solid lines are a guide to the eye.

5.4 Conclusions

In conclusion, we were able to isolate the new cyclic complexes $\{Co^{II}_9\}$, $\{Co^{II}_8\}$, $\{Co^{II}_6\}$ and the propeller-like $\{Co^{II}_3\}$ complex, incorporating the ligands *tert*-butylphosphonic acid, ethylphosphonic acid and phenylphosphonic acid along with 3,5-dimethylpyrazole. These complexes are:

- $[Co^{II}_9(t\text{BuPO}_3)_3(\text{dmpz})_{12}(\text{Hdmpz})_6]\cdot x\text{MeCN}\cdot y\text{H}_2\text{O}$ (**6**·x$\text{MeCN}\cdot y\text{H}_2\text{O}$),
- $[Co^{II}_3(t\text{BuPO}_3)_2(\text{Hdmpz})_4\text{Br}_2]$ (**7**),
- $[Co^{II}_8(\text{EtPO}_3)_3(\text{dmpz})_{10}(\text{Hdmpz})_6]\cdot x\text{MeCN}\cdot y\text{H}_2\text{O}$ (**8**(MeCN)),
- $[\text{HNEt}_3][Co^{II}_8(\text{EtPO}_3)_3(\text{dmpz})_{10}(\text{Hdmpz})_6][\text{ClO}_4]\cdot x\text{DCM}\cdot y\text{H}_2\text{O}$ (**9a**(DCM)),
- $[\text{HNEt}_3][Co^{II}_8(\text{EtPO}_3)_3(\text{dmpz})_{10}(\text{Hdmpz})_6][\text{ClO}_4]\cdot 0.75(\text{Hdmpz})\cdot 2.25\text{DCE}\cdot\text{H}_2\text{O}$ (**9b**(DCE)) and
- $[\text{HNEt}_3][Co^{II}_6(\text{PhPO}_3)_3(\text{dmpz})_6(\text{Hdmpz})_6][\text{ClO}_4]\cdot\text{DCM}$ (**11**·DCM).

Depending on the substituted phosphonate ligand and/or the synthetic procedure followed, we managed to gain some control over the nuclearity of the final product. Moreover, we are able to isolate different solvate analogues for the complexes $\{Co^{II}_9\}$ and $\{Co^{II}_8\}$, while with the introduction of the terminal Cl^- and Br^- we were able to inhibit the molecular assembly, and obtained the complexes $[Co^{II}_3(\text{dmpz})_4(\text{Hdmpz})_2\text{Cl}_2]$ (**10**) and $[\text{HNEt}_4]_2[Co^{II}_2(\text{dmpz})_2\text{Cl}_4]$ (**12**). Magnetic characterisation was carried out only for **6** and **7**, due to limited time available on the SQUID magnetometer and/or the need to refine the synthetic procedures for some of the complexes. Dc susceptibility studies revealed dominant antiferromagnetic exchange interactions for both **6** and **7**. Fitting the magnetic data for **7** the following values were extracted: $J = -0.85$ (±0.005) cm^{-1}, $g = 2.35$, $D = -1.57$ (±0.027) cm^{-1}, suggesting that **7** is in the weak exchange limit, where the spin-orbit contribution is larger than the exchange interaction. Dynamic ac magnetic studies showed only the onset of the out-of-phase ac signals for **6**, whereas complex **7** does not display slow magnetic relaxation. The variety of the nuclearities observed in this work, with the change of either the phosphonate ligand and/or the reaction conditions, shows once again the flexibility of the phosphonate ligands. Although a large number of phosphonate complexes have been already reported, considerable potential still exists in the coordination chemistry of phosphonates. Finally, the vast applications of metal-phosphonate complexes in numerous fields[1], makes the synthesis of such complexes even more attractive.

5.5 References

1. J. Goura and V. Chandrasekhar, *Chemical Reviews*, 2015, **115**, 6854-6965.
2. A. Cabeza and M. A. G. Aranda, in *Metal Phosphonate Chemistry: From Synthesis to Applications.*, eds. A. Clearfield and K. Demadis, RSC Publishing, Cambridge, UK, 2012, p. 107−132.
3. K. Maeda, *Microporous and Mesoporous Materials*, 2004, **73**, 47-55.
4. L. Ma, C. Abney and W. Lin, *Chemical Society Reviews*, 2009, **38**, 1248-1256.
5. J.-G. Mao, *Coordination Chemistry Reviews*, 2007, **251**, 1493-1520.
6. J. Amalric, P. H. Mutin, G. Guerrero, A. Ponche, A. Sotto and J.-P. Lavigne, *Journal of Materials Chemistry*, 2009, **19**, 141-149.
7. J. Galezowska and E. Gumienna-Kontecka, *Coordination Chemistry Reviews*, 2012, **256**, 105-124.
8. S.-S. Bao and L.-M. Zheng, *Coordination Chemistry Reviews*, 2016, **319**, 63-85.
9. K. A. Gopal, S. and R. E. P. Winpenny, in *Metal Phosphonate Chemistry: From Synthesis to Applications.*, eds. A. Clearfield and K. Demadis, RSC Publishing, Cambridge, UK, 2012, p. 364−419.
10. L.-M. Zheng and Y. Duan, in *Metal Phosphonate Chemistry: From Synthesis to Applications.*, eds. A. Clearfield and K. Demadis, RSC Publishing, Cambridge, UK, 2012, p. 235−278.
11. K. H. Zangana, E. M. Pineda, I. J. Vitorica-Yrezabal, E. J. L. McInnes and R. E. P. Winpenny, *Dalton Transactions*, 2014, **43**, 13242-13249.
12. V. Chandrasekhar, L. Nagarajan, R. Clérac, S. Ghosh and S. Verma, *Inorganic Chemistry*, 2008, **47**, 1067-1073.
13. V. Chandrasekhar, J. Goura and E. C. Sañudo, *Inorganic Chemistry*, 2012, **51**, 8479-8487.
14. H. Tian, S.-S. Bao and L.-M. Zheng, *Chemical Communications*, 2016, **52**, 2314-2317.
15. V. Chandrasekhar and P. Sasikumar, *Dalton Transactions*, 2008, 6475-6480.
16. J. A. Sheikh, H. S. Jena, A. Clearfield and S. Konar, *Accounts of Chemical Research*, 2016, **49**, 1093-1103.
17. V. Baskar, M. Shanmugam, E. C. Sañudo, M. Shanmugam, D. Collison, E. J. L. McInnes, Q. Wei and R. E. P. Winpenny, *Chemical Communications*, 2007, 37-39.
18. X. Tang, J. Hua, Y. Ma, A. Hori, R. Yuan and R. Matsuda, *Inorganica Chimica Acta*, 2018, **482**, 900-904.
19. E. K. Brechin, R. A. Coxall, A. Parkin, S. Parsons, P. A. Tasker and R. E. P. Winpenny, *Angewandte Chemie International Edition*, 2001, **40**, 2700-2703.
20. V. Chandrasekhar, T. Senapati, A. Dey and E. C. Sañudo, *Inorganic Chemistry*, 2011, **50**, 1420-1428.
21. H. Tian, S.-S. Bao and L.-M. Zheng, *Dalton Transactions*, 2015, **44**, 14208-14212.
22. K. Su, F. Jiang, J. Qian, Y. Gai, M. Wu, S. M. Bawaked, M. Mokhtar, S. A. Al-Thabaiti and M. Hong, *Crystal Growth & Design*, 2014, **14**, 3116-3123.
23. N. P. Burkovskaya, M. E. Nikiforova, M. A. Kiskin, A. S. Lermontov, A. S. Bogomyakov, V. S. Mironov, Z. V. Dobrokhotova, V. I. Pekhnyo, A. A. Sidorov, V. M. Novotortsev and I. L. Eremenko, *Polyhedron*, 2011, **30**, 2941-2949.
24. M. Wang, C.-B. Ma, D.-Q. Yuan, H.-S. Wang, C.-N. Chen and Q.-T. Liu, *Inorganic Chemistry*, 2008, **47**, 5580-5590.
25. B. A. Breeze, M. Shanmugam, F. Tuna and R. E. P. Winpenny, *Chemical Communications*, 2007, 5185-5187.
26. S. Langley, M. Helliwell, R. Sessoli, S. J. Teat and R. E. P. Winpenny, *Inorganic Chemistry*, 2008, **47**, 497-507.

27. J. A. Sheikh, H. S. Jena, A. Adhikary, S. Khatua and S. Konar, *Inorganic Chemistry*, 2013, **52**, 9717-9719.
28. V. Chandrasekhar, L. Nagarajan, S. Hossain, K. Gopal, S. Ghosh and S. Verma, *Inorganic Chemistry*, 2012, **51**, 5605-5616.
29. R. Murugavel, S. Kuppuswamy, A. N. Maity and M. P. Singh, *Inorganic Chemistry*, 2009, **48**, 183-192.
30. R. Murugavel, S. Kuppuswamy, N. Gogoi, A. Steiner, J. Bacsa, R. Boomishankar and K. G. Suresh, *Chemistry – An Asian Journal*, 2009, **4**, 143-153.
31. V. Chandrasekhar and L. Nagarajan, *Dalton Transactions*, 2009, 6712-6714.
32. J. Goura, P. Bag, V. Mereacre, A. K. Powell and V. Chandrasekhar, *Inorganic Chemistry*, 2014, **53**, 8147-8154.
33. V. Chandrasekhar, D. Sahoo and R. K. Metre, *CrystEngComm*, 2013, **15**, 7419-7422.
34. D. Sahoo, R. Suriyanarayanan and V. Chandrasekhar, *Crystal Growth & Design*, 2014, **14**, 2725-2728.
35. S. K. Gupta, S. Kuppuswamy, J. P. S. Walsh, E. J. L. McInnes and R. Murugavel, *Dalton Transactions*, 2015, **44**, 5587-5601.
36. S. Langley, M. Helliwell, R. Sessoli, S. J. Teat and R. E. P. Winpenny, *Dalton Transactions*, 2009, 3102-3110.
37. S. Ali, C. A. Muryn, F. Tuna and R. E. P. Winpenny, *Dalton Transactions*, 2010, **39**, 9588-9597.
38. Y.-Z. Zheng, M. Evangelisti and R. E. P. Winpenny, *Chemical Science*, 2011, **2**, 99-102.
39. A. Spek, *Acta Crystallographica Section D*, 2009, **65**, 148-155.
40. N. E. Brese and M. O'Keeffe, *Acta Crystallographica Section B*, 1991, **47**, 192-197.
41. I. D. Brown, Brockhouse Institute for Materials Research, McMaster University, Hamilton, Ontario Canada. idbrown@mcmaster.ca, https://www.iucr.org/__data/assets/file/0007/126574/bvparm2016.cif.
42. C. Jordi, A. Pere and A. Santiago, *Chemistry – A European Journal*, 2004, **10**, 190-207.
43. M. Pinsky and D. Avnir, *Inorganic Chemistry*, 1998, **37**, 5575-5582.
44. V. Chandrasekhar, S. Kingsley, B. Rhatigan, M. K. Lam and A. L. Rheingold, *Inorganic Chemistry*, 2002, **41**, 1030-1032.
45. M. K. Ehlert, S. J. Rettig, A. Storr, R. C. Thompson and J. Trotter, *Canadian Journal of Chemistry*, 1993, **71**, 1425-1436.
46. K. S. Chong, S. J. Rettig, A. Storr and J. Trotter, *Canadian Journal of Chemistry*, 1979, **57**, 3119-3125.
47. U. P. Singh, V. Aggarwal and A. K. Sharma, *Inorganica Chimica Acta*, 2007, **360**, 3226-3232.
48. H. N. Miras, H. Zhao, R. Herchel, C. Rinaldi, S. Pérez and R. G. Raptis, *European Journal of Inorganic Chemistry*, 2008, **2008**, 4745-4755.
49. W. C. Davies, E. B. Evans and F. L. Hulbert, *Journal of the Chemical Society (Resumed)*, 1939, 412-418.
50. C. Lampropoulos, K. A. Abboud, T. C. Stamatatos and G. Christou, *Inorganic Chemistry*, 2009, **48**, 813-815.
51. L. Alcazar, B. Cordero, J. Esteban, V. Tangoulis, M. Font-Bardia, T. Calvet and A. Escuer, *Dalton Transactions*, 2013, **42**, 12334-12345.
52. J. Esteban, M. Font-Bardia and A. Escuer, *European Journal of Inorganic Chemistry*, 2013, **2013**, 5274-5280.
53. J. Esteban, M. Font-Bardia, J. S. Costa, S. J. Teat and A. Escuer, *Inorganic Chemistry*, 2014, **53**, 3194-3203.

54. P. Gomez-Romero, N. Casan-Pastor, A. Ben-Hussein and G. B. Jameson, *Journal of the American Chemical Society*, 1988, **110**, 1988-1990.
55. R. Das and K. Nag, *Inorganic Chemistry*, 1991, **30**, 2831-2833.
56. M. D. Godbole, M. P. Puig, S. Tanase, H. Kooijman, A. L. Spek and E. Bouwman, *Inorganica Chimica Acta*, 2007, **360**, 1954-1960.
57. T. Liu, Y.-J. Zhang, Z.-M. Wang and S. Gao, *Journal of the American Chemical Society*, 2008, **130**, 10500-10501.
58. R. Ferreirós-Martínez, D. Esteban-Gómez, A. de Blas, C. Platas-Iglesias and T. Rodríguez-Blas, *Inorganic Chemistry*, 2009, **48**, 11821-11831.
59. R. Ferreirós-Martínez, D. Esteban-Gómez, C. Platas-Iglesias, A. de Blas and T. Rodríguez-Blas, *Inorganic Chemistry*, 2009, **48**, 10976-10987.
60. R. Ferreirós-Martínez, D. Esteban-Gómez, É. Tóth, A. de Blas, C. Platas-Iglesias and T. Rodríguez-Blas, *Inorganic Chemistry*, 2011, **50**, 3772-3784.
61. M. Inoue, T. Suzuki, Y. Sunatsuki, A. Fuyuhiro and N. Re, *Chemistry Letters*, 2014, **43**, 784-786.
62. C. M. Álvarez, R. García-Rodríguez and D. Miguel, *Dalton Transactions*, 2016, **45**, 963-972.
63. E. P. McMoran, D. R. Powell, F. Perez, G. T. Rowe and L. Yang, *Inorganic Chemistry*, 2016, **55**, 11462-11472.
64. P. S. Perlepe, L. Cunha-Silva, K. J. Gagnon, S. J. Teat, C. Lampropoulos, A. Escuer and T. C. Stamatatos, *Inorganic Chemistry*, 2016, **55**, 1270-1277.
65. S. I. Sampani, E. Loukopoulos, M. Azam, K. Griffiths, A. Abdul-Sada, G. Tizzard, S. Coles, A. Escuer, A. Tsipis and G. E. Kostakis, *CrystEngComm*, 2018, **20**, 1411-1421.
66. S. Gomez-Coca, E. Cremades, N. Aliaga-Alcalde and E. Ruiz, *Journal of the American Chemical Society*, 2013, **135**, 7010-7018.
67. S. Tripathi, A. Dey, M. Shanmugam, R. Suriya Narayanan and V. Chandrsekhar, ch. Cobalt(II) Complexes as Single-Ion Magnets, in *Topics in Organometallic Chemistry.* , Springer, Berlin, Heidelberg, 2018.
68. J. I. van der Vlugt, S. Demeshko, S. Dechert and F. Meyer, *Inorganic Chemistry*, 2008, **47**, 1576-1585.
69. A. Sachse, S. Demeshko and F. Meyer, *Dalton Transactions*, 2009, 7756-7764.
70. T. Shiga, T. Matsumoto, M. Noguchi, T. Onuki, N. Hoshino, G. N. Newton, M. Nakano and H. Oshio, *Chemistry – An Asian Journal*, 2009, **4**, 1660-1663.
71. J. Tong, S. Demeshko, M. John, S. Dechert and F. Meyer, *Inorganic Chemistry*, 2016, **55**, 4362-4372.
72. S. Khanra, S. Konar, A. Clearfield, M. Helliwell, E. J. L. McInnes, E. Tolis, F. Tuna and R. E. P. Winpenny, *Inorganic Chemistry*, 2009, **48**, 5338-5349.
73. M. Wang, C.-B. Ma, X.-Y. Li, C.-N. Chen and Q.-T. Liu, *Journal of Molecular Structure*, 2009, **920**, 242-247.
74. N. F. Chilton, R. P. Anderson, L. D. Turner, A. Soncini and K. S. Murray, *Journal of Computational Chemistry*, 2013, **34**, 1164-1175.
75. R. L. Carlin, *Magnetochemistry*, Springer-Verlag Berlin Heidelberg, 1986.
76. L. F. Chibotaru, in *Molecular Nanomagnets and Related Phenomena*, ed. S. Gao, Springer Berlin Heidelberg, Berlin, Heidelberg, 2015, pp. 185-229.
77. F. El Hallak, P. Rosa, P. Vidal, I. Sheikin, M. Dressel and J. van Slageren, *EPL (Europhysics Letters)*, 2011, **95**, 57002.
78. V. Hoeke, K. Gieb, P. Müller, L. Ungur, L. F. Chibotaru, M. Heidemeier, E. Krickemeyer, A. Stammler, H. Bögge, C. Schröder, J. Schnack and T. Glaser, *Chemical Science*, 2012, **3**, 2868-2882.

79. F. El-Khatib, B. Cahier, F. Shao, M. López-Jordà, R. Guillot, E. Rivière, H. Hafez, Z. Saad, J.-J. Girerd, N. Guihéry and T. Mallah, *Inorganic Chemistry*, 2017, **56**, 4601-4608.
80. J.-J. Liu, S.-D. Jiang, P. Neugebauer, J. van Slageren, Y. Lan, W. Wernsdorfer, B.-W. Wang and S. Gao, *Inorganic Chemistry*, 2017, **56**, 2417-2425.
81. F. El-Khatib, B. Cahier, M. López-Jordà, R. Guillot, E. Rivière, H. Hafez, Z. Saad, N. Guihéry and T. Mallah, *European Journal of Inorganic Chemistry*, 2018, **2018**, 469-476.
82. A. Tsohos, S. Dionyssopoulou, C. P. Raptopoulou, A. Terzis, E. G. Bakalbassis and S. P. Perlepes, *Angewandte Chemie International Edition*, 1999, **38**, 983-985.
83. E. Fursova, O. Kuznetsova, V. Ovcharenko, G. Romanenko, V. Ikorskii, I. Eremenko and A. Sidorov, *Polyhedron*, 2007, **26**, 2079-2088.
84. G. S. Papaefstathiou, A. K. Boudalis, T. C. Stamatatos, C. J. Milios, C. G. Efthymiou, C. P. Raptopoulou, A. Terzis, V. Psycharis, Y. Sanakis, R. Vicente, A. Escuer, J.-P. Tuchagues and S. P. Perlepes, *Polyhedron*, 2007, **26**, 2089-2094.
85. L. N. Dawe, K. V. Shuvaev and L. K. Thompson, *Inorganic Chemistry*, 2009, **48**, 3323-3341.
86. S. K. Langley, M. Helliwell, S. J. Teat and R. E. P. Winpenny, *Dalton Trans.*, 2012, **41**, 12807-12817.
87. W. Shentang, B. Yanfeng, H. Xinxin, Z. Xiaofei and L. Wuping, *Zeitschrift fur Anorganische und Allgemeine Chemie*, 2017, **643**, 160-165.
88. E. K. Brechin, S. G. Harris, S. Parsons and R. E. P. Winpenny, *Angewandte Chemie International Edition in English*, 1997, **36**, 1967-1969.
89. S. Biswas, M. Tonigold, M. Speldrich, P. Kögerler and D. Volkmer, *European Journal of Inorganic Chemistry*, 2009, **2009**, 3094-3101.
90. T. C. Stamatatos, C. P. Raptopoulou, S. P. Perlepes and A. K. Boudalis, *Polyhedron*, 2011, **30**, 3026-3033.
91. K. A. Schulte, K. R. Vignesh and K. R. Dunbar, *Chemical Science*, 2018, **9**, 9018-9026.

Chapter 6

Investigation of the magnetic properties in a family of six-coordinate mononuclear lanthanide complexes

Contents

6. Investigation of the magnetic properties in a family of six-coordinate mononuclear lanthanide complexes.

6.1 Introduction

The majority of lanthanide ions exhibit a strong spin-orbit coupling (SOC) due to the large unquenched angular momentum, and therefore they are ideal candidates for SMM (single-molecule magnet) or SIM (single-ion magnet) behaviour. The maximisation of the observed energy barrier is essential in order to achieve larger blocking temperatures; for lanthanides this could be realised by focusing on key features such as: (i) the stabilisation of degenerate $\pm m_J$ states possessing the highest value, (ii) large energy differences between the ground and excited m_J states and (iii) strong axiality of the m_J states in order to quench the quantum tunnelling of the magnetisation (QTM).[1, 2] As discussed in Chapter 1, J.D. Rinehart and J.R. Long developed a simple model for the 4*f* free ions to predict the ligand architectures with high symmetry that will exhibit strong magnetic anisotropy, based on J. Sievers publication '*Asphericity of 4f-Shells in Their Hund's Rule Ground States*'.[3, 4] Moreover, theoretical calculations by L. Ungur and L.F. Chibotaru predicted that for lower coordination numbers and in high symmetry geometries (such as linear), the highest m_J = 15/2 state can be stabilised for Dy^{III}, and the energy difference between the ground and excited states is predicted to be large (*e.g.* ~1800 cm^{-1} for linear geometry).[5] However, lanthanide ions usually adopt higher coordination numbers with lower symmetry, therefore synthetic chemists have focused in geometries that could provide a pseudo-linear environment, such as pseudo-O_h [6-8] or D_{5h}[9-15] containing two negatively-charged ligands in axial positions with short bond lengths, and much weaker ligand donors in equatorial positions.[16] In this way, a strong uniaxial symmetry is promoted, where the electron density of the ligand is concentrated on the L−Ln−L axis, resulting in a greater axiality of the $\pm m_J$ states, thus quenching the quantum tunnelling. In the case of D_{5h} symmetry more studies have been reported, whereas for pseudo-O_h symmetry only a few examples have been studied.

In this chapter we report the synthesis of a family of new mononuclear six-coordinate lanthanide complexes with the molecular formula $[Ln^{III}(Cy_3PO)_2Cl_3(EtOH)]\cdot yEtOH$ (Cy_3PO = tricyclohexylphosphine oxide) (Ln^{III} = Tb (**13**), Dy (**14**), Ho (**15**), Er (**16**) and Y (**17**), where y = 0.5 for **14** and y = 1 for **13**, **15**−**17**). The metal centres adopt a distorted octahedral geometry with the average axial bonds being shorter than the average equatorial ones. Moreover, we performed magnetic studies for the Tb^{III}, Dy^{III} and Ho^{III} analogues, revealing slow magnetic relaxation only for the Dy^{III} analogue.

6.2 Synthesis

$[Ln^{III}(Cy_3PO)_2Cl_3(EtOH)]\cdot EtOH$ (Ln^{III} = Tb (**13**), Ho (**15**) and Y (**17**)) : A hot solution of $LnCl_3\cdot 6H_2O$ (0.66 mmol, 246 mg (**Tb**), 250 mg (**Ho**) or 200 mg (**Y**)) in EtOH (8 ml) was added to a hot solution of Cy_3PO (0.96 mmol, 290 mg) in EtOH (6 ml) and left to stir at 60 ºC for 1 hour. The solution was filtered while still warm and left to slowly evaporate to give colourless cube-like crystals after 1 day. Elemental analysis calcd(%) for $TbP_2Cl_3C_{40}H_{80}O_5$ (**13**$\cdot H_2O$): C 49.62%, H 8.33%, N 0%, found: C 49.90%, H 8.36%, N 0%. Elemental analysis calcd(%) for $HoP_2Cl_3C_{40}H_{82}O_6$ (**15**$\cdot 2H_2O$): C: 48.42%, H: 8.33% and N: 0%, found: C: 48.01%, H: 8.70% and N: 0%. Elemental analysis calcd(%) for $YP_2Cl_3C_{40}H_{84}O_7$ (**17**$\cdot 3H_2O$): C: 51.42%, H: 9.06% and N: 0%, found: C: 50.93%, H: 8.68% and N: 0%.

$[Ln^{III}(Cy_3PO)_2Cl_3(EtOH)]\cdot yEtOH$ (Ln^{III} = Dy (**14**) and y = 0.5, Er (**16**) and y = 1) : In a hot solution of EtOH (15 ml) the metal salt $LnCl_3\cdot 6H_2O$ (0.35 mmol, 132 mg (**Dy**) or 134 mg (**Er**)) and the ligand Cy_3PO (0.65 mmol, 193 mg) were added simultaneously and the solution was stirred for 1 hour at 60 ºC. The solution was filtered while still warm and left to slowly evaporate to give colourless cube-like crystals after 1 day for complex **14**. For the Er compound layering the solution with liquid hexane gave light pink cube-like crystals after 1 week for complex **16**. Elemental analysis calcd(%) for $DyP_2Cl_3C_{39}H_{74.5}O_{3.5}$ (**14**): C: 50.35%, H: 8.07% and N: 0%, found: C: 50.31%, H: 8.30% and N: 0%. Elemental analysis calcd(%) for $ErP_2Cl_3C_{40}H_{85}O_{7.5}$ (**16**$\cdot 3.5H_2O$): C: 47.02%, H: 8.39% and N: 0%, found: C: 46.91, H: 8.25% and N: 0.04%.

6.3 Results and discussion

Lanthanide complexes incorporating phosphine oxide ligands have been studied extensively due to their technological applications in various fields such as reprocessing of nuclear fuels, photoluminescent devices and many more.[17] Depending on the bulkiness of the substituents on the phosphine oxide, a variety of coordination numbers and geometries have been observed.[17] The ligand Cy_3PO (Cy_3PO = tricyclohexylphosphine oxide) has been previously employed in the synthesis of such complexes, with the lanthanide ions adopting various coordination numbers and geometries.[18-21] Amongst them there are two seven-coordinate Dy^{III} complexes $[Dy(Cy_3PO)_2(H_2O)_5]Cl_3\cdot(Cy_3PO)\cdot H_2O\cdot EtOH$ (**I**) and $[Dy(Cy_3PO)_2(H_2O)_5]Br_3\cdot 2(Cy_3PO)\cdot 2H_2O\cdot 2EtOH$ (**II**) with the Dy^{III} ion adopting a pentagonal bipyramidal geometry; two Cy_3PO ligands are located in axial positions and five water molecules in the equatorial plane. Other analogues of complex **I** have also been reported with Er^{III} and Y^{III}.[13, 19] Complexes **I** and **II** were magnetically characterised

by Y. Chen *et al.* revealing interesting magnetic behaviour, with magnetic hysteresis up to 11 and 20 K (sweep rate 200 Oe/s) for **I** and **II**, repsectively.[13]

Our group has previously studied the influence of high pressure on the structural and magnetic properties of various complexes[22-25]; we are currently working towards the synthesis of lanthanide complexes adopting D_{5h} symmetry by incorporating phosphine oxide ligands[12] in order to study them under high pressure. Therefore we decided to study also the magnetic properties of the pentagonal bipyramidal complexes **I** and **II** under pressure (this work is still in progress). However, during our efforts to isolate complex **I** we also managed to isolate the new six-coordinate complex $[Dy^{III}(Cy_3PO)_2Cl_3(EtOH)]\cdot 0.5EtOH$ with the metal ion adopting a distorted octahedral geometry. Furthermore, we synthesised other analogues with the same molecular formula (with one molecule of EtOH co-crystallised) with Tb^{III}, Ho^{III}, Er^{III} and Y^{III} metal ions. As discussed before the magnetic characterisation of Ln complexes in octahedral or pseudo-octahedral geometry is scarce, hence the investigation of the magnetic properties of these complexes was of interest.

Crystal structure analysis

All complexes crystallise in the orthorhombic space group $P2_12_12_1$ and they are isomorphous (only the nature of the metal centre Ln^{III} changes) (Fig. 6.1 left) with half molecule of EtOH co-crystallised in **14** (Dy) and one EtOH molecule for **13** (Tb), **15** (Ho), **16** (Er) and **17** (Y). Selected crystallographic data for all complexes can be found in Tables 6.1 and 6.2. All Ln^{III} centres are six-coordinate adopting a distorted octahedral geometry with two Cy_3PO ligands being located in axial positions, while three Cl^- ions and one EtOH molecule are in equatorial positions. The axial M–O bonds are shorter (~2.2 Å) than the average M–Cl and M–O equatorial bonds (~2.5 Å), and continuous shape measures (CShMs)[26, 27] for each metal centre, gave the values of 1.13, 1.06, 1.10, 0.99 and 1.01 (where 0 corresponds to the ideal polyhedron) for Tb (**13**), Dy (**14**), Ho (**15**), Er (**16**) and Y (**17**), respectively (Table A6.1 in the appendix). The oxidation states of all metal ions were confirmed with BVS analysis.[28, 29] The asymmetric unit for all complexes contains a molecule of $[Ln^{III}(Cy_3PO)_2Cl_3(EtOH)]$ and a molecule of EtOH (half molecule for the Dy^{III} analogue) crystallised in the lattice and the crystal packing is the same for all structures (Fig. 6.1 right). The shortest intermolecular M···M distance is ~10 Å in all the analogues and hydrogen bonds are present between the coordinated and the co-crystallised EtOH molecules.

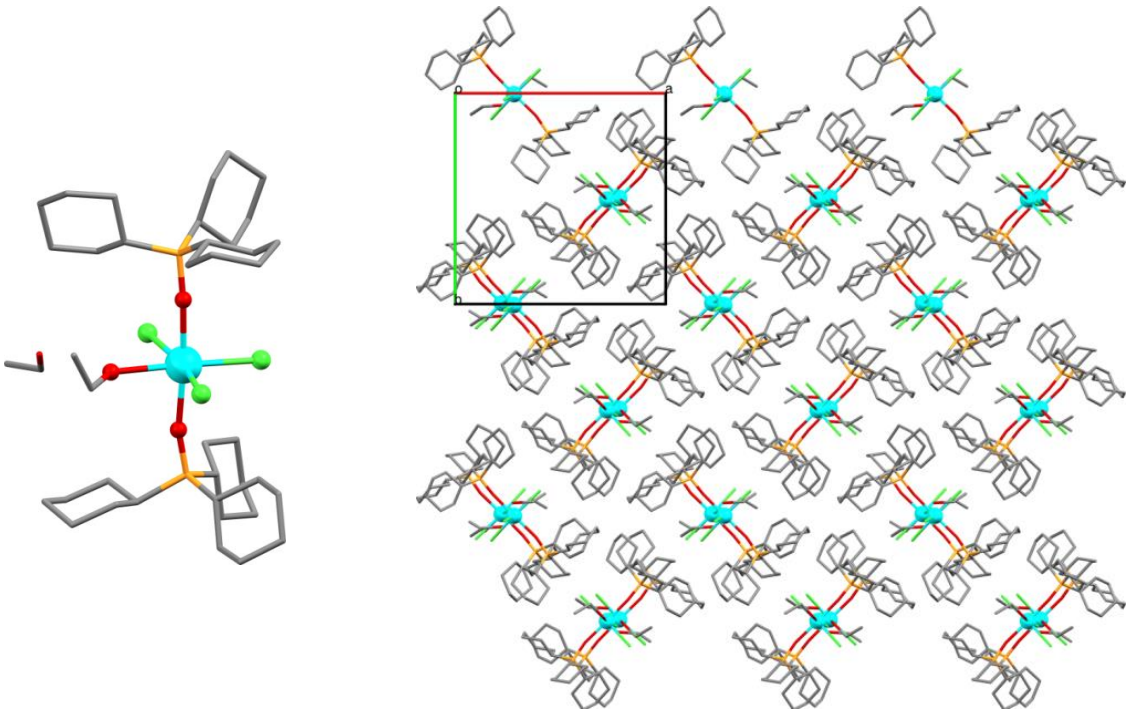

Figure 6.1 *Left)* The molecular structure of $[Ln^{III}(Cy_3PO)_2Cl_3(EtOH)]\cdot yEtOH$ (Ln^{III} = Tb (**13**), Dy (**14**), Ho (**15**), Er (**16**) and Y (**17**), where y = 0.5 for **14** and y = 1 for **13**, **15**−**17**). *Right)* The crystal packing of $[Ln^{III}(Cy_3PO)_2Cl_3(EtOH)]\cdot yEtOH$ along the crystallographic *c*-axis. Colour code: Ln^{III}: turquoise, O: red, P: orange, Cl: green, C: grey. Hydrogen atoms are omitted for clarity. (space group: $P2_12_12_1$)

Table 6.1. Data collection and crystallographic parameters for complexes **13**, **14** and **15**.

Chemical formula	$C_{38}H_{72}Cl_3O_3P_2Tb\cdot C_2H_6O$ (**13**)	$C_{38}H_{71.5}Cl_3O_3P_2Dy\cdot 0.5(C_2H_6O)$ (**14**)	$C_{38}H_{72}Cl_3O_3P_2Ho\cdot C_2H_6O$ (**15**)
M_r	950.23	930.27	956.24
Crystal system, space group	Orthorhombic, $P2_12_12_1$	Orthorhombic, $P2_12_12_1$	Orthorhombic, $P2_12_12_1$
Temperature (K)	150	298	150
***a*, *b*, *c* (Å)**	15.4302 (15), 15.4616 (14), 19.6814 (18)	15.5551 (5), 15.5558 (4), 19.8296 (5)	15.3880 (8), 15.4388 (9), 19.6742 (10)
***V* (Å^3)**	4695.5 (8)	4798.2 (2)	4674.0 (4)
Z	4	4	4
Radiation type	Mo *K*α	Mo *K*α	Mo *K*α
***μ* (mm^{-1})**	1.78	1.82	1.97
Crystal size (mm)	0.07 × 0.07 × 0.07	0.16 × 0.06 × 0.04	0.17 × 0.07 × 0.06
Diffractometer	Bruker D8 VENTURE	Bruker D8 VENTURE	Bruker D8 VENTURE
No. of measured, independent and observed [$I > 2\sigma(I)$] reflections	65162, 10740, 10303	42984, 10924, 10294	57826, 10698, 9937
R_{int}	0.057	0.028	0.059
$R[F^2 > 2\sigma(F^2)]$, $wR(F^2)$,	0.034, 0.080, 1.02	0.029, 0.080, 1.01	0.035, 0.085, 1.04

GOF on F^2			
No. of reflections	10740	10924	10698
No. of parameters	454	467	420
No. of restraints	11	51	40
Δ>max, Δ>min (e Å^{-3})	0.86, -0.63	0.58, -0.31	0.89, -0.68

Table 6.2. Data collection and crystallographic parameters for complexes **16** and **17**.

Chemical formula	$C_{38}H_{72}Cl_3O_3P_2Er \cdot C_2H_6O$ (**16**)	$C_{38}H_{72}Cl_3O_3P_2Y \cdot C_2H_6O$ (**17**)
***M*$_r$**	958.57	880.22
Crystal system, space group	Orthorhombic, $P2_12_12_1$	Orthorhombic, $P2_12_12_1$
Temperature (K)	293	298
***a*, *b*, *c* (Å)**	15.5406 (3), 15.5503 (3), 19.8173 (4)	15.5448 (18), 15.5639 (18), 19.812 (2)
***V* (Å^3)**	4789.07 (16)	4793.2 (9)
Z	4	4
Radiation type	Mo *K*α	Mo *K*α
***μ* (mm^{-1})**	2.02	1.49
Crystal size (mm)	0.13 × 0.09 × 0.02	0.17 × 0.09 × 0.06
Diffractometer	Bruker D8 VENTURE	Bruker *APEX*-II CCD
No. of measured, independent and observed [*I* > 2σ(*I*)] reflections	44266, 10876, 9603	34690, 10823, 8266
***R*$_{int}$**	0.030	0.054
R*[F^2 > 2σ(F^2)], *wR*(F^2), *GOF on F^2	0.029, 0.069, 1.03	0.050, 0.136, 1.04
No. of reflections	10876	10823
No. of parameters	450	448
No. of restraints	46	30
Δ>max, Δ>min (e Å^{-3})	0.69, -0.66	0.34, -0.36

Powder X-ray diffraction (PXRD) analysis

In order to examine if the samples are phase pure, PXRD measurements were carried out for complexes **13** – **17**. Figure 6.2 shows the calculated and experimental PXRD patterns of each complex. It is clear that only the experimental PXRD pattern of complex **14** (Dy) is consistent with the calculated one, whereas for complexes **13** (Tb), **15** (Ho), **16** (Er) and **17** (Y) there is a significant deviation from the calculated ones.

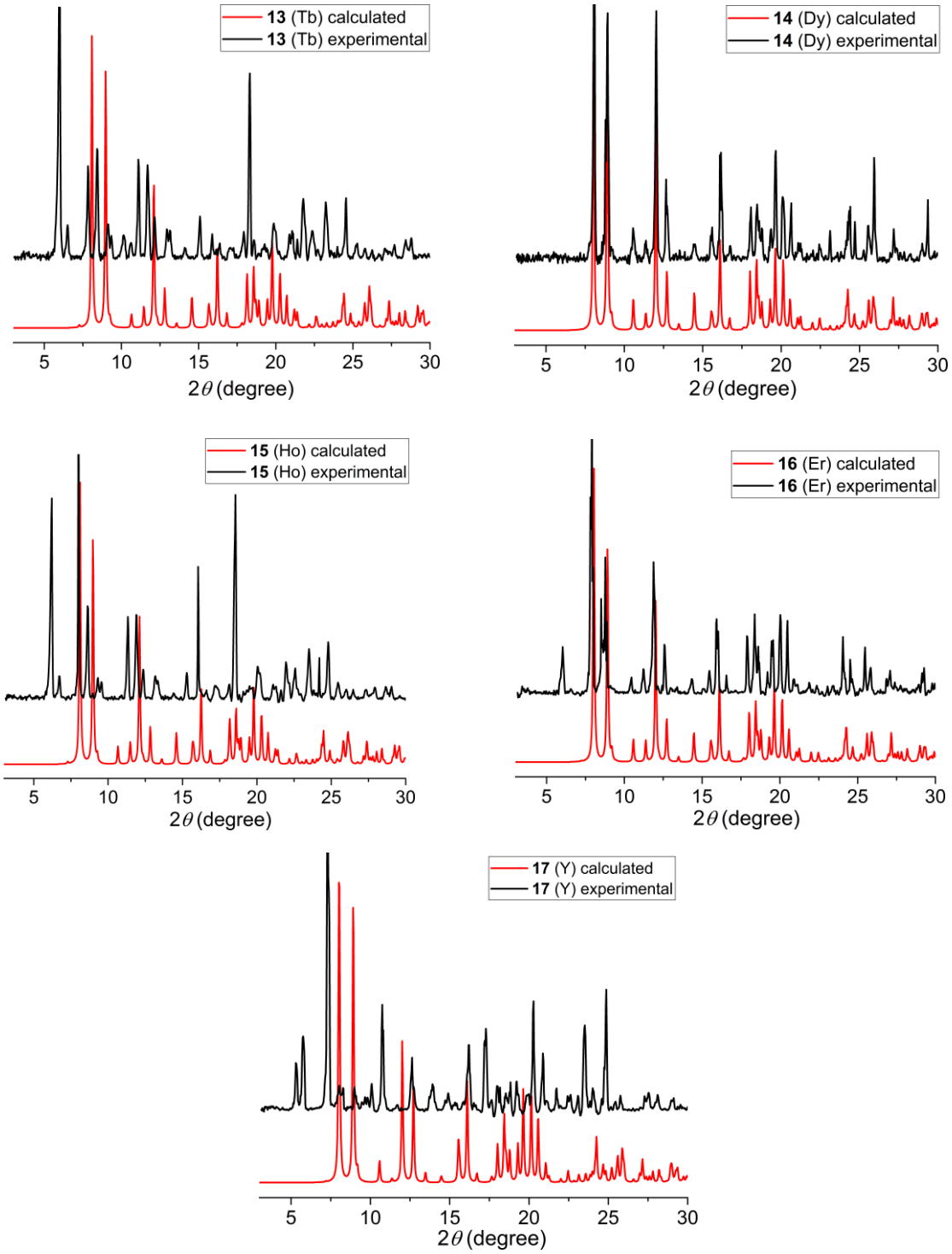

Figure 6.2 The calculated (red) and experimental (black) PXRD patterns (3−30°) of complexes **13** – **17.** The PXRD measurements were performed at room temperature. The single-crystal data for complexes **13**, **14**, **15**, **16** and **17** were collected at 150, 298, 150, 293 and 298 K, respectively.

As discussed previously the ligand Cy_3PO can form seven-coordinate mononuclear complexes with Dy^{III}, Er^{III} and Y^{III} ($[Ln^{III}(Cy_3PO)_2(H_2O)_5]Cl_3\cdot(Cy_3PO)\cdot H_2O\cdot EtOH$, Ln= Dy (**I**), Er (**III**) and Y (**IV**))[13, 19], where the Ln centres adopt a pentagonal bypiramidal geometry (PBP), with five water molecules in the equatorial plane and two Cy_3PO ligands in axial positions (Fig. 6.3 left). Hence, this prompted us to compare the calculated PXRD patterns of the seven-coordinate complexes (Fig. 6.4) with the experimental PXRD patterns of **13** (Tb), **15** (Ho), **16** (Er) and **17** (Y), in order to examine if the seven-coordinate complexes are isolated instead of the six-coordinate ones.

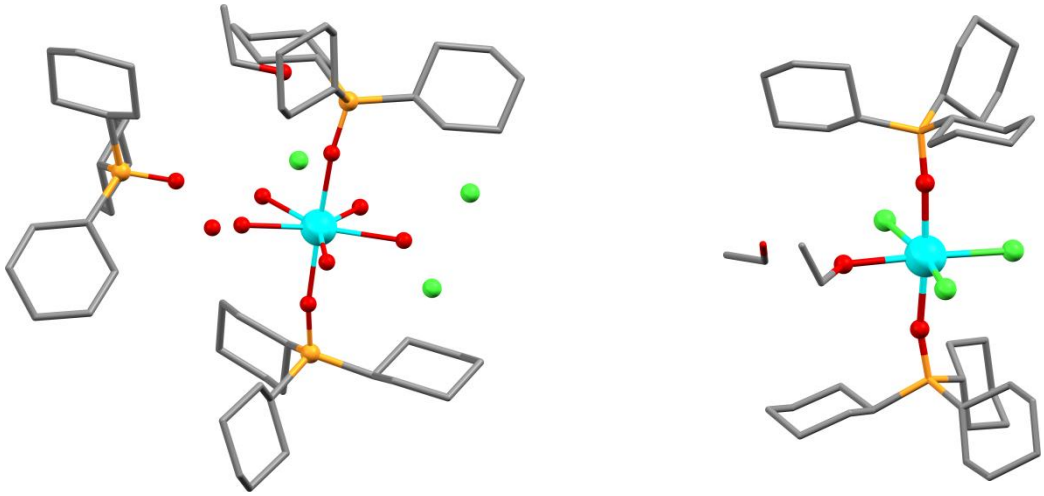

Figure 6.3 *Left)* The molecular structure of the seven-coordinate (PBP) $[Ln^{III}(Cy_3PO)_2(H_2O)_5]Cl_3\cdot(Cy_3PO)\cdot H_2O\cdot EtOH$. *Right)* The molecular structure of the six-coordinate (Oh) $[Ln^{III}(Cy_3PO)_2Cl_3(EtOH)]\cdot EtOH$. Colour code: Ln^{III}: turquoise, O: red, P: orange, Cl: green, C: grey. Hydrogen atoms are omitted for clarity.

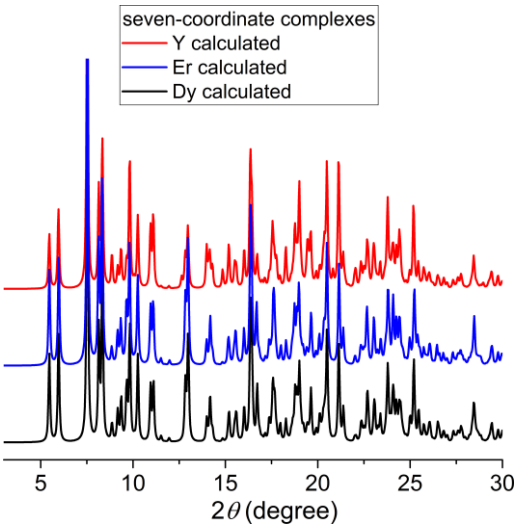

Figure 6.4 The calculated PXRD patterns (3−30°) of the seven-coordinate complexes $[Ln^{III}(Cy_3PO)_2(H_2O)_5]Cl_3\cdot(Cy_3PO)\cdot H_2O\cdot EtOH$, Ln= Dy (**I**), Er (**III**) and Y (**IV**). [13, 19]

Since the calculated PXRD patterns of the seven-coordinate PBP complexes are similar, only the pattern of the Er analogue will be used for comparison. Firstly, we examined the experimental patterns of **16** (Er) and **17** (Y) with the calculated pattern of the seven-coordinate Er complex (Fig. 6.5). There is a deviation among the calculated and the experimental patterns, however the presence of peaks at lower angles (~5.8º) suggests that possibly a mixture of the seven- and six-coordinate complexes is present in the samples of **16** (Er) and **17** (Y).

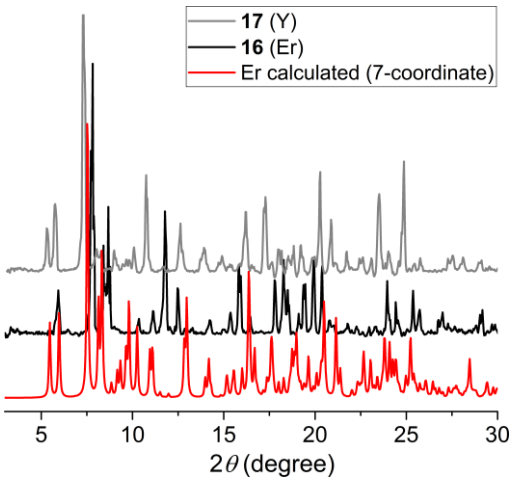

Figure 6.5 The experimental PXRD patterns (3−30°) of complexes **16** (Er) and **17** (Y) (black and grey lines) and the calculated PXRD pattern of the seven-coordinate Er complex (red line)**.** The PXRD measurements were performed at room temperature and the calculated pattern is generated from the single-crystal data collected at 120 K.[19]

Elemental analysis for **16** (Er) and **17** (Y) revealed the presence of H_2O molecules in the samples (see Section 6.2), a further indication of the presence of the seven-coordinate PBP complexes in the samples of **16** (Er) and **17** (Y). There are no analogues of Tb^{III} or Ho^{III} for the seven-coordinate complexes, therefore we decided to compare the calculated PXRD pattern of the seven-coordinate Er complex with the experimental ones for complexes **13** (Tb) and **15** (Ho) (Fig. 6.6). Again, the presence of peaks at lower angles could be due to a mixture of six- and seven-coordinate complexes in the bulk samples of **13** (Tb) and **15** (Ho), however no firm conclusion can be reached for these complexes. In addition, elemental analysis suggests the presence of molecules of water in the **13** (Tb) and **15** (Ho) samples (see Section 6.2).

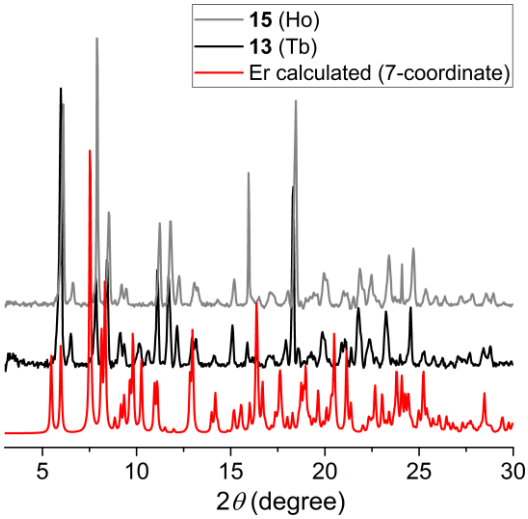

Figure 6.6 The experimental PXRD patterns (3−30°) of complexes **13** (Tb) and **15** (Ho) (black and grey lines) and the calculated PXRD pattern of the seven-coordinate Er complex (red line)**.** The PXRD measurements were performed at room temperature and the calculated pattern is generated from the single-crystal data collected at 120 K.[19]

Instead of performing the collection and filtration of the samples under normal atmosphere (air), we decided to use inert atmosphere (nitrogen) for **13** (Tb), **15** (Ho), **16** (Er) and **17** (Y) in order to avoid the presence of H_2O molecules during the drying process of the samples. PXRD measurements for **13** (Tb), **15** (Ho), **16** (Er) and **17** (Y) were also carried out under inert atmosphere (Fig. 6.7 and 6.8). We can observe that under these conditions the match of the calculated and experimental PXRD patterns for the six-coordinate complexes is satisfactory. Hence, we can conclude that the bulk samples no longer contain a mixture of six- and seven-coordinate complexes, and contain only the six-coordinate complexes **13** (Tb), **15** (Ho), **16** (Er) and **17** (Y).

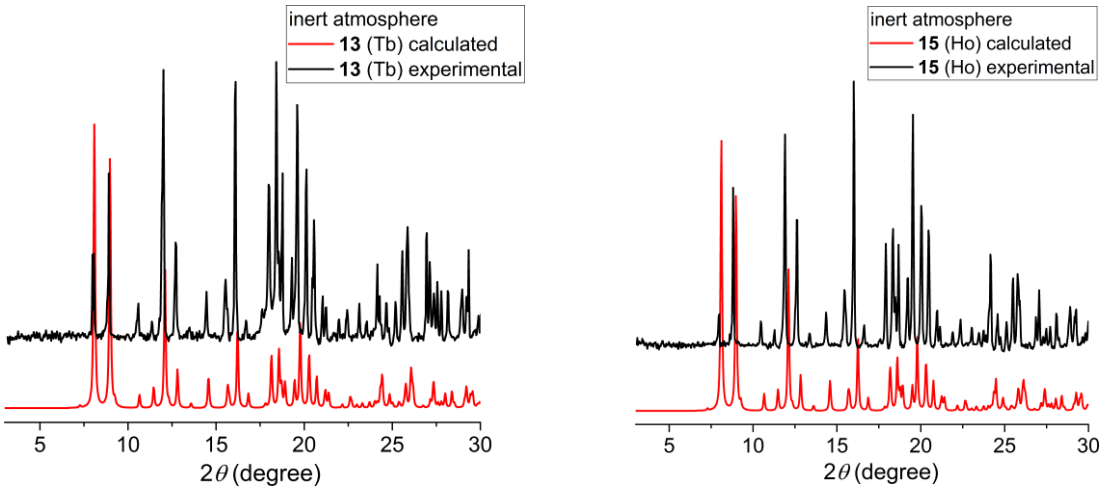

Figure 6.7 The calculated (red) and experimental (black) PXRD patterns (3−30°) of complexes **13** (Tb) and **15** (Ho). The experimental PXRD data were collected under inert atmosphere and at room temperature. The single-crystal data for complexes **13** and **15** were collected at 150 K.

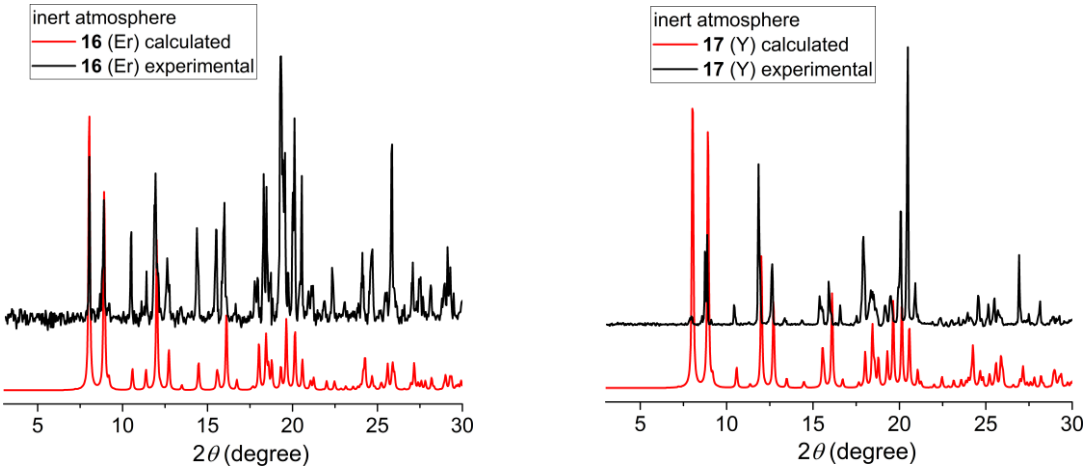

Figure 6.8 The calculated (red) and experimental (black) PXRD patterns (3−30°) of complexes **16** (Er) and **17** (Y). The experimental PXRD data were collected under inert atmosphere and at room temperature. The single-crystal data for complexes **16** and **17** were collected at 293 and 298 K, respectively.

Magnetic characterisation

All the magnetic measurements performed for complexes **13** (Tb) and **15** (Ho) were carried out under inert atmosphere and the experimental apparatus used is described in Chapter 2.

Variable temperature dc susceptibility measurements were carried out for complexes **13** (Tb), **14** (Dy) and **15** (Ho) in a field of 1000 Oe in the 290 – 2 K temperature range (Fig. 6.9). Due to time limitation no magnetic measurements were performed for **16** (Er), however this is in our future work for this project. At room temperature the $\chi_M T$ values are 11.40, 13.76 and 13.94 $cm^3\ mol^{-1}\ K$ for **13** (Tb), **14** (Dy) and **15** (Ho) respectively, consistent with the theoretical ones 11.82 (Tb^{III}, $^7F_6$ and g = 3/2), 14.17 (Dy^{III}, $^6H_{15/2}$ and g = 4/3) and 14.07 (Ho^{III}, $^5I_8$ g = 5/4) $cm^3\ mol^{-1}\ K$. Upon cooling, $\chi_M T$ for **14** (Dy) and **15** (Ho) decreases slowly until ~14 K and then decreases rapidly until 2 K to reach 8.88 and 9.75 $cm^3\ mol^{-1}\ K$ respectively; whereas for **13** (Tb) $\chi_M T$ decreases slowly until ~40 K and then decreases rapidly until 2 K to reach 5.75 $cm^3\ mol^{-1}\ K$. This decrease could be attributed to the thermal depopulation of excited m_J sublevels of the Ln^{III} ion and the presence of magnetic anisotropy. Additionally, at temperatures of 2, 4 and 6 K the magnetisation versus field plots for **13** (Tb), **14** (Dy) and **15** (Ho) (Fig. 6.10) do not reach saturation at the highest available field of 5 T, a further indication of magnetic anisotropy. This behaviour is consistent with other examples of six-coordinate mononuclear Ln^{III} complexes.[30-33]

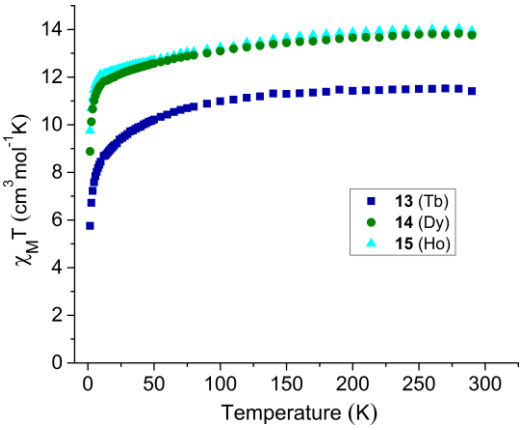

Figure 6.9 χ_MT *versus* Temperature data for complexes **13** (blue squares), **14** (green circles) and **15** (light blue tringles) in a field of 1000 Oe from 290 – 2 K.

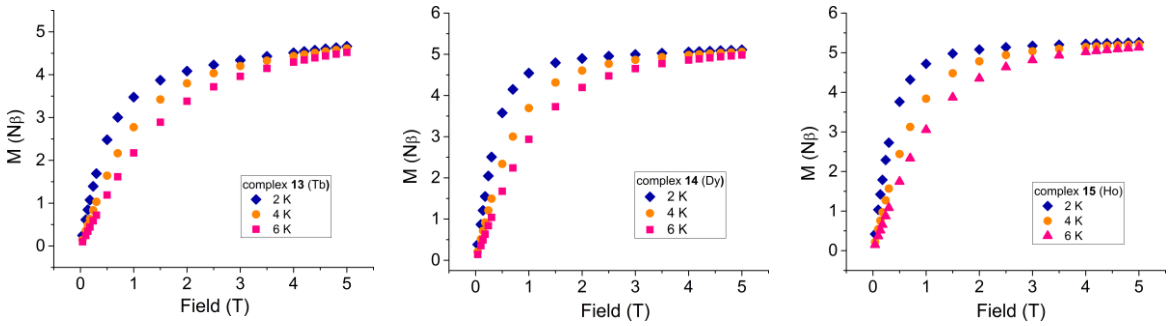

Figure 6.10 Magnetisation *versus* Field plots for **13** (Tb), **14** (Dy) and **15** (Ho) from left to right, at temperatures 2, 4 and 6 K.

The dynamic magnetic properties of complexes **13** (Tb), **14** (Dy) and **15** (Ho) were also studied. In zero applied dc field **13** (Tb) does not display any out-of-phase signal, whereas **14** (Dy) and **15** (Ho) display only the onset of a weak χ'' signal, due to efficient zero-field quantum tunnelling (Fig. A6.1 in the appendix). By using an applied dc field of 2000 Oe to suppress tunnelling, no significant change of the χ'' signal is observed for complexes **13** (Tb) and **15** (Ho) (Fig. A6.2 in the appendix). This could be attributed to fast tunnelling relaxation in the ground $\pm m_J$ state, a usual phenomenon for non-Kramers ions due to the mixing of the m_J states caused by perturbations, such as transverse crystal-field anisotropy, intermolecular magnetic interactions, and interactions with nuclear magnetic spins.[34-36] However, for complex **14** (Dy) (Fig. A6.2 in the appendix) we observe that for the lowest frequency (1 Hz) at ~4 K the χ'' signal is stronger than for the rest of the frequencies, but when we move to higher temperatures (~10 K) the signal drops for the 1 Hz frequency and becomes slightly stronger for the other frequencies. This observation

prompted us to examine the temperature dependence of the ac signals at higher temperatures than 10 K, in the frequency range 1 – 300 Hz, in the absence and presence of a dc field (Fig. 6.11) in order to extract more information. Again in the absence of a dc field **14** (Dy) shows only the onset of the out-of-phase signals, however with the application of a dc field of 2000 Oe fully formed χ'' peaks are observed until ~10 K.

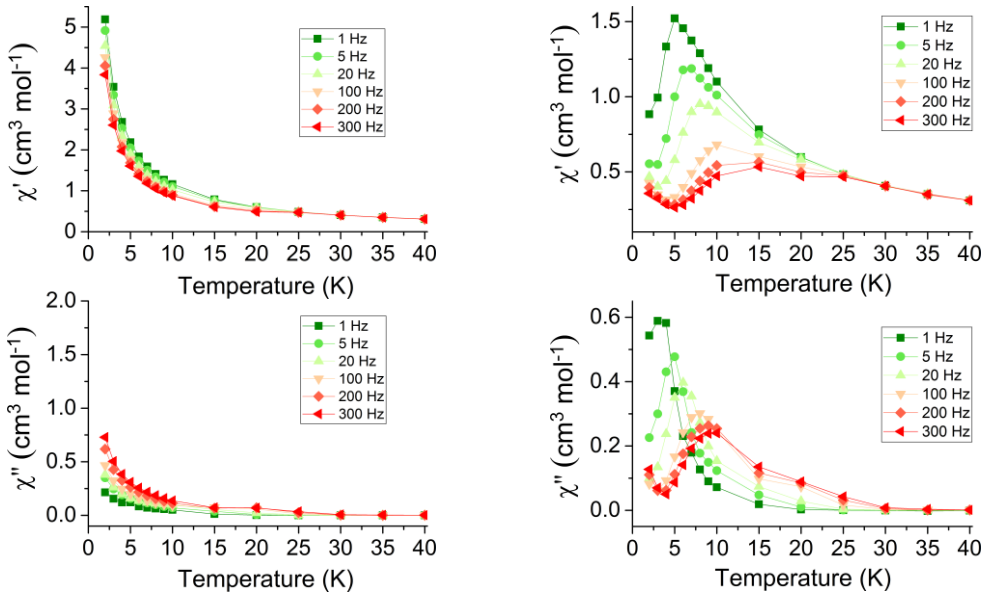

Figure 6.11 Temperature dependence of the in-phase (*top*) and the out-of-phase (*bottom*) ac susceptibility signals in 0 (*left*) and 2000 (*right*) Oe dc field, in the frequency range 1 – 1488 Hz, for complex **14** (Dy). The solid lines are a guide to the eye.

Variable dc fields (200 − 4000 Oe) were applied to **14** (Dy) at 2, 5 and 10 K (Fig. 6.12) in order to obtain the optimum dc field (field sweep ac susceptibility experiments), at which the characteristic relaxation time of the magnetisation (τ) possesses the largest value. Although no maxima are present at 2 K, it is clear that the field dependence of the out-of-phase peaks is more pronounced at 2 K, and becomes less important at 5 and 10 K. We can observe that at temperatures 5 and 10 K (thermally activated regime) the peaks of the χ'' signal do not shift significantly with the change of the applied dc field, except at the lowest and highest fields (200 and 4000 Oe). However, at 2 K the shift of the χ'' signal is greater, which suggests that the field dependent relaxation processes, *i.e.* quantum tunnelling and the direct process, are dominant.

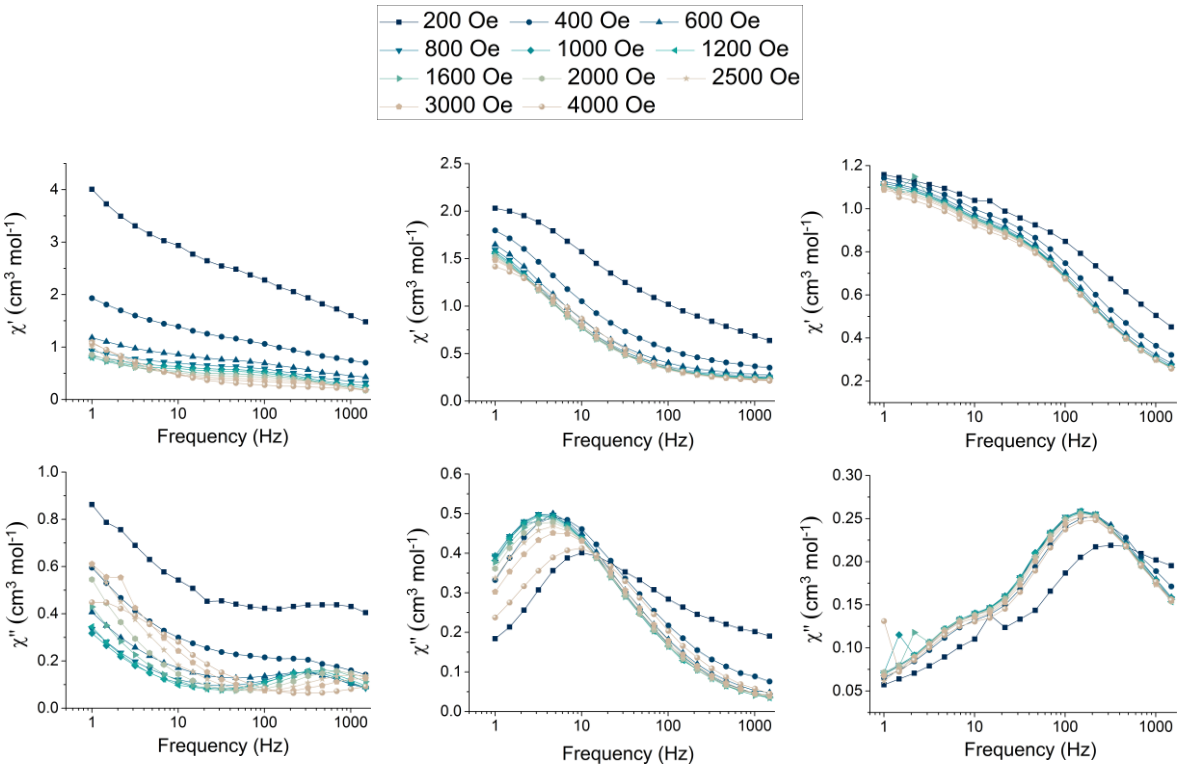

Figure 6.12 Frequency dependent in-phase (*top*) and out-of-phase (*bottom*) ac susceptibility signals for complex **14** (Dy) under different applied dc fields at 2 K (*left*), 5 K (*middle*) and 10 K (*right*). The solid lines are a guide to the eye.

Taking into consideration the dependence of the relaxation times τ (which were calculated with the programme CC-FIT[37, 38]) with the field at temperatures 5 and 10 K, the optimum field was obtained at 1000 Oe (Fig. A6.3 in the appendix). The frequency dependence of the in-phase and out-of-phase magnetic susceptibility of **14** (Dy) was measured under the optimum dc field, in the 2 − 30 K temperature range (Fig. 6.13). Attempts to fit the Cole-Cole plot (out-of-phase versus in-phase signals) for the entire temperature range 2 − 30 K were not successful, due to the presence of multiple relaxation times and processes (Fig. A6.4 in the appendix). Hence, the fit was performed for the temperature range of 3.5 – 8 K with the programme CC-FIT[37, 38] (Fig. 6.14 left) and the τ and α parameters were extracted for each temperature (Table A6.2 in the appendix). The values for parameter α were found to be ~0.4, indicative of a larger distribution of relaxation times. The τ values were used to construct an Arrhenius plot (Fig. 6.14 right) for the temperatures 3.5 – 8 K, from which the relaxation parameters of $\Delta E/k_B$ (energy barrier) and τ_0 (pre-exponential factor) were extracted from equation 6.1:

$$\ln(\tau) = \ln(\tau_0) + \frac{\Delta E}{k_B T} \qquad (6.1)$$

Fitting within the linear region (Orbach relaxation mechanism) the values $\Delta E/k_B$ = 32.2 (±0.4) K and τ_0 = 6.2 x 10^{-5} s were extracted. In Table 6.3 (CSD search, database of 2018) previously reported mononuclear six-coordinate Dy^{III} complexes can be found (adopting either trigonal prismatic or pseudo-octahedral geometry). It is clear that the largest energy barriers are observed in organometallic complexes and complex $[(L^{CO})Dy(N^*)_2]$ (non-organometallic) which adopts a distorted trigonal prismatic geometry. The energy barrier for complex **14** (Dy) is amongst the highest for non-organometallic complexes adopting distorted octahedral geometry.

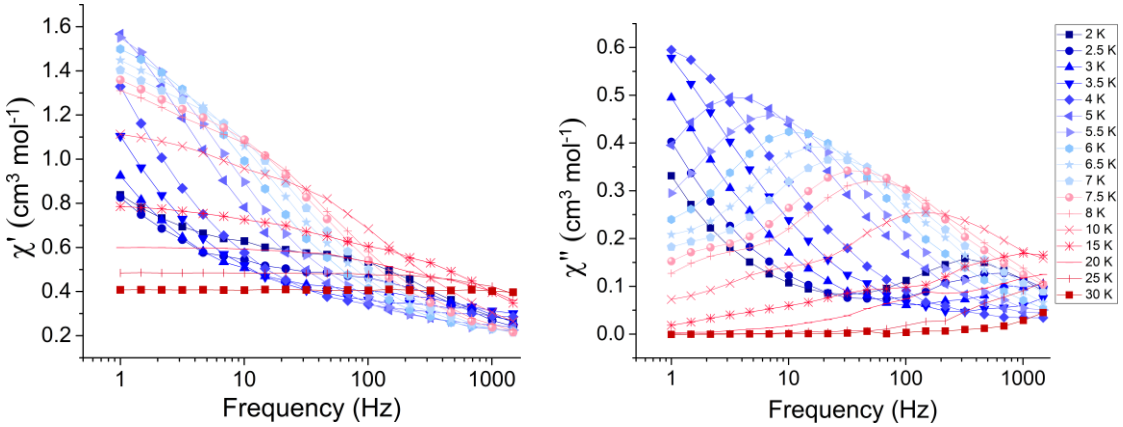

Figure 6.13 Frequency dependent in-phase (*left*) and out-of-phase (*right*) susceptibility signals for complex **14** (Dy) in 1000 Oe dc applied magnetic field. The solid lines are a guide to the eye.

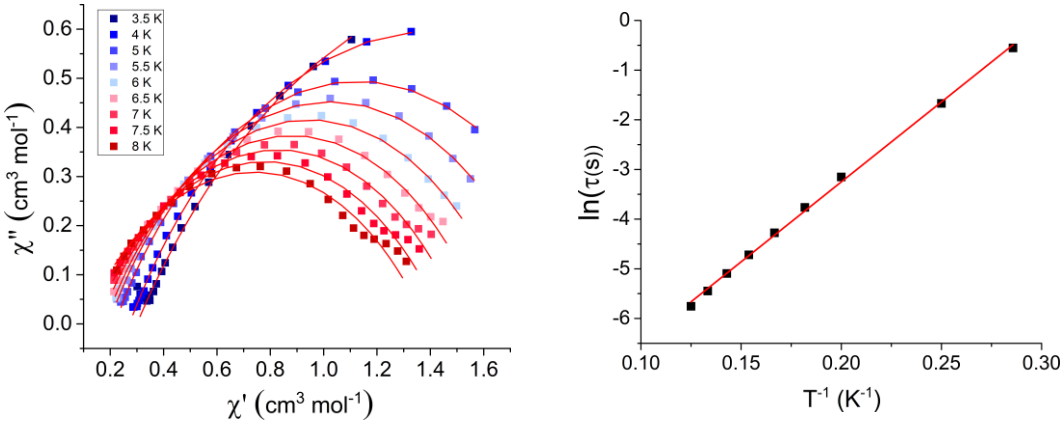

Figure 6.14 *Left)* Cole–Cole plot of the ac magnetic susceptibility of **14** (Dy) at 1000 Oe for the 3.5 – 8 K temperature range. The solid lines correspond to the fit (CC-FIT).[37, 38] *Right)* The plot of ln(τ) vs T^{-1} **14** (Dy) in the 3.5 – 8 K temperature range. The solid red line represents the best fit to the Arrhenius law (eqn 6.1).

Table 6.3 Magnetic data of other reported mononuclear six-coordinate Dy^{III} complexes (U_{eff} values were obtained from fitting of the temperature-dependent ac susceptibility data).

Complex	U_{eff} (K)	τ_0 (s)	dc field	Geometry[§]	Ref.
[a] $[C_{12}mim]_3[DyBr_6]$	-	-	-	O_h	39
$Dy[H(\mu\text{-}H)BPz^{Me2}{}_2]_3$ (diluted Dy 1: Y 130)	24.5	$4x10^{-7}$	no	TP	40
[b,c] $[Zn_2DyL^1_2]NO_3{\cdot}H_2O$	-	-	yes	O_h	8
[d] $Dy(Bp^{Me})_3$	-	-	yes	TP	31
* $Dy(Bc^{Me})_3$	47.2	$6x10^{-9}$	yes	TP	31
* $Dy(Bc^{Me})_3$ (12 mol % dilution with Y)	48.3	$4.2x10^{-9}$	yes	TP	31
$[DyIr_6(ppy)_{12}(bpp)_2(bpppH)_4](CF_3SO_3){\cdot}8H_2O$	42.9	$3.8x10^{-8}$	yes	O_h	6
$[Dy(AlMe_4)_3]$	-	-	yes	O_h	41
$[Dy(AlMe_4)_3]$ (diluted Dy 1: Y 20)	14.4	$2.9x10^{-7}$	yes	O_h	41
[e,#] $[Dy(H_3L^2)_2]Cl_3{\cdot}6H_2O$	-	-	-	O_h	32
[f,#] $[DyL^3Cl_2(THF)_2]$	-	-	-	O_h	42
[d] $[Dy\{(S)\text{-}NEBA\}_3]$	-	-	yes	O_h	43
[b] $[Dy(L_{OEt})_2](PF_6)$	-	-	yes	O_h	44
[b] $[Dy(L_{OEt})_2](PF_6)$ (diluted Dy 1: Y 20)	-	-	yes	O_h	44
$[Dy(L_{OiPr})_2](PF_6)$	13	$6.4x10^{-7}$	yes	O_h	44
$*[Li(THF)_4][DyFc_3(THF)_2Li_2]$	159	$6x10^{-8}$	no	TP	45
$*[Li(THF)_4][DyFc_3(THF)_2Li_2]$ (diluted Dy 1: Y 11.7)	155	$3.3x10^{-8}$	no	TP	45
[g] $[(L^{CO})Dy(N^*)_2]$	190	$1.7x10^{-7}$	no	TP	7
[h] $Dy[Zn(L^4)Cl]_3{\cdot}xMeOH{\cdot}yH_2O$	7	-	yes	O_h	46
[d] $[Dy(Tpm)Cl_3]{\cdot}2MeCN$	-	-	yes	O_h	33
[i,*] $[Dy(BIPM^{TMS})_2][K(18C6)(THF)_2]$	721 / 813	$1.1x10^{-12}$ / $5.6x10^{-13}$	no	O_h	47

[a] No dynamic studies have been reported for this complex.
[b] Other processes are involved instead of the Orbach process.
[c] L^1 = 2,2',2''-(((nitrilo-tris(ethane-2,1-diyl))tris(azanediyl))tris(methylene))tris-(4-bromo-phenol)
[d] Only the onset of the out-of-phase signals are observed.
[e] H_3L^2 = tris((2-hydroxy-5-n-butyl benzoate)aminoethyl)-amine
[f] L^3 = 2,4,6-$Me_3C_6H_2$-NC(Me)CHC(Me)N-2,4,6-$Me_3C_6H_2$
[g] $L^{CO}H$ = {*N*-[(2-MeO)-C_6H_5]}N=C(Me)CH=C(Me)N(H){*N'*-[(2-MeO)C_6H_5]}, HN* = $HN(SiMe_3)_2$
[h] H_2L^4 = 2,2'-[1,2-ethanediylbis[(methylimino)methylene]]bis[4,5-dimethylphenol]
[i] This complex exhibits two thermally activated energy barriers.
* Organometallic complex.
[#] No magnetic relaxation was observed.
[§] Deviations from the ideal geometry may be present but they are not mentioned here.
TP = trigonal prism, deviations from the ideal geometry may be present
Oh = octahedron, deviations from the ideal geometry may be present

Unfortunately, during our work on this project a paper including the Dy analogue was published by Y. Wang *et al.*[48] This paper is focused on the magnetodielectric properties of the compound and also the dynamic magnetic properties were studied (Fig. 6.15). Comparing our experimental results with the published ones we observed some differences. Instead of the optimum 1000 Oe dc field that we obtained from the field sweep experiments, Y. Wang *et al.* use a dc field of 1200 Oe. Moreover, the plot of the out-of-phase versus in-phase signals that we obtained indicates multiple relaxation times and processes (Fig. A6.4 in the appendix), whereas in the published results it is clear that a narrow distribution of relaxation times is present ($\alpha \approx 0.1$) for the range of 8 – 24 K. In order to compare the reported ac susceptibility signals with our results we plotted the χ' and χ'' signals versus temperature where we noticed that the signals at higher frequencies were 'noisy' (Fig. A6.5 in the appendix). The cause of these 'noisy' data could be due to an experimental error during the measurement, therefore we decided to perform again the frequency dependent ac susceptibility experiments for the same sample. However, we observed completely different magnetic behaviour than our previous results and this could be due to the damage of the sample over time (the sample was prepared more than four months prior to the re-measurement). The publication of the Dy analogue and the expensive nature of the magnetic measurements prevented us from performing any further experiments/measurements for this complex.

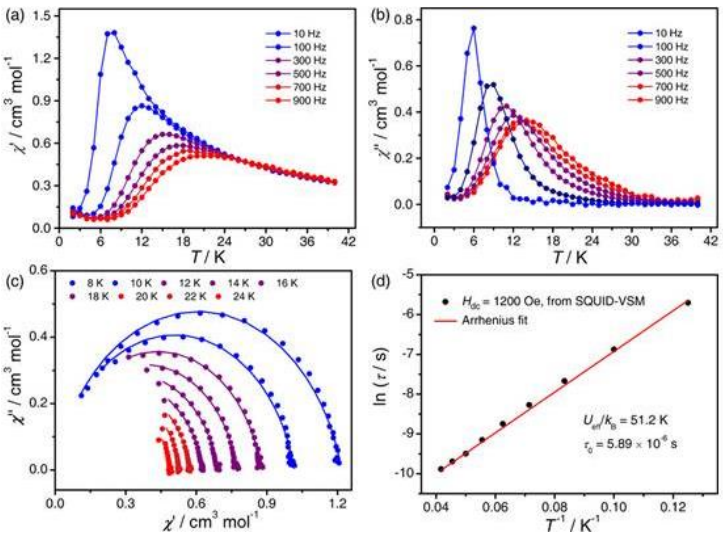

Figure 6.15 *a and b)* In-phase (χ') and out-of-phase (χ'') ac magnetic susceptibility signals versus temperature in a 1200 Oe dc field. The solid lines are a guide to the eye. *c)* Cole–Cole plots in a 1200 Oe dc field. The solid lines represent a best fit to the generalized Debye model. *d)* temperature dependence of the relaxation time (τ). The solid red line corresponds to the best fit to the Arrhenius law. Reprinted with permission from Y.-X. Wang, Y. Ma, Y. Chai, W. Shi, Y. Sun and P. Cheng, *J Am Chem Soc*, 2018, **140**, 7795-7798. Copyright 2019 American Chemical Society.[48]

6.4 Conclusions

The synthesis of five new mononuclear six-coordinate complexes with molecular formula $[Ln^{III}(Cy_3PO)_2Cl_3(EtOH)]\cdot yEtOH$ (Cy_3PO = tricyclohexylphosphine oxide) (Ln^{III} = Tb (**13**), Dy (**14**), Ho (**15**), Er (**16**) and Y (**17**) and y= 0.5 for Dy and y = 1 for the rest) is presented here. All metal centres adopt a distorted octahedral geometry, while powder X-ray diffraction analysis revealed that all complexes except the Dy analogue are air-sensitive. When the samples are collected and filtered under normal atmosphere (air), then a mixture of the six-coordinate pseudo-octahedral and the seven-coordinate pentagonal bipyramidal complexes is obtained. However, when the collection and filtration of the samples is performed under inert atmosphere (nitrogen), then pure samples of the six-coordinate **13** (Tb), **15** (Ho), **16** (Er) and **17** (Y) complexes are obtained. We investigated the static and dynamic magnetic properties of complexes **13** (Tb), **14** (Dy) and **15** (Ho), and field induced slow magnetic relaxation was observed for **14** (Dy). Fit of the ln(τ) versus T data with the Arrhenius law (Orbach relaxation process) for the 3.5 – 8 K temperature range afforded the values of $\Delta E/k_B$ = 32.2 (±0.4) K (energy barrier) and τ_0 = 6.2 x 10^{-5} s (pre-exponential factor). Complex **14** (Dy) exhibits a high energy barrier in comparison with other reported non-organometallic six-coordinate complexes in pseudo-octahedral geometry.

6.5 References

1. S. G. McAdams, A.-M. Ariciu, A. K. Kostopoulos, J. P. S. Walsh and F. Tuna, *Coordination Chemistry Reviews*, 2017, **346**, 216-239.
2. A. Dey, P. Kalita and V. Chandrasekhar, *ACS Omega*, 2018, 9462-9475.
3. J. Sievers, *Zeitschrift für Physik B Condensed Matter*, 1982, **45**, 289-296.
4. J. D. Rinehart and J. R. Long, *Chemical Science*, 2011, **2**, 2078-2085.
5. L. Ungur and L. F. Chibotaru, *Inorganic Chemistry*, 2016, **55**, 10043-10056.
6. D. Zeng, M. Ren, S.-S. Bao, L. Li and L.-M. Zheng, *Chemical Communications*, 2014, **50**, 8356-8359.
7. S.-S. Liu, Y.-S. Meng, Y.-Q. Zhang, Z.-S. Meng, K. Lang, Z.-L. Zhu, C.-F. Shang, B.-W. Wang and S. Gao, *Inorganic Chemistry*, 2017, **56**, 7320-7323.
8. J.-L. Liu, Y.-C. Chen, Y.-Z. Zheng, W.-Q. Lin, L. Ungur, W. Wernsdorfer, L. F. Chibotaru and M.-L. Tong, *Chemical Science*, 2013, **4**, 3310-3316.
9. Y.-S. Ding, N. F. Chilton, R. E. P. Winpenny and Y.-Z. Zheng, *Angewandte Chemie International Edition*, 2016, **55**, 16071-16074.
10. S. K. Gupta, T. Rajeshkumar, G. Rajaraman and R. Murugavel, *Chemical Science*, 2016, **7**, 5181-5191.
11. J. Liu, Y.-C. Chen, J.-L. Liu, V. Vieru, L. Ungur, J.-H. Jia, L. F. Chibotaru, Y. Lan, W. Wernsdorfer, S. Gao, X.-M. Chen and M.-L. Tong, *Journal of the American Chemical Society*, 2016, **138**, 5441-5450.
12. A. B. Canaj, M. K. Singh, C. Wilson, G. Rajaraman and M. Murrie, *Chemical Communications*, 2018, **54**, 8273-8276.
13. Y.-C. Chen, J.-L. Liu, L. Ungur, J. Liu, Q.-W. Li, L.-F. Wang, Z.-P. Ni, L. F. Chibotaru, X.-M. Chen and M.-L. Tong, *Journal of the American Chemical Society*, 2016, **138**, 2829-2837.
14. Y.-C. Chen, J.-L. Liu, Y. Lan, Z.-Q. Zhong, A. Mansikkamäki, L. Ungur, Q.-W. Li, J.-H. Jia, L. F. Chibotaru, J.-B. Han, W. Wernsdorfer, X.-M. Chen and M.-L. Tong, *Chemistry – A European Journal*, 2017, **23**, 5708-5715.
15. Y.-C. Chen, J.-L. Liu, W. Wernsdorfer, D. Liu, L. F. Chibotaru, X.-M. Chen and M.-L. Tong, *Angewandte Chemie International Edition*, 2017, **56**, 4996-5000.
16. A. Dey, P. Kalita and V. Chandrasekhar, *ACS Omega*, 2018, **3**, 9462-9475.
17. A. W. G. Platt, *Coordination Chemistry Reviews*, 2017, **340**, 62-78.
18. A. P. Hunter, A. M. J. Lees and A. W. G. Platt, *Polyhedron*, 2007, **26**, 4865-4876.
19. A. M. J. Lees and A. W. G. Platt, *Polyhedron*, 2014, **67**, 368-372.
20. A. Bowden, A. M. J. Lees and A. W. G. Platt, *Polyhedron*, 2015, **91**, 110-119.
21. S. J. Coles, M. B. Pitak and A. W. G. Platt, *European Journal of Inorganic Chemistry*, 2017, **2017**, 1464-1471.
22. A. Prescimone, C. J. Milios, S. Moggach, J. E. Warren, A. R. Lennie, J. Sanchez-Benitez, K. Kamenev, R. Bircher, M. Murrie, S. Parsons and E. K. Brechin, *Angewandte Chemie International Edition*, 2008, **47**, 2828-2831.
23. P. Parois, S. A. Moggach, J. Sanchez-Benitez, K. V. Kamenev, A. R. Lennie, J. E. Warren, E. K. Brechin, S. Parsons and M. Murrie, *Chemical Communications*, 2010, **46**, 1881-1883.
24. G. A. Craig, C. H. Woodall, S. C. McKellar, M. R. Probert, K. V. Kamenev, S. A. Moggach, E. K. Brechin, S. Parsons and M. Murrie, *Dalton Transactions*, 2015, **44**, 18324-18328.
25. G. A. Craig, A. Sarkar, C. H. Woodall, M. A. Hay, K. E. R. Marriott, K. V. Kamenev, S. A. Moggach, E. K. Brechin, S. Parsons, G. Rajaraman and M. Murrie, *Chemical Science*, 2018, **9**, 1551-1559.
26. M. Pinsky and D. Avnir, *Inorganic Chemistry*, 1998, **37**, 5575-5582.
27. S. Alvarez, D. Avnir, M. Llunell and M. Pinsky, *New Journal of Chemistry*, 2002, **26**, 996-1009.

28. N. E. Brese and M. O'Keeffe, *Acta Crystallographica Section B*, 1991, **47**, 192-197.
29. I. D. Brown, Brockhouse Institute for Materials Research, McMaster University, Hamilton, Ontario Canada. idbrown@mcmaster.ca, https://www.iucr.org/__data/assets/file/0007/126574/bvparm2016.cif.
30. S. Tanase, S. Sottini, V. Marvaud, E. J. J. Groenen and L.-M. Chamoreau, *European Journal of Inorganic Chemistry*, 2010, **2010**, 3478-3483.
31. K. R. Meihaus, S. G. Minasian, W. W. Lukens, S. A. Kozimor, D. K. Shuh, T. Tyliszczak and J. R. Long, *Journal of the American Chemical Society*, 2014, **136**, 6056-6068.
32. D. E. Janzen, M. Juchum, S. R. Presow, T. K. Ronson, W. Mohr, R. Clérac, H. L. C. Feltham and S. Brooker, *Supramolecular Chemistry*, 2016, **28**, 125-140.
33. J. Long, D. M. Lyubov, T. V. Mahrova, A. V. Cherkasov, G. K. Fukin, Y. Guari, J. Larionova and A. A. Trifonov, *Dalton Transactions*, 2018, **47**, 5153-5156.
34. T. Kajiwara, *Angewandte Chemie International Edition*, 2017, **56**, 11306-11308.
35. Y.-C. Chen, J.-L. Liu, W. Wernsdorfer, D. Liu, L. F. Chibotaru, X.-M. Chen and M.-L. Tong, *Angewandte Chemie*, 2017, **129**, 5078-5082.
36. S. K. Gupta, T. Rajeshkumar, G. Rajaraman and R. Murugavel, *Dalton Transactions*, 2018, **47**, 357-366.
37. CC-FIT Copyright © 2014 Nicholas F. Chilton.
38. Y.-N. Guo, G.-F. Xu, Y. Guo and J. Tang, *Dalton Transactions*, 2011, **40**, 9953-9963.
39. A. Getsis, B. Balke, C. Felser and A.-V. Mudring, *Crystal Growth & Design*, 2009, **9**, 4429-4437.
40. K. R. Meihaus, J. D. Rinehart and J. R. Long, *Inorganic Chemistry*, 2011, **50**, 8484-8489.
41. S. N. König, N. F. Chilton, C. Maichle-Mössmer, E. M. Pineda, T. Pugh, R. Anwander and R. A. Layfield, *Dalton Transactions*, 2014, **43**, 3035-3038.
42. S. V. Klementyeva, M. Y. Afonin, A. S. Bogomyakov, M. T. Gamer, P. W. Roesky and S. N. Konchenko, *European Journal of Inorganic Chemistry*, 2016, **2016**, 3666-3672.
43. M. He, Z. Chen, E. M. Pineda, X. Liu, E. Bouwman, M. Ruben and P. W. Roesky, *European Journal of Inorganic Chemistry*, 2016, **2016**, 5512-5518.
44. K. S. Lim, J. J. Baldoví, S. Jiang, B. H. Koo, D. W. Kang, W. R. Lee, E. K. Koh, A. Gaita-Ariño, E. Coronado, M. Slota, L. Bogani and C. S. Hong, *Inorganic Chemistry*, 2017, **56**, 4911-4917.
45. T. P. Latendresse, N. S. Bhuvanesh and M. Nippe, *Journal of the American Chemical Society*, 2017, **139**, 8058-8061.
46. M.-J. Liu, J. Yuan, Y.-Q. Zhang, H.-L. Sun, C.-M. Liu and H.-Z. Kou, *Dalton Transactions*, 2017, **46**, 13035-13042.
47. M. Gregson, N. F. Chilton, A.-M. Ariciu, F. Tuna, I. F. Crowe, W. Lewis, A. J. Blake, D. Collison, E. J. L. McInnes, R. E. P. Winpenny and S. T. Liddle, *Chemical Science*, 2016, **7**, 155-165.
48. Y.-X. Wang, Y. Ma, Y. Chai, W. Shi, Y. Sun and P. Cheng, *Journal of the American Chemical Society*, 2018, **140**, 7795-7798.

Chapter 7

A multipocket pyrazolone-based ligand in the synthesis of Co^{II}-4*f* and 4*f* polynuclear complexes

Contents

7. A multipocket pyrazolone-based ligand in the synthesis of Co^{II}-4*f* and 4*f* polynuclear complexes.

7.1 Introduction

The coordination chemistry of the ligand 2,6-bis[4(1-*N*-phenyl-3-methyl-pyrazolium-5-one)carbonyl]pyridinium trichloride (= $[H_5L]\cdot 3Cl$)[1] (Fig. 7.1) in conjunction with Co^{II} and/or 4*f* metal ions is presented in this final experimental chapter. As discussed previously throughout this thesis, the synthesis and characterisation of polynuclear 3*d* and/or 4*f* complexes attracts a great attention due to their interesting properties and applications in various scientific fields.[2-7] More specifically, in the field of molecular magnetism 3*d*-4*f* complexes present some advantages in contrast with pure 3*d* or 4*f* systems. Firstly, the contribution of the strong spin-orbit coupling (SOC) of 4*f* ions could lead to large axial magnetic anisotropy; moreover, the magnetic exchange between the 3*d* ions may effectively supress the quantum tunnelling of the magnetisation (QTM) [8-12] (as discussed in Chapter 1).

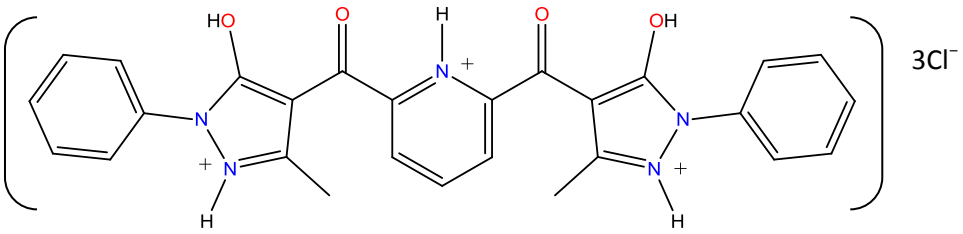

Figure 7.1 The structure of the ligand 2,6-bis[4(1-*N*-phenyl-3-methyl-pyrazolium-5-one)carbonyl]pyridinium trichloride (= $[H_5L]\cdot 3Cl$).[1]

The main synthetic approaches towards the synthesis of such mixed-metal complexes are: i) serendipitous assembly, by using flexible ligands in combination with the metal centres without any control of the final outcome; ii) the rational-design approach, by incorporating designed ligands (such as polycompartmental ligands) that could impose certain geometries (with or without the presence of co-ligands); and finally iii) the building-block approach, where pre-designed metal complexes are used as precursors along with co-ligands to produce high nuclearity clusters.[8, 12-14] In this work the rational-design approach is investigated with the above polydentate ligand. Polycompartmental ligands, similar to $[H_5L]\cdot 3Cl$, such as bis-β-diketones[15-22] and Schiff base ligands[8] (Schemes 7.1 and 7.2) have been widely used towards the synthesis of mixed-metal complexes, and they have shown a variety of 3*d*, 3*d*-4*f* and 4*f* structures, with some of these results exhibiting SMM behaviour.[23-27] Such ligands are designed to possess multiple

coordination pockets for both 3*d* and 4*f* metals; furthermore, they possess bulky and/or aromatic groups, which could help the separation between neighbouring molecules and/or the stabilisation of a complex during the crystallisation process (through *π*-*π* or hydrogen-*π* interactions). Hence, we were interested in exploring the chemistry of the reported $[H_5L]\cdot 3Cl$ ligand[1] with Co^{II} and 4*f* metal ions. To the best of our knowledge this ligand has been reported incorporating only Rh and Sn metal centres,[1] and no results have been reported with any other metal.

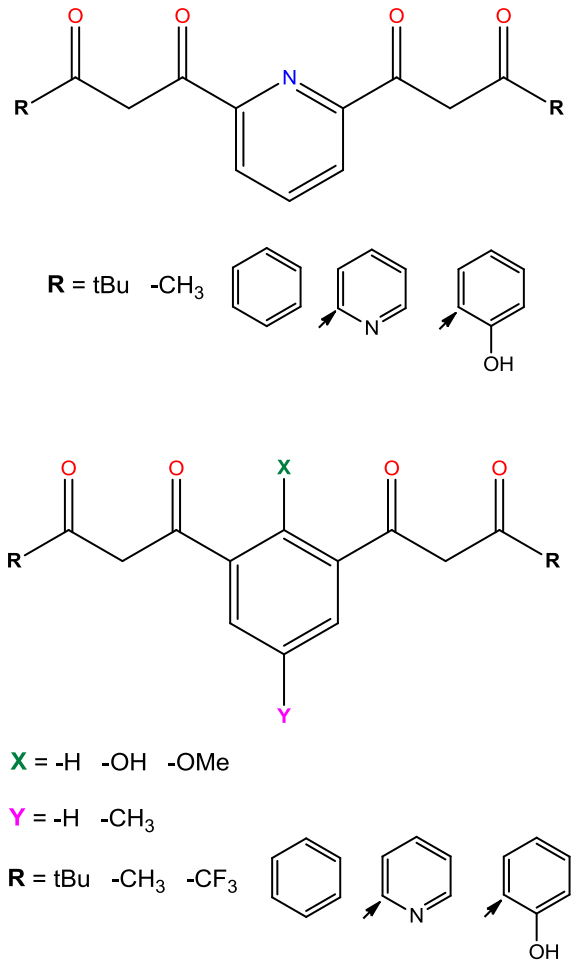

Scheme 7.1 Illustration of bis-β-diketone ligands with similar backbones as in $[H_5L]\cdot 3Cl$. The arrows show the position of the bond between the backbone and the R group.

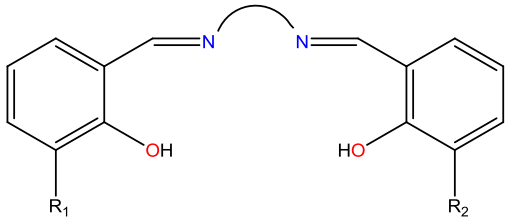

Scheme 7.2 Illustration of the backbone of the Schiff-base ligands derived from salicylaldehyde (or substituted salicyladehyde with different R_1 and R_2 groups) and various diamines (curved black line).[8]

We report the synthesis and structural characterisation of seven new Co(II)-4*f* and 4*f* complexes utilising the ligand 2,6-bis[4(1-*N*-phenyl-3-methyl-pyrazolium-5-one)carbonyl]pyridinium trichloride (= $[H_5L]\cdot 3Cl$)[1] (Fig. 7.1). These complexes are:

- $[La^{III}_9(L^{2-})_7(NO_3)_4(CO_3)_4(OH)(H_2O)_8]\cdot xMeCN\cdot yH_2O$ (**18**$\cdot xMeCN\cdot yH_2O$),
- $[HNEt_3][Ce^{III}_3(HL^{-})_2(NO_3)_7(H_2O)_2][Cl]\cdot xMeCN\cdot yH_2O\cdot zEt_2O$ (**19a**) and $[HNEt_3][Ce^{III}_3(HL^{2-})(H_2L)(NO_3)_7(H_2O)_2][Cl]\cdot xMeCN\cdot yH_2O\cdot zEt_2O$ (**19b**) (see Section 7.3.1 for further details about this complex),
- $[Dy^{III}(HL^{-})_2(H_2O)_4][Cl]\cdot xMeCN\cdot yH_2O$ (**20**$\cdot xMeCN\cdot yH_2O$),
- $[Co^{II}_2Ln^{III}(L^{2-})_2(NO_3)_{2.3}Cl_{0.7}(MeCN)]$ where Ln = La (**21**) and Ce (**22**),
- $[HNEt_3][Co^{II}Dy^{III}_2(L^{2-})_4(HL^{-})(H_2O)_2]\cdot xMeCN\cdot yH_2O$ (**23**$\cdot xMeCN\cdot yH_2O$) and
- $[Gd^{III}_6(L^{2-})_4(OH)_4(O^{2-})(MeOH)_6(H_2O)_2][NO_3]_{3.75}[Cl]_{0.25}\cdot xMeOH\cdot yH_2O$ (**24**$\cdot xMeOH\cdot yH_2O$).

Dc and ac magnetic studies were performed only for the Co(II)-4*f* complexes **21** – **23**. The magnetic susceptibility data for complexes $\{Co^{II}_2La^{III}\}$ and $\{Co^{II}_2Ce^{III}\}$ indicate the presence of a significant magnetic anisotropy, while the dynamic ac experiments revealed the presence of the onset of a weak out-of-phase signal, even under an applied dc field. Complex **23**, $\{Co^{II}Dy^{III}_2\}$, exhibits slow magnetic relaxation in a 3000 Oe dc field, and the fit of the ac magnetic susceptibility data suggests that Raman and Orbach processes are involved, with Raman being the dominant relaxation process (n = 5.5).

7.2 Synthesis

Ligand $[H_5L]\cdot 3Cl$ (= 2,6-bis[4(1-*N*-phenyl-3-methyl-pyrazolium-5-one)carbonyl]pyridinium trichloride) : The ligand $[H_5L]\cdot 3Cl$ was synthesised according the synthetic procedure found in the literature.[1, 28] Into a solution of 3-methyl-1-phenyl-5-pyrazolone (0.029 mol, 5 g) in 1,4-dioxane (100 ml), $Ca(OH)_2$ (0.054 mol, 4 g) was added and the resulted mixture was refluxed at 110 ºC for 1 hour. A solution of 2,6-pyridine-dicarbonyl-dichloride (0.014 mol, 2.9 g) in 1,4-dioxane (10 ml) was added to the above mixture dropwise. The resulted mixture was refluxed for another 24 hours and then left to cool down to room temperature to give a dark orange solution with brown precipitate. The solution was filtered and the obtained precipitate was treated with ~350 ml of 2 M HCl. The precipitate was further treated with concentrated HCl and MeOH in 1:2 ratio under heating to give a clear orange solution which was left to cool down to room temperature yielding a yellow precipitate (~88%). The product was characterised by ^{1}H−NMR in $CDCl_3$ and the assignment of H was performed considering that reported in the literature (see scheme below).[1] ^{1}H−NMR, δ (ppm): 2.2 (s, $6H_a$, methyl group of pz), 7.2 (t, $2H_b$ b, aromatic H of phenyl group), 7.4 (t, $4H_c$, aromatic H of phenyl group), 7.7 (d, $4H_d$, aromatic H of phenyl group), 8.2 – 8.3 (multiplet, $3H_e$, pyridyl group) (Scheme A7.1 in the appendix).

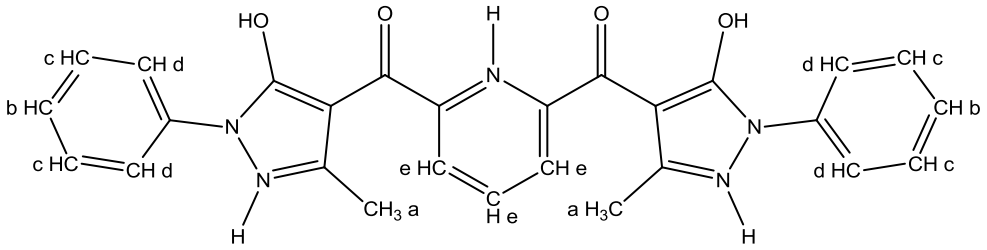

$[La^{III}_9(L^{2-})_7(NO_3)_4(CO_3)_4(OH)(H_2O)_8]\cdot xMeCN\cdot yH_2O$ (18·xMeCN·yH$_2$O) : A solution of $[H_5L]\cdot 3Cl$ (0.2 mmol, 117 mg) and NEt_3 (~0.5 mmol, 0.08 ml) in MeCN (10 ml) was stirred at room temperature for 5 minutes and then $CoCl_2\cdot 6H_2O$ (0.2 mmol, 48 mg) and $La(NO_3)_3\cdot 6H_2O$ (0.4 mmol, 173 mg) were added simultaneously. The mixture was stirred for ~20 hours to give a clear dark green solution. The solution was left to slowly evaporate at room temperature to give orange hexagonal plate-like crystals after ~1 week (~30% yield). We were unable to obtain a satisfactory elemental analysis for this complex (see Section 7.3.1).

$[HNEt_3][Ce^{III}_3(HL^-)_2(NO_3)_7(H_2O)_2][Cl]\cdot xMeCN\cdot yH_2O\cdot zEt_2O$ (19a) and $[HNEt_3][Ce^{III}_3(HL^{2-})(H_2L)(NO_3)_7(H_2O)_2][Cl]\cdot xMeCN\cdot yH_2O\cdot zEt_2O$ (19b) (see Section 7.3.1 for further details about this complex) : A solution of $[H_5L]\cdot 3Cl$ (0.2 mmol, 117 mg) and NEt_3 (~0.5 mmol, 0.08 ml) in MeCN (10 ml) was stirred at room temperature for 5 minutes and then $CoCl_2\cdot 6H_2O$ (0.2 mmol, 48 mg) and $Ce(NO_3)_3\cdot 6H_2O$ (0.4 mmol, 174 mg) were added simultaneously. The mixture was stirred for ~20 hours to give a clear green solution. Slow evaporation and vapour diffusion of the solution with Et_2O yielded yellow column-like crystals after ~1 week (~35% yield). Elemental analysis calcd(%) for $C_{60}H_{76}Ce_3ClN_{18}O_{40}$ (**19**$\cdot 9H_2O$): C 33.59%, H 3.57%, N 11.75%, found: C 33.90%, H 4.12%, N 12.12%.

$[Dy^{III}(HL^-)_2(H_2O)_4][Cl]\cdot xMeCN\cdot yH_2O$ (20$\cdot$xMeCN$\cdot yH_2O$) : A solution of $[H_5L]\cdot 3Cl$ (0.2 mmol, 117 mg) and NEt_3 (~0.5 mmol, 0.08 ml) in MeCN/MeOH (10 ml/5 ml) was stirred at room temperature for 5 minutes and then $CoCl_2\cdot 6H_2O$ (0.2 mmol, 48 mg) and $Dy(NO_3)_3\cdot xH_2O$ (0.4 mmol, 140 mg) were added simultaneously. The mixture was stirred for ~20 hours to give a green solution with a small quantity of light brown precipitate. The solution was filtered and left to slowly evaporate in a sealed vial at room temperature, and yellow block-like crystals were obtained after ~3 weeks (~9% yield). We were unable to obtain a satisfactory elemental analysis for this complex (see Section 7.3.1).

$[Co^{II}_2Ln^{III}(L^{2-})_2(NO_3)_{2.3}Cl_{0.7}(MeCN)]$, where Ln = La (21) and Ce (22) : A solution of $[H_5L]\cdot 3Cl$ (0.2 mmol, 117 mg) and NEt_3 (~0.5 mmol, 0.08 ml) in MeCN (10 ml) was stirred at room temperature for 5 minutes and then $Co(NO_3)_2\cdot 6H_2O$ (0.2 mmol, 58 mg) and $Ln(NO_3)_3\cdot 6H_2O$ (0.4 mmol, 173 mg for La, 174 mg for Ce) were added. The mixture was stirred for 10 minutes and afterwards it was placed in a Teflon lined autoclave and heated to 100 °C, at a rate of 2 °C/min. The temperature was held at 100 °C for 12 hours and then the solution was allowed to cool to room temperature at a rate of 0.1 °C/min yielding a dark green solution with red-brown block-like crystals (~23% yield for both complexes). Elemental analysis calcd(%) for $LaC_{56}H_{45}Cl_{0.7}Co_2N_{13.3}O_{16.9}$: C 46.19%, H 3.11%, N 12.79%, found: C 45.92%, H 3.02%, N 13.27%, which corresponds to $[Co^{II}_2La^{III}(L^{2-})_2(NO_3)_{2.3}Cl_{0.7}(MeCN)]\cdot 2H_2O$ and for $CeC_{56}H_{47}Cl_{0.7}Co_2N_{13.3}O_{17.9}$ calcd(%): C 45.58%, H 3.21%, N 12.63%, found: C 45.22%, H 3.32%, N 12.75%, which corresponds to $[Co^{II}_2Ce^{III}(L^{2-})_2(NO_3)_{2.3}Cl_{0.7}(MeCN)]\cdot 3H_2O$.

$[HNEt_3][Co^{II}Dy^{III}_2(L^{2-})_4(HL^-)(H_2O)_2]\cdot xMeCN\cdot yH_2O$ (23$\cdot$xMeCN$\cdot yH_2O$) : A solution of $[H_5L]\cdot 3Cl$ (0.2 mmol, 117 mg) and NEt_3 (~0.5 mmol, 0.08 ml) in MeCN (10 ml) was stirred at room temperature for 5 minutes and then $CoBr_2$ (0.2 mmol, 44 mg) and $Dy(NO_3)_3\cdot 6H_2O$ (0.1 mmol, 38 mg) were added. The mixture was stirred for 10 minutes and afterwards it was placed in a Teflon lined autoclave and heated to 140 °C, at a rate of 5 °C/min. The

temperature was held at 140 °C for 60 hours and then the solution was allowed to cool to room temperature at a rate of 0.1 °C/min yielding a dark green solution with a small quantity of light brown precipitate. The solution was filtered and left to slowly evaporate in a loosely closed vial at room temperature, and yellow block-like crystals were obtained after ~ 2 months (~12% yield). Elemental analysis calcd(%) for $C_{143}H_{135}CoDy_2N_{27}O_{30}$ (**23**·MeCN·8H_2O): C 55.48%, H 4.40%, N 12.21%, found: C 55.27%, H 4.43%, N 12.33%.

$[Gd^{III}_6(L^{2-})_4(OH)_4(O^{2-})(MeOH)_6(H_2O)_2][NO_3]_{3.75}[Cl]_{0.25}$·xMeOH·y$H_2O$ (24) : A solution of $[H_5L]$·3Cl (0.25 mmol, 144 mg), $CoCl_2$·6H_2O (0.3 mmol, 71 mg), $Gd(NO_3)_3$·6H_2O (0.6 mmol, 270 mg) and NEt_3 (1 mmol, 0.15 ml) in MeOH (15 ml) was placed in a Teflon lined autoclave and heated to 100 °C, at a rate of 2 °C/min. The temperature was held at 100 °C for 12 hours and then the solution was allowed to cool to room temperature at a rate of 0.1 °C/min yielding an orange solution. The solution was left to slowly evaporate in a loosely closed vial at room temperature, and orange block-like crystals were obtained after ~ 1 month (~10% yield). We were unable to obtain a satisfactory elemental analysis for this complex (see Section 7.3.2).

7.3 Results and discussion

The ligand $[H_5L]$·3Cl (Fig. 7.2) was prepared (according to the literature[1, 28]) from the condensation reaction between 2,6-pyridine-dicarbonyl-dichloride and 3-methyl-1-phenyl-5-pyrazolone in 1,4-dioxane catalysed by $Ca(OH)_2$. The product was treated with diluted HCl in order to destroy any undecomposed calcium complexes, and recrystallization from a mixture of MeOH and concentrated HCl yielded the desired product (for the full experimental procedure see Section 7.2).

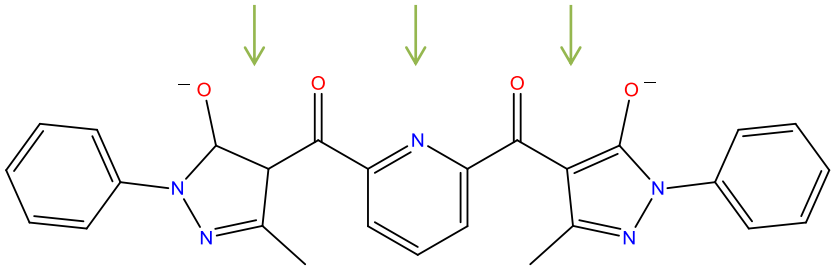

Figure 7.2 The fully deprotonated ligand L^{2-}. The green arrows show the possible coordination pockets.

Reactions at ambient conditions incorporating both Co^{II} and Ln^{III} metal salts were performed using the ligand $[H_5L]\cdot 3Cl$; however, we were not able to isolate any products suitable for characterisation with single-crystal X-ray diffraction (SCXRD) including both metal centres. Instead, we obtained a pure 4*f* complex, a new $\{La^{III}_9\}$ with molecular formula $[La^{III}_9(L^{2-})_7(NO_3)_4(CO_3)_4(OH)(H_2O)_8]\cdot xMeCN\cdot yH_2O$ (**18**·xMeCN·yH_2O) (Fig. 7.3), from the reaction of $CoCl_2\cdot 6H_2O$ and $La(NO_3)_3\cdot 6H_2O$ with the ligand $[H_5L]\cdot 3Cl$, in MeCN and in the presence of NEt_3. Although there was no source of CO_3^{2-} in the reaction, there are four carbonate ligands in the final product. Most likely, the presence of CO_3^{2-} can be ascribed to the fixation of atmospheric CO_2, which has been previously observed in high nuclearity Ln structures.[29-32] It is worth mentioning that according to a CSD search (database of February 2019) only one nonanuclear La-based structure has been reported so far, the heterometallic complex $[C_5H_6N][ULa_9O_8Cl_{15}(O_3SCF_3)_6(NC_5H_5)_9]$.[33] Hence, complex **18** is the first homometallic $\{La^{III}_9\}$ complex.

When the La^{III} ion is replaced with Ce^{III}, instead of the $\{Ce^{III}_9\}$ analogue that we might expect to isolate, a new $\{Ce^{III}_3\}$ complex is obtained, $[HNEt_3][Ce^{III}_3(HL^{-})_2(NO_3)_7(H_2O)_2][Cl]\cdot xMeCN\cdot yH_2O\cdot zEt_2O$ (**19a**) and $[HNEt_3][Ce^{III}_3(HL^{2-})(H_2L)(NO_3)_7(H_2O)_2][Cl]\cdot xMeCN\cdot yH_2O\cdot zEt_2O$ (**19b**) (Fig. 7.4) (see Section 7.3.1 for further details about this complex). Attempts to isolate other $\{Ln^{III}_9\}$ or $\{Ln^{III}_3\}$ analogues were not successful; this could possibly be attributed to the decreasing Ln^{III} size along the lanthanide series (lanthanide contraction) and the high coordination numbers of the La (nine, ten and eleven) and Ce (ten and twelve) centres (see Section 7.3.1), and/or the presence/absence of CO_3^{2-}.

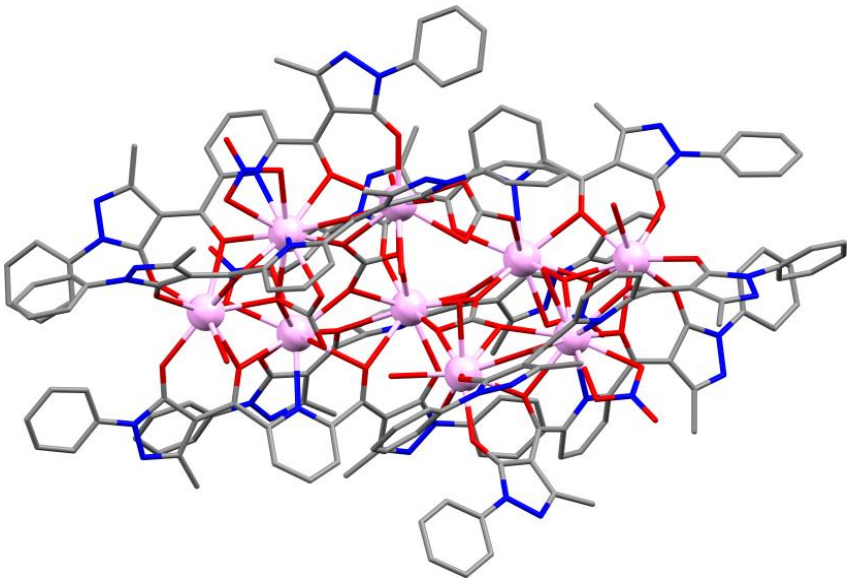

Figure 7.3 The molecular structure of **18**. Colour code: La^{III}: light pink, O: red, N: blue, C: grey. Hydrogen atoms are omitted for clarity.

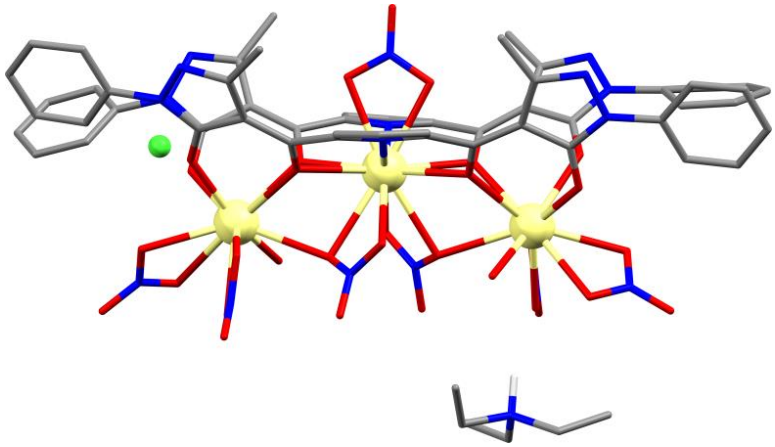

Figure 7.4 The molecular structure of **19**. Colour code: Ce^{III}: light yellow, O: red, N: blue, Cl: green C: grey. Hydrogen atoms are omitted for clarity except for the H of the protonated NEt_3.

Various changes in the synthetic procedure were investigated, such as change of the metal salts, the ratio of the reactants and/or change of solvent. As a result we managed to obtain a new mononuclear Dy^{III} complex with molecular formula $[Dy^{III}(HL^{-})_2(H_2O)_4][Cl]\cdot xMeCN\cdot yH_2O$ (**20**$\cdot xMeCN\cdot yH_2O$) (Fig. 7.5), from the reaction of $CoCl_2\cdot 6H_2O$ and $Dy(NO_3)_3\cdot xH_2O$ with the ligand $[H_5L]\cdot 3Cl$, in a mixture of MeCN/MeOH and in the presence of NEt_3. There is still ongoing work for the refinement of the synthetic procedure (low yield) and the full characterisation of **20** (*e.g.* powder X-ray diffraction, elemental analysis etc.).

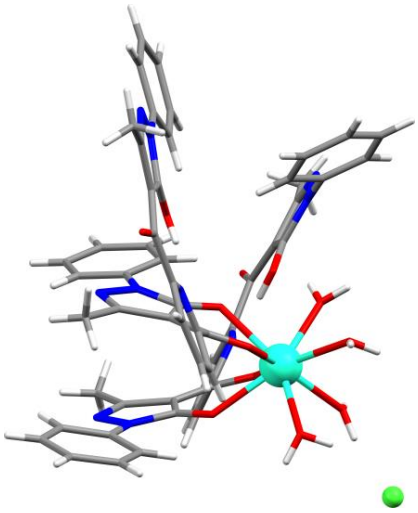

Figure 7.5 The molecular structure of $[Dy^{III}(HL^{-})_2(H_2O)_4][Cl]$ (**20**). Colour code: Dy^{III}: turquoise, O: red, N: blue, Cl: green, C: grey, H: white.

As discussed above, the isolation of mixed Co^{II}-Ln^{III} complexes using ambient conditions was not successful. Hence, we used solvothermal synthesis instead, which has proved a useful synthetic tool throughout this thesis. The reaction of $Co(NO_3)_2{\cdot}6H_2O$, $Ln(NO_3)_3{\cdot}6H_2O$ (Ln = La or Ce) and $[H_5L]{\cdot}3Cl$, in MeCN and in the presence of NEt_3 under solvothermal conditions (100 °C for 12 hours), yielded two new trinuclear complexes with molecular formula $[Co^{II}_2Ln^{III}(L^{2-})_2(NO_3)_{2.3}Cl_{0.7}(MeCN)]$ (Fig. 7.6), where Ln = La (**21**) and Ce (**22**). Attempts to isolate other Ln analogues were not successful, possibly due to the decrease of the Ln^{III} size along the lanthanide series.

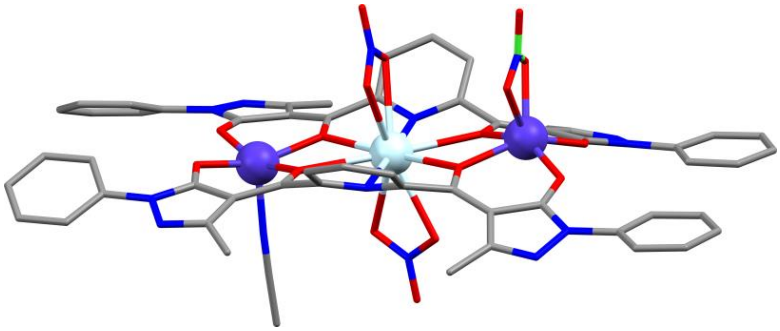

Figure 7.6 The molecular structure of $[Co^{II}_2Ln^{III}(L^{2-})_2(NO_3)_{2.3}Cl_{0.7}(MeCN)]$ (Ln = La (**21**) or Ce (**22**)). Colour code: Co^{II}: violet, Ln^{III}: light blue, Cl: green, O: red, N: blue, C: grey. Hydrogen atoms are omitted for clarity.

Again a variety of changes in the synthetic procedure were investigated (i.e. change of metal salts, the ratio of reactants, change of solvent and/or different temperatures and experiment duration). The change of the metal salts from $Co(NO_3)_2{\cdot}6H_2O$ and $Ln(NO_3)_3{\cdot}6H_2O$ (La or Ce), to $CoBr_2$ and $Dy(NO_3)_3{\cdot}xH_2O$, and under different solvothermal conditions (140 °C for 60 hours), yielded a new $\{Co^{II}Dy^{III}_2\}$ complex, $[HNEt_3][Co^{II}Dy^{III}_2(L^{2-})_4(HL^{-})(H_2O)_2]{\cdot}xMeCN{\cdot}yH_2O$ (**23**·xMeCN·yH_2O) (Fig. 7.7). Preliminary results, which will not be discussed in this thesis, show that the $\{Co^{II}Gd^{III}_2\}$ analogue can also be isolated, and therefore work is still needed towards the synthesis of other lanthanide analogues of complex **23**. Finally, the reaction between $CoCl_2{\cdot}6H_2O$, $Gd(NO_3)_3{\cdot}6H_2O$ and $[H_5L]{\cdot}3Cl$, in MeOH and in the presence of NEt_3 under solvothermal conditions (100 °C for 12 hours), yielded a new $\{Gd^{III}_6\}$ complex, $[Gd^{III}_6(L^{2-})_4(OH)_4(O^{2-})(MeOH)_6(H_2O)_2][NO_3]_{3.75}[Cl]_{0.25}{\cdot}xMeOH{\cdot}yH_2O$ (**24**·xMeOH·yH_2O) (Fig. 7.8). Scheme 7.3 summarises the different synthetic routes followed to isolate complexes **18** – **24**.

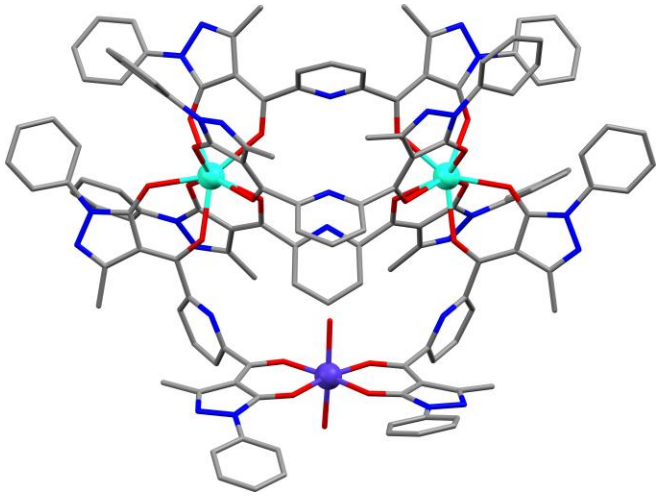

Figure 7.7 The molecular structure of the $[Co^{II}Dy^{III}_2(L^{2-})_4(HL^{-})(H_2O)_2]^{-}$ unit. Colour code: Co^{II}: violet, Dy^{III}: turquoise, O: red, N: blue, C: grey. Hydrogen atoms are omitted for clarity.

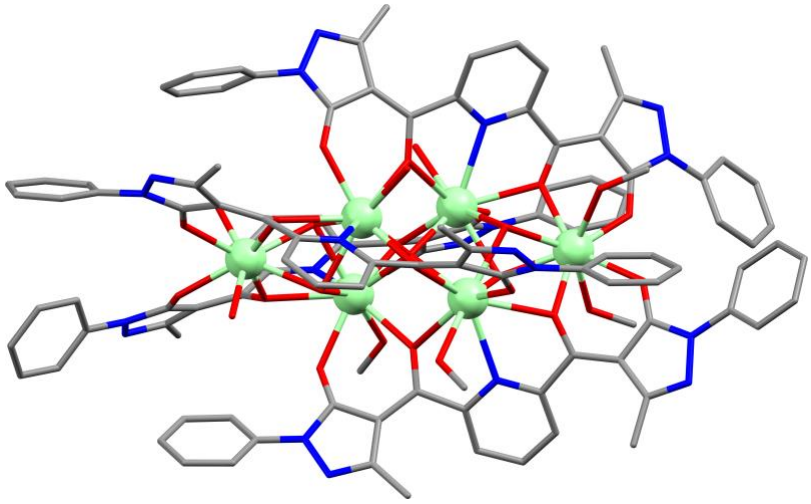

Figure 7.8 The molecular structure of the $[Gd^{III}_6(L^{2-})_4(OH)_4(O^{2-})(MeOH)_6(H_2O)_2]^{4+}$ unit. Colour code: Gd^{III}: light green, O: red, N: blue, C: grey. Hydrogen atoms are omitted for clarity.

Scheme 7.3 The different synthetic routes followed to isolate complexes **18** – **24**.

7.3.1 Ambient conditions

Single-crystal and powder X-ray diffraction analysis

Note: The quality of the single-crystal X-ray diffraction (SCXRD) data of complexes **18** and **19** was unfortunately low due to the poor quality of the crystals and their degradation after a short period of time. A significant amount of disordered solvent molecules are present in the crystal lattice in both complexes (*vide infra*), and therefore it is possible that the loss of solvent causes the degradation of the crystals. The data collected for **18** allowed us to extract the molecular structure; however, the agreement factors are not satisfactory. Moreover, the data for **19** allowed us to propose a molecular structure (*vide infra*), however additional data are needed.

Selected crystallographic data for complexes **18−20** can be found in Table A7.1 in the appendix.

$[La^{III}_9(L^{2-})_7(NO_3)_4(CO_3)_4(OH)(H_2O)_8]\cdot xMeCN\cdot yH_2O$ ($18\cdot xMeCN\cdot yH_2O$)

Complex **18**·xMeCN·yH_2O crystallises in the monoclinic space group $P2_1/c$ and the asymmetric unit contains a full molecule of $[La^{III}_9(L^{2-})_7(NO_3)_4(CO_3)_4(OH)(H_2O)_8]$ and co-crystallised molecules of solvent. Only one molecule of MeCN could be modelled due to a region of poorly defined and disordered molecules of solvent in **18**. The routine SQUEEZE (in PLATON)[34] was used to identify the solvent voids and account for the electron density within them, calculated to contain 3078 e^- per unit cell, corresponding to approximately ~770 e^- per molecule. A mixture of molecules of solvent could be present in the crystal lattice and therefore it was not possible to determine the number of MeCN and/or H_2O molecules that are co-crystallised. The large amount of solvent in the crystal lattice is not unusual, especially for high nuclearity complexes.[35, 36] Additionally, elemental analysis for **18**·xMeCN·yH_2O was not satisfactory, possibly due to the presence of impurities and/or the desolvation of the sample. Note that the reaction forming complex **18**·xMeCN·yH_2O included a Co(II) source ($Co(NO_3)_2$), however the final product does not contain any Co(II) ions.

The $\{La^{III}_9\}$ metallic core of **18** could be described as two horseshoes formed by La1–La5 and La5–La9 centres which are connected on one edge (La5) (Fig. 7.9); the planes defined by the La centres of each horseshoe form an angle of ~80 º (Fig. 7.10).

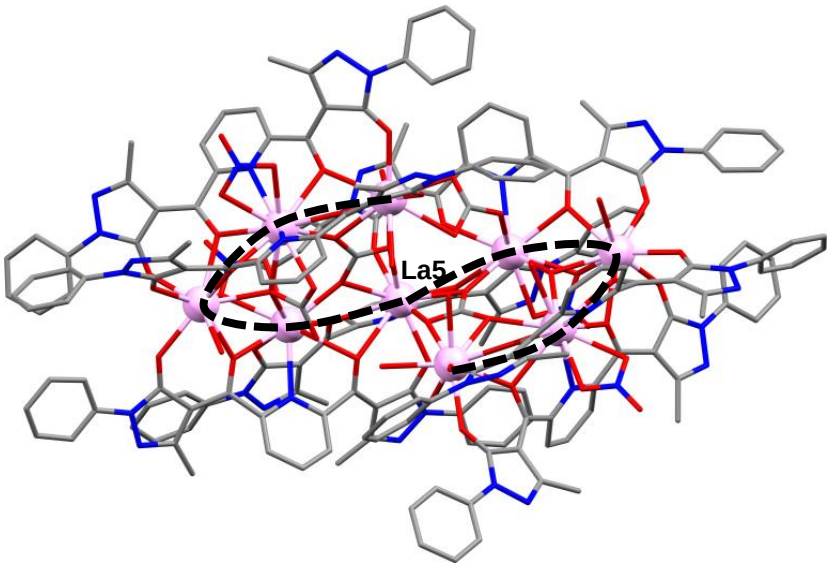

Figure 7.9 The molecular structure of **18**. The black dashed lines represent the two horseshoes formed by La1–La5 and La5–La9. Colour code: La^{III}: light pink, O: red, N: blue, C: grey. Hydrogen atoms are omitted for clarity.

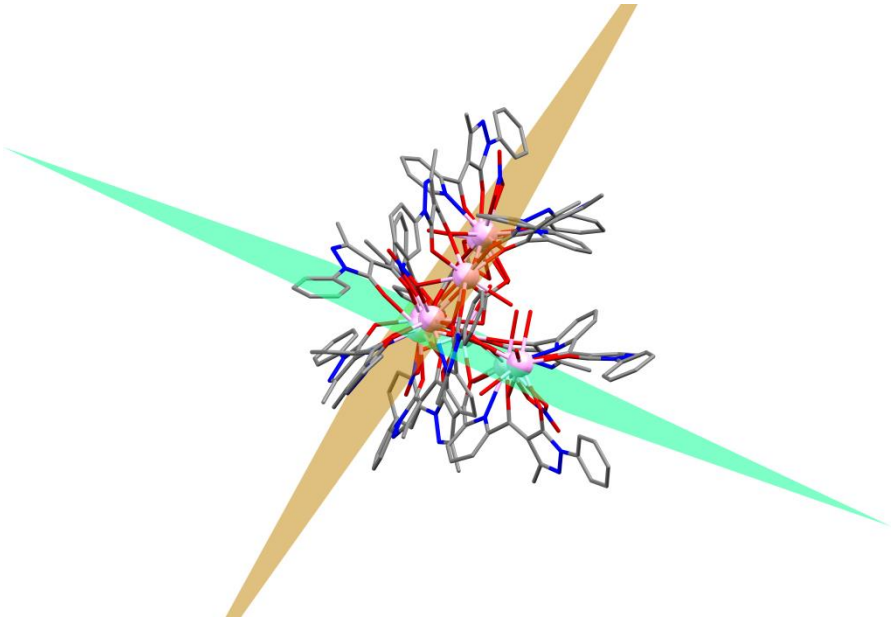

Figure 7.10 The molecular structure of **18**. The orange and green planes are defined by the La1–La5 and La5–La9 centres respectively. Colour code: La^{III}: light pink, O: red, N: blue, C: grey. Hydrogen atoms are omitted for clarity.

There are nine crystallographically independent La^{III} centres which are bridged by seven doubly deprotonated L^{2-} ligands, the 'outer shell' of the molecule (Fig. 7.11) and four CO_3^{2-} ligands and one hydroxide bridge, the 'inner core' of the molecule (Fig. 7.12). Four of the La atoms are ten-coordinate (La1 and La4–La6), three are nine-coordinate (La3,

La7 and La9) and two are eleven-coordinate (La2 and La8) (Fig. A7.1 in the appendix), with terminal molecules of water and/or chelating NO_3^- ligands completing their coordination spheres. Continuous shape measures (CShMs)[37-41] were used to determine the distortion around each La ion (Tables 7.1–7.3).

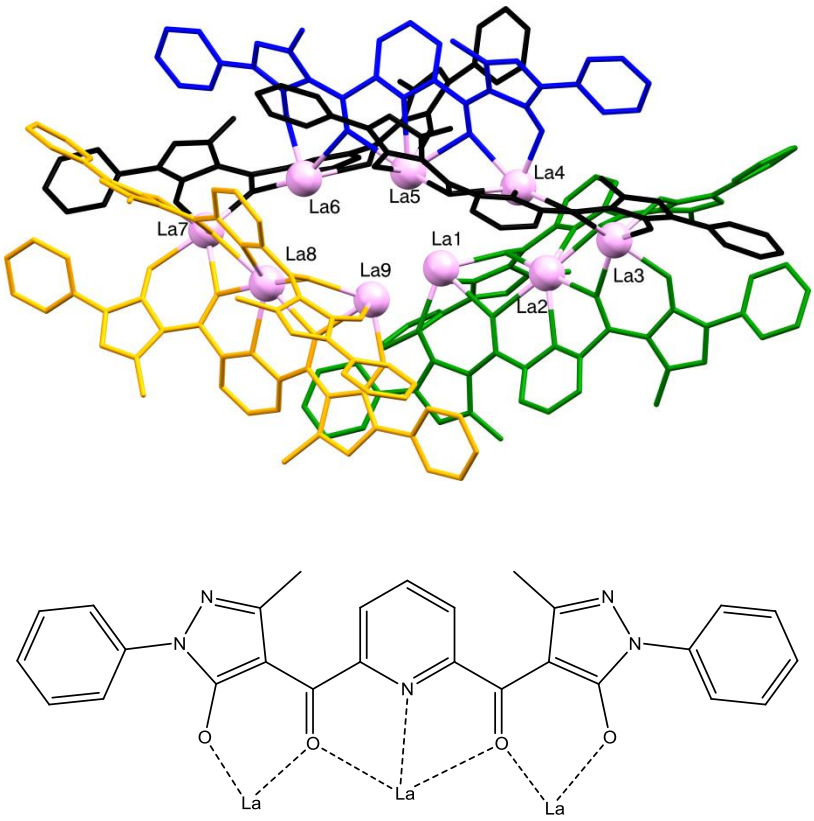

Figure 7.11 *Top)* Illustration of the 'outer shell' of **18** bridged only by the L^{2-} ligands. The ligands are represented with different colours for clarity. Green: the two ligands bridging La1–La3, Blue: the ligand bridging La4–La6, Yellow: the two ligands bridging La7–La9 and Black: the two ligands bridging the atoms La3–La5 and La5–La7, respectively. La^{III}: light pink. Hydrogen atoms are omitted for clarity. *Bottom)* Illustration of the bridging mode of the seven L^{2-} ligands.

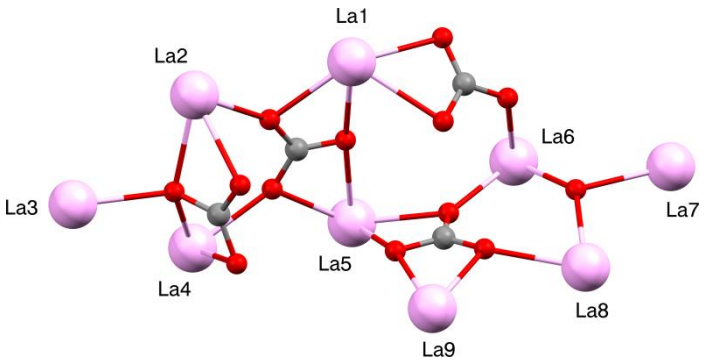

Figure 7.12 Illustration of the 'inner core' of **18** bridged only by the carbonate and hydroxide bridges. Colour code: La^{III}: light pink, O: red, C: grey.

Table 7.1 The CShMs[37-39] values calculated with the program SHAPE for the two closest geometries for each nine-coordinate La atom.

La 9-coordinate	Spherical tricapped trigonal prism (D_{3h})	Spherical capped square antiprism (C_{4v})	Muffin (C_s)
La3	0.60	0.88	-
La7	1.07	1.08	-
La9	-	1.50	1.41

Table 7.2 The CShMs[37, 40] values calculated with the program SHAPE for the two closest geometries for each ten-coordinate La atom.

La 10-coordinate	Sphenocorona (J87) (C_{2v})	Bicapped square antiprism (J17) (D_{4d})	Tetradecahe-dron (C_{2v})	Staggered Dodecahedron (D_2)
La1	3.21	3.52	-	-
La4	2.68	-	3.45	-
La5	5.21	-	-	5.86
La6	2.05	-	5.09	-

Table 7.3 The CShMs[37, 41] values calculated with the program SHAPE for the two closest geometries for each eleven-coordinate La atom.

La 11-coordinate	Capped pentagonal antiprism (J11) (C_{5v})	Augmented sphenocorona (J87) (C_s)
La2	1.48	5.26
La8	1.09	5.08

The crystal packing of the structure is shown in Fig. 7.13. Intramolecular hydrogen bonds (between the water molecules and the carbonate ligands) and hydrogen-π interactions (between the aromatic rings) are present within the molecule, while hydrogen bonds and hydrogen-π interactions occur between neighbouring molecules (for clarity these are not shown). The shortest intermolecular La···La' distances are ~9.6 Å.

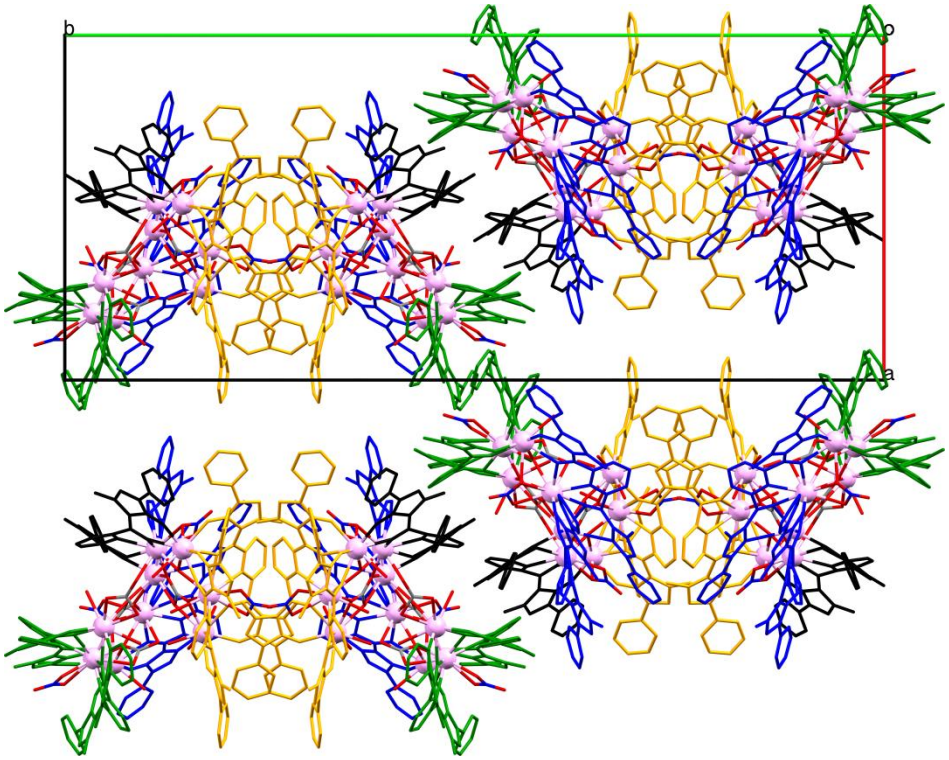

Figure 7.13 The crystal packing of **18** ($P2_1/c$) along the crystallographic *c*-axis. The ligands are represented with different colours for clarity (as in Fig. 7.11). Green: the two ligands bridging La1–La3, Blue: the ligand bridging La4–La6, Yellow: the two ligands bridging La7–La9 and Black: the two ligands bridging the atoms La3–La5 and La5–La7, respectively. Colour code: La^{III}: light pink, N: blue, O: red. Hydrogen atoms are omitted for clarity.

$[HNEt_3][Ce^{III}_3(HL^-)_2(NO_3)_7(H_2O)_2][Cl]\cdot xMeCN\cdot yH_2O\cdot zEt_2O$ (19a) and $[HNEt_3][Ce^{III}_3(HL^{2-})(H_2L)(NO_3)_7(H_2O)_2][Cl]\cdot xMeCN\cdot yH_2O\cdot zEt_2O$ (19b)

As mentioned previously, the quality of the SCXRD data of complex **19** was low due to the poor quality of the crystals and their degradation after a short period of time. The data of **19** allowed us to propose two possible molecular formulae: $[HNEt_3][Ce^{III}_3\mathbf{(HL^-)_2}(NO_3)_7(H_2O)_2][Cl]\cdot xMeCN\cdot yH_2O\cdot zEt_2O$ (**19a**) or $[HNEt_3][Ce^{III}_3\mathbf{(L^{2-})(H_2L)}(NO_3)_7(H_2O)_2][Cl]\cdot xMeCN\cdot yH_2O\cdot zEt_2O$ (**19b**), however additional data are needed to finalise the structure. Complex **19** (Fig. 7.14) crystallises in the monoclinic $P2_1/c$ space group and the asymmetric unit contains a molecule of $[Ce^{III}_3(HL^-)_2(NO_3)_7(H_2O)_2]$ (or $[Ce^{III}_3(L^{2-})(H_2L)(NO_3)_7(H_2O)_2]$), one $[HNEt_3]^+$ cation, one Cl^- ion and co-crystallised molecules of solvent (possible solvents are MeCN, H_2O and/or Et_2O).

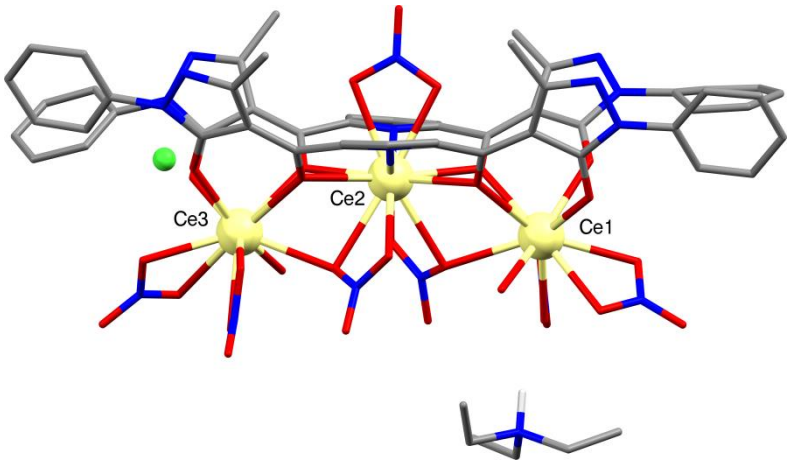

Figure 7.14 The molecular structure of **19**. Colour code: Ce: light yellow, O: red, N: blue, Cl: green, C: grey, H: white. Hydrogen atoms are omitted for clarity except for the H of the protonated NEt_3.

BVS analysis[42, 43] revealed that all three Ce centres are in +3 oxidation state with bonds in the range of 2.4 – 2.7 Å. There are seven coordinated NO_3^- molecules, five of which are chelating and two of them are in bridging mode 2.21 (see Appendix for Harris notation). Moreover, there is one $[HNEt_3]^+$ cation and one Cl^- in the crystal lattice. We propose that the NEt_3 is protonated due to the presence of electron density near the N atom, and the position of the NEt_3 near the molecule (Fig. A7.2 in the appendix), which suggests the presence of a hydrogen bond between the $[HNEt_3]^+$ and a coordinated NO_3^- molecule (N−H···O, with N···O distance ~2.87 Å).The presence of the Cl^- ion was also confirmed by Energy-dispersive X-ray spectroscopy (EDX) (Fig. A7.3 in the appendix). In order for the charge balance to be satisfied, we propose two possible molecular formulae: i) either the two ligands are singly deprotonated $[HNEt_3][Ce^{III}_3\mathbf{(HL^-)_2}(NO_3)_7(H_2O)_2][Cl]$ (**19a**) or ii) one ligand is doubly deprotonated and the other one is neutral $[HNEt_3][Ce^{III}_3\mathbf{(L^{2-})(H_2L)}(NO_3)_7(H_2O)_2][Cl]$ (**19b**). However, due to the multiple possible protonated sites of the ligand (Fig. 7.15) and the low quality of the SCXRD data, we are not able to determine which ligands are protonated. Additionally, comparing the bond distances within the ligand of complex **19** and complexes **20** (includes singly deprotonated ligand) and **21** (includes doubly deprotonated ligand) (*vide infra*), we were not able to infer any other information about the position of the protons (Fig. A7.4 in the appendix).

The two edge Ce centres (Ce1 and Ce3) are ten-coordinate whereas the central Ce2 is twelve-coordinate. The CShMs[37, 40] values calculated with SHAPE (Table 7.4 where 0 is the ideal polyhedron) suggest that Ce1 and Ce3 adopt a distorted geometry between sphenocorona and bicapped square antiprism, while Ce2 adopts distorted icosahedron geometry. The coordination spheres of Ce1 and Ce3 consist of two chelating NO_3^-, one O

atom from a bridging NO_3^- in 2.21 mode, one H_2O and four O atoms from the ligands. The coordination sphere of Ce2 consists of one chelating NO_3^- molecule, four O atoms from two bridging NO_3^- in 2.21 mode, and four O and two N atoms from the ligands.

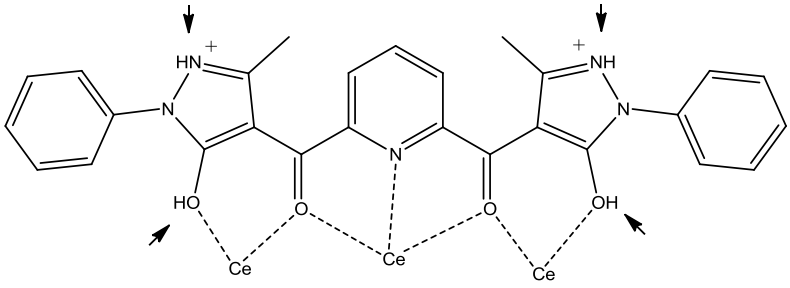

Figure 7.15 Illustration of the bridging mode of the two ligands and the possible protonated sites.

Table 7.4 The CShMs[37, 40, 41] values calculated with the program SHAPE for the two closest geometries for each Ce atom.

Ce 10-coordinate	Sphenocorona (J87) (C_{2v})	Bicapped square antiprism (J17) (D_{4d})
Ce1	3.53	3.77
Ce3	3.29	3.48
Ce 12-coordinate	**Icosahedron (I_h)**	**Johnson elongated pentagonal bipyramid (J16) (D_{6h})**
Ce2	1.60	3.49

Due to a region of poorly defined and disordered molecules of solvent in **19** no molecules of solvent could be modelled. The routine SQUEEZE (in PLATON)[34] was used to identify the solvent voids and account for the electron density within them, calculated to contain 1237 e^- per unit cell, corresponding to approximately ~309 e^- per molecule. A mixture of molecules of solvent could be present (MeCN, H_2O and/or Et_2O) in the crystal lattice and therefore it was not possible to determine the number of solvent molecules. Moreover, elemental analysis for **19** suggests the presence of nine water molecules indicating the desolvation of the sample (see Section 7.2). The crystal packing of the structure is shown in Fig. 7.16. The shortest Ce···Ce distance is ~7 Å.

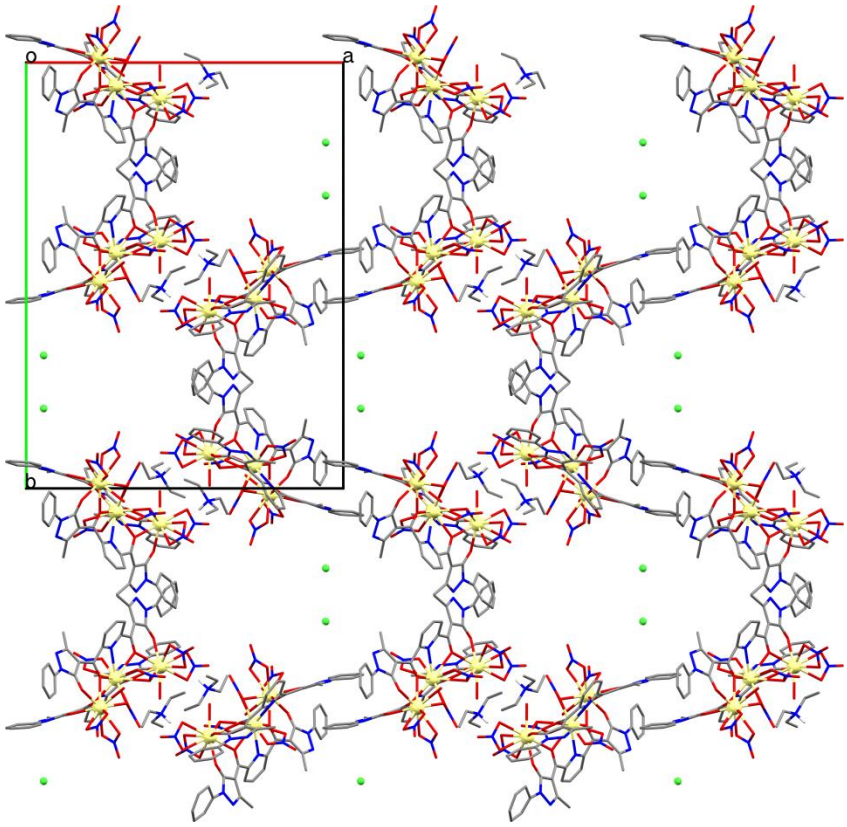

Figure 7.16 The crystal packing of **19** ($P2_1/c$) along the crystallographic *c*-axis. Colour code: Ce^{III}: light yellow, O: red, C: grey, N: blue, Cl: green. Hydrogen atoms are omitted for clarity.

$[Dy^{III}(HL^{-})_2(H_2O)_4][Cl]\cdot xMeCN\cdot yH_2O$ (**20**·xMeCN·yH_2O)

Complex **20**·xMeCN·yH_2O crystallises in the monoclinic *C*2/*c* space group; the asymmetric unit consists of a full molecule of $[Dy^{III}(HL^{-})_2(H_2O)_4]^{+}$**,** one Cl^{-} ion and molecules of solvent co-crystallised in the lattice. The Dy ion is eight-coordinate with four O atoms originating from two singly deprotonated ligands (HL^{-}), and four coordinated water molecules (Fig.7.17), while the charge balance is satisfied by the co-crystallised Cl^{-} ion. The HL^{-} ligands and the four water molecules are in a *cis* configuration[44] relative to each other (Fig.7.17). Continuous shape measures[45] propose a slightly distorted square antiprismatic (SAP) geometry with a value of 0.28 (where 0 corresponds to the ideal polyhedron). BVS analysis[42, 43] confirmed the oxidation state of Dy^{III}. Some key geometrical parameters of the square antiprismatic geometry that directly affect the SMM performance are shown in Fig. 7.18: d_{pp}, the shortest distance between the two $\{O_4\}$ squares; d_{in}, the shortest O···O distance in a $\{O_4\}$ square; φ, the angle between the diagonals of the two $\{O_4\}$ squares (skew angle); and α, the angle between the C_4 axis and the direction described by a Ln–O bond.[46] For complex **20** these parameters are d_{pp} = 2.39 Å, d_{in} = 2.78 and 2.80 Å (for the two $\{O_4\}$ squares respectively), φ = 46.5 º and α = 57.9 º.

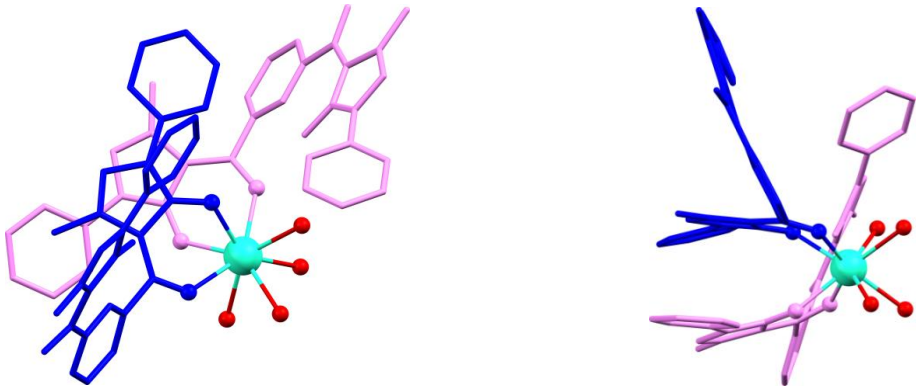

Figure 7.17 The molecular structure of the $[Dy^{III}(HL^{-})_2(H_2O)_4]^+$ unit. Each ligand is represented with a different colour (blue and pink) for clarity. Colour code: Dy^{III}: turquoise, O: red. Hydrogen atoms are omitted for clarity.

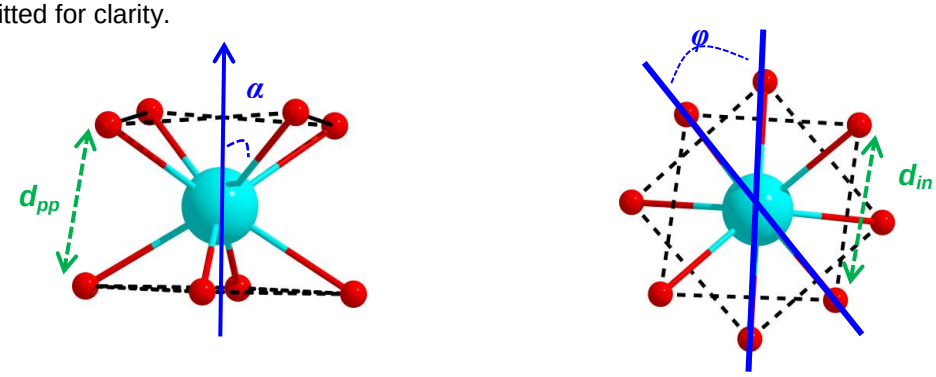

Figure 7.18 Illustration of the structural parameters d_{pp} and α (*left*), and d_{in} and φ (*right*) for the $\{DyO_8\}$ SAP geometry. See text for further details. Colour code: Dy^{III}: turquoise, O: red.

For the ideal SAP geometry (D_{4d} symmetry) these parameters are $d_{pp} = d_{in}$, φ = 45 º and α = 54.74 º. The deviation of φ from 45 º will result in the lowering of the D_{4d} symmetry, thus leading to the presence of transverse anisotropy which promotes the quantum tunnelling of the magnetisation (QTM). Moreover, the α angle is associated with the elongation (α < 54.74 º) or compression (α > 54.74 º) along the C_4 axis; the sign of the crystal-field parameter B_2^0 (see Chapter 1 for further details about the crystal-field parameters) changes from negative to positive with the variation from elongated to compressed SAP for the oblate lanthanide ions, whereas the reverse trend is observed for the prolate lanthanide ions.[46] In order to achieve high performance SMM behaviour, a negative uniaxial magnetic anisotropy, associated with negative B_2^0, is required to stabilise a high m_J ground-state.[46] Complex **20** possesses a compressed SAP geometry (α = 57.9), and therefore a positive B_2^0 is predicted, which could possibly lead to the absence of SMM properties.

Only one molecule of MeCN and half molecule of water could be modelled due to a region of poorly defined and disordered molecules of solvent in **20**. The routine SQUEEZE (in PLATON)[34] was used to identify the solvent voids and account for the electron density within them, calculated to contain 202 e^- per unit cell, corresponding to approximately ~25 e^- per molecule. Approximately two molecules of water or one MeCN molecule could correspond to ~25 e^-, therefore the exact nature of the co-crystallised solvent molecules could not be determined. Additionally, elemental analysis for **20**·xMeCN·yH_2O was not satisfactory, possibly due to the presence of impurities and/or the desolvation of the sample. Note that the reaction forming complex **20**·xMeCN·yH_2O included a Co(II) source ($Co(NO_3)_2$), however the final product does not contain any Co(II) ions. The crystal packing is shown in Fig. 7.19. Intramolecular hydrogen bonds, hydrogen-*π* and *π*-*π* interactions are present between the aromatic rings (Fig. A7.5 in the appendix), while hydrogen bonds and *π*-*π* interactions occur between neighbouring molecules (Fig. A7.6 in the appendix). The shortest intermolecular Dy···Dy' distances are ~9 Å.

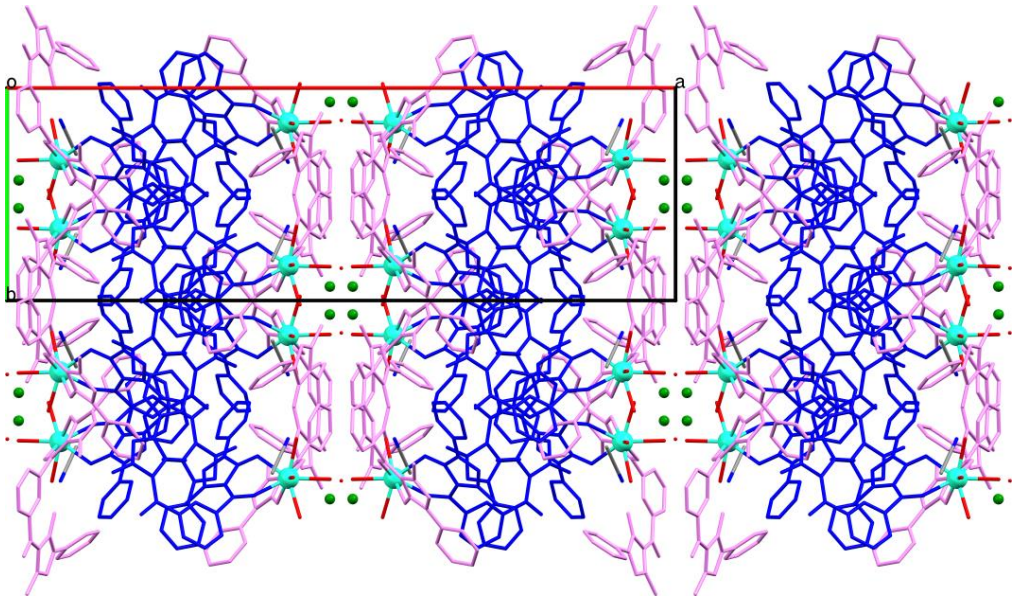

Figure 7.19 The crystal packing of **20** (*C*2/*c*) along the crystallographic *c*-axis with the modelled co-crystallised solvents (MeCN and H_2O). Each ligand in one molecule is represented with a different colour (blue and pink) for clarity. Colour code: Dy^{III}: turquoise, O: red, C: grey, N: blue, Cl: green. Hydrogen atoms are omitted for clarity.

The experimental powder X-ray diffraction (PXRD) patterns for complexes **18** – **20** were not satisfactory, possibly due to the loss of solvent, and therefore the loss of crystallinity, and/or the presence of impurities. As discussed previously, elemental analyses for **18**·xMeCN·yH_2O and **20**·xMeCN·yH_2O were not satisfactory, indicating the presence of impurities, whereas the elemental analysis for **19** suggests the desolvation of the sample.

As future work, our intention is to perform PXRD measurements for **19** under inert atmosphere, in order to examine if it is possible to obtain a satisfactory PXRD pattern. Moreover, refinement of the experimental procedures of complexes **18**·x$MeCN·yH_2O$ and **20**·x$MeCN·yH_2O$ is needed, in order to isolate pure samples.

7.3.2 Solvothermal conditions

Selected crystallographic data for complexes **21**−**24** can be found in Tables A7.2 and A7.3 in the appendix.

Single-crystal and powder X-ray diffraction analysis

$[Co^{II}_2Ln^{III}(L^{2-})_2(NO_3)_{2.3}Cl_{0.7}(MeCN)]$, where Ln = La (21) and Ce (22)

Complexes **21** and **22** are isostructural and therefore only the structure of **21** will be described. Complex **21** (Fig. 7.20) crystallises in the monoclinic space group $P2_1/m$ and the asymmetric unit contains a half molecule of $[Co^{II}_2La^{III}(L^{2-})_2(NO_3)_{2.3}Cl_{0.7}(MeCN)]$. The three metal centres are bridged by two doubly deprotonated L^{2-} ligands (adopting the same bridging mode as in complexes $\{La^{III}_9\}$ and $\{Ce^{III}_3\}$) in an almost linear Co−La−Co arrangement. Co1 is penta-coordinate adopting a slightly distorted square pyramidal geometry (SPY), with four O atoms in the equatorial plane originating from the L^{2-} ligands, while the apical position is occupied by a terminally bound MeCN molecule. The equatorial plane of Co2 is also occupied by four O atoms from the L^{2-} ligands, however the axial position is occupied by a mixture of Cl^- and NO_3^- anions in a 0.7:0.3 ratio (Fig. 7.20). Therefore, there is a mixture of penta- and hexa-coordinate Co2 adopting slightly distorted SPY and distorted trigonal prism geometries, respectively. In both complexes **21** and **22** Co1 is located ~0.37 Å outside the basal $\{O_4\}$ plane, while Co2 is located ~0.54 Å outside the $\{O_4\}$ plane. The Ln (La or Ce) is ten-coordinate adopting a slightly distorted staggered dodecahedron, with four O and two N atoms in the equatorial plane originating from the L^{2-} ligands, and two chelating NO_3^- ligands in axial positions. Continuous shape measures were performed for all metal centres for both **21** and **22**, and the extracted values are shown in Tables 7.5 and 7.6. BVS analysis[42, 43] confirmed the oxidation states of all metal centres Co^{II}, La^{III} and Ce^{III}. Similar structures in an almost linear Co^{II}−Ln^{III}−Co^{II} arrangement have been previously reported; however the majority of these complexes contain hexa-coordinate Co centres[22, 47-51] and only a few contain penta-coordinate centres.[52-54] Additionally, it is worth noting that the presence of the Cl^-/NO_3^- mixture could make the interpretation of the magnetic data difficult, since different coordination environments of the Co centres can lead to different magnetic behaviour (*vide infra*).

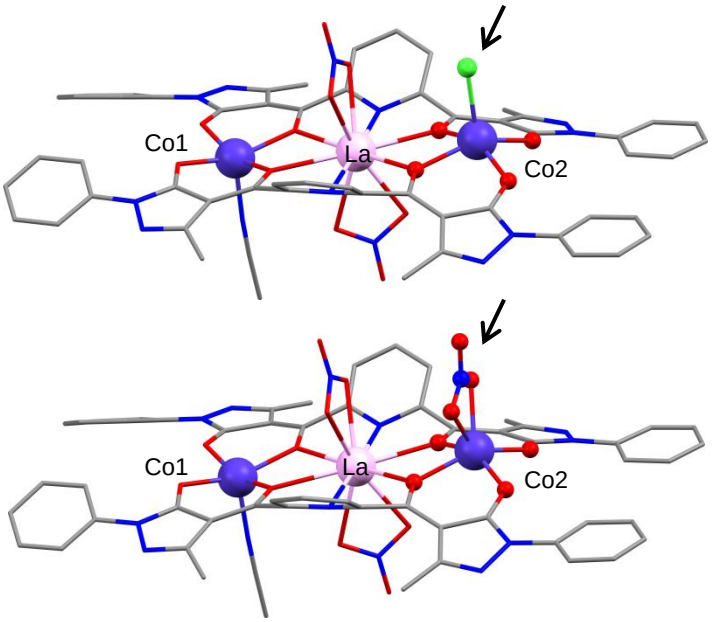

Figure 7.20 The molecular structure of **21** showing both of the anion sites in Co2 (see text for further details). Colour code: Co^{II}: violet, La^{III}: light pink, Cl: green, O: red, N: blue, C: grey. Hydrogen atoms are omitted for clarity.

Table 7.5 The CShMs values calculated with the program SHAPE[40, 55-57] for the closest geometries for each metal atom in complex **21**. The value 0 corresponds to the ideal polyhedron. Co2 contains a mixture of Cl^- and NO_3^- anions in a 0.7:0.3 ratio, hence there is a mixture of penta- and hexa-coordinate Co2.

Complex 21	Spherical square pyramid (C_{4v})	Trigonal prism (D_{3h})	Staggered Dodecahedron (D_2)
Co1	0.19		
Co2	0.62	1.16	
La			0.55

Table 7.6 The CShMs values calculated with the program SHAPE[40, 55-57] for the closest geometries for each metal atom in complex **22**. The value 0 corresponds to the ideal polyhedron. Co2 contains a mixture of Cl^- and NO_3^- anions in a 0.7:0.3 ratio, hence there is a mixture of penta- and hexa-coordinate Co2.

Complex 22	Spherical square pyramid (C_{4v})	Trigonal prism (D_{3h})	Staggered Dodecahedron (D_2)
Co1	0.20		
Co2	0.66	1.04	
Ce			0.49

The crystal packing is shown in Fig. 7.21. Intermolecular *π*-*π* interactions occur between the aromatic pyrazolone and phenyl rings of neighbouring molecules (Fig. A7.7 in the appendix). The shortest intermolecular Co···Co' and La···La' distances are ~7.6 and ~10 Å, respectively, while the intramolecular Co···Co' distance is also ~7.6 Å.

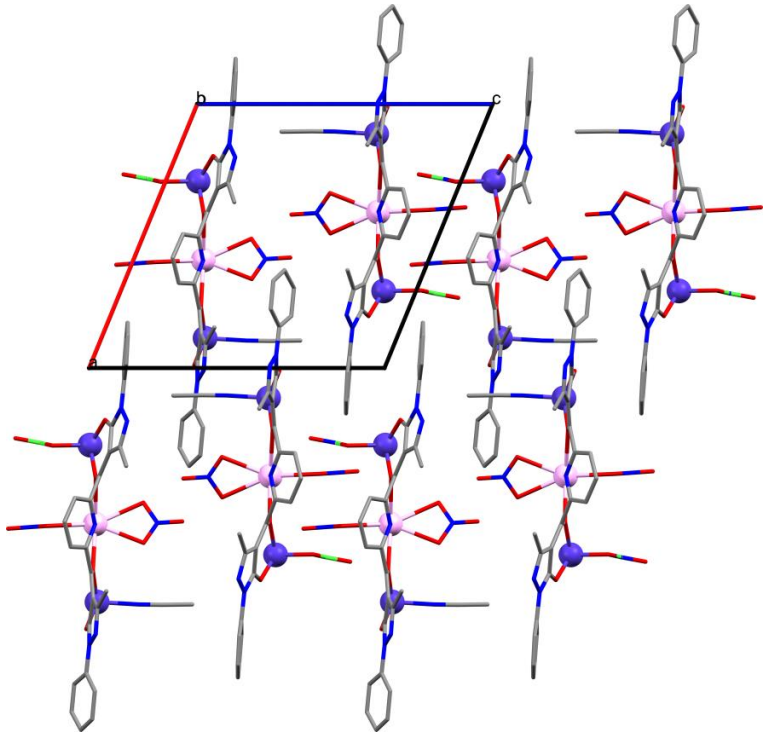

Figure 7.21 The crystal packing of **21** ($P12_1/m1$) along the crystallographic *b*-axis. Colour code: Co^{II}: violet, La^{III}: light pink, Cl: green, O: red, N: blue, C: grey. Hydrogen atoms are omitted for clarity.

The experimental PXRD patterns of complexes **21** and **22** (Fig. 7.22) are consistent with the calculated ones from the single crystal structures of **21** and **22**, respectively; therefore, we can conclude that the samples are phase pure. The calculated PXRD patterns for both complexes were generated from the single-crystal data collected at room temperature, and the experimental PXRD patterns were also measured at room temperature. Elemental analysis revealed that **21** and **22** are slightly hygroscopic (**21**·$2H_2O$ and **22**·$3H_2O$); however, the experimental and calculated PXRD patterns are in good agreement, and therefore we can assume that the crystal structure has not changed. The solvated complexes **21**·$2H_2O$ and **22**·$3H_2O$ are used for the magnetic characterisation (*vide infra*).

Additionally, Energy−dispersive X−ray spectroscopy (EDX) was performed for **21**·$2H_2O$ and **22**·$3H_2O$ to examine the homogeneity of the bulk crystalline sample and to confirm the metal ratios found with SCXRD (*vide infra*).

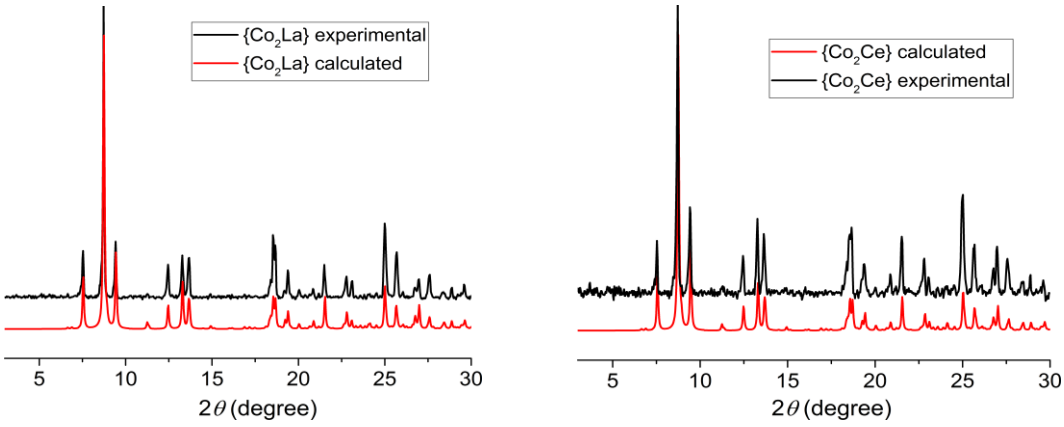

Figure 7.22 *Left)* The PXRD patterns (3−30°) of $\{Co_2La\}$. *Right)* The PXRD patterns (3−30°) of $\{Co_2Ce\}$. The red lines represent the calculated PXRD patterns for **21** and **22** and the black lines the experimental ones for **21**·2H_2O and **22**·3H_2O. The experimental PXRD patterns were measured at room temperature, and the calculated patterns are generated from the single-crystal data collected also at room temperature.

$[HNEt_3][Co^{II}Dy^{III}_2(L^{2-})_4(HL^-)(H_2O)_2]\cdot xH_2O\cdot yMeCN$ (**23**·x$MeCN$·yH_2O)

Complex **23**·x$MeCN$·yH_2O (Fig. 7.23) crystallises in the monoclinic $P2_1/c$ space group and the asymmetric unit contains one full molecule of $[Co^{II}Dy^{III}_2(L^{2-})_4(HL^-)(H_2O)_2]^-$, one $[HNEt_3]^+$ cation and co-crystallised solvent molecules. Due to a region of poorly defined and disordered molecules of solvent in **23** only one molecule of MeCN and four molecules of water could be modelled. Three of the water molecules are located in the centre of the molecule and form hydrogen bonds with the coordinated water molecules and the pyridyl rings (Fig. A7.8 in the appendix). The routine SQUEEZE (in PLATON)[34] was used to identify the solvent voids and account for the electron density within them, calculated to contain 1267 e^- per unit cell, corresponding to approximately ~317 e^- per molecule. A mixture of molecules of solvent could be present (MeCN and/or H_2O) in the crystal lattice and therefore it was not possible to determine the number of solvent molecules. Elemental analysis (see Section 7.2) suggests that one molecule of MeCN and eight molecules of water are present in the sample (indicating the desolvation of the sample); therefore, complex **23**·x$MeCN$·yH_2O will be referred to as **23**·$MeCN$·8H_2O hereafter.

The oxidation states of Co^{II} and the two Dy^{III} are confirmed with BVS analysis[42, 43]. We propose that NEt_3 is protonated due to the presence of electron density near the N atom, and the position of the NEt_3 near a co-crystallised water molecule (Fig. 7.23), which

suggests the presence of a hydrogen bond. This is not unusual as previously seen throughout this thesis (complexes $\{Co^{II}_2\}$, $\{Co^{II}_6\}$, $\{Co^{II}_8\}$ in Chapter 5 and $\{Ce^{III}_3\}$ in the present Chapter). Hence, in order for the charge balance to be satisfied, one of the ligands should be protonated. However, due to the large amount of solvent molecules, and therefore large electron density around the molecule, it was not possible to determine which one of the ligands is protonated (as also previously seen in the $\{Ce^{III}_3\}$ complex).

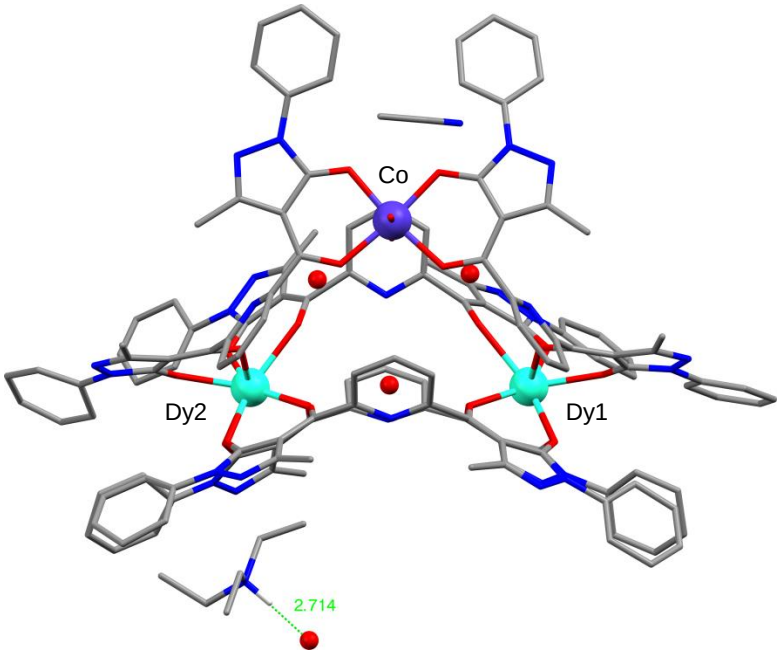

Figure 7.23 The molecular structure of **23**·MeCN·4H_2O (only the modelled molecules of MeCN and H_2O are shown here). The green dashed line shows the N···O distance between the $[HNEt_3]^+$ cation and a H_2O molecule. Colour code: Co^{II}: violet, Dy^{III}: turquoise, O: red, N: blue, C: grey, H: white. Hydrogen atoms are omitted for clarity except for the H of the protonated NEt_3.

Three of the ligands bridge the two Dy atoms, while the other two ligands bridge each Dy atom (Dy1 and Dy2) with the Co(II) centre (Fig. 7.24); all of the ligands adopt the same bridging mode as previously seen in the complexes $\{La^{III}_9\}$, $\{Ce^{III}_3\}$ and $\{Co^{II}_2Ln^{III}\}$. The Co centre is hexa-coordinate with a distorted octahedral geometry, and its coordination sphere consists of four oxygen atoms in the equatorial plane, originating from the ligands, while two molecules of water are found in the axial positions. Dy1 and Dy2 are both eight-coordinate adopting a distorted square antiprism geometry (SAP), with eight oxygen atoms in their coordination spheres originating from the ligands. The CShMs values calculated with SHAPE[45, 57] are 0.64 for Co, and 0.21 and 0.23 for Dy1 and Dy2 respectively (where 0 is the ideal polyhedron). As previously discussed for the mononuclear complex **20**, there are some key geometrical parameters of the square antiprismatic geometry that directly affect the SMM performance: d_{pp}, the distance

between the two $\{O_4\}$ squares; d_{in}, the shorter O···O distance in a $\{O_4\}$ square; φ, the angle between the diagonals of the two $\{O_4\}$ squares (skew angle); and α, the angle between the C_4 axis and the direction described by a Ln–O bond.[46]

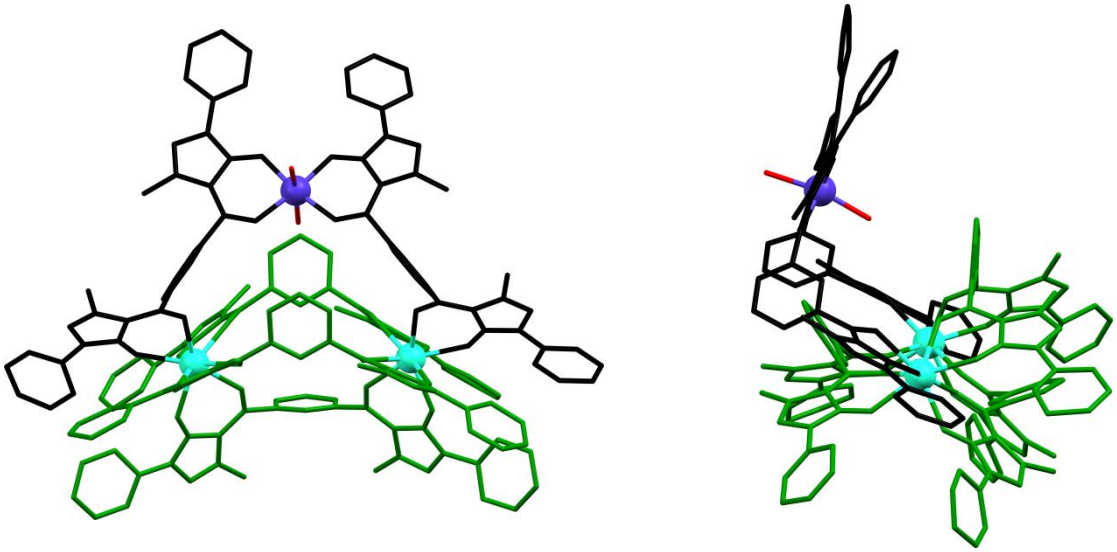

Figure 7.24 The molecular structure of $[Co^{II}Dy^{III}_2(L^{2-})_4(HL^-)(H_2O)_2]^-$ unit. The three ligands bridging the Dy^{III} atoms are represented in green colour, while the two ligands bridging the Dy^{III} atoms with the Co^{II} are represented in black colour for clarity. Colour code: Co^{II}: violet, Dy^{III}: turquoise, O: red. Hydrogen atoms are omitted for clarity.

For complex **23**·MeCN·8H_2O these parameters are: d_{pp} = 2.43 Å, d_{in} = 2.78 and 2.80 Å (for the two $\{O_4\}$ squares respectively), φ = 49 º, α = 58.07 º for Dy1; and d_{pp} = 2.45 Å, d_{in} = 2.76 and 2.80 Å (for the two $\{O_4\}$ squares respectively), φ = 49.42 º, α = 57.97 º for Dy2. The deviation of φ from 45 º (ideal SAP geometry) will result in the lowering of the D_{4d} symmetry, thus leading to the presence of transverse anisotropy which promotes the quantum tunnelling of the magnetisation (QTM). Moreover, due to the compressed SAP geometries of the Dy centres, a positive B_2^0 is expected[46], as previously discussed for complex **20**. The crystal packing of **23**·MeCN·8H_2O is shown in Fig. 7.25. Intramolecular hydrogen-π interactions are present, while hydrogen bonds, π-π and hydrogen-π interactions occur between neighbouring molecules (for clarity these are not shown). The shortest intermolecular Co···Co' and Dy···Dy' distances are ~8.3 and ~11.8 Å respectively.

To the best of our knowledge complex **23**·MeCN·8H_2O is only the third $\{Co^{II}Dy^{III}_2\}$ complex to be reported, with $[Dy^{III}_2Co^{II}(L^1)_8]\cdot 6H_2O$ (HL^1 = salicylic aldehyde) (**I**)[11] and $\{[Co^{II}_2(HTRI)_3(H_2O)_6][Dy^{III}_2Co^{II}(HCAM)_6(H_2O)_4]\cdot 22H_2O\}$ (**II**)[58] (HTRI = 1,2,4-triazole, H_3CAM = 4-hydroxyl-2,6-pyridicarboxylic acid) being reported in the literature so far (CSD search, database February 2019). The linear complex **I** shows interesting magnetic behaviour, including ferromagnetic exchange interactions and slow magnetic relaxation in zero dc field.[11]

The PXRD pattern for complex **23**·MeCN·$8H_2O$ was not satisfactory, possibly due to loss of solvent (as also indicated by elemental analysis, see Section 7.2) and therefore loss of crystallinity. Additionally, Energy−dispersive X−ray spectroscopy (EDX) was performed for **23**·MeCN·$8H_2O$ in order to examine the homogeneity of the bulk crystalline sample and to confirm the metal ratios found with single-crystal X-ray diffraction (*vide infra*).

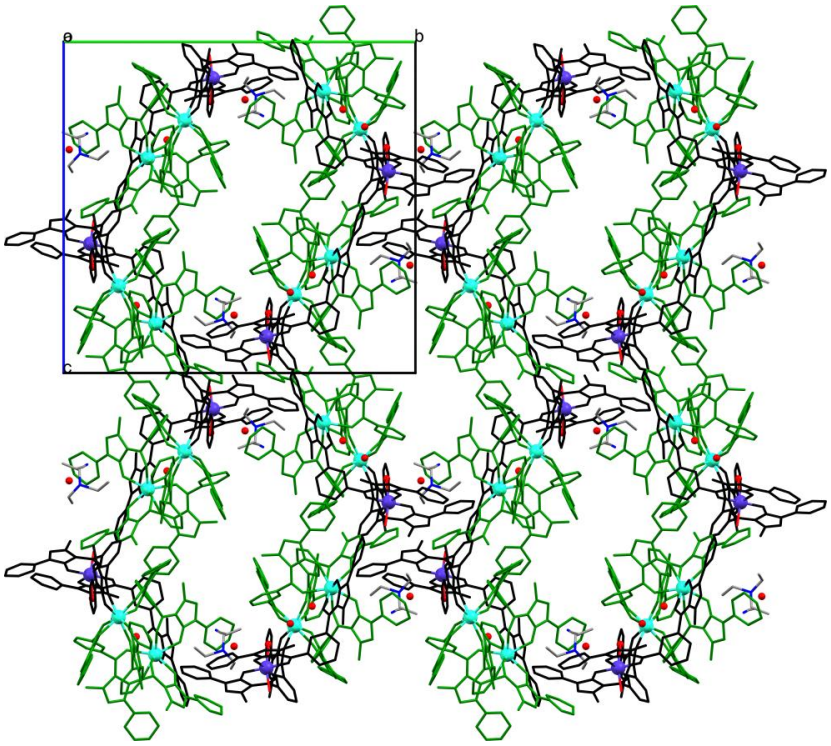

Figure 7.25 The crystal packing of **23**·MeCN·$4H_2O$ ($P2_1/c$) (only the modelled MeCN and H_2O molecules are shown here) along the crystallographic *a*-axis. The three ligands bridging the Dy^{III} atoms are represented in green colour, while the two ligands bridging the Dy^{III} atoms with the Co^{II} are represented in black colour for clarity. Colour code: Co^{II}: violet, Dy^{III}: turquoise, O: red, N: blue, C: grey. Hydrogen atoms are omitted for clarity.

$[Gd^{III}_6(L^{2-})_4(OH)_4(O^{2-})(MeOH)_6(H_2O)_2][NO_3]_{3.75}[Cl]_{0.25}$·xMeOH·y$H_2O$ (**24**·xMeOH·yH_2O)

Complex **24**·xMeOH·yH_2O (Fig. 7.26) crystallises in the triclinic space group $P\bar{1}$ and the asymmetric unit contains one molecule of $[Gd^{III}_6(L^{2-})_4(OH)_4(O^{2-})(MeOH)_6(H_2O)_2]^{4+}$, three fully occupied NO_3^- molecules and a mixture of NO_3^- and Cl^- with chemical occupancies of 0.75 and 0.25, respectively in the crystal lattice, and co-crystallised molecules of solvent. Due to a region of poorly defined and disordered molecules of solvent in **24**, only 1.5 molecules of H_2O and 2.75 molecules of MeOH could be modelled. The routine SQUEEZE (in PLATON)[34] was used to identify the solvent voids and account for the electron density within them, calculated to contain 96 e^- per unit cell, corresponding to approximately 48 e^- per molecule. A mixture of molecules of solvent could be present in

the crystal lattice and therefore it was not possible to determine the number of MeOH and/or H_2O molecules that are co-crystallised. Additionally, elemental analysis for **24**·xMeOH·yH_2O was not satisfactory, possibly due to the presence of impurities and/or the desolvation of the sample. Note that the reaction forming complex **24**·xMeOH·yH_2O included a Co(II) source ($Co(NO_3)_2$), however the final product does not contain any Co(II) ions.

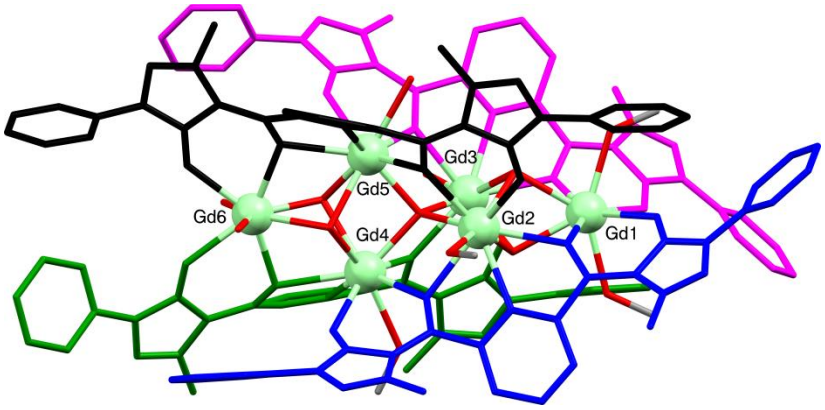

Figure 7.26 The molecular structure of the $[Gd^{III}_6(L^{2-})_4(OH)_4(O^{2-})(MeOH)_6(H_2O)_2]^{4+}$ unit. Each ligand is represented with a different colour (blue, black, green and pink) for clarity. Colour code: Gd^{III}: light green, O: red, C: grey. Hydrogen atoms are omitted for clarity.

There are six crystallographically independent Gd^{III} centres which are bridged with each other by four doubly deprotonated L^{2-} ligands (Fig. 7.27), one oxide and four hydroxide bridges. The coordination spheres of Gd1, Gd2 and Gd4 are completed by terminally bound MeOH molecules, whereas Gd3, Gd5 and Gd6 contain a mix of terminally bound MeOH and H_2O molecules. Gd1−Gd3 and Gd4−Gd6 form two triangles, while Gd2−Gd5 form a tetrahedron (Fig 7.28). Gd1 and Gd6 are eight-coordinate adopting distorted square antiprismatic geometry, whereas Gd2−Gd5 are nine-coordinate adopting distorted muffin geometry (Fig. A7.9 in the appendix). The CShMs values calculated with SHAPE are shown in Tables 7.7 and 7.8.

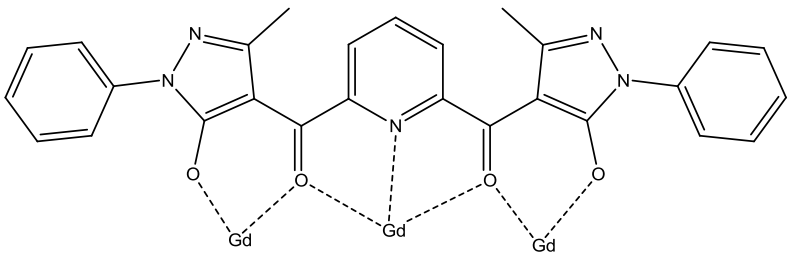

Figure 7.27 Illustration of the bridging mode of the four L^{2-} ligands.

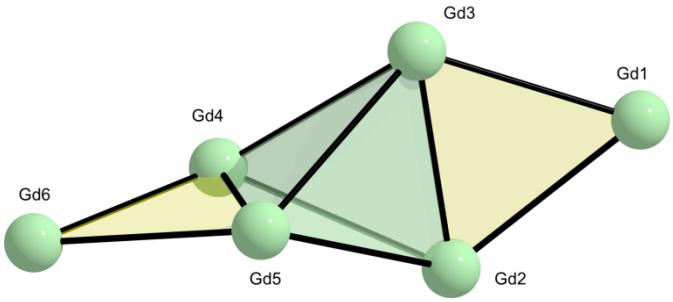

Figure 7.28 Illustration of the $\{Gd^{III}_6\}$ core of **24**. Gd: light green, green tetrahedron: formed by Gd2−Gd5, yellow triangles: formed by Gd1−Gd3 and Gd4−Gd6.

Table 7.7 The CShMs values calculated with the program SHAPE for the two closest geometries for each eight-coordinate Gd atom.

Gd 8-coordinate	Square antiprism (D_{4d})	Triangular dodecahedron (D_{2d})
Gd1	0.77	1.93
Gd6	1.10	1.54

Table 7.8 The CShMs[37-39] values calculated with the program SHAPE for the two closest geometries for each nine-coordinate Gd atom.

Gd 9-coordinate	Muffin (C_s)	Spherical capped square antiprism (C_{4v})
Gd2	1.624	2.170
Gd3	1.725	2.048
Gd4	1.769	2.100
Gd5	1.356	1.973

The crystal packing is shown in Fig. 7.29. Intermolecular hydrogen bonds are present between the coordinated H_2O and MeOH molecules and the nitrate ions, and between the molecules of co-crystallised solvent and the N atoms of the pyrazolone ligands; moreover, hydrogen-π interactions occur between the solvent molecules and the aromatic rings. The shortest intermolecular Gd···Gd' distance is ~10 Å. The experimental powder X-ray diffraction (PXRD) pattern for complex **24**·xMeOH·yH_2O was not satisfactory, possibly due

to the presence of impurities and/or the loss of solvent, and therefore the loss of crystallinity. As future work for this project is the refinement of the synthetic procedure of **24** in order to isolate a pure sample.

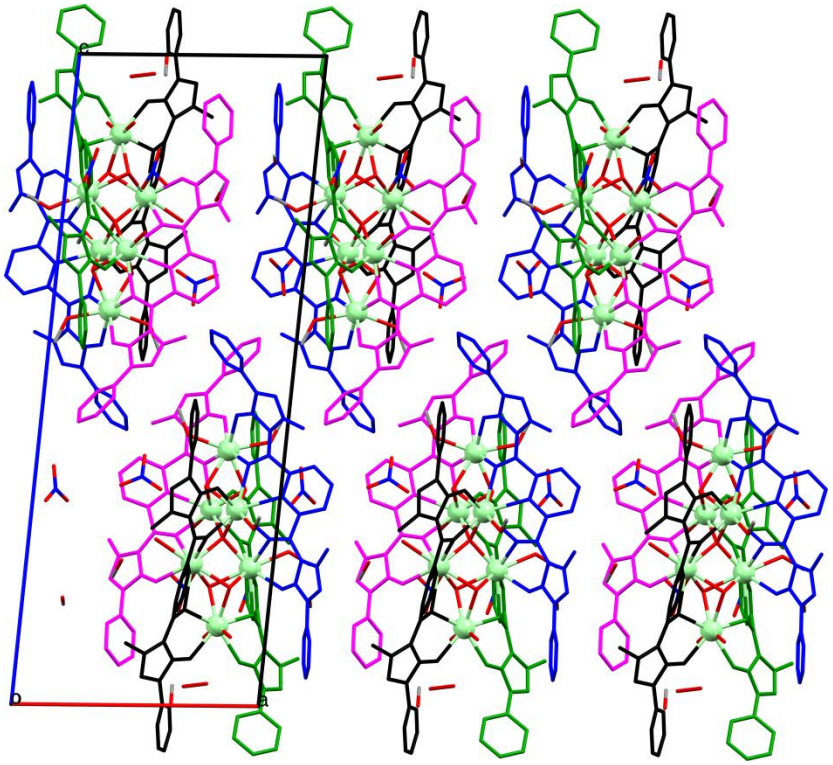

Figure 7.29 The crystal packing of **24**·xMeOH·yH_2O ($P\bar{1}$) (only the modelled MeOH and H_2O molecules are shown here) along the crystallographic *b*-axis. Each ligand is represented with a different colour (blue, black, green and pink) for clarity. Colour code: Gd^{III}: light green, O: red, N: blue, C: grey. Hydrogen atoms are omitted for clarity.

Energy−dispersive X−ray spectroscopy (EDX)

EDX experiments were performed for complexes {Co_2La} (**21**·2H_2O) and {Co_2Ce} (**22**·3H_2O) in order to examine the homogeneity of the bulk crystalline sample and to confirm the metal ratios found with SCXRD (Fig 7.30 and 7.31). The average Co:La ratio found for **21**·2H_2O is ~2:1 (Avg. Atomic% Co:La is ~63:37, Table A7.4 in the appecdix) and for **22**·3H_2O the Co:Ce ratio found is also ~2:1 (Avg. Atomic% Co:Ce is ~66:33, Table A7.5 in the appecdix). These results are consistent with the SCXRD analysis.

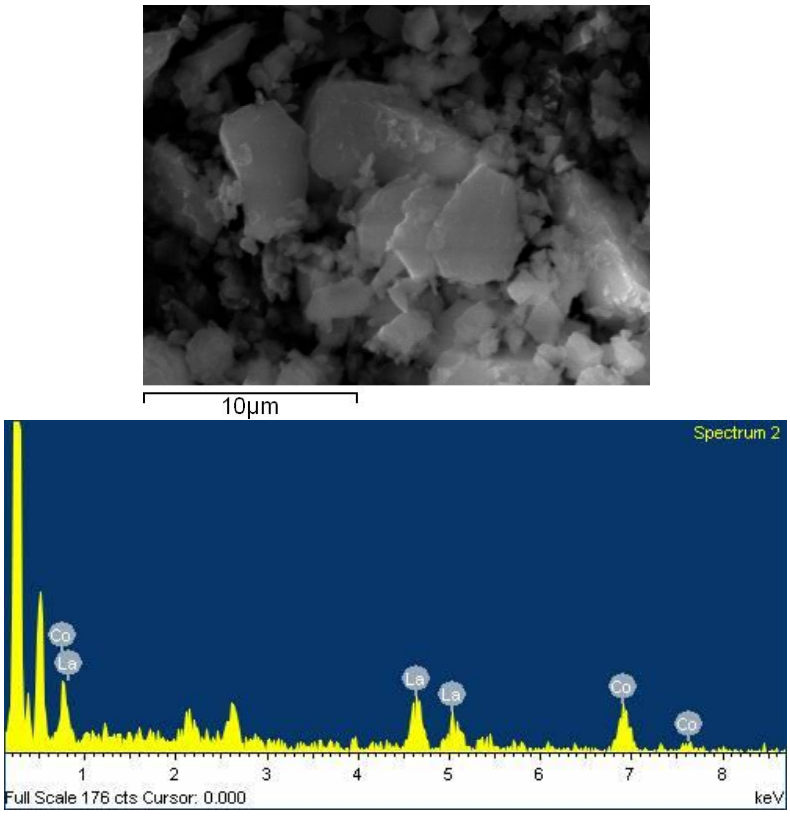

Figure 7.30 EDX spectrum (*bottom*) and elemental map (*top*) showing the distribution of Co and La in a bulk sample of **21**·2H_2O. Co: red and La: green.

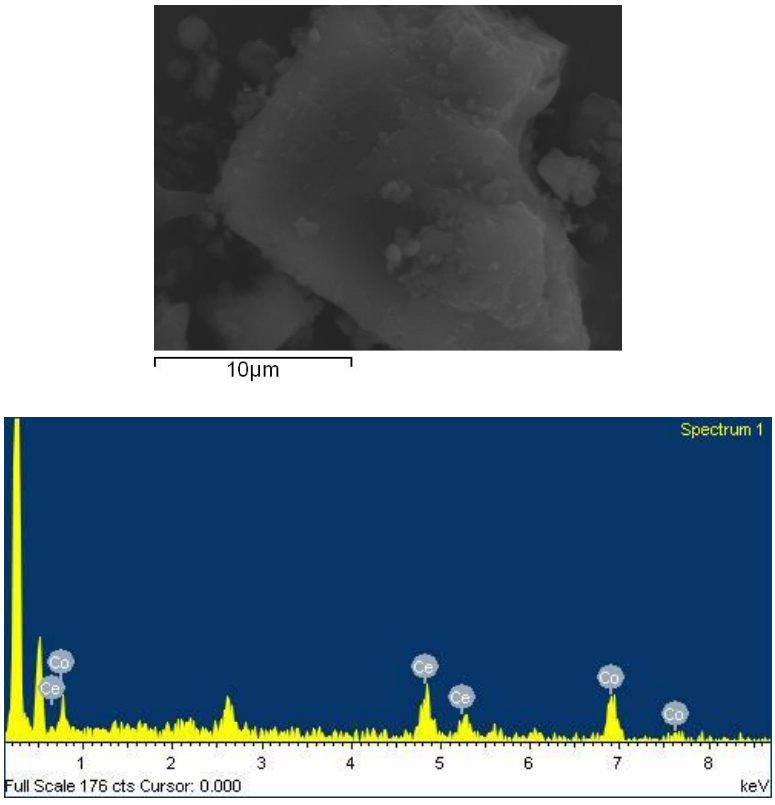

Figure 7.31 EDX spectrum (*bottom*) and elemental map (*top*) showing the distribution of Co and Ce in a bulk sample of **22**·3H_2O. Ce: red and Co: green.

EDX experiments were also performed for complex **23**·MeCN·$8H_2O$ in order to examine the homogeneity of the bulk crystalline sample and to confirm the metal ratios found with SCXRD (Fig 7.32). The average Co:Dy ratio found for **23**·MeCN·$8H_2O$ is ~1:2 (Avg. Atomic% Co:Dy is ~32:68, Table A7.6 in the appecdix). These results are consistent with the SCXRD analysis.

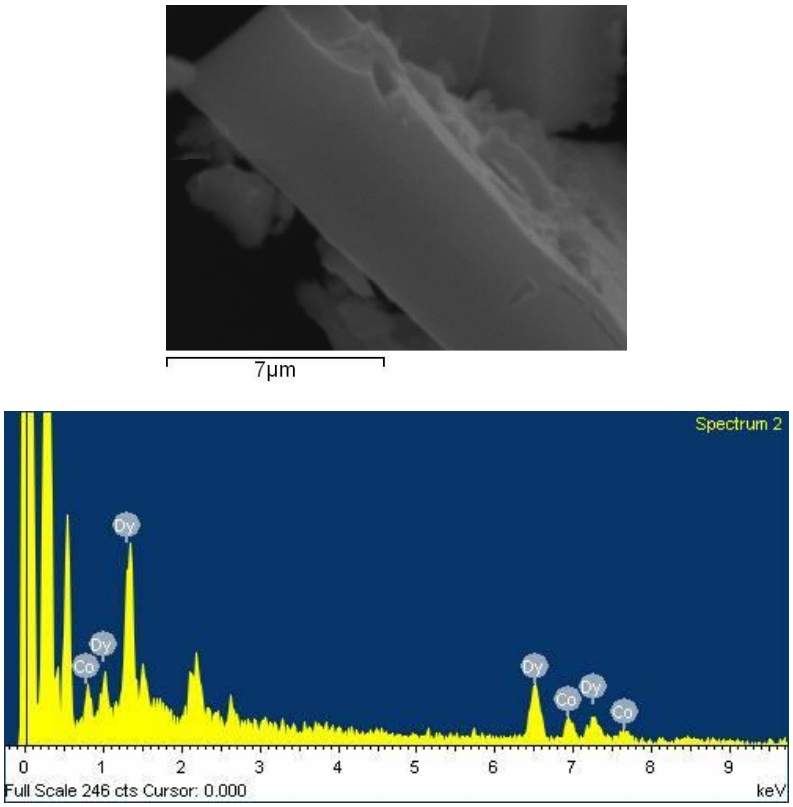

Figure 7.32 EDX spectrum (*bottom*) and elemental map (*top*) showing the distribution of Co and Dy in a bulk sample of **23**·MeCN·$8H_2O$. Co: red and Dy: green.

Magnetic characterisation

***Note*:** Only the Co(II)-4*f* complexes $[Co^{II}_2La^{III}(L^{2-})_2(NO_3)_{2.3}Cl_{0.7}(MeCN)]\cdot 2H_2O$ (**21**·$2H_2O$), $[Co^{II}_2Ce^{III}(L^{2-})_2(NO_3)_{2.3}Cl_{0.7}(MeCN)]\cdot 3H_2O$ (**22**·$3H_2O$) and $[HNEt_3][Co^{II}Dy^{III}_2(L^{2-})_4(HL^{-})(H_2O)_2]\cdot MeCN\cdot 8H_2O$ (**23**·MeCN·$8H_2O$) are studied here.

Variable temperature dc susceptibility measurements were carried out for complexes **21**·$2H_2O$, **22**·$3H_2O$ (Fig. 7.33 left) and **23**·MeCN·$8H_2O$ (*vide infra*) in a field of 1000 Oe in the 290 – 2 K temperature range. The $\chi_M T$ values at room temperature for **21**·$2H_2O$ and **22**·$3H_2O$ are 5.70 and 5.98 $cm^3\ mol^{-1}$ K, respectively. These values are higher than the theoretical spin-only values $\chi_M T$ = 3.76 $cm^3\ mol^{-1}$ K for two non-interacting high-spin Co^{II} (S = 3/2 and g = 2) and one La^{III} (diamagnetic), and $\chi_M T$ = 4.52 $cm^3\ mol^{-1}$ K for two non-interacting high-spin Co^{II} (S = 3/2 and g = 2) and one Ce^{III} ($^2F_{5/2}$, $g = {}^6/_7$). This is indicative of a significant orbital contribution, which is expected for highly anisotropic square pyramidal and trigonal prismatic Co^{II} ions.[59, 60] $\chi_M T$ gradually decreases for both complexes with the lowering of temperature until ~80 K and then decreases rapidly to reach ~2.6 and ~2.4 $cm^3\ mol^{-1}$ K at 2 K, for **21**·$2H_2O$ and **22**·$3H_2O$ respectively. This decrease could be attributed to the presence of magnetic anisotropy and/or weak antiferromagnetic interaction between the Co(II) centres in **21**·$2H_2O$; whereas for **22**·$3H_2O$ this could be attributed to the presence of magnetic anisotropy, the thermal depopulation of excited m_J sublevels of the Ce^{III} and/or weak antiferromagnetic exchange interactions. Additionally, magnetisation versus field plots at 2, 4 and 6 K did not saturate, suggesting the presence of significant zero-field splitting (ZFS) (Fig. 7.33 right).

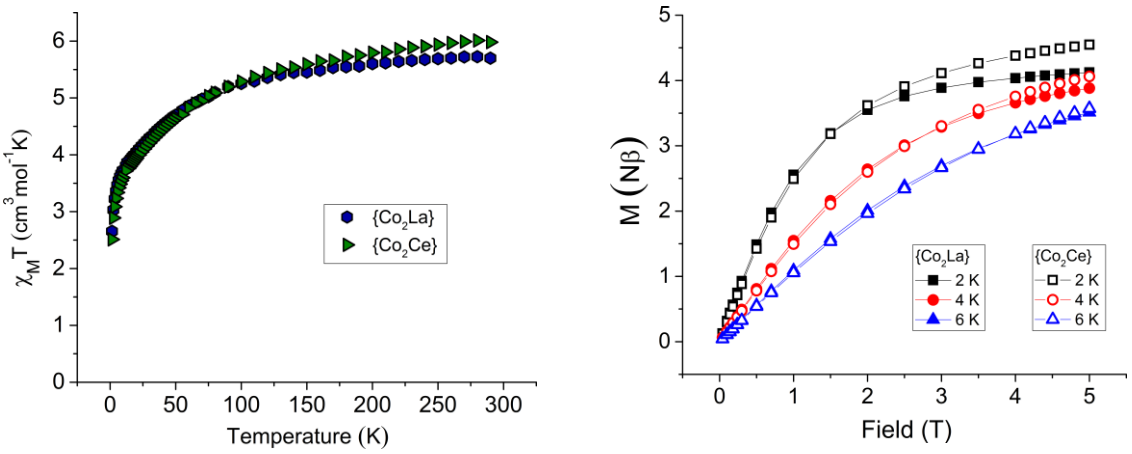

Figure 7.33 *Left)* $\chi_M T$ versus Temperature data for **21**·$2H_2O$ (blue) and **22**·$3H_2O$ (green) in a field of 1000 Oe from 290 – 2 K. *Right*) Magnetisation versus Field data at temperatures 2, 4 and 6 K for complexes **21**·$2H_2O$ (solid symbols) and **22**·$3H_2O$ (open symbols). The solid lines are a guide for the eye.

The dc magnetic susceptibility data and the magnetisation curves of **21**·2H_2O were fitted simultaneously using the programme PHI[61]. Due to the fact that the intramolecular and intermolecular Co···Co' distances are similar (~7.6 Å) and therefore it may be difficult to distinguish them, we used the following effective Hamiltonian equation[62] (equation 7.1) including also the intermolecular parameter *zj*:

$$\hat{H} = -2J(\hat{S}_1 \cdot \hat{S}_2) + D\sum_{i=1}^{2}\left(\hat{S}_{iz}^2 - \frac{1}{3}S_i(S_i+1)\right) + \sum_{i=1}^{2}\mu_B \vec{B}\cdot\vec{g}\cdot\hat{S}_i \quad (7.1)$$

Equation 7.1 takes into account the coupling between the Co^{II} ions (*J*), the axial ZFS for the Co^{II} ions (*D*) which is equal for both centres and the Zeeman interaction, in that order. The rhombic ZFS term (*E*) was not introduced in order to avoid overparameterisation. The above parameters could display a large range of values depending on factors such as the geometrical features of the metal centres and/or the intramolecular and intermolecular Co···Co' distances. Hence, a survey of the parameters *D* and *g* was performed with programme PHI[61] in order to extract some initial values (Fig. A7.10 in the appendix). The survey suggests that there is not a unique solution for *D*, which could adopt either positive or negative values, and the *g* factor is found within the range ~2.3 – 2.6. Taking into account these results, we fitted the data considering two cases: one with a positive *D* and one with a negative *D*. Figure 7.34 shows the fitting of the experimental data, while Table 7.9 shows the extracted values for each case along with the residual errors.

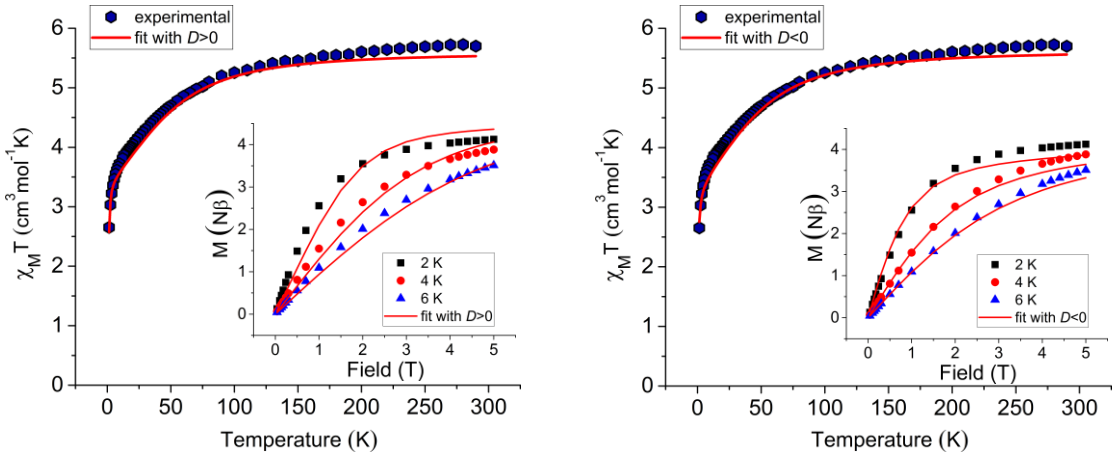

Figure 7.34 $\chi_M T$ versus Temperature data for **21**·2H_2O in a field of 1000 Oe from 290–2 K. *Inset*: Magnetisation versus field data at temperatures 2, 4, and 6 K for **21**·2H_2O. The red solid lines represent the fit with **eqn 7.1** (including the *zj* parameter): fit with *D*>0 (*left*) and *D*<0 (*right*) (see the text for details).

Table 7.9 Magnetic parameters for **21**·2H_2O extracted with programme PHI[61] using equation 7.1.

Equation 7.1				
D **(cm^{-1})**	***g***	***J*** **(cm^{-1})**	***zj*** **(cm^{-1})**	**Residual (%)**
+57.04 (±1.24)	2.44	−0.20 (±0.007)	0.035 (±0.003)	81.14
−54.69 (±1.72)	2.45	0.055 (±0.009)	−0.048 (±0.004)	99.99

The extracted *D* and *g* values are in agreement with previously reported high anisotropy penta- and hexa-coordinate Co(II) complexes with square pyramidal and trigonal prismatic geometries[63-69], while the small *J* and *zj* values are reasonable considering that the intra- and intermolecular Co···Co' distances are ~7.6 Å and therefore weak magnetic exchange (due to dipolar interactions) is expected.[70-74] The axial ZFS parameters and the *g* values are similar for negative and positive *D* values. However, a negative *J* and positive *zj* is obtained for *D*>0, whereas the opposite applies for *D*<0 (*J*>0 and *zj*<0). Furthermore, the residual error for *D*>0 is significant, an indication that the agreement between the experimental data and the fit is not good, as also can be seen in the M vs H data (Fig. 7.34 left inset); whereas for *D*<0 the residual is 99.99% indicating a good agreement between the experimental data and the fit (Fig. 7.34 right inset). However, we are aware that the inclusion of all the above parameters could lead to overparameterisation. Hence, we also fitted the data with eqn 7.1 excluding the *zj* parameter, and with eqn 7.2 (see below) where the *J* parameter is omitted but including the zj parameter. Again, the rhombic ZFS term (*E*) was not introduced in order to avoid further overparameterisation. Table 7.10 shows the extracted values for both equations.

$$\hat{H} = -2J(\hat{S}_1 \cdot \hat{S}_2) + D\sum_{i=1}^{2}\left(\hat{S}_{iz}^2 - \frac{1}{3}S_i(S_i+1)\right) + \sum_{i=1}^{2}\mu_B \vec{B}\cdot\vec{\vec{g}}\cdot\hat{S}_i \quad (7.1)$$

$$\hat{H} = D\sum_{i=1}^{2}\left(\hat{S}_{iz}^2 - \frac{1}{3}S_i(S_i+1)\right) + \sum_{i=1}^{2}\mu_B \vec{B}\cdot\vec{\vec{g}}\cdot\hat{S}_i \quad (7.2)$$

Fitting of the data with eqn 7.1 revealed that in the case of *D*>0 the fit of the susceptibility data was satisfactory; however the fit of the M vs H data shows a discrepancy from the experimental data (Fig. 7.35 left). The opposite behaviour is observed for *D*<0; the fit of the M vs H data is satisfactory but not for the susceptibility data (Fig. 7.35 right). The residual error for both fits is ~99.98 – 99.99%. Although we can observe that in both cases the |*D*| value is relatively high and equal to ~55 – 60 cm^{-1}, further investigation is needed to determine the sign of *D* and to determine the exact value of *g* (*e.g.* HFEPR, theoretical studies).

Table 7.10 Magnetic parameters for **21**·2H_2O extracted with programme PHI[61] using eqns 7.1 and 7.2.

Equation 7.1			
D **(cm^{-1})**	***g***	***J*** **(cm^{-1})**	**R (%)**
+55.40 (±1.61)	2.44	−0.10 (±0.011)	99.97
−62.79 (±2.03)	2.56	−0.030 (±0.003)	99.99
Equation 7.2			
D **(cm^{-1})**	***g***	***zj*** **(cm^{-1})**	**R (%)**
+54.45 (±1.77)	2.44	−0.22 (±0.004)	86.20
−36.61 (±0.92)	2.48	−0.072 (±0.019)	86.25

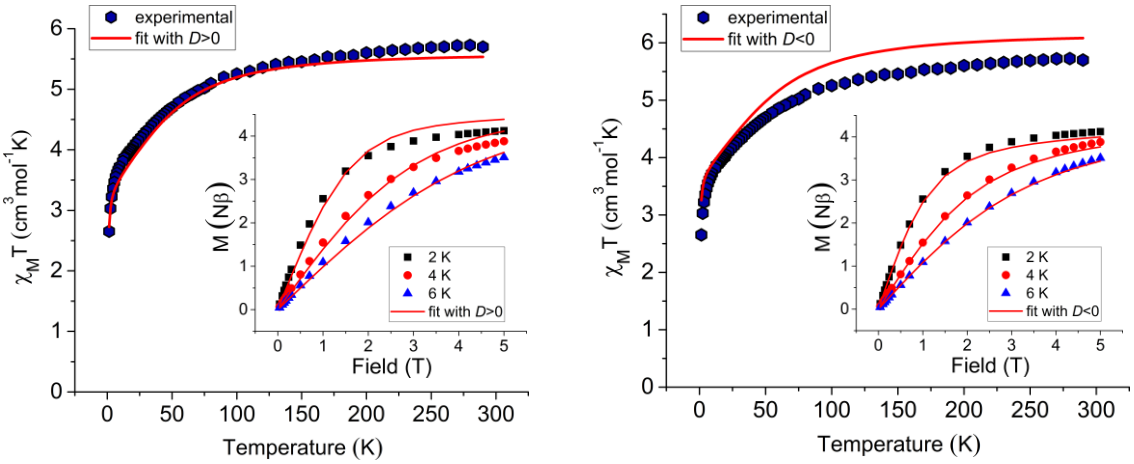

Figure 7.35 $\chi_M T$ versus Temperature data for **21**·2H_2O in a field of 1000 Oe from 290–2 K. *Inset*: Magnetisation versus field data at temperatures 2, 4, and 6 K for **21**·2H_2O. The red solid lines represent the fit with **eqn 7.1** (excluding the *zj* parameter): fit with *D*>0 (*left*) and *D*<0 (*right*) (see the text for details).

Furthermore, fitting of the data with eqn 7.2 (Fig. 7.36), including the *zj* parameter, revealed that in the case of *D*>0 the fit of the susceptibility data was satisfactory; however the fit of the M vs H data shows a discrepancy from the experimental data. Again, the opposite behaviour is observed for a *D*<0; the fit of the M vs H data is satisfactory but not for the susceptibility data. The fit of the data with eqn 7.2 and positive *D* produced similar parameters as with eqn 7.1 with and without the introduction of *zj* (Tables 7.9 and 7.10);

however, this is not the case for negative *D* (Table 7.10), where the magnetic anisotropy is notably lower using eqn 7.2.

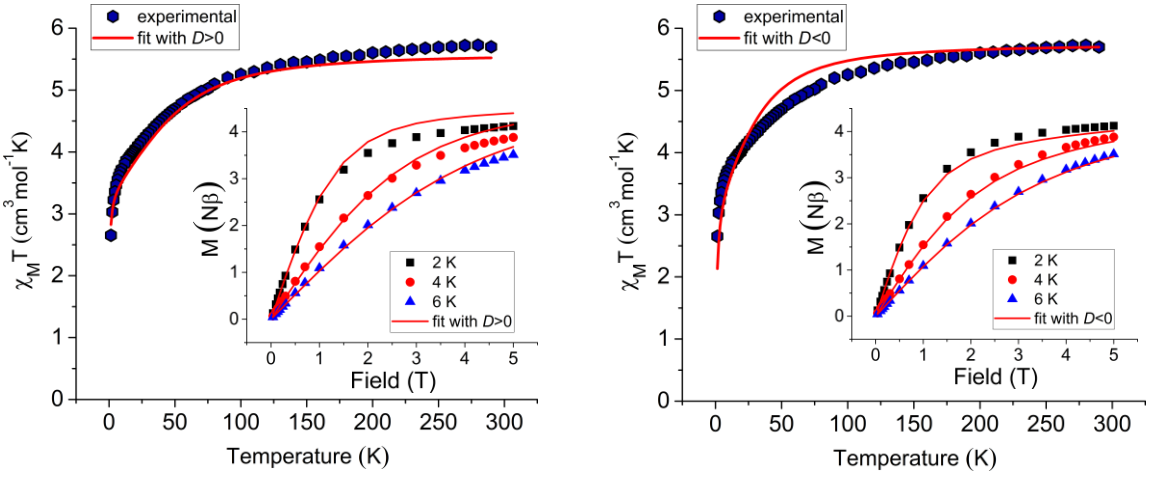

Figure 7.36 $\chi_M T$ versus Temperature data for **21**·2H_2O in a field of 1000 Oe from 290–2 K. *Inset*: Magnetisation versus field data at temperatures 2, 4, and 6 K for **21**·2H_2O. The red solid lines represent the fit with **eqn 7.2** (including the *zj* parameter): fit with *D*>0 (*left*) and *D*<0 (*right*) (see the text for details).

Additionally, the residuals of the fits with eqn 7.2 are relatively poor (~86%), which could be indicative that a model including only intermolecular interactions (*zj*) is not accurate. Moreover, the fact that in almost all the cases |*D*| = 55 – 60 cm^{-1} and *g* = ~2.44 – 2.50, is a strong indication of the presence of high anisotropy. Nevertheless, due to the complexity of this system, *i.e.* the presence of a mixture of penta- and hexa-coordinate Co(II) centres and similar intra- and intermolecular Co···Co' distances (~7.6 Å), we could not extract any final values for the magnetic parameters. Further investigation is needed to determine the sign of the axial ZFS parameter, *D*, and the value of *g* (*e.g.* HFEPR, theoretical studies). Finally, due to the fact that *J* and *zj* exhibit very small values, we also fitted the data with equation 7.2 excluding the parameter *zj*, in order to examine if it is possible to fit the data without any magnetic interaction between the Co(II) centres. However, low quality fits were produced (especially at low temperatures) with residuals ~65 − 85%, indicating that a model with no magnetic interactions between the Co(II) centres is not accurate (Fig. A7.11 and Table A7.7 in the appendix).

In order to fit the susceptibility and magnetisation data of complex **22**·3H_2O, theoretical studies are needed in order to determine the crystal field parameters arising from the distorted geometry of the Ce(III) centre. In addition, as seen for complex **21**·2H_2O there are multiple possible ways to fit the data (*i.e.* there is no unique solution for *D*, and the *J*

and *zj* parameters adopt similar values), and therefore the addition of the Ce(III) centre in the fitting of the data would be very challenging. Hence, no fit was performed for **22**·3H_2O.

Alternating current (ac) susceptibility measurements were performed for complexes **21**·2H_2O and **22**·3H_2O in the temperature range 10−2 K, in a 3 Oe ac field and in the frequency range 1–1488 Hz, in order to examine if there is slow magnetic relaxation. In the absence of a dc field none of the complexes show any out-of-phase signals (Fig. 7.37 left and 7.38 left). However, with the application of a 2000 Oe dc field complex **21**·2H_2O shows the onset of a weak χ'' signal (Fig. 7.37 right), whereas complex **22**·3H_2O shows only the onset of a very weak χ'' signal (Fig. 7.38 right). Due to the weak χ'' signal in both complexes, we did not expect to see any improvement in the signal by performing an isothermal field sweep ac measurement; hence no further magnetic measurements were carried out. The absence of slow magnetic relaxation could be attributed to: the presence of transverse anisotropy due to deviations from the ideal geometries[75, 76] (although the *E* term was not accounted for during the fit of the dc data due to overparameterisation); intermolecular *π*-*π* interactions and dipolar interactions[63, 77], and/or hyperfine interactions[63, 77], all of which can facilitate a faster magnetic relaxation.

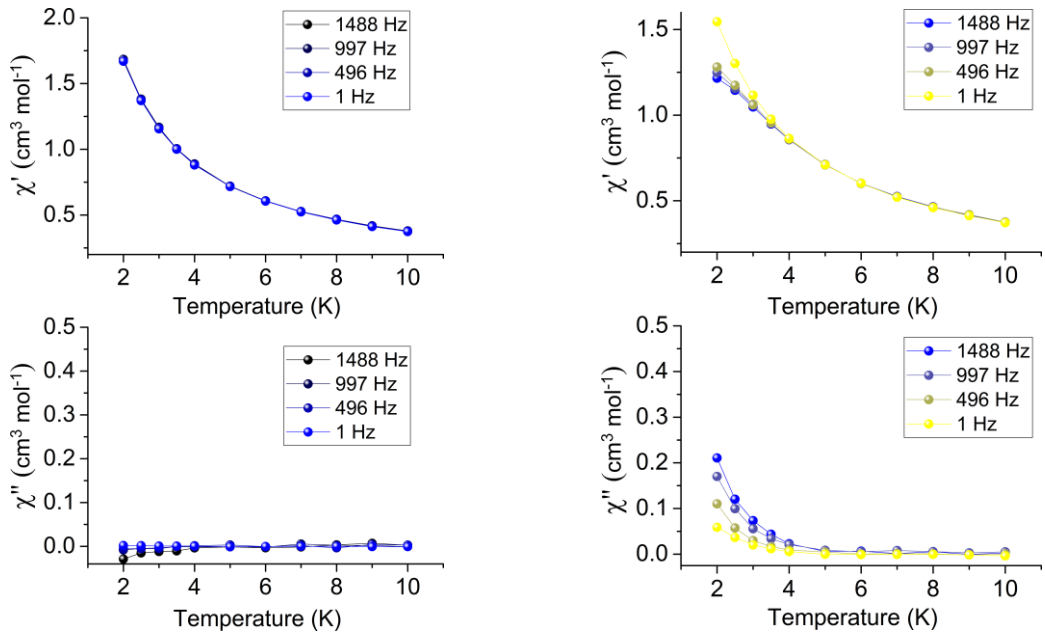

Figure 7.37 Temperature dependence of the in-phase (*top*) and the out-of-phase (*bottom*) ac susceptibility signals in 0 (*left*) and 2000 (*right*) Oe dc field, in the frequency range 1 – 1488 Hz, for complex **21**·2H_2O. The solid lines are a guide to the eye.

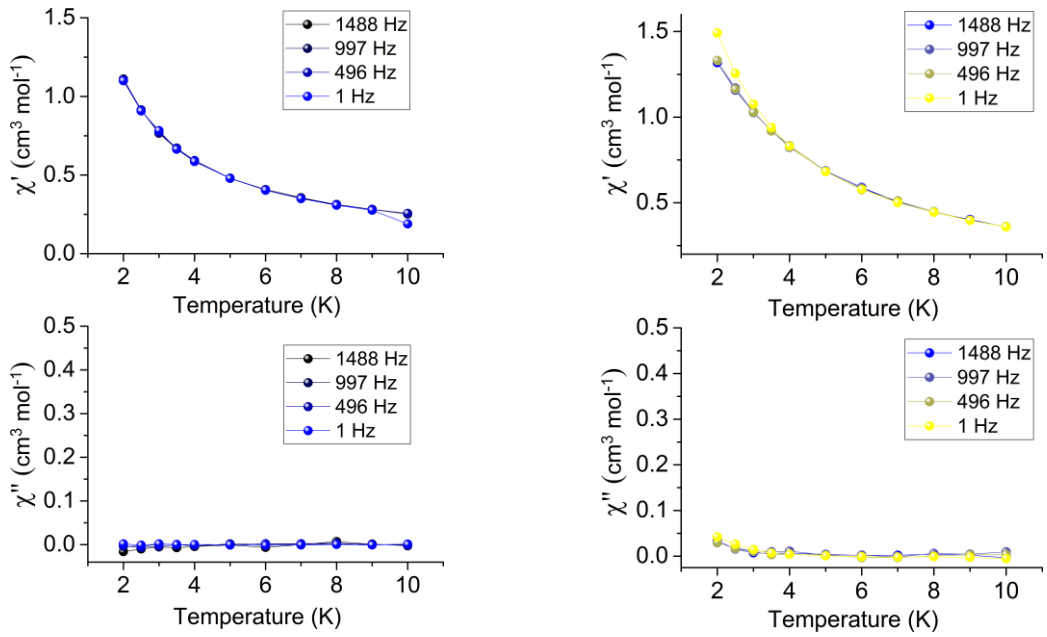

Figure 7.38 Temperature dependence of the in-phase (*top*) and the out-of-phase (*bottom*) ac susceptibility signals in 0 (*left*) and 2000 (*right*) Oe dc field, in the frequency range 1 – 1488 Hz, for complex **22**·3H_2O. The solid lines are a guide to the eye.

Figure 7.39 (left) shows the dc $\chi_M T$ versus temperature data for **23**·MeCN·8H_2O in a field of 1000 Oe and in the 290–2 K temperature range. The $\chi_M T$ value at room temperature is ~31 cm^3 mol^{-1} K, which is in good agreement with the expected value for two non-interacting Dy(III) ($^6H_{15/2}$ and g = 4/3) and one high-spin Co(II) (S = 3/2 and $g \approx 2.38$). This indicates the presence of a significant magnetic anisotropy, which is expected for highly anisotropic Co^{II} ions in a distorted octahedral geometry.[78-81] $\chi_M T$ gradually decreases on decreasing temperature until ~60 K and then drops rapidly to reach ~17.9 cm^3 mol^{-1} K at 2 K. This may be attributed to the presence of magnetic anisotropy, the thermal depopulation of excited m_J sublevels of Dy(III) and/or weak antiferromagnetic interactions (Co···Dy and Dy···Dy ~8.5 Å). Additionally, magnetisation versus field plots at 2, 4 and 6 K did not saturate, indicating of the presence of significant magnetic anisotropy (Fig. 7.39 right).

The dynamic magnetic properties of **23**·MeCN·8H_2O were also studied. In zero applied dc field, **23**·MeCN·8H_2O displays only the onset of a weak χ'' signal due to efficient zero-field quantum tunnelling (Fig. 7.40 left). By using an applied dc field of 2000 Oe to suppress tunnelling, a slight change of the χ'' signal is observed (Fig. 7.40 right)

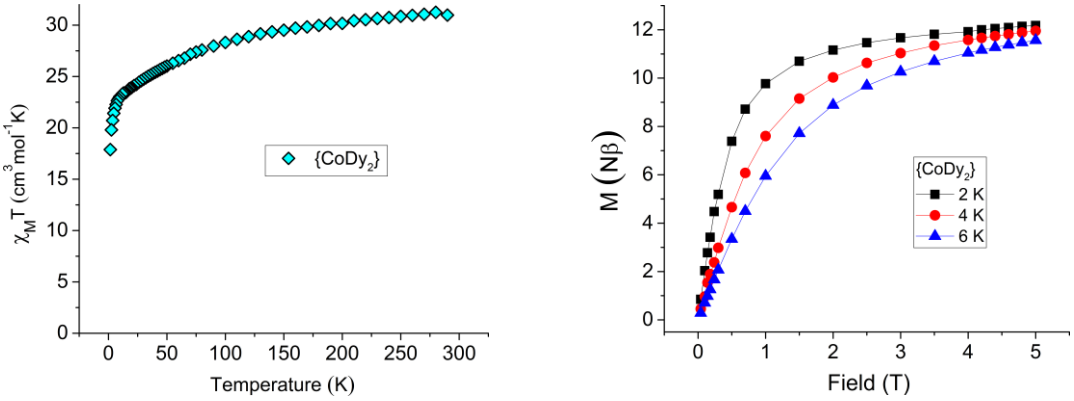

Figure 7.39 *Left)* $\chi_M T$ versus Temperature data for complex **23**·MeCN·8H_2O in a field of 1000 Oe from 290 – 2 K. *Right)* Magnetisation versus Field data at temperatures 2, 4 and 6 K. The solid lines are a guide to the eye.

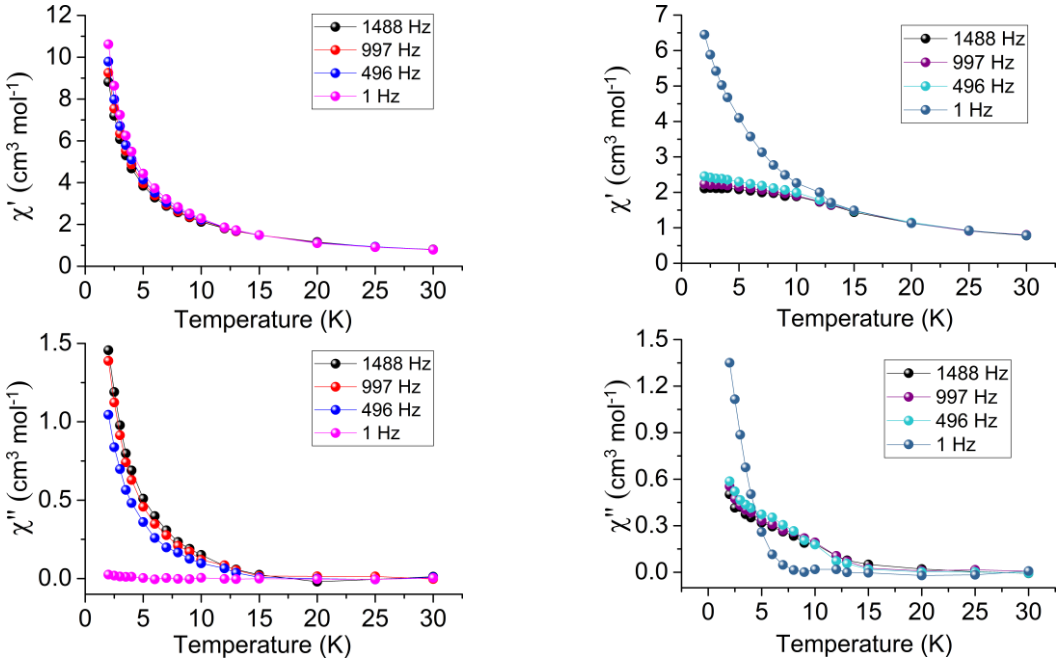

Figure 7.40 Temperature dependence of the in-phase (*top*) and the out-of-phase (*bottom*) ac susceptibility signals in 0 (*left*) and 2000 (*right*) Oe dc field, in the frequency range 1 – 1488 Hz, for complex **23**·MeCN·8H_2O. The solid lines are a guide to the eye.

Despite the fact that the χ'' signal is weak, the shape of the out-of-phase signal around 6 K prompted us to investigate further the dependence of the ac signals with the field. Variable dc fields (200 − 7000 Oe) were applied to **23**·MeCN·8H_2O at 6 K (Fig. 7.41 left) and indeed we observe a field dependence at higher frequencies. In order to obtain the optimum dc field at which the characteristic relaxation time of the magnetisation (τ)

possesses the largest value, we fitted the Cole−Cole plot and extracted the τ values (Fig. 7.41 right). The optimum field was observed at 3000 Oe and hence the frequency dependence of the in-phase and out-of-phase magnetic susceptibility was measured under this field, in the 2 − 18 K temperature range (Fig. 7.42).

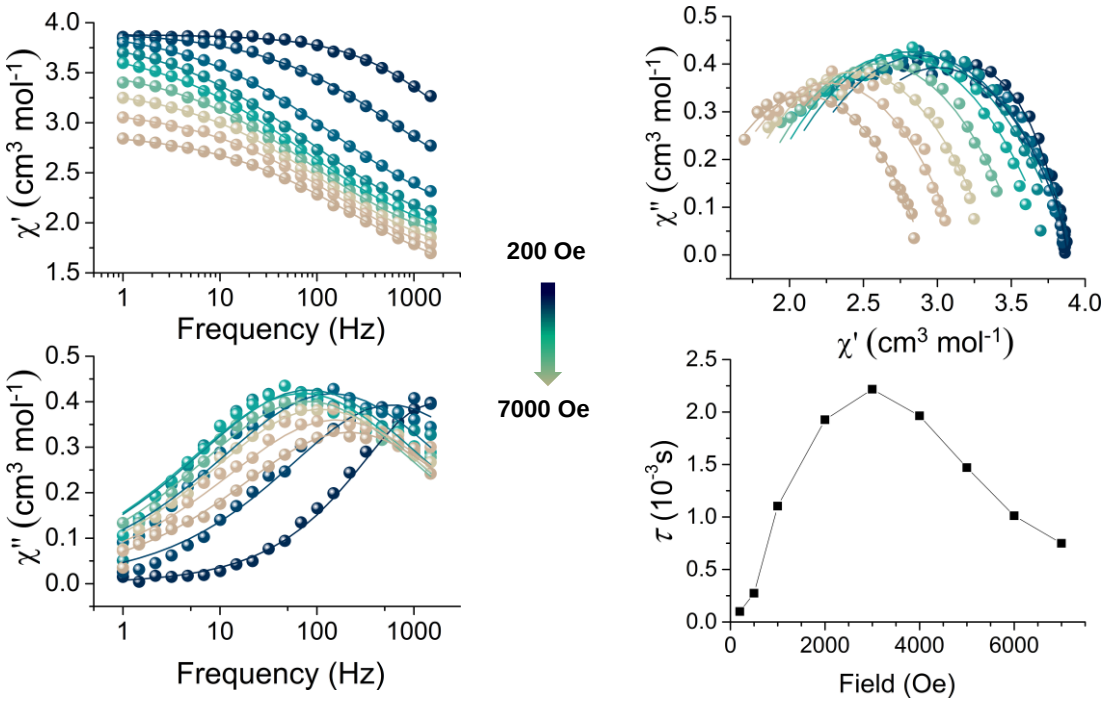

Figure 7.41 *Left)* Frequency dependent in-phase (*top*) and out-of-phase (*bottom*) ac susceptibility signals for complex **23**·MeCN·8H_2O under different applied dc fields at 6 K (the solid lines correspond to the fit with CC-FIT[82, 83]) *Right)* Cole–Cole plot of the ac magnetic susceptibility at variable fields at 6 K (*top*) (the solid lines correspond to the fit with CC-FIT[82, 83]) and the plot of τ vs field (*bottom*) (the solid line is a guide for the eye).

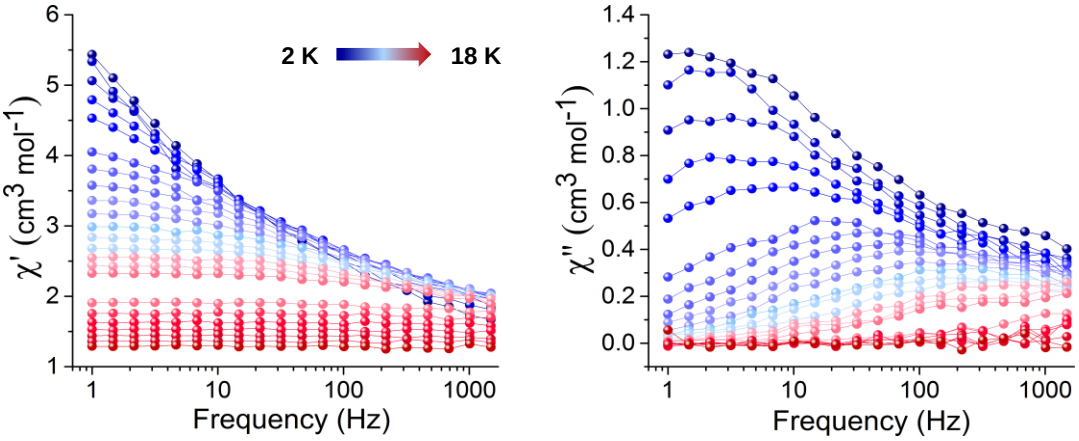

Figure 7.42 Frequency dependent in-phase (*left*) and out-of-phase (*right*) susceptibility signals for complex **23**·MeCN·8H_2O in 3000 Oe dc applied magnetic field. The solid lines are a guide to the eye.

Attempts to fit the Cole−Cole plot for the entire temperature range 2 − 18 K were not successful; hence, the fit was performed for the temperature range 3.5 – 10 K with the programme CC-FIT[82, 83] (Fig. 7.43). The τ and α parameters were extracted for each temperature (Table 7.11). The values for parameter α were found to be ~0.4 – 0.7, indicative of a larger distribution of relaxation times and possible multiple relaxation pathways in **23**·MeCN·8H_2O.

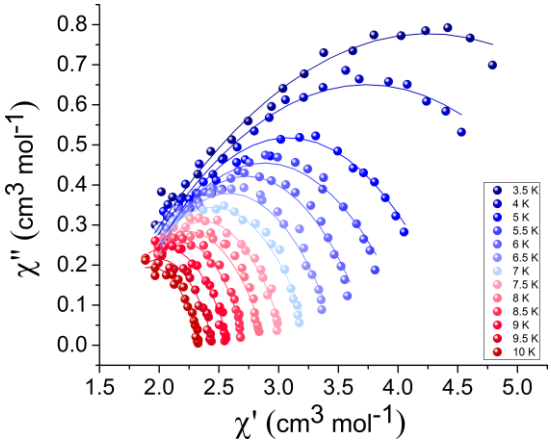

Figure 7.43 The Cole–Cole plot of the ac magnetic susceptibility of **23**·MeCN·8H_2O at 3000 Oe for the 3.5 – 10 K temperature range. The solid lines correspond to the fit (CC-FIT).[82, 83]

Table 7.11 Cole-Cole fit values of **23**·MeCN·8H_2O with an applied dc field of 3000 Oe.

Temperatures (K)	χ_S (cm^3 mol^{-1})	χ_T (cm^3 mol^{-1})	τ (s)	α	Residual
3.5	1.42851	7.06775	0.05498	0.65738	0.02622
4	1.477	5.99658	0.02361	0.6432	0.01874
5	1.62059	4.53936	0.00546	0.56573	0.03424
5.5	1.60486	4.15888	0.00329	0.56432	0.01982
6	1.67152	3.79381	0.00231	0.51812	0.01979
6.5	1.65609	3.51135	0.00138	0.50606	0.01408
7	1.60943	3.28668	9.96592E-4	0.50342	0.018
7.5	1.68272	3.05915	8.10249E-4	0.46257	0.01286
8	1.5696	2.89887	4.66319E-4	0.48479	0.01437
8.5	1.68018	2.72074	4.79332E-4	0.41762	0.00856
9	1.50897	2.58789	2.38346E-4	0.46045	0.01191

9.5	1.54758	2.45561	2.0102E-4	0.43711	0.00931
10	1.51502	2.34418	1.4795E-4	0.43939	0.00612

The τ values were used to construct an ln(τ) – ln(T) plot (Fig. 7.44 left) for the temperatures 3.5 – 10 K; it is clear that τ obeys the T^{-n} law with n = 5.5, suggesting that the Raman process should be the dominant relaxation process.[84] However, as mentioned above, the broad distribution of the relaxation times suggests the presence of multiple relaxation processes and therefore other processes should be included in the fit, as shown in equation 7.3:

$$\tau^{-1} = AH^{m}T + \frac{B_1}{1+B_2H^2} + CT^{n} + \tau_0^{-1}\exp(\frac{-\Delta E}{k_BT}) \qquad (7.3)$$

The terms are the direct, tunnelling, Raman and Orbach contributions, in that order. Attempts to fit the data with the above equation did not produce any reasonable results. Additionally, we attempted to fit the τ versus field data using only the terms for direct and tunnelling processes (which are dependent on field) to extract the parameters *A*, B_1, and B_2, however with no success. This could be an indication that there is a more complicated dependence of τ with the field. Figure 7.44 (right) shows the τ^{-1} versus T plot where the Raman, Orbach and direct processes are fitted separately.

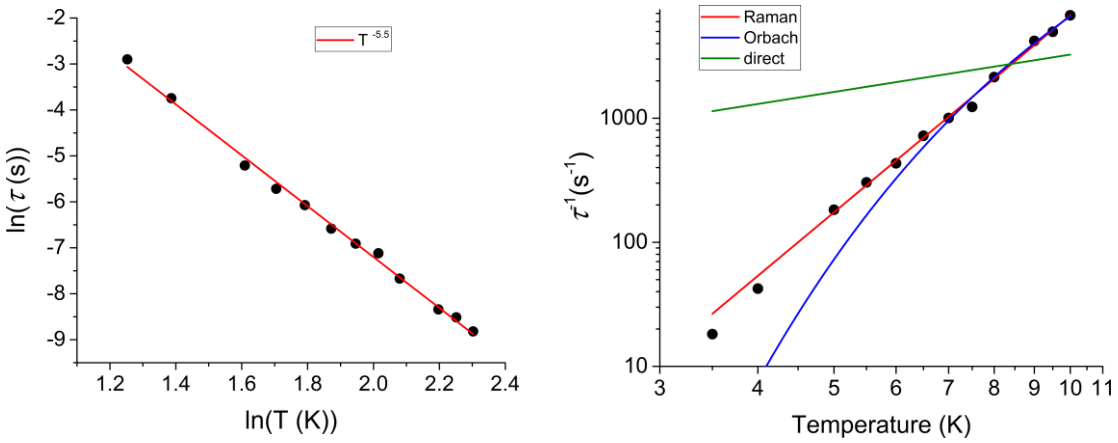

Figure 7.44 *Left)* The plot of ln(τ) vs ln(T) for **23**·MeCN·8H_2O in the temperature range 3.5 – 10 K. The red solid line corresponds to the fit with the power law $T^{-5.5}$. *Right)* The plot of τ^{-1} vs T for **23**·MeCN·8H_2O in the temperature range 3.5 – 10 K. Each solid line corresponds to the fit using Raman (red), Orbach (blue) or direct (green) process.

The extracted parameters for the Raman process are C = 0.036 K^{-n} s^{-1} and n = 5.28, and for Orbach are $\Delta E/k_B$ = 45.1 (±1.8) K and τ_0 = 1.5 x 10^{-6} s, whereas the quality of the fit using only the direct process is poor and there is a big discrepancy with the experimental data. The above values for the Raman and Orbach processes are consistent with other Co^{II}/Dy^{III} complexes[85-90]; however, attempts to fit the data with a combination of the Raman and Orbach processes produced large errors. Hence, theoretical studies are needed in order to gain a better insight into the contribution of each process to the slow relaxation of the magnetisation.[86, 91, 92]

As mentioned earlier in this chapter there are only two $\{Co^{II}Dy^{III}_2\}$ complexes reported in the literature, and only one of them has been magnetically characterised, complex $[Dy^{III}_2Co^{II}(L^1)_8]\cdot 6H_2O$ (HL^1 = salicylicaldehyde) (**I**)[11]. Complex **I** has a linear Dy−Co−Dy metallic core, and exhibits dominant ferromagnetic exchange interactions. Dynamic ac experiments revealed temperature and frequency dependence in zero dc field in the 1.9 – 16 K temperature range. The relaxation times extracted from the fit of the Cole−Cole plot were plotted as ln(τ) versus T^{-1} as shown in Fig. 7.45; the modelling of the higher and lower temperatures with the Arrhenius law ($\ln(\tau) = \ln(\tau_0) + \frac{U_{eff}}{k_B T}$, where U_{eff}/k_B = energy barrier and τ_0 = pre-exponential factor) produced the following values: $U_{eff}/k_B \approx 17$ K and τ_0 = 3.55 x 10^{-5} s for T < 5 K and $U_{eff}/k_B \approx 127$ K and τ_0 = 1.69 x 10^{-9} s for T > 5 K. Xiao-Lei Li *et al.* report that this behaviour suggests that at higher T the relaxation occurs through the excited Kramers doublets of individual Dy(III) ions[11], while at low temperatures the weak coupling between Dy(III) ions and Co(II) becomes more important.[93-95]

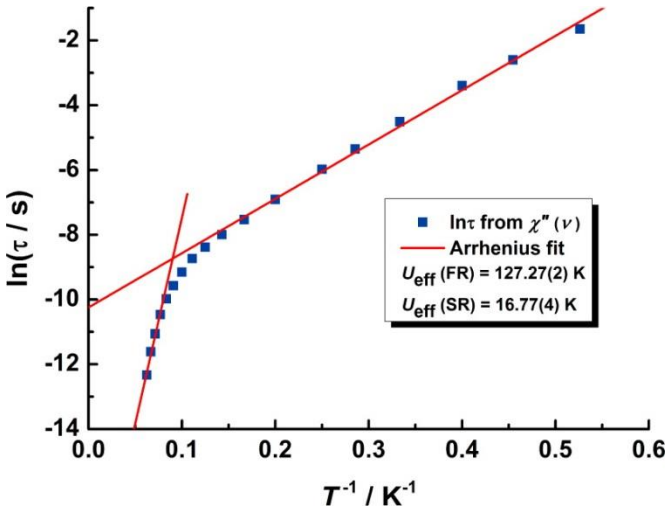

Figure 7.45 Magnetization relaxation time, ln(τ) vs T^{-1} plot for **I** in zero dc field in the 1.9 – 16 K temperature range. The solid lines are fitted with the Arrhenius law (see text).[11]

In the case of **23**·MeCN·$8H_2O$, only after the application of a dc field fully formed χ'' signals are observed, an indication of the presence of QTM. Moreover, the intramolecular Co···Dy and Dy···Dy distances are ~8.5 Å, and therefore the absence or only a weak magnetic exchange (due to dipolar interactions) is expected. Hence, we propose that the above hypothesis is not applicable for **23**·MeCN·$8H_2O$, and a model including both the Raman and Orbach processes is more accurate. However, without theoretical calculations we cannot come to a strong conclusion.

7.4 Conclusions

In this chapter we have investigated the coordination chemistry of the multipocket ligand $[H_5L]\cdot 3Cl$ (= 2,6-bis[4(1-*N*-phenyl-3-methyl-pyrazolium-5-one)carbonyl]pyridinium trichloride) along with Co(II) and 4*f* metal ions. We showed the versatility of this ligand, which can lead to pure 4*f* or mixed metal Co(II)-4*f* complexes, with nuclearities varying from 1 to 9 metal centres. As a result we managed to isolate seven new complexes:

- $[La^{III}_9(L^{2-})_7(NO_3)_4(CO_3)_4(OH)(H_2O)_8]\cdot xMeCN\cdot yH_2O$ (**18**$\cdot xMeCN\cdot yH_2O$),
- $[HNEt_3][Ce^{III}_3(HL^{-})_2(NO_3)_7(H_2O)_2][Cl]\cdot xMeCN\cdot yH_2O\cdot zEt_2O$ (**19a**) and $[HNEt_3][Ce^{III}_3(HL^{2-})(H_2L)(NO_3)_7(H_2O)_2][Cl]\cdot xMeCN\cdot yH_2O\cdot zEt_2O$ (**19b**),
- $[Dy^{III}(HL^{-})_2(H_2O)_4][Cl]\cdot xMeCN\cdot yH_2O$ (**20**$\cdot xMeCN\cdot yH_2O$),
- $[Co^{II}_2Ln^{III}(L^{2-})_2(NO_3)_{2.3}Cl_{0.7}(MeCN)]$ where Ln = La (**21**) and Ce (**22**),
- $[HNEt_3][Co^{II}Dy^{III}_2(L^{2-})_4(HL^{-})(H_2O)_2]\cdot xMeCN\cdot yH_2O$ (**23**$\cdot xMeCN\cdot yH_2O$) and
- $[Gd^{III}_6(L^{2-})_4(OH)_4(O^{2-})(MeOH)_6(H_2O)_2][NO_3]_{3.75}[Cl]_{0.25}\cdot xMeOH\cdot yH_2O$ (**24**$\cdot xMeOH\cdot yH_2O$).

Complex **18**$\cdot xMeCN\cdot yH_2O$ is the first homometallic $\{La^{III}_9\}$ complex, while complex **23**$\cdot xMeCN\cdot yH_2O$ is only the third $\{Co^{II}Dy^{III}_2\}$ to be reported. Full magnetic characterisation was performed for the Co(II)-4*f* complexes, with complexes $\{Co^{II}_2La^{III}\}$ and $\{Co^{II}_2Ce^{III}\}$ exhibiting a large magnetic anisotropy, but only the onset of out-of-phase signals under an applied dc field. The absence of slow magnetic relaxation could be attributed to the presence of quantum tunnelling which could be induced by: the presence of transverse anisotropy, intermolecular *π*-*π* interactions and dipolar interactions, and/or hyperfine interactions. Complex $\{Co^{II}Dy^{III}_2\}$ on the other hand, displays slow magnetic relaxation in a 3000 Oe dc field. Interpretation of the ac magnetic susceptibility data suggests that the dominant relaxation process is Raman with parameters: C = 0.036 K^{-n} s^{-1} and n = 5.28; however, the Orbach process should not be excluded, and the fit of the higher temperature region with the Arrhenius law produces an energy barrier of $\Delta E/k_B$ = 45.1 (±1.8) K with τ_0 = 1.5 x 10^{-6} s, which is well within the highest values for other reported Co^{II}/Dy^{III} complexes.

Finally, this work could be further extended with the introduction of co-ligands and/or the use of the smaller complexes as building blocks (*e.g.* $\{Ce^{III}_3\}$, $\{Dy^{III}\}$ and $\{Co^{II}_2Ln^{III}\}$) towards the synthesis of even higher nuclearity clusters. Additionally, due to the synthetic flexibility of ligand $[H_5L]\cdot 3Cl$, other 3*d* metal ions could be introduced in the presence, or absence, of 4*f* metal ions in order to explore further its coordination chemistry.

7.5 References

1. C. Pettinari, F. Marchetti, A. Drozdov, V. Vertlib and S. Troyanov, *Inorganic Chemistry Communications*, 2001, **4**, 290-293.
2. J. Ferrando-Soria, J. Vallejo, M. Castellano, J. Martínez-Lillo, E. Pardo, J. Cano, I. Castro, F. Lloret, R. Ruiz-García and M. Julve, *Coordination Chemistry Reviews*, 2017, **339**, 17-103.
3. Y.-Z. Zheng, G.-J. Zhou, Z. Zheng and R. E. P. Winpenny, *Chemical Society Reviews*, 2014, **43**, 1462-1475.
4. R. Brimblecombe, G. F. Swiegers, G. C. Dismukes and L. Spiccia, *Angewandte Chemie International Edition*, 2008, **47**, 7335-7338.
5. G. Maayan, N. Gluz and G. Christou, *Nature Catalysis*, 2018, **1**, 48-54.
6. G. Guthausen, J. R. Machado, B. Luy, A. Baniodeh, A. K. Powell, S. Krämer, F. Ranzinger, M. P. Herrling, S. Lackner and H. Horn, *Dalton Trans.*, 2015, **44**, 5032-5040.
7. M. Murrie, *Polyhedron*, 2018, **150**, 1-9.
8. K. Liu, W. Shi and P. Cheng, *Coordination Chemistry Reviews*, 2015, **289-290**, 74-122.
9. K. R. Vignesh, S. K. Langley, K. S. Murray and G. Rajaraman, *Chemistry – A European Journal*, 2017, **23**, 1654-1666.
10. S. K. Langley, D. P. Wielechowski, V. Vieru, N. F. Chilton, B. Moubaraki, B. F. Abrahams, L. F. Chibotaru and K. S. Murray, *Angewandte Chemie International Edition*, 2013, **52**, 12014-12019.
11. X.-L. Li, F.-Y. Min, C. Wang, S.-Y. Lin, Z. Liu and J. Tang, *Inorganic Chemistry*, 2015, **54**, 4337-4344.
12. R. Sessoli and A. K. Powell, *Coordination Chemistry Reviews*, 2009, **253**, 2328-2341.
13. K. S. Pedersen, J. Bendix and R. Clérac, *Chemical Communications*, 2014, **50**, 4396-4415.
14. C. Papatriantafyllopoulou, E. E. Moushi, G. Christou and A. J. Tasiopoulos, *Chemical Society Reviews*, 2016, **45**, 1597-1628.
15. T. Shiga, M. Ohba and H. Ōkawa, *Inorganic Chemistry*, 2004, **43**, 4435-4446.
16. T. Shiga, N. Ito, A. Hidaka, H. Ōkawa, S. Kitagawa and M. Ohba, *Inorganic Chemistry*, 2007, **46**, 3492-3501.
17. D. Aguilà, L. A. Barrios, O. Roubeau, S. J. Teat and G. Aromí, *Chemical Communications*, 2011, **47**, 707-709.
18. J. Shi, Y. Hou, W. Chu, X. Shi, H. Gu, B. Wang and Z. Sun, *Inorganic Chemistry*, 2013, **52**, 5013-5022.
19. A. S. Dinca, S. Shova, A. E. Ion, C. Maxim, F. Lloret, M. Julve and M. Andruh, *Dalton Transactions*, 2015, **44**, 7148-7151.
20. V. Velasco, D. Aguilà, L. A. Barrios, I. Borilovic, O. Roubeau, J. Ribas-Ariño, M. Fumanal, S. J. Teat and G. Aromí, *Chemical Science*, 2015, **6**, 123-131.
21. L. A. Barrios, D. Aguilà, O. Roubeau, K. S. Murray and G. Aromí, *Australian Journal of Chemistry*, 2009, **62**, 1130-1136.
22. T. N. Trieu, M. H. Nguyen, U. Abram and H. H. Nguyen, *Zeitschrift fur Anorganische und Allgemeine Chemie*, 2015, **641**, 863-870.
23. T. Shiga, H. Ōkawa, S. Kitagawa and M. Ohba, *Journal of the American Chemical Society*, 2006, **128**, 16426-16427.
24. Y.-N. Guo, G.-F. Xu, W. Wernsdorfer, L. Ungur, Y. Guo, J. Tang, H.-J. Zhang, L. F. Chibotaru and A. K. Powell, *Journal of the American Chemical Society*, 2011, **133**, 11948-11951.
25. H.-X. Zhang, S.-Y. Wang, W.-M. Wang, H.-L. Gao and J.-Z. Cui, *Inorganic Chemistry Communications*, 2015, **62**, 94-97.

26. D. Aguilà, V. Velasco, L. A. Barrios, J. González-Fabra, C. Bo, S. J. Teat, O. Roubeau and G. Aromí, *Inorganic Chemistry*, 2018, **57**, 8429-8439.
27. J. Long, *Frontiers in Chemistry*, 2019, **7**.
28. B. S. Jensen, *Acta Chemica Scandinavica*, 1959, 1668-1670.
29. L. Natrajan, J. Pécaut and M. Mazzanti, *Dalton Transactions*, 2006, 1002-1005.
30. H. Ke, L. Zhao, G.-F. Xu, Y.-N. Guo, J. Tang, X.-Y. Zhang and H.-J. Zhang, *Dalton Transactions*, 2009, 10609-10613.
31. L. Zhao, S. Xue and J. Tang, *Inorganic Chemistry*, 2012, **51**, 5994-5996.
32. Y. Zhou, X.-Y. Zheng, J. Cai, Z.-F. Hong, Z.-H. Yan, X.-J. Kong, Y.-P. Ren, L.-S. Long and L.-S. Zheng, *Inorganic Chemistry*, 2017, **56**, 2037-2041.
33. P. C. Leverd, D. Rinaldo and M. Nierlich, *Journal of the Chemical Society, Dalton Transactions*, 2002, 829-831.
34. A. Spek, *Acta Crystallographica Section D*, 2009, **65**, 148-155.
35. B. Içli, N. Christinat, J. Tönnemann, C. Schüttler, R. Scopelliti and K. Severin, *Journal of the American Chemical Society*, 2009, **131**, 3154-3155.
36. C. M. Beavers, A. V. Prosverin, J. D. Cashion, K. R. Dunbar and A. F. Richards, *Inorganic Chemistry*, 2013, **52**, 1670-1672.
37. M. Pinsky and D. Avnir, *Inorganic Chemistry*, 1998, **37**, 5575-5582.
38. A. Ruiz-Martínez, D. Casanova and S. Alvarez, *Chemistry – A European Journal*, 2008, **14**, 1291-1303.
39. A. Ruiz-Martínez, D. Casanova and S. Alvarez, *Dalton Transactions*, 2008, 2583-2591.
40. A. Ruiz-Martínez and S. Alvarez, *Chemistry – A European Journal*, 2009, **15**, 7470-7480.
41. A. Ruiz-Martínez, D. Casanova and S. Alvarez, *Chemistry – A European Journal*, 2010, **16**, 6567-6581.
42. N. E. Brese and M. O'Keeffe, *Acta Crystallographica Section B*, 1991, **47**, 192-197.
43. I. D. Brown, Brockhouse Institute for Materials Research, McMaster University, Hamilton, Ontario Canada. idbrown@mcmaster.ca, https://www.iucr.org/__data/assets/file/0007/126574/bvparm2016.cif.
44. J. Wu, J. Jung, P. Zhang, H. Zhang, J. Tang and B. Le Guennic, *Chemical Science*, 2016, **7**, 3632-3639.
45. D. Casanova, M. Llunell, P. Alemany and S. Alvarez, *Chemistry – A European Journal*, 2005, **11**, 1479-1494.
46. J. Tang and P. Zhang, *Lanthanide Single Molecule Magnets*, Springer, Berlin, Heidelberg, Springer-Verlag Berlin Heidelberg 2015.
47. T. Yamaguchi, J.-P. Costes, Y. Kishima, M. Kojima, Y. Sunatsuki, N. Bréfuel, J.-P. Tuchagues, L. Vendier and W. Wernsdorfer, *Inorganic Chemistry*, 2010, **49**, 9125-9135.
48. C. Benelli, E. Borgogelli, M. Formica, V. Fusi, L. Giorgi, E. Macedi, M. Micheloni, P. Paoli and P. Rossi, *Dalton Transactions*, 2013, **42**, 5848-5859.
49. V. Chandrasekhar, S. Das, A. Dey, S. Hossain, S. Kundu and E. Colacio, *European Journal of Inorganic Chemistry*, 2014, **2014**, 397-406.
50. R. Modak, Y. Sikdar, A. E. Thuijs, G. Christou and S. Goswami, *Inorganic Chemistry*, 2016, **55**, 10192-10202.
51. J.-P. Costes, G. Novitchi, V. Vieru, L. F. Chibotaru, C. Duhayon, L. Vendier, J.-P. Majoral and W. Wernsdorfer, *Inorganic Chemistry*, 2019, **58**, 756-768.
52. B. Wu, *Journal of Coordination Chemistry*, 2008, **61**, 2558-2562.
53. B. Wu and C.-X. Zhao, *Acta Crystallographica Section E*, 2010, **66**, m1075.

54. Y. Zhu, F. Luo, X.-F. Feng, Z.-W. Liao, Y.-M. Song, H.-X. Huang, X.-Z. Tian, G.-M. Sun and M.-B. Luo, *Australian Journal of Chemistry*, 2013, **66**, 75-83.
55. M. Pinsky and D. Avnir, *Inorganic Chemistry*, 1998, **37**, 5575-5582.
56. S. Alvarez and M. Llunell, *Journal of the Chemical Society, Dalton Transactions*, 2000, 3288-3303.
57. S. Alvarez, D. Avnir, M. Llunell and M. Pinsky, *New Journal of Chemistry*, 2002, **26**, 996-1009.
58. X.-Q. Zhao, D.-X. Bao, J. Wang, S. Xiang and Y.-C. Li, *Inorganica Chimica Acta*, 2017, **466**, 110-116.
59. S. Tripathi, A. Dey, M. Shanmugam, R. Suriya Narayanan and V. Chandrsekhar, ch. Cobalt(II) Complexes as Single-Ion Magnets, in *Topics in Organometallic Chemistry.* , Springer, Berlin, Heidelberg, 2018.
60. S. Gomez-Coca, E. Cremades, N. Aliaga-Alcalde and E. Ruiz, *Journal of the American Chemical Society*, 2013, **135**, 7010-7018.
61. N. F. Chilton, R. P. Anderson, L. D. Turner, A. Soncini and K. S. Murray, *Journal of Computational Chemistry*, 2013, **34**, 1164-1175.
62. R. L. Carlin, *Magnetochemistry*, Springer-Verlag Berlin Heidelberg, 1986.
63. T. Jurca, A. Farghal, P.-H. Lin, I. Korobkov, M. Murugesu and D. S. Richeson, *Journal of the American Chemical Society*, 2011, **133**, 15814-15817.
64. C. Rajnák, J. Titiš, O. Fuhr, M. Ruben and R. Boča, *Inorganic Chemistry*, 2014, **53**, 8200-8202.
65. A. K. Mondal, J. Jover, E. Ruiz and S. Konar, *Chemical Communications*, 2017, **53**, 5338-5341.
66. Y.-Y. Zhu, C. Cui, Y.-Q. Zhang, J.-H. Jia, X. Guo, C. Gao, K. Qian, S.-D. Jiang, B.-W. Wang, Z.-M. Wang and S. Gao, *Chemical Science*, 2013, **4**, 1802-1806.
67. V. V. Novikov, A. A. Pavlov, Y. V. Nelyubina, M.-E. Boulon, O. A. Varzatskii, Y. Z. Voloshin and R. E. P. Winpenny, *Journal of the American Chemical Society*, 2015, **137**, 9792-9795.
68. Y. Peng, T. Bodenstein, K. Fink, V. Mereacre, C. E. Anson and A. K. Powell, *Physical Chemistry Chemical Physics*, 2016, **18**, 30135-30143.
69. B. Yao, Y.-F. Deng, T. Li, J. Xiong, B.-W. Wang, Z. Zheng and Y.-Z. Zhang, *Inorganic Chemistry*, 2018, **57**, 14047-14051.
70. W. Wernsdorfer, N. Aliaga-Alcalde, D. N. Hendrickson and G. Christou, *Nature*, 2002, **416**, 406-409.
71. A. Das, K. Gieb, Y. Krupskaya, S. Demeshko, S. Dechert, R. Klingeler, V. Kataev, B. Büchner, P. Müller and F. Meyer, *Journal of the American Chemical Society*, 2011, **133**, 3433-3443.
72. W. Huang, T. Liu, D. Wu, J. Cheng, Z. W. Ouyang and C. Duan, *Dalton Transactions*, 2013, **42**, 15326-15331.
73. H. Grove, J. Sletten, M. Julve, F. Lloret, L. Lezama, J. Carranza, S. Parsons and P. Rillema, *Journal of Molecular Structure*, 2002, **606**, 253-265.
74. M. A. Lemes, F. Magnan, B. Gabidullin and J. Brusso, *Dalton Transactions*, 2018, **47**, 4678-4684.
75. I. Nemec, R. Marx, R. Herchel, P. Neugebauer, J. van Slageren and Z. Trávníček, *Dalton Transactions*, 2015, **44**, 15014-15021.
76. A. K. Mondal, T. Goswami, A. Misra and S. Konar, *Inorganic Chemistry*, 2017, **56**, 6870-6878.
77. S. Vaidya, S. Tewary, S. K. Singh, S. K. Langley, K. S. Murray, Y. Lan, W. Wernsdorfer, G. Rajaraman and M. Shanmugam, *Inorganic Chemistry*, 2016, **55**, 9564-9578.
78. J. Vallejo, I. Castro, R. Ruiz-García, J. Cano, M. Julve, F. Lloret, G. De Munno, W. Wernsdorfer and E. Pardo, *Journal of the American Chemical Society*, 2012, **134**, 15704-15707.
79. V. Chandrasekhar, A. Dey, A. J. Mota and E. Colacio, *Inorganic Chemistry*, 2013, **52**, 4554-4561.
80. S. Gómez-Coca, A. Urtizberea, E. Cremades, P. J. Alonso, A. Camón, E. Ruiz and F. Luis, *Nature Communications*, 2014, **5**, 4300.
81. R. Herchel, L. Váhovská, I. Potočňák and Z. Trávníček, *Inorganic Chemistry*, 2014, **53**, 5896-5898.
82. CC-FIT Copyright © 2014 Nicholas F. Chilton.

83. Y.-N. Guo, G.-F. Xu, Y. Guo and J. Tang, *Dalton Transactions*, 2011, **40**, 9953-9963.
84. Z.-X. Jiang, J.-L. Liu, Y.-C. Chen, J. Liu, J.-H. Lia and M.-L. Tong, *Chemical Communications*, 2016, 6261.
85. S. M. T. Abtab, M. C. Majee, M. Maity, J. Titiš, R. Boča and M. Chaudhury, *Inorganic Chemistry*, 2014, **53**, 1295-1306.
86. F.-H. Zhao, H. Li, Y.-X. Che, J.-M. Zheng, V. Vieru, L. F. Chibotaru, F. Grandjean and G. J. Long, *Inorganic Chemistry*, 2014, **53**, 9785-9799.
87. J.-L. Liu, J.-Y. Wu, G.-Z. Huang, Y.-C. Chen, J.-H. Jia, L. Ungur, L. F. Chibotaru, X.-M. Chen and M.-L. Tong, *Scientific Reports*, 2015, **5**, 16621.
88. G. Novitchi, S. Shova, Y. Lan, W. Wernsdorfer and C. Train, *Inorganic Chemistry*, 2016, **55**, 12122-12125.
89. J. Li, R.-M. Wei, T.-C. Pu, F. Cao, L. Yang, Y. Han, Y.-Q. Zhang, J.-L. Zuo and Y. Song, *Inorganic Chemistry Frontiers*, 2017, **4**, 114-122.
90. M. C. Majee, S. M. Towsif Abtab, D. Mondal, M. Maity, M. Weselski, M. Witwicki, A. Bieńko, M. Antkowiak, G. Kamieniarz and M. Chaudhury, *Dalton Transactions*, 2018, **47**, 3425-3439.
91. J. Li, R.-M. Wei, T.-C. Pu, F. Cao, L. Yang, Y. Han, Y.-Q. Zhang, J.-L. Zuo and Y. Song, *Inorg. Chem. Front.*, 2017, 114.
92. F.-X. Shen, H.-Q. Li, H. Miao, D. Shao, X.-Q. Wei, L. Shi, Y.-Q. Zhang and X.-Y. Wang, *Inorganic Chemistry*, 2018, **57**, 15526-15536.
93. L.-F. Zou, L. Zhao, Y.-N. Guo, G.-M. Yu, Y. Guo, J. Tang and Y.-H. Li, *Chemical Communications*, 2011, 8659.
94. K. C. Mondal, A. Sundt, Y. Lan, G. E. Kostakis, O. Waldmann, L. Ungur, L. F. Chibotaru, C. E. Anson and A. K. Powell, *Angewandte Chemie International Edition*, 2012, **51**, 7550-7554.
95. Y. Peng, V. Mereacre, C. E. Anson and A. K. Powell, *Dalton Trans.*, 2017, 5337.

Chapter 8

Conclusions

8. Conclusions

Throughout this PhD thesis we investigated the coordination chemistry of different polydentate ligands that could promote certain geometries, incorporating Co^{II} in the presence or absence of lanthanide ions, towards the synthesis, structural and magnetic characterisation of mononuclear and polynuclear complexes. The polydentate ligands used in this work are the ligand bicine (= *N,N*-Bis(2-hydroxyethyl)glycine), a series of substituted phosphonic acids (RPO_3H_2) in conjunction with 3,5-dimethylpyrazole, and the multipocket ligand 2,6-bis[4(1-*N*-phenyl-3-methyl-pyrazolium-5-one)carbonyl]pyridinium trichloride (= $[H_5L]\cdot 3Cl$). In addition, the ligand pyrazole, in combination with dibenzoylmethane and acetylacetone, was also used. As a result we managed to isolate twenty new homometallic and heterometallic Co/4*f* complexes where the cobalt ion shows coordination numbers of four, five or six, adopting a variety of geometries. These complexes can be divided into four groups depending on the nature of the ligand. Moreover, the monodentate ligand tricyclohexylphosphine oxide was used in conjunction with lanthanides leading to a family of mononuclear Ln^{III} complexes. Structural characterisation was carried out for all complexes, whereas static and dynamic magnetic studies were performed for selected complexes.

The first group includes one mononuclear and two new nonanuclear cobalt-based complexes with the ligand bicine (= H_3bic); these complexes are: $[Co^{II}(H_2bic)Cl]$ (**1**), $[Co^{II}_9(Hbic)_4(bic)_2Cl_4]$ (**2**) and its solvomorph $[Co^{II}_9(Hbic)_4(bic)_2Cl_4]\cdot 12H_2O$ (**2**$\cdot 12H_2O$). Although the molecular structure of **1** has been previously reported, we present a new and simpler synthetic route for the isolation of **1**. Single-crystal X-ray diffraction (SCXRD) studies showed that the cobalt centre in **1** adopts a distorted trigonal bipyramidal (TBP) geometry, while complexes **2** and **2**$\cdot 12H_2O$ show an unusual metallic core, consisting of a $\{Co^{II}_7\}$ disk-like structure (where the Co^{II} centres adopt distorted octahedral geometries) with two adjacent tetrahedral Co^{II} centres. Solvothermal conditions resulted in a mixture of the complexes **1**, **2** and **2**$\cdot 12H_2O$; however, by using microwave-assisted heating the selectivity is improved and **1**, **2** and **2**$\cdot 12H_2O$ can be isolated separately. This project highlights the potential of microwave−assisted synthesis as a useful tool in the synthesis of polymetallic complexes using polydentate ligands, where bench or solvothermal synthesis leads to a mixture of products. Magnetic characterisation for **1**, **2** and **2**$\cdot 12H_2O$ revealed that **1** and **2**$\cdot 12H_2O$ do not display slow magnetic relaxation, due to significant quantum tunnelling of the magnetisation (QTM), whereas **2** shows the onset of the out-of-phase signals in a zero and an applied dc field.

The ligands pyrazole (= Hpz), dibenzoylmethane (= HDBM) and acetylacetone (= Hacac) were used in the second category of complexes, and the mixed-valence complexes $[Co^{II}Co^{III}_2(\mu_3\text{-OH})(\mu\text{-pz})_4(DBM)_3]\cdot 2THF$ (**3**·2THF), $[Co^{II}Co^{III}_2(\mu_3\text{-OH})(\mu\text{-pz})_4(DBM)_3]\cdot 2MeCN$ (**4**·2MeCN) and $[Co^{II}Co^{III}_2(\mu_3\text{-OH})(\mu\text{-pz})_4(acac)_3]$ (**5**) were synthesised. Complex **4**·2MeCN is a new solvate of the previously reported **3**·2THF, while complex **5** is a new analogue based on the same triangular motif as in **3**·2THF and **4**·2MeCN; the Co^{II} adopts a slightly distorted TBP geometry (with an increase in distortion among the complexes, **3** < **4** < **5**), whereas the two Co^{III} centres adopt an octahedral geometry. Dc and ac magnetic studies were performed for the three complexes. High-field/frequency EPR (HFEPR) measurements were carried out for **4** suggesting a positive *D* parameter (easy-plane magnetic anisotropy) with *E*/*D* ~0.17, which was further confirmed by the fit of the dc magnetic data. The fit of the dc data for complexes **3**·2THF and **5** suggest that an easy-plane magnetic anisotropy is present in these complexes too. The dynamic ac studies under an applied dc field evidence slow magnetic relaxation for **3**·2THF and **4**, whereas complex **5** exhibits only the onset of the out-of-phase ac signals at low temperature. Magneto-structural correlations showed that the rhombicity expressed as the |*E*/*D*| ratio, follows the trend **3** < **4** ≈ **5**, which is consistent with the increase of the distortion of the TBP geometry (**3** < **4** < **5**). Although the geometric distortion plays an important role in the slow relaxation of the magnetisation, the difference of the dynamic magnetic properties among the three complexes could be also attributed to the presence, change or absence of solvent molecules in the crystal lattice of the complexes; however, theoretical studies are needed in order to elucidate further the differences in the magnetic properties. The incorporation of high magnetic anisotropy Co^{II} centres into polynuclear systems containing other high-spin paramagnetic centres is of interest for the design of novel single-molecule magnets (SMMs), and therefore further work in this project could be undertaken in order to incorporate high-spin M^{III} metal ions.

The third family contains new Co^{II}-based cyclic complexes adopting different nuclearities, $\{Co^{II}_6\}$, $\{Co^{II}_8\}$ and $\{Co^{II}_9\}$ and a propeller-like $\{Co^{II}_3\}$ complex, employing the ligand dimethylpyrazole (= Hdmpz) with the substituted phosphonate ligands ($[RPO_3]^{2-}$): *tert*-butylphosphonic acid (= $t\text{BuPO}_3\text{H}_2$), ethylphosphonic acid (= EtPO_3H_2) and phenylphosphonic acid (= PhPO_3H_2). These complexes are:

- $[Co^{II}_9(t\text{BuPO}_3)_3(dmpz)_{12}(Hdmpz)_6]\cdot x\text{MeCN}\cdot y\text{H}_2\text{O}$ (**6**·x$\text{MeCN}\cdot y\text{H}_2\text{O}$),
- $[Co^{II}_3(t\text{BuPO}_3)_2(Hdmpz)_4\text{Br}_2]$ (**7**),
- $[Co^{II}_8(\text{EtPO}_3)_3(dmpz)_{10}(Hdmpz)_6]\cdot x\text{MeCN}\cdot y\text{H}_2\text{O}$ (**8**(MeCN)),
- $[\text{HNEt}_3][Co^{II}_8(\text{EtPO}_3)_3(dmpz)_{10}(Hdmpz)_6][\text{ClO}_4]\cdot x\text{DCM}\cdot y\text{H}_2\text{O}$ (**9a**(DCM)),

- $[HNEt_3][Co^{II}_8(EtPO_3)_3(dmpz)_{10}(Hdmpz)_6][ClO_4]\cdot 0.75(Hdmpz)\cdot 2.25DCE\cdot H_2O$ (**9b**(DCE)) and
- $[HNEt_3][Co^{II}_6(PhPO_3)_3(dmpz)_6(Hdmpz)_6][ClO_4]\cdot DCM$ (**11**·DCM).

In addition, the complexes $[Co^{II}_3(dmpz)_4(Hdmpz)_2Cl_2]$ (**10**) and $[HNEt_4]_2[Co^{II}_2(dmpz)_2Cl_4]$ (**12**) were also isolated without the presence of a phosphonate ligand. The Co^{II} centres in all complexes adopt a slightly distorted tetrahedral geometry. The nuclearity of the final product can be tuned by the change of the phosphonate ligand, tBuPO$_3$H$_2$ $\{Co^{II}_9\}$ → EtPO$_3$H$_2$ $\{Co^{II}_8\}$ → PhPO$_3$H$_2$ $\{Co^{II}_6\}$, or by the change of the synthetic procedure from solvothermal ($\{Co^{II}_9\}$) to reflux (propeller-like $\{Co^{II}_3\}$). Complexes **6** and **7** were magnetically characterised and both show dominant antiferromagnetic exchange interactions. The fit of the dc data for **7** suggests that it is in the weak exchange limit (the spin-orbit contribution is larger than the exchange interaction). Dynamic ac magnetic studies showed only the onset of the out-of-phase ac signals at low temperature for **6**, whereas complex **7** does not display slow magnetic relaxation.

A new family of six-coordinate mononuclear Ln^{III} complexes was obtained by utilising the monodentate ligand tricyclohexylphosphine oxide (= Cy_3PO), with molecular formula $[Ln^{III}(Cy_3PO)_2Cl_3(EtOH)]\cdot yEtOH$, where Ln^{III} = Tb (**13**), Dy (**14**), Ho (**15**), Er (**16**) and Y (**17**), and y = 0.5 for **14** and y = 1 for **13**, **15−17**. SCXRD analysis showed that all metal centres adopt a distorted octahedral geometry, while PXRD analysis revealed that all complexes are moisture-sensitive, except the Dy analogue. The static and dynamic magnetic properties of complexes **13** (Tb), **14** (Dy) and **15** (Ho) were investigated, and field induced slow magnetic relaxation was observed only for **14** (Dy). The fit of the ac data produced an energy barrier of ~32 K, which is among the highest for non-organometallic six-coordinate complexes in pseudo-octahedral geometry.

Finally, the last group of complexes incorporates the ligand 2,6-bis[4(1-*N*-phenyl-3-methyl-pyrazolium-5-one)carbonyl]pyridinium trichloride (= $[H_5L]\cdot 3Cl$). To the best of our knowledge this ligand has been reported including only Rh and Sn metal centres. We managed to obtain seven new 4*f* and Co(II)-4*f* complexes with various metallic cores, $\{La^{III}_9\}$, $\{Ce^{III}_3\}$, $\{Dy^{III}\}$, $\{Co^{II}_2Ln^{III}\}$, $\{Co^{II}Dy^{III}_2\}$ and $\{Gd^{III}_6\}$. These complexes are:

- $[La^{III}_9(L^{2-})_7(NO_3)_4(CO_3)_4(OH)(H_2O)_8]\cdot xMeCN\cdot yH_2O$ (**18**·xMeCN·yH$_2$O),
- $[HNEt_3][Ce^{III}_3(HL^{-})_2(NO_3)_7(H_2O)_2][Cl]\cdot xMeCN\cdot yH_2O\cdot zEt_2O$ (**19a**), $[HNEt_3][Ce^{III}_3(HL^{2-})(H_2L)(NO_3)_7(H_2O)_2][Cl]\cdot xMeCN\cdot yH_2O\cdot zEt_2O$ (**19b**),
- $[Dy^{III}(HL^{-})_2(H_2O)_4][Cl]\cdot xMeCN\cdot yH_2O$ (**20**·xMeCN·yH$_2$O),
- $[Co^{II}_2Ln^{III}(L^{2-})_2(NO_3)_{2.3}Cl_{0.7}(MeCN)]$ where Ln = La (**21**) and Ce (**22**),
- $[HNEt_3][Co^{II}Dy^{III}_2(L^{2-})_4(HL^{-})(H_2O)_2]\cdot xMeCN\cdot yH_2O$ (**23**·xMeCN·yH$_2$O) and

- $[Gd^{III}_6(L^{2-})_4(OH)_4(O^{2-})(MeOH)_6(H_2O)_2][NO_3]_{3.75}[Cl]_{0.25}\cdot xMeOH\cdot yH_2O$ (**24**$\cdot xMeOH\cdot yH_2O$).

Complex **18**$\cdot xMeCN\cdot yH_2O$ is the first homometallic $\{La^{III}_9\}$ complex, while complex **23**$\cdot xMeCN\cdot yH_2O$ is only the third $\{Co^{II}Dy^{III}_2\}$ complex reported. Dc and ac magnetic studies were carried out for the Co(II)-4*f* complexes. Complexes $\{Co^{II}_2La^{III}\}$ and $\{Co^{II}_2Ce^{III}\}$ exhibit a large magnetic anisotropy, but only the onset of the out-of-phase ac signals under an applied dc field. Complex $\{Co^{II}Dy^{III}_2\}$ displays field induced slow magnetic relaxation with an energy barrier of 45.1 K, which is among the highest values for other reported polynuclear Co^{II}/Dy^{III} complexes. This project highlights the versatility of the ligand $[H_5L]\cdot 3Cl$ and the its potential use in the design of new polynuclear pure 4*f* and/or 3*d*/4*f* complexes.

Future work on the above projects will involve the confirmation of the zero-field parameters (ZFS) of complexes **3**$\cdot$2THF and **5** using HFEPR studies, and the synthesis of other analogues of the $\{Co^{II}Co^{III}_2\}$ family by replacing the diamagnetic Co^{III} with high-spin M^{III} ions (*e.g.* Fe^{III}, Cr^{III}), in order to combine the high anisotropy TBP Co^{II} with a high-psin ground-state. Moreover, the magnetic properties of the cyclic complexes **8**(MeCN), **9a**(DCM), **9b**(DCE) and **11**$\cdot$DCM are going to be investigated in order to examine the effect of the nuclearity and/or the change of the co-crystallised solvent in the slow relaxation of the magnetisation. The magnetic properties of the six-coordinate mononuclear complex **16** (Er) will also be investigated, and diluted samples of **13** (Tb), **14** (Dy) and **15** (Ho) with the Y analogue will be synthesised in order to examine their magnetic properties. Moreover, the pure 4*f* complexes incorporating the ligand $[H_5L]\cdot 3Cl$, **18**$\cdot xMeCN\cdot yH_2O$, **19**, **20**$\cdot xMeCN\cdot yH_2O$ and **24**$\cdot xMeOH\cdot yH_2O$, will be further investigated to improve their synthetic procedures, in order to complete their structural and magnetic characterisation, while other Ln^{III} analogues of complex **23**$\cdot xMeCN\cdot yH_2O$, $\{Co^{II}Dy^{III}_2\}$, will be synthesised and characterised. Finally, theoretical calculations are needed in order to further elucidate the magnetic properties of complexes **21**, **22** and **23**$\cdot xMeCN\cdot yH_2O$ and further understand the origin or absence of the slow magnetic relaxation in these complexes.

In conclusion, the work in this thesis highlights the use of carefully chosen polydentate ligands in the directed synthesis of Co(II)-based complexes in the presence or absence of 4*f* ions. Using a variety of synthetic procedures homometallic and heterometallic Co(II)/4*f* complexes were synthesised, with nuclearities varying from 1 to 9 metal centres, where the cobalt centre adopts different coordination numbers and geometries, in an attempt to tune the magnetic properties.

Appendix

Contents

Appendix

Appendix

Chapter 3

Table A3.1 The CShMs [1, 2] values calculated with the program SHAPE for each geometry for the five-coordinate Co^{II} in complex **1**.

Geometry	Value
Pentagon (D_{5h})	34.70
Vacant octahedron (C_{4v})	6.75
Trigonal bipyramid (D_{3h})	**1.42**
Spherical square pyramid (C_{4v})	5.53
Johnson trigonal bipyramid (D_{3h})	2.63

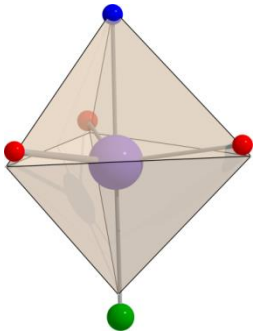

Figure A3.1 The closest reference polyhedron for TBP geometry calculated with SHAPE [1, 2] for Co^{II} of complex **1**. Colour code: Co^{II}: violet, Cl: green, O: red, N: blue, bonds: grey.

Table A3.2 The CShMs [3, 4] values calculated with the program SHAPE for each Co^{II} centre in complex **2.**

Co	Octahedron (O_h)	Trigonal prism (D_{3h})	Tetrahedron (T_d)
Co1	**1.3**	-	-
Co2	**3.3**	-	-
Co3	**4.5**	5.3	-
Co4	**4.8**	5.4	-
Co5	-	-	**0.8**

Table A3.3 The CShMs [3, 4] values calculated with the program SHAPE for each Co^{II} centre in complex **2**·12H_2O.

Co	Octahedron (O_h)	Trigonal prism (D_{3h})	Tetrahedron (T_d)
Co1	**1.3**	-	-
Co2	**3.7**	-	-
Co3	**3.8**	-	-
Co4	**4.7**	5.3	-
Co5	-	-	**0.7**

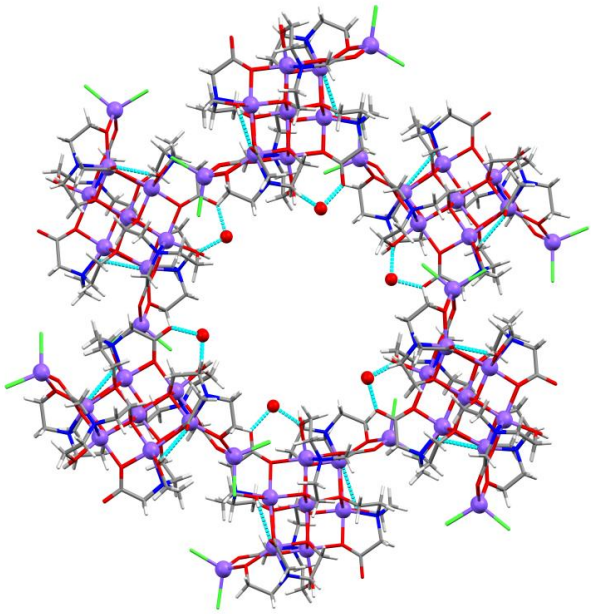

Figure A3.2 Illustration of the intramolecular and intermolecular interactions through the hydrogen bonds (light blue dashed lines) for complex **2**·12H_2O. Only the modelled H_2O sites are shown here, however further water molecules are present in the channels and were accounted for using SQUEEZE. [5]

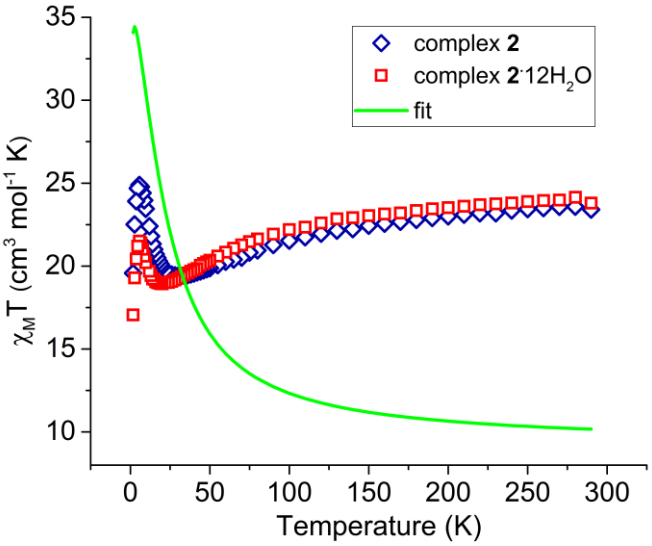

Figure A3.3 Variable temperature dc magnetic susceptibility data for **2** (blue) and **2**·12H_2O (red) in a field of 1000 Oe from 290–2 K. The green solid line corresponds to the fit with PHI (see main text for details).

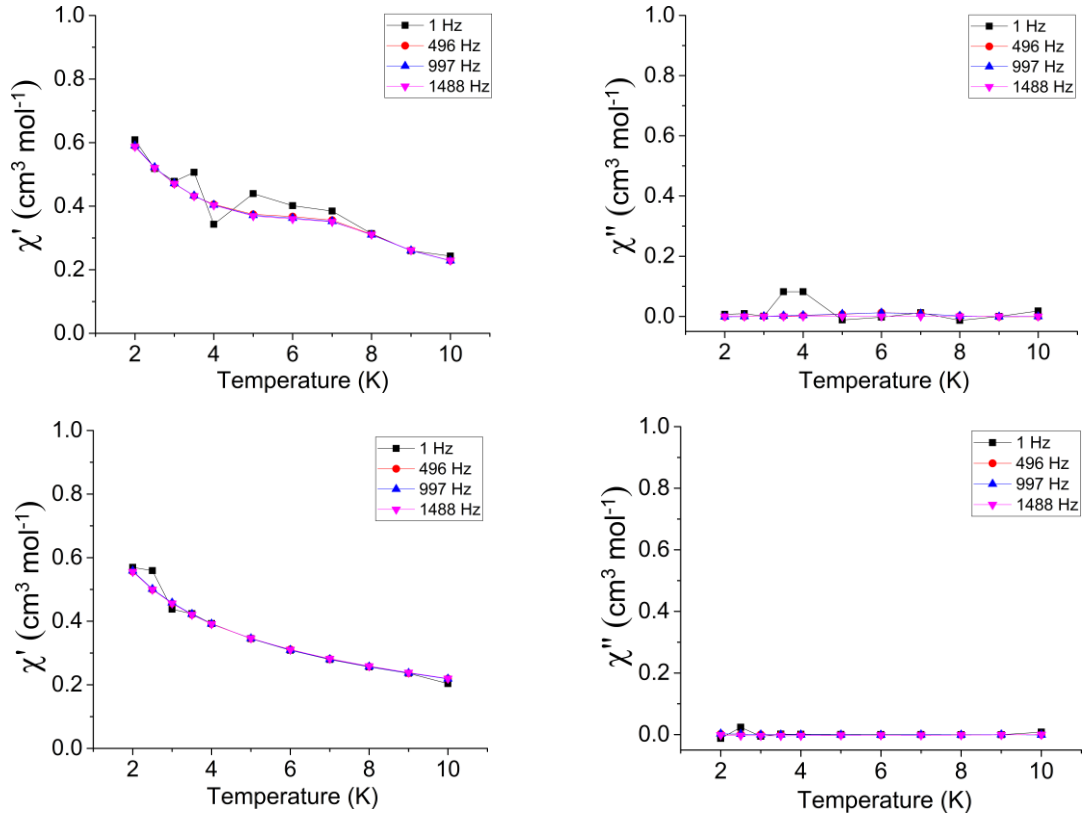

Figure A3.4 *Top)* Temperature dependence of the in-phase (*left*) and out-of-phase (*right*) magnetic susceptibility in zero dc field for complex **1** with ac frequencies of 1−1488 Hz. *Bottom)* Temperature dependence of the in-phase (*left*) and out-of-phase (*right*) magnetic susceptibility in a 2000 Oe dc field for complex **1** with ac frequencies of 1−1488 Hz.

A3. References

1. M. Pinsky and D. Avnir, *Inorg Chem*, 1998, **37**, 5575-5582.
2. S. Alvarez and M. Llunell, *J Chem Soc, Dalton Trans*, 2000, 3288-3303.
3. S. Alvarez, D. Avnir, M. Llunell and M. Pinsky, *New J Chem*, 2002, **26**, 996-1009.
4. C. Jordi, A. Pere and A. Santiago, *Chemistry – A European Journal*, 2004, **10**, 190-207.
5. A. Spek, *Acta Crystallographica Section C*, 2015, **71**, 9-18.

Chapter 4

Table A4.1 The CShMs [1, 2] values calculated with the program SHAPE for each geometry for the five-coordinate Co^{II} in complexes **3**, **4** and **5**.

Geometry	Complex 3	Complex 4	Complex 5
Pentagon (D_{5h})	35.71	35.94	35.68
Vacant octahedron (C_{4v})	7.19	7.10	7.06
Trigonal bipyramid (D_{3h})	**0.27**	**0.33**	**0.54**
Spherical square pyramid (C_{4v})	5.45	5.55	5.17
Johnson trigonal bipyramid (D_{3h})	2.38	2.35	2.56

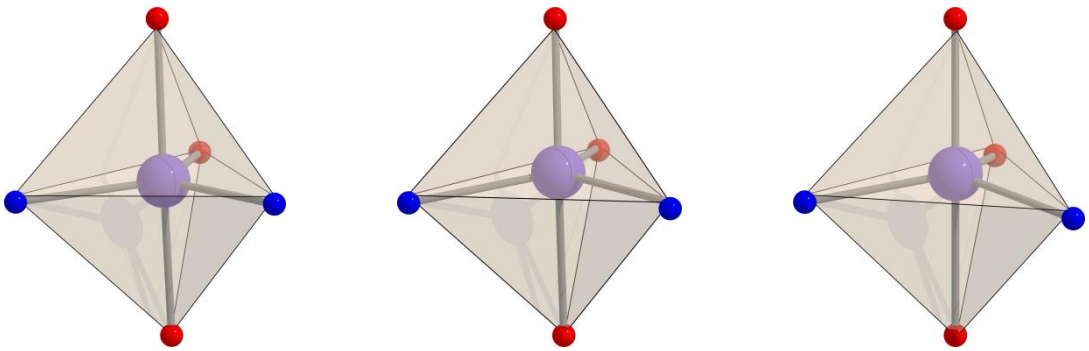

Figure A4.1 The closest reference polyhedron for TBP geometry calculated with SHAPE [1, 2] for Co^{II} of complexes **3**, **4** and **5** from left to right. Colour code: Co^{II}: violet, O: red, N: blue, bonds: grey.

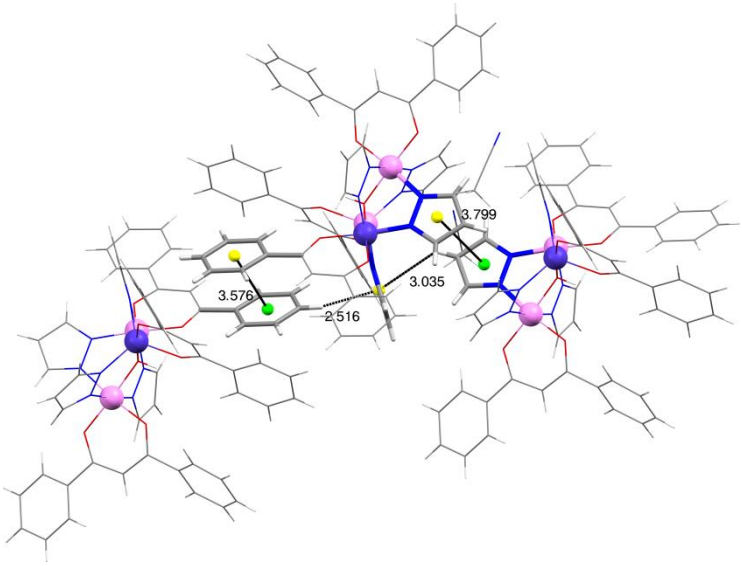

Figure A4.2 Illustration of the hydrogen-π and π-π intermolecular interactions in $[Co^{II}Co^{III}_2(\mu_3\text{-}OH)(\mu\text{-}pz)_4(DBM)_3]$. The yellow spheres (central molecule) and the green spheres (side molecules) represent the centroids of the phenyl and pyrazolate rings. The dashed black lines show the distances (in Å) between the centroids, and between the hydrogens and the centroids. Colour code: Co^{II}: violet, Co^{III}: pink, O: red, N: blue, C: grey, H: white.

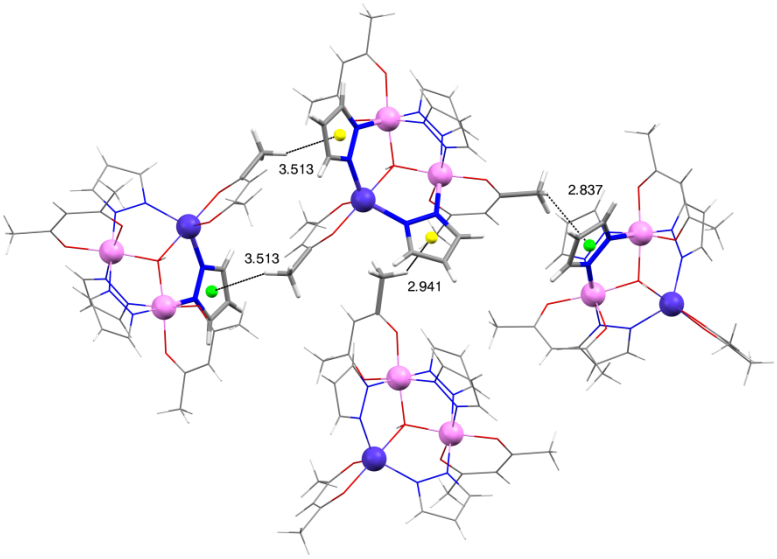

Figure A4.3 Illustration of the hydrogen-π intermolecular interactions in complex **5**. The yellow spheres (central molecule) and the green spheres (side molecules) represent the centroids of the pyrazolate rings. The dashed black lines show the distances (in Å) between the hydrogens and the centroids. Colour code: Co^{II}: violet, Co^{III}: pink, O: red, N: blue, C: grey, H: white.

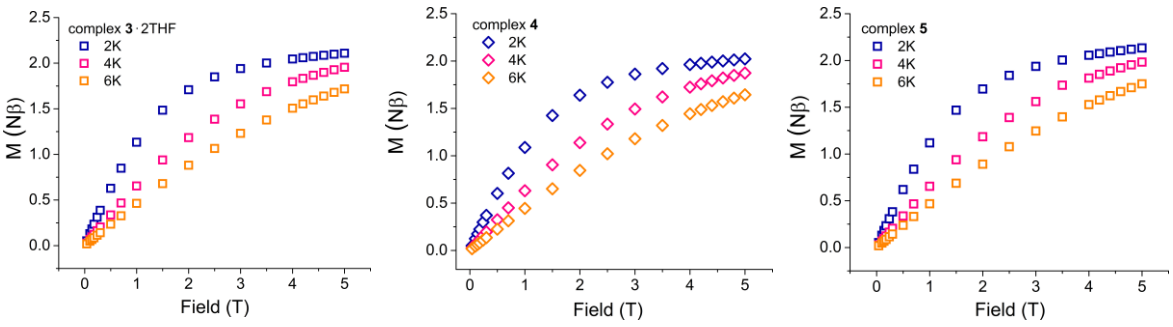

Figure A4.4 Magnetisation *versus* Field data for **3**·2THF, **4** and **5** from left to right, at temperatures 2, 4 and 6 K.

High-field/frequency EPR (HFEPR) analysis

A representative series of temperature-dependent EPR spectra recorded at a frequency of 203.2 GHz are displayed in Figure A4.5. Spectral features are clearly visible at all temperatures that are clustered into three groups, which we have labelled g_x^{eff}, g_y^{eff} and g_z^{eff}, representing the three components of the effective Landé-tensor associated with the lowest-lying Kramers doublet of the s = 3/2 ground state manifold. All of the features exhibit the same temperature dependence, i.e., they increase uniformly in intensity with decreasing temperature, confirming their assignment as ground state-transitions. Within each cluster, one can clearly resolve two distinct resonances of more-or-less equal intensity, suggesting the presence of discrete species within the powdered sample, having distinct spin-Hamiltonian parameters; a weaker signal is also discernible in between the two main g_y^{eff} resonances. It is apparent that one of the resonances within each pair is sharper than the other. Assuming that the observation of multiple resonances is due to a distribution of microenvironments, then the distribution width should be a unique fingerprint for each set of resonances. Hence, the resonance linewidths provide a means of distinguishing the two microenvironments. We have thus labelled the sharper resonances with open symbols and the broader ones with closed symbols (see also Fig. A4.6). The associated g^{eff} values are then obtained from fits to resonance positions deduced at multiple frequencies, as shown in Figure A4.5: (sharp) g_x^{eff} = 5.11(2), g_y^{eff} = 3.51(3) and g_z^{eff} = 1.98(1); (broad) g_x^{eff} = 5.47(2), g_y^{eff} = 3.27(1) and g_z^{eff} = 1.91(1). As can be seen, the species with the sharper distribution is less rhombic whilst the species with the broader distribution is more rhombic.

Although it is not possible to constrain the zero-field splitting parameters D and E on the basis of EPR transitions associated with the lowest Kramers doublet, it is possible to constrain the sign of D. The observation of two g^{eff} values well above 2.00, and one near

or below 2.00, is indicative of an easy-plane type anisotropy (positive *D* value for the *s* = 3/2 ground state). Moreover, both species are appreciably rhombic. In fact, one can deduce values for the *E*/*D* ratio and the real *g*-tensor components associated with the *s* = 3/2 spin state from the following perturbative expressions:

$$g_x^{\text{eff}} = g_x\left(1+\frac{1+3\gamma}{\sqrt{1+3\gamma^2}}\right);\ \ g_y^{\text{eff}} = g_y\left(1+\frac{1-3\gamma}{\sqrt{1+3\gamma^2}}\right);\ \ g_z^{\text{eff}} = g_z\left(\frac{2}{\sqrt{1+3\gamma^2}}-1\right), \quad (E1)$$

where γ = *E*/*D*. If we then make the assumption/approximation that $g_x = g_y$ (due to over-parameterization), we obtain the following parameters for the two species: (sharp) *E*/*D* = 0.13, g_{xy} = 2.18 and g_z = 2.07; (broad) *E*/*D* = 0.17, g_{xy} = 2.23 and g_z = 2.08.

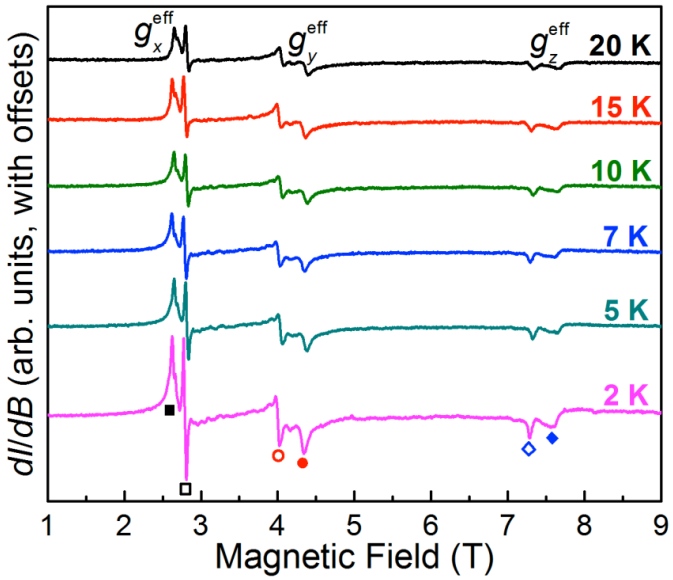

Figure A4.5 Variable temperature EPR spectra recorded at a frequency of 203.2 GHz. Each cluster of peaks has been labelled at the top of the figure according to the corresponding component of the effective *g*-tensor associated with the lowest Kramers doublet. Within each cluster, the two resonances have been labelled with open and closed symbols according to the same scheme as in Figure A4.6 (see text for further explanation).

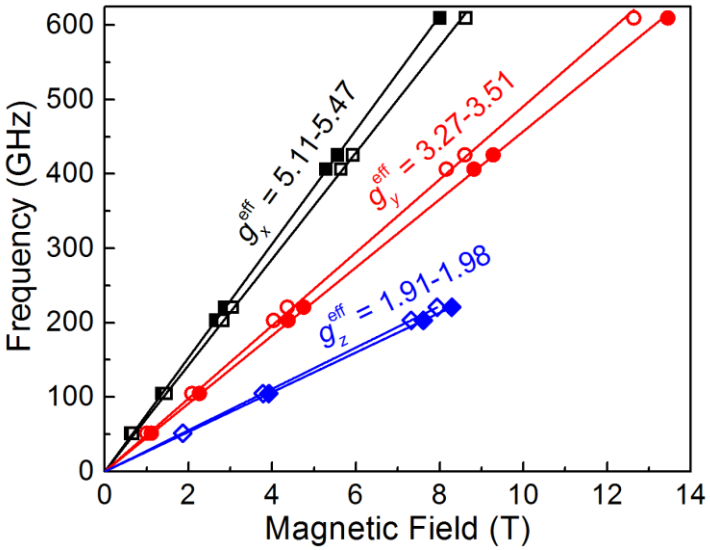

Figure A4.6 Frequency versus field plot of the resonance positions obtained from multi-frequency measurements. Effective *g*-values are deduced from linear fits (solid lines) to each data set, which are labelled by open and closed symbols of different shape/colour (see text and Fig. A4.5 for further explanation).

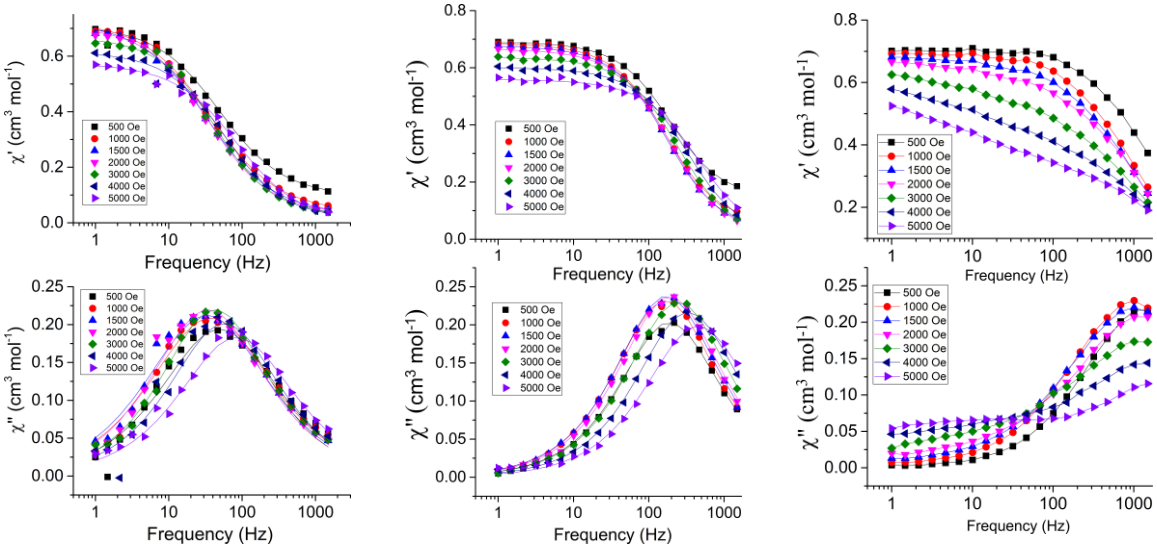

Figure A4.7 Frequency dependent in-phase (*top*) and out-of-phase (*bottom*) ac susceptibility signals for complexes **3**·2THF, **4** and **5** from left to right, under different applied dc fields at 2 K. The solid lines in **3**·2THF and **4** correspond to the fit (CC-FIT)[6, 7] and in **5** are a guide to the eye.

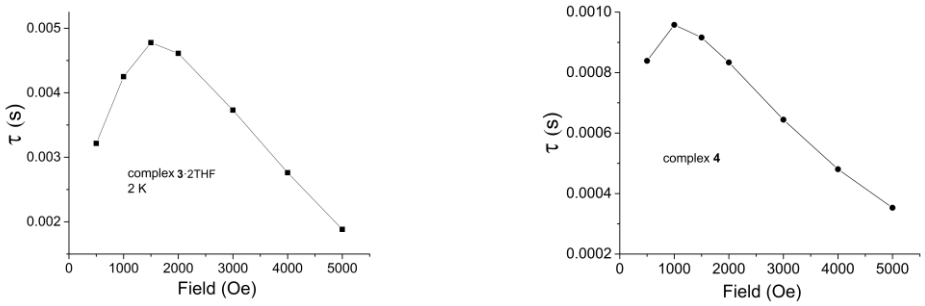

Figure 4.8 Plots of τ values versus the applied dc fields for **3**·2THF (*left*) and **4** (*right*) (the solid lines are a guide to the eye).

Table A4.2 Cole-Cole fit values of **3**·2THF with an applied dc field of 1500 Oe.

Temperatures (K)	χ_S ($cm^3\ mol^{-1}$)	χ_T ($cm^3\ mol^{-1}$)	τ (s)	α	Residual
1.8	0.0278	0.81652	0.00591	0.28158	0.00269
1.9	0.02602	0.78578	0.00527	0.29155	0.00314
2	0.02388	0.74352	0.00465	0.30146	0.00266
2.1	0.02945	0.70956	0.00408	0.29228	0.00305
2.2	0.02332	0.70344	0.00387	0.31276	0.00862
2.3	0.02594	0.66311	0.00328	0.30733	0.00449
2.4	0.0205	0.63158	0.00286	0.3257	0.00268
2.5	0.02767	0.60473	0.0025	0.30697	0.00433
3	0.02787	0.50575	0.00138	0.30847	0.00355
4	0.04505	0.37881	2.85205E-4	0.11949	6.16742E-4
5	0.05081	0.30774	3.77365E-5	1.58506E-17	5.6639E-4
6	1.51028E-14	0.26102	7.75622E-6	3.10523E-17	3.88076E-4
7	1.72947E-14	0.22928	8.29874E-6	3.73435E-17	1.74279E-4
8	1.97344E-14	0.2043	9.47838E-6	5.31624E-17	3.1063E-4

Table A4.3 Cole-Cole fit values of **4** with an applied dc field of 1000 Oe.

Temperatures (K)	χ_S (cm^3 mol^{-1})	χ_T (cm^3 mol^{-1})	τ (s)	α	Residual
1.8	0.0944	0.7578	0.00118	0.07583	8.89019E-4
1.9	0.09329	0.71788	0.00104	0.0672	6.35762E-4
2	0.08652	0.68422	9.10805E-4	0.06602	8.29472E-4
2.1	0.08313	0.65207	7.96867E-4	0.06488	6.02254E-4
2.2	0.08288	0.63173	7.35232E-4	0.06046	6.24752E-4
2.3	0.0802	0.60365	6.42118E-4	0.06318	0.00101
2.4	0.07414	0.57554	5.58096E-4	0.06147	5.21084E-4
2.5	0.07494	0.55269	4.88918E-4	0.05617	8.33139E-4
3	0.05875	0.46473	2.42197E-4	0.04731	2.59381E-4
4	2.34714E-14	0.35582	4.4607E-5	0.01709	3.97576E-4
5	1.22048E-13	0.29048	1.0541E-5	5.01916E-15	1.53258E-4
6	2.00013E-13	0.24918	4.28986E-6	6.62081E-15	8.00794E-5
7	2.66706E-13	0.21656	1.02535E-6	9.3036E-15	1.31357E-4
8	1.05928E-13	0.19374	3.92638E-6	2.00359E-14	1.46443E-4

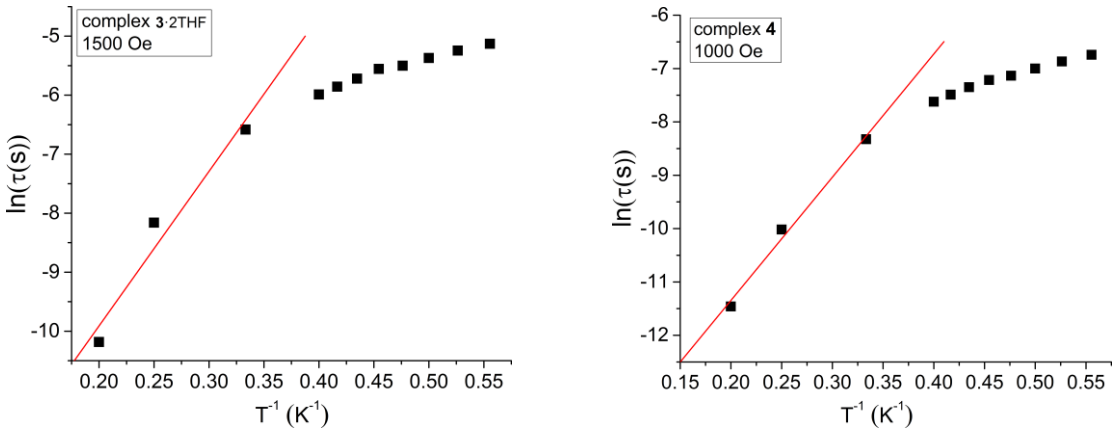

Figure 4.9 Arrhenius plots of ln(τ) data versus T^{-1} of **3**·2THF (*left*) and **4** (*right*) at 1500 Oe and 1000 Oe, respectively, in the temperature range of 1.8 – 5 K. The solid red lines represent the fit only with Orbach process (ln(τ) = ln(τ_0) + $\Delta E/k_BT$) at higher temperatures.

Table A4.4 Bond lengths (Å) of Co1 for **3**·2THF.

Co1	O1B (a)	2.154(2)
Co1	O1 (a)	2.015(2)
Co1	O2 (e)	1.981(2)
Co1	N6 (e)	2.002(2)
Co1	N7 (e)	1.991(2)

(a): axial, (e): equatorial

Table A4.5 Bond lengths (Å) of Co1 for **4**·2MeCN.

Co1	O1 (a)	2.169(3)
Co1	O2B (a)	2.010(3)
Co1	O1B (e)	1.970(3)
Co1	N15 (e)	1.999(3)
Co1	N7 (e)	1.993(3)

(a): axial, (e): equatorial

Table A4.6 Bond lengths (Å) of Co1 for **5**.

Co1	O1 (a)	2.161(2)
Co1	O2 (a)	2.008(2)
Co1	O3 (e)	1.970(2)
Co1	N1 (e)	2.000(2)
Co1	N6 (e)	1.992(2)

(a): axial, (e): equatorial

Table A4.7 Angles (º) of Co1 with the ligand atoms for **3**·2THF.

N7	**Co1 (p)**	N6	120.72(8)
N6	**Co1 (p)**	O2	118.66(7)
N7	**Co1 (p)**	O2	118.01(8)
O1	**Co1**	N6	97.26(7)
O1	**Co1**	O2	91.51(7)
O1	**Co1**	N7	97.28(8)
O1B	**Co1**	O2	86.01(6)
O1B	**Co1**	N7	84.57(7)
O1B	**Co1**	N6	83.30(7)
O1	**Co1 (a)**	O1B	177.41(7)

(a): axial, (p): in the plane

Table A4.8 Angles (º) of Co1 with the ligand atoms for **4**·2MeCN.

N7	**Co1 (p)**	N15	122.0(1)
O1B	**Co1 (p)**	N7	117.2(1)
O1B	**Co1 (p)**	N15	117.7(1)
O2B	**Co1**	O1B	91.6(1)
O2B	**Co1**	N7	97.6(1)
O2B	**Co1**	N15	98.3(1)
O1	**Co1**	O1B	84.0(1)
O1	**Co1**	N15	83.6(1)
O1	**Co1**	N7	84.7(1)
O2B	**Co1 (a)**	O1	175.5(1)

(a): axial, (p): in the plane

Table A4.9 Angles (º) of Co1 with the ligand atoms for **5**.

N1	**Co1 (p)**	N6	123.71(7)
N1	**Co1 (p)**	O3	117.63(7)
O3	**Co1 (p)**	N6	113.88(7)
O2	**Co1**	O3	93.07(6)
O2	**Co1**	N6	100.34(7)
O2	**Co1**	N1	98.10(7)
O1	**Co1**	N1	83.61(7)
O1	**Co1**	O3	79.91(6)
O1	**Co1**	N6	84.41(6)
O1	**Co1 (a)**	O2	172.72(6)

(a): axial, (p): in the plane

A4. References

1. M. Pinsky and D. Avnir, *Inorganic Chemistry*, 1998, **37**, 5575-5582.
2. S. Alvarez and M. Llunell, *Journal of the Chemical Society, Dalton Transactions*, 2000, 3288-3303.
3. S. Alvarez, D. Avnir, M. Llunell and M. Pinsky, *New Journal of Chemistry*, 2002, **26**, 996-1009.
4. C. Jordi, A. Pere and A. Santiago, *Chemistry – A European Journal*, 2004, **10**, 190-207.
5. A. Spek, *Acta Crystallographica Section C*, 2015, **71**, 9-18.
6. CC-FIT Copyright © 2014 Nicholas F. Chilton.
7. Y.-N. Guo, G.-F. Xu, Y. Guo and J. Tang, *Dalton Transactions*, 2011, **40**, 9953-9963.

Chapter 5

Complex $[Co^{II}_9(t\text{-}butPO_3)_3(dmpz)_{12}(Hdmpz)_6]\cdot xDCM\cdot yH_2O$

Hdmpz (0.6 mmol, 58 mg) and tBuPO$_3$H$_2$ (0.1 mmol, 14 mg) in DCM (15 ml) was added to a solution of Co(ClO$_4$)$_2$·6H$_2$O (0.3 mmol, 116 mg) in DCM (25 ml) in the presence of NEt$_3$ (1 mmol, 0.15 ml) and the mixture was stirred at room temperature for ~20 h. The resulted purple solution was layered with liquid hexane to give purple block-like crystals after 1 week (<5% yield).

Single-crystal X-ray difraction revealed that the complex $[Co^{II}_9(t\text{-}butPO_3)_3(dmpz)_{12}(Hdmpz)_6]\cdot xDCM\cdot yH_2O$ crystallises in the triclinic $P\bar{1}$ space group, and the metallic core is similar as in complex **6**. Due to a region of poorly defined and disordered molecules of solvent the routine SQUEEZE (in PLATON)[1] was used to identify the solvent voids and account for the electron density within them. The solvent voids were calculated to contain 509 e^- per unit cell, corresponding to approximately 254.5 e^- per molecule. A combination of molecules of solvent could be present in the crystal lattice and therefore it was not possible to determine the number of DCM and/or H$_2$O molecules that are co-crystallised.

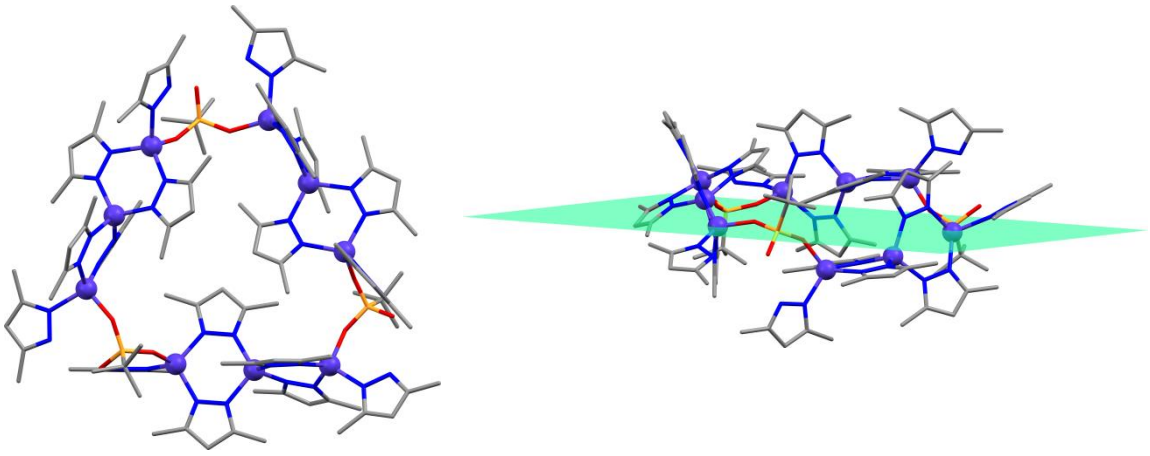

Figure A5.1 The molecular structure of complex $[Co^{II}_9(t\text{-}butPO_3)_3(dmpz)_{12}(Hdmpz)_6]$. The green plane is defined by the P atoms of the $[t\text{BuPO}_3]^{2-}$ phosphonate ligands. Colour code: Co^{II}: violet, O: red, N: blue, C: grey, P: orange. Hydrogen atoms are omitted for clarity.

Table A5.1 The CShMs values calculated with the program SHAPE[2, 3] for each Co^{II} centre in complex **6**. The lowest and highest values are highlighted in red.

Co	Tetrahedron (T_d)
Co1	0.158
Co2	0.063
Co3	0.331
Co4	0.193
Co5	0.074
Co6	0.134
Co7	0.117
Co8	0.433
Co9	0.212

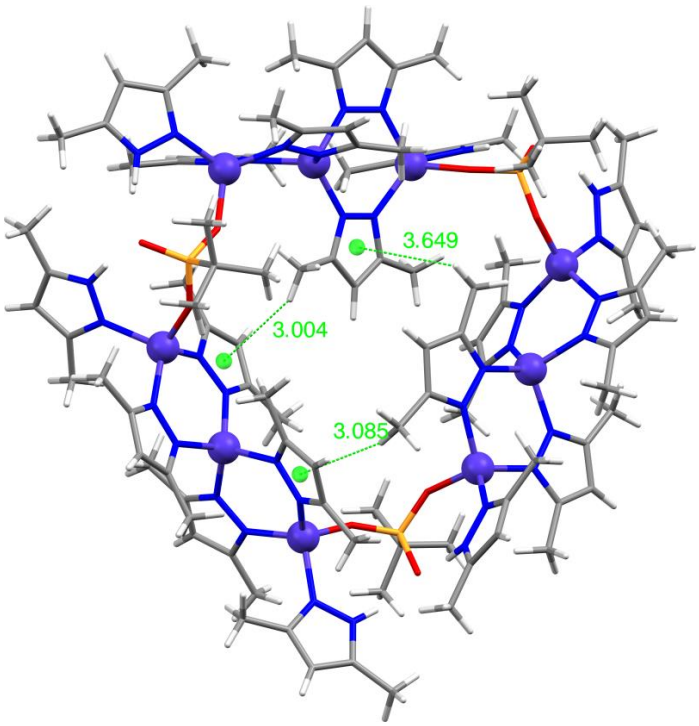

Figure A5.2 Illustration of the hydrogen-π intramolecular interactions in complex **6**. The green spheres represent the centroids of the $dmpz^-$ rings. The dashed green lines show the distances (in Å) between the centroids and the hydrogens. Colour code: Co^{II}: violet, O: red, N: blue, P: orange, C: grey, H: white.

Table A5.2 The CShMs values calculated with the program SHAPE[2, 3] for each Co^{II} centre in complex **7**.

Co	Square (D_{4h})	Tetrahedron (T_d)	Seesaw (C_{2v})
Co1	27.91	**0.54**	6.59
Co2	32.01	**1.71**	8.34
Co3	32.12	**1.64**	8.43

Table A5.3 The CShMs values calculated with the program SHAPE[2, 3] for each Co^{II} centre in complex **8**(MeCN). The lowest and highest values are highlighted in red.

Co	Tetrahedron (T_d)
Co1	0.174
Co2	0.055
Co3	0.292
Co4	0.090
Co5	0.085
Co6	0.250
Co7	0.511
Co8	0.061

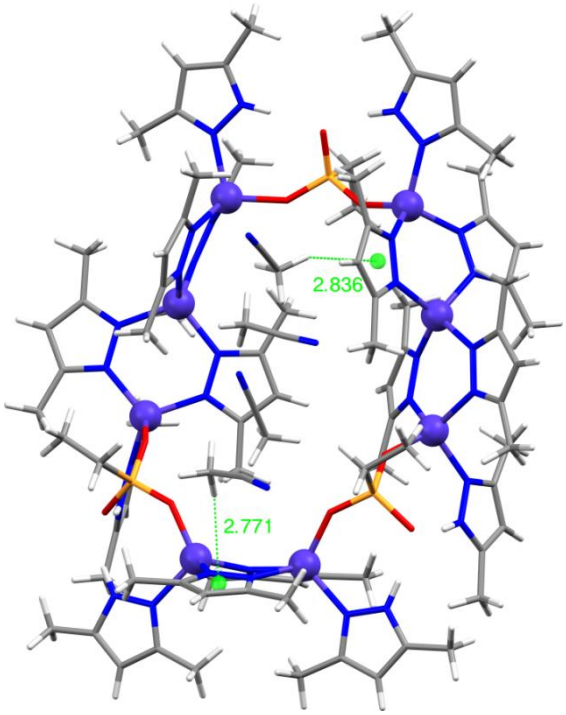

Figure A5.3 Illustration of the hydrogen-π intermolecular interactions in complex **8**(MeCN). The green spheres represent the centroids of the $dmpz^-$ rings. The dashed green lines show the distances (in Å) between the centroids and the hydrogens. Colour code: Co^{II}: violet, O: red, N: blue, P: orange, C: grey, H: white.

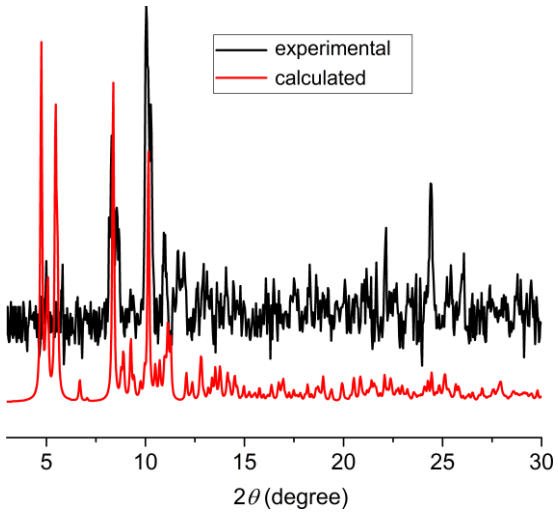

Figure A5.4 The experimental PXRD pattern (3−30°) of the desolvated complex **9a**(DCM). The red line represents the calculated PXRD pattern for complex **9a**(DCM) and the black line the experimental one. The experimental PXRD pattern was measured at room temperature, while the calculated pattern is generated from the single-crystal data collected at 150 K.

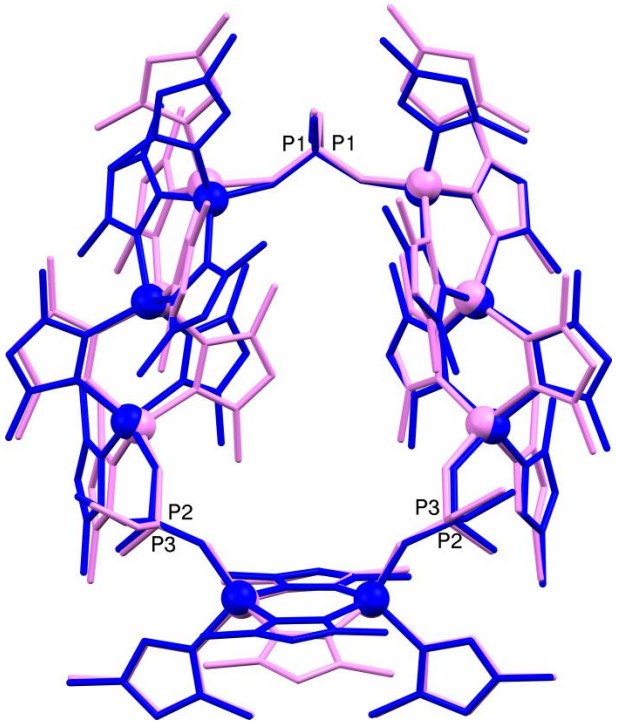

Figure A5.5 Overlay of the molecular structures of **8**(MeCN) (pink) and **9a**(DCM) (blue). The co-crystallised molecules of solvent, $[HNEt_3]^+$ and ClO_4^- are omitted for clarity. Hydrogen atoms are also omitted for clarity.

Table A5.4 The CShMs values calculated with the program SHAPE[2, 3] for each Co^{II} centre in complexes **9a**(DCM) and **9a**(DCE). The lowest and highest values are highlighted in red.

Co	Tetrahedron (T_d)/ **9a**(DCM)	Tetrahedron (T_d)/ **9a**(DCE)
Co1	0.061	0.156
Co2	0.242	0.232
Co3	0.291	0.171
Co4	0.187	0.089
Co5	0.171	0.125
Co6	0.171	0.314
Co7	0.162	0.510
Co8	0.071	0.153

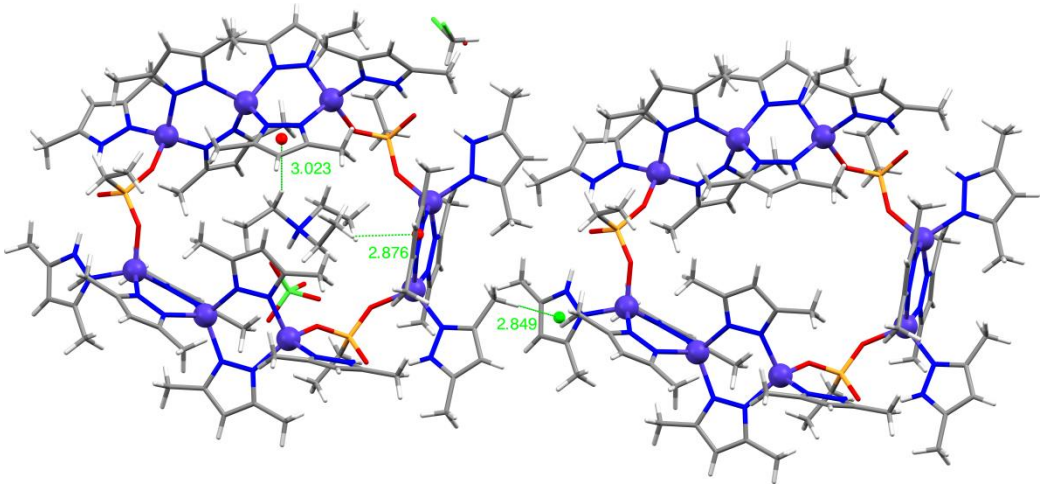

Figure A5.6 Illustration of the hydrogen-π intramolecular and intermolecular interactions in complex **9a**(DCM). The red spheres represent the centroids of the $dmpz^-$ rings in the same molecule, whereas the green spheres represent the centroids of the $dmpz^-$ rings from neighbouring molecules. The dashed green lines show the distances (in Å) between the centroids and the hydrogens. Colour code: Co^{II}: violet, O: red, N: blue, P: orange, C: grey, H: white, Cl: green.

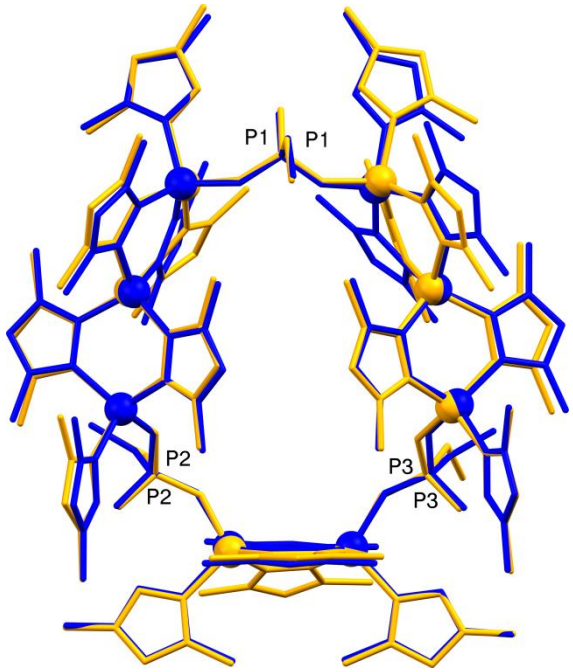

Figure A5.7 Overlay of the molecular structures of **9a**(DCM) (blue) and **9b**(DCE) (yellow). The co-crystallised molecules of solvent, Hdmpz, $[HNEt_3]^+$ and ClO_4^- are omitted for clarity. Hydrogen atoms are also omitted for clarity.

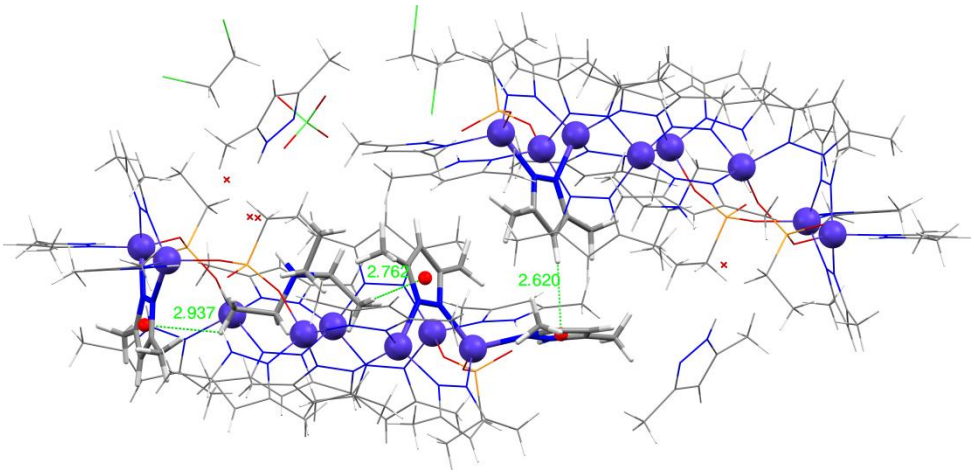

Figure A5.8 Illustration of the hydrogen-π intramolecular and intermolecular interactions in complex **9b**(DCE). The red spheres represent the centroids of the dmpz$^-$ rings in the same molecule. The dashed green lines show the distances (in Å) between the centroids and the hydrogens. Colour code: Co^{II}: violet, O: red, N: blue, P: orange, C: grey, H: white, Cl: green.

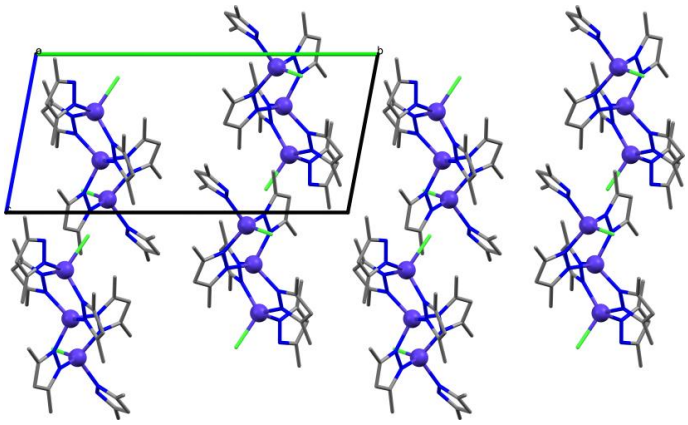

Figure A5.9 The crystal packing of **10** along the crystallographic *a*-axis. Colour code: Co^{II}: violet, N: blue, C: grey, Cl: green. Hydrogen atoms are omitted for clarity.

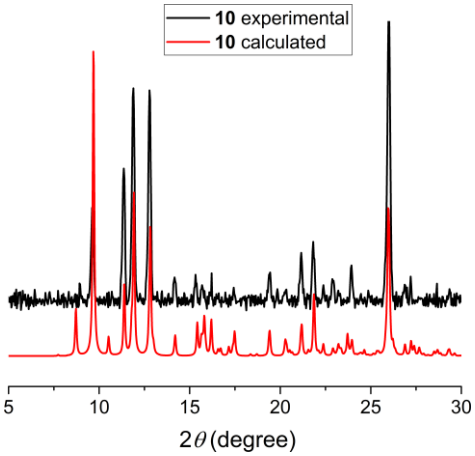

Figure A5.10 The experimental PXRD pattern (5−30^o) of **10**. The red line represents the calculated PXRD pattern for complex **10** and the black line the experimental one. The experimental PXRD pattern was measured at room temperature, and the calculated pattern is generated from the single-crystal data collected at 295 K.[4]

Table A5.5 The CShMs values calculated with the program SHAPE[2, 3] for each Co^{II} centre in complex **11**·DCM. The lowest and highest values are highlighted in red.

Co	Tetrahedron (T_d)
Co1	0.208
Co2	0.265
Co3	0.106
Co4	0.099
Co5	0.218
Co6	0.165

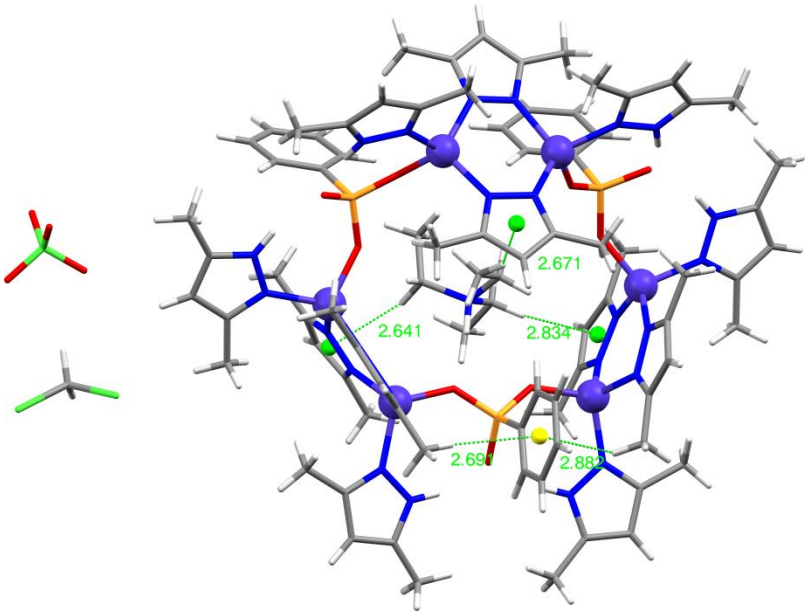

Figure A5.11 Illustration of the hydrogen-π intermolecular and intramolecular interactions in complex **11**·DCM. The green spheres represent the centroids of the $dmpz^-$ rings, while the yellow sphere represents the centroid of the phenyl ring. The dashed green lines show the distances (in Å) between the centroids and the hydrogens. Colour code: Co^{II}: violet, O: red, N: blue, P: orange, C: grey, H: white, Cl: green.

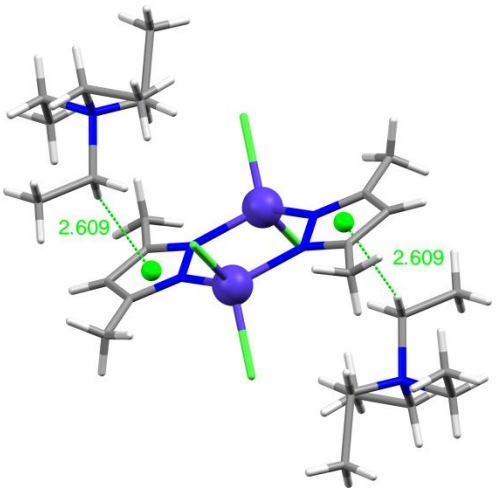

Figure A5.12 Illustration of the hydrogen-π intermolecular interactions in complex **12**. The green spheres represent the centroids of the dmpz$^-$ rings. The dashed green lines show the distances (in Å) between the centroids and the hydrogens. Colour code: Co^{II}: violet, N: blue, C: grey, H: white, Cl: green.

Table A5.6 Data collection and crystallographic parameters for complexes **6** and **7**.

Chemical formula	$C_{102}H_{159}Co_9N_{36}O_9P_3$ (**6**)	$C_{28}H_{50}Br_2Co_3N_8O_6P_2$ (**7**)
M_r	2656.92	993.31
Crystal system, space group	Triclinic, $P\bar{1}$	Triclinic, $P\bar{1}$
Temperature (K)	150	273
***a*, *b*, *c* (Å)**	19.0607 (11), 20.2221 (11), 21.6653 (13)	10.3097 (10), 10.3341 (10), 11.2890 (11)
α, β, γ (°)	78.031 (2), 66.318 (2), 85.452 (2)	75.342 (4), 64.140 (3), 69.826 (3)
***V* (Å^3)**	7481.3 (8)	1008.38 (17)
Z	2	1
Radiation type	Mo *K*α	Mo *K*α
μ (mm^{-1})	1.06	3.33
Crystal size (mm)	0.2 × 0.17 × 0.03	0.17 × 0.11 × 0.01
Diffractometer	Bruker D8 VENTURE	Bruker D8 VENTURE
T_{min}, T_{max}	0.669, 0.745	0.571, 0.746
No. of measured, independent and observed [$I > 2\sigma(I)$] reflections	119802, 27375, 19445	4577, 4577, 3693
R_{int}	0.073	0.046
$R[F^2 > 2\sigma(F^2)]$, $wR(F^2)$, S	0.062, 0.154, 1.04	0.044, 0.106, 1.12
No. of reflections	27375	4577
No. of parameters	1477	225
No. of restraints	1380	107
Δ>max, Δ>min (e Å^{-3})	1.21, −1.13	0.91, -0.71

Table A5.7 Data collection and crystallographic parameters for complexes **8**(MeCN), **9a**(DCM) and **9b**(DCE).

Chemical formula	$C_{86}H_{133}Co_8N_{32}O_9P_3·4(C_2H_3N)$ (**8**·4(MeCN))	$C_{86}H_{133}Co_8N_{32}O_9P_3·C_6H_{16}N·ClO_4·0.5(CH_2Cl_2)·0.5(H_2O)$ (**9a**·0.5(DCM)·0.5(H_2O))	$C_{86}H_{133}Co_8N_{32}O_9P_3·ClO_4·2.25(C_2H_4Cl_2)·C_6H_{16}N·0.75(C_5H_8N_2)·O$ (**9b**·2.25DCE·0.75(Hdmpz)·H_2O)
M_r	2487.80	2576.70	2837.99
Crystal system, space group	Triclinic, $P\bar{1}$	Triclinic, $P\bar{1}$	Triclinic, $P\bar{1}$
Temperature (K)	150	150	150
***a*, *b*, *c* (Å)**	17.6918 (13), 19.2794 (14), 22.2531 (16)	19.3671 (9), 20.2703 (9), 20.5324 (11)	18.2026 (11), 19.3632 (11), 21.9160 (13)
α, β, γ (°)	104.487 (2), 107.379 (2), 107.962 (2)	66.918 (2), 66.587 (2), 83.709 (2)	79.005 (2), 69.208 (2), 67.410 (2)
***V* (Å^3)**	6382.2 (8)	6794.5 (6)	6654.2 (7)
Z	2	2	2
Radiation type	Mo *K*α	Mo *K*α	Mo *K*α
μ (mm^{-1})	1.11	1.09	1.19
Crystal size (mm)	0.3 × 0.17 × 0.05	0.25 × 0.2 × 0.02	0.2 × 0.15 × 0.04
Diffractometer	Bruker D8 VENTURE	Bruker D8 VENTURE	Bruker D8 VENTURE
No. of measured, independent and observed [$I > 2\sigma(I)$] reflections	72997, 25869, 20191	117186, 24764, 18519	138607, 30411, 21869
R_{int}	0.033	0.061	0.068
$R[F^2 > 2\sigma(F^2)]$, $wR(F^2)$, GOF on F^2	0.062, 0.169, 1.04	0.066, 0.214, 1.03	0.043, 0.134, 1.04
No. of reflections	25869	24764	30411
No. of parameters	1375	1365	1588
No. of restraints	2	19	N/A
Δ>max, Δ>min (e Å^{-3})	1.09, −0.94	2.13, −2.43	1.02, −0.93

Table A5.8 Data collection and crystallographic parameters for complexes **11**·DCM and **12**.

Chemical formula	$C_{78}H_{105}Co_6N_{24}O_9P_3·ClO_4·CH_2Cl_2·C_6H_{16}N$ (**11**·DCM)	$C_{10}H_{14}Cl_4Co_2N_4·2(C_8H_{20}N)$ (**12**)
M_r	2255.92	710.41
Crystal system, space group	Monoclinic, $P2_1/n$	Monoclinic, $P2_1/c$
Temperature (K)	100	273
***a*, *b*, *c* (Å)**	18.0818 (5), 26.3962 (8), 23.0996 (7)	9.4495 (16), 16.616 (3), 11.855 (2)
α, β, γ (°)	107.486 (3)	110.561 (6)
***V* (Å^3)**	10515.7 (6)	1742.9 (6)
Z	4	2
Radiation type	Cu *K*α	Mo *K*α
μ (mm^{-1})	8.93	1.28
Crystal size (mm)	0.08 × 0.06 × 0.03	0.2 × 0.2 × 0.2
Diffractometer	Rigaku 007HF equipped with Varimax confocal mirrors and an AFC11 goniometer and HyPix 6000 detector	Bruker D8 VENTURE
No. of measured, independent	98090, 19119, 10584	28443, 4009, 3187

and observed [$I > 2\sigma(I)$] reflections		
R_{int}	0.163	0.063
$R[F^2 > 2\sigma(F^2)]$, $wR(F^2)$, GOF on F^2	0.066, 0.159, 0.98	0.058, 0.187, 1.07
No. of reflections	19119	4009
No. of parameters	1243	210
No. of restraints	N/A	28
Δ>max, Δ>min (e Å^{-3})	0.39, −0.58	1.16, −0.43

A5. References

1. A. Spek, *Acta Crystallographica Section D*, 2009, **65**, 148-155.
2. C. Jordi, A. Pere and A. Santiago, *Chemistry – A European Journal*, 2004, **10**, 190-207.
3. M. Pinsky and D. Avnir, *Inorg Chem*, 1998, **37**, 5575-5582.
4. M. K. Ehlert, S. J. Rettig, A. Storr, R. C. Thompson and J. Trotter, *Can J Chem*, 1993, **71**, 1425-1436.

Chapter 6

Table A6.1 The CShMs values calculated with the program SHAPE for each geometry for the six-coordinate M^{III} in complexes **13 − 17**.[3, 5]

Geometry	Tb (13)	Dy (14)	Ho (15)	Er (16)	Y (17)
Hexagon (D_{6h})	33.39	33.53	33.63	33.32	33.31
Pentagonal pyramid (C_{5v})	27.55	27.42	27.57	27.79	27.53
Octahedron (O_h)	**1.13**	**1.06**	**1.10**	**0.99**	**1.01**
Trigonal prism (D_{3h})	14.46	14.85	14.50	15.15	14.94
Johnson pentagonal pyramid J2 (C_{5v})	30.27	30.07	30.21	30.44	30.20

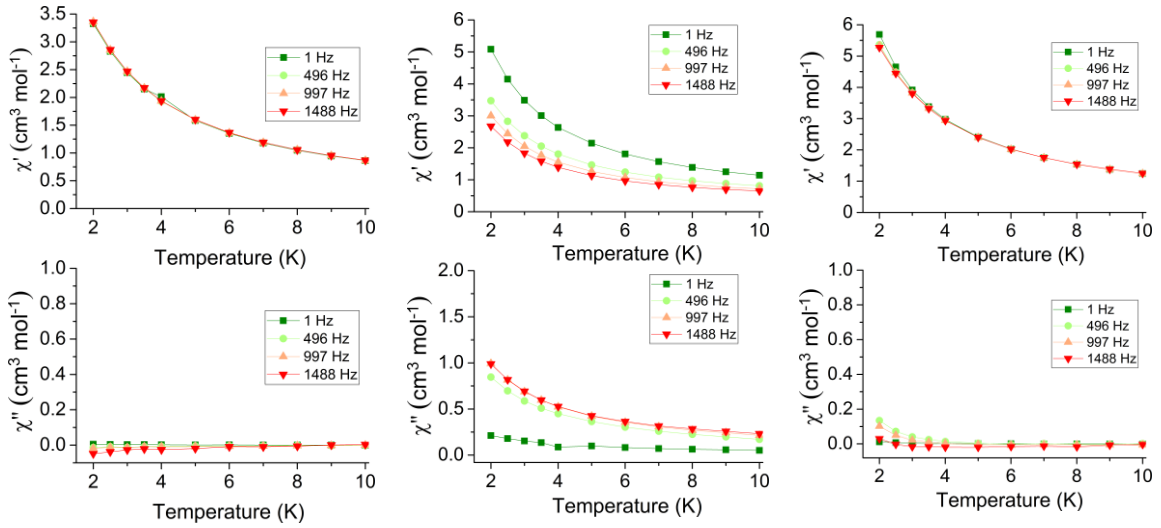

Figure A6.1 Temperature dependence of the in-phase (top) and the out-of-phase (bottom) ac susceptibility signals in zero dc field and in the frequency range 1 – 1488 Hz, for complexes **13** (Tb), **14** (Dy) and **15** (Ho) from left to right. The solid lines are a guide to the eye.

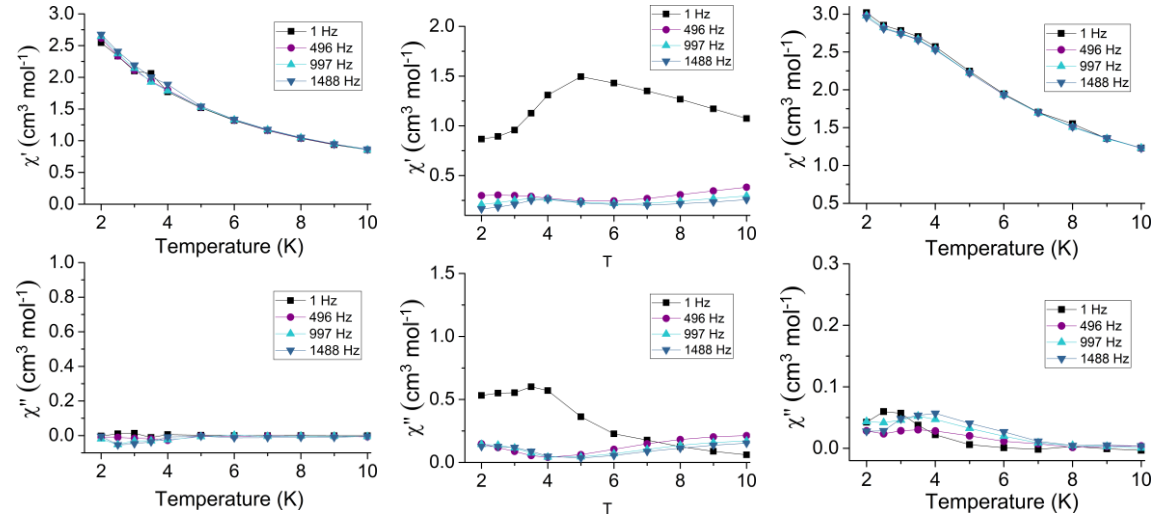

Figure A6.2 Temperature dependence of the in-phase (top) and the out-of-phase (bottom) ac susceptibility signals in 2000 Oe dc field and in the frequency range 1 – 1488 Hz, for complexes **13** (Tb), **14** (Dy) and **15** (Ho) from left to right. The solid lines are a guide to the eye.

Field sweep ac susceptibility experiments

Fitting the data (with programme CC-FIT[6, 7]) at 5 K with one time constant (τ), gave the values of τ = 0.009 – 0.04 s and α = 0.35 – 0.5, producing a satisfactory fit (Fig. A6.3 left

top). However, at 10 K two time constants (τ_1 and τ_2) were necessary in order to obtain a satisfactory fit (Fig. A6.3 left bottom). The values extracted are τ_1 = 0.0004 – 0.0008 s and α_1 = 0.03 – 0.07 and τ_2 = 0.0003 – 0.003 s and α_2 = 0.6 – 0.7. The optimum field (1000 Oe) was obtained after consideration of both field sweep measurements at 5 and 10 K by plotting the relaxation times versus the applied dc fields (Fig. A6.3 right).

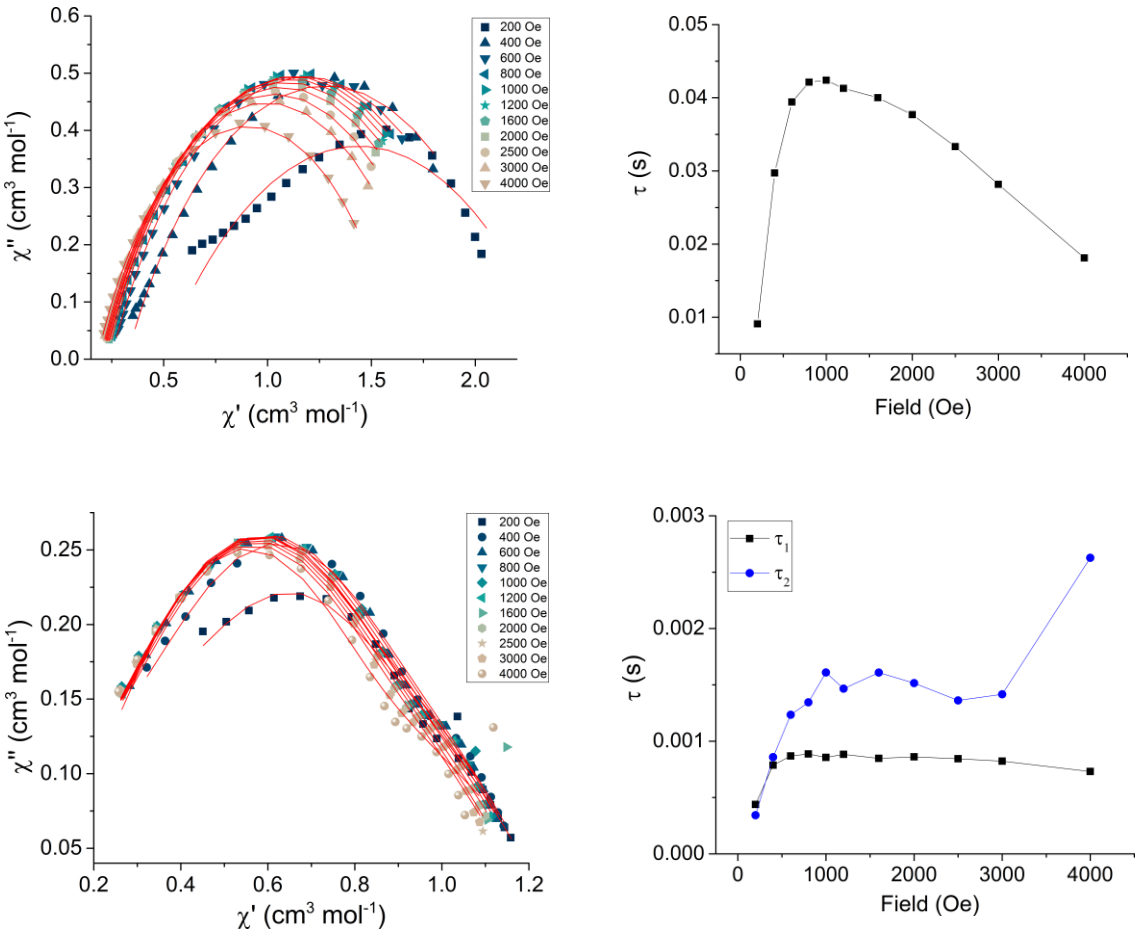

Figure A6.3 *Left)* Cole–Cole plots of the ac magnetic susceptibility of **14** (Dy), at 5 K (*top*) and 10 K (*bottom*) under variable dc fields (200 – 4000 Oe). The red lines correspond to the fit (CC-FIT).[6, 7] *Right)*: Plot of the relaxation time (τ) as a function of the applied dc magnetic field at 5 K (*top*) and 10 K (*bottom*). The solid lines are a guide to the eye.

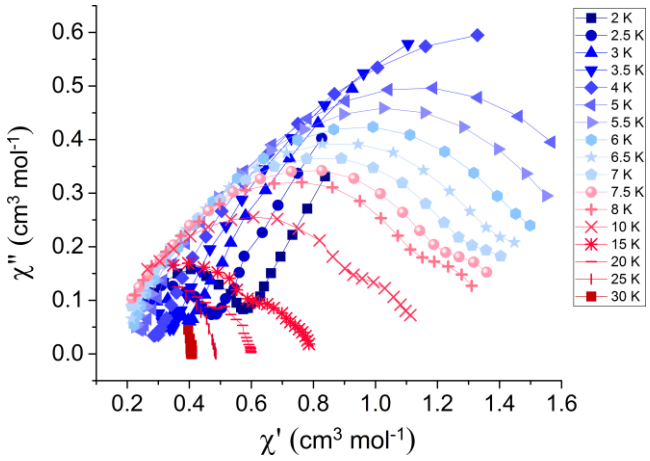

Figure A6.4 Cole–Cole plot of the ac magnetic susceptibility of complex **14** (Dy) at 1000 Oe. The solid lines are a guide to the eye.

Table A6.2 Cole-Cole fit values of **14** (Dy) with an applied dc field of 1000 Oe.

Temperatures (K)	χ_S (cm^3 mol^{-1})	χ_T (cm^3 mol^{-1})	τ (s)	α	Residual
3.5	3.00E-01	3.11E+00	5.75E-01	4.20E-01	8.11E-03
4	2.72E-01	2.54E+00	1.88E-01	3.84E-01	7.71E-04
5	2.17E-01	2.04E+00	4.28E-02	3.67E-01	3.68E-04
5.5	1.93E-01	1.86E+00	2.32E-02	3.65E-01	6.30E-04
6	1.79E-01	1.71E+00	1.39E-02	3.68E-01	1.69E-03
6.5	1.58E-01	1.61E+00	8.92E-03	3.79E-01	3.91E-03
7	1.38E-01	1.52E+00	6.13E-03	3.98E-01	6.30E-03
7.5	1.14E-01	1.45E+00	4.31E-03	4.15E-01	7.71E-03
8	9.83E-02	1.38E+00	3.17E-03	4.29E-01	8.40E-03

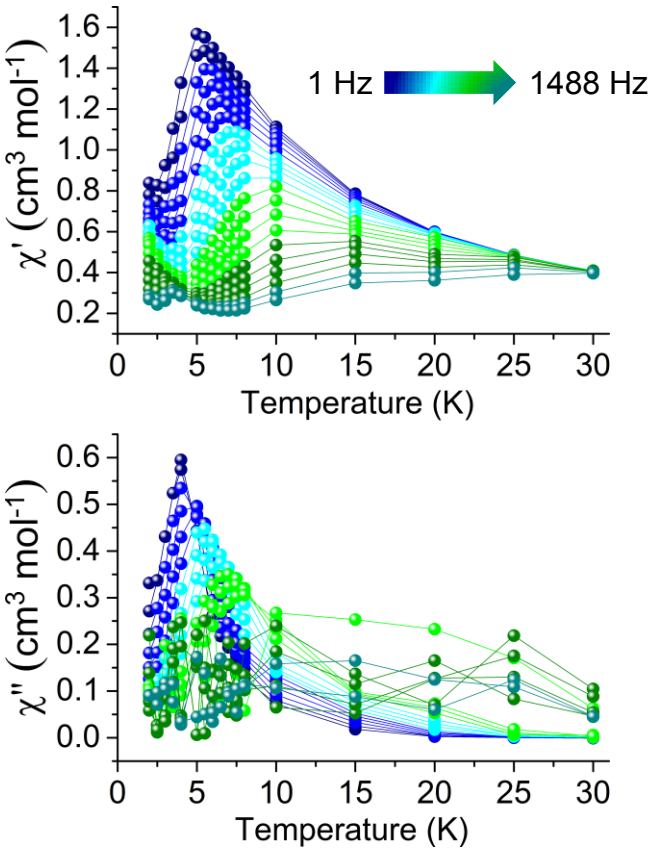

Figure A6.5 Temperature dependence of the in-phase (*top*) and the out-of-phase (*bottom*) ac susceptibility signals in 1000 Oe dc field and in the frequency range 1 – 1488 Hz for complex **14** (Dy). The solid lines are a guide to the eye.

A6. References

1. M. Pinsky and D. Avnir, *Inorg Chem*, 1998, **37**, 5575-5582.
2. S. Alvarez, D. Avnir, M. Llunell and M. Pinsky, *New J Chem*, 2002, **26**, 996-1009.
3. CC-FIT Copyright © 2014 Nicholas F. Chilton.
4. Y.-N. Guo, G.-F. Xu, Y. Guo and J. Tang, *Dalton Transactions*, 2011, **40**, 9953-9963.

Chapter 7

Table A7.1 Data collection and crystallographic parameters for complexes **18**·xMeCN·yH_2O, **19** and **20**·xMeCN·yH_2O.

Chemical formula	$C_{193}H_{149}La_9N_{39}O_{61}\cdot C_2H_3N$ (**18**·MeCN)	$C_{54}H_{42}Ce_3N_{17}O_{31}\cdot Cl\cdot C_6H_{16}N$ (**19**)	$C_{54}H_{48}DyN_{10}O_{12}\cdot C_2H_3N\cdot Cl\cdot 0.5(H_2O)$ (**20**·MeCN·0.5H_2O)
M_r	5281.75	1983.05	1276.53
Crystal system, space group	Monoclinic, $P2_1/c$	Monoclinic, $P2_1/c$	Monoclinic, $C2/c$
Temperature (K)	100	100	150
***a*, *b*, *c* (Å)**	21.9875 (6), 52.2519 (7), 22.8085 (3)	24.9578 (5), 33.3149 (13), 13.4054 (2)	45.3961 (18), 11.9875 (4), 25.5995 (10)
α, β, γ (°)	90.6607 (18)	96.5157 (16)	123.784 (1)
***V* (Å^3)**	26202.6 (9)	11074.2 (5)	11578.5 (8)
Z	4	4	8
Radiation type	Mo *K*α	Cu *K*α	Mo *K*α
μ (mm^{-1})	0.38	10.15	1.41
Crystal size (mm)	0.14 × 0.09 × 0.05	0.11 × 0.03 × 0.02	0.1 × 0.03 × 0.01
Diffractometer	XtaLAB AFC12 (RCD3): Kappa single	XtaLAB AFC11 (RCD3): quarter-chi single	Bruker D8 VENTURE
No. of measured, independent and observed [$I > 2\sigma(I)$] reflections	298819, 57947, 36863	95540, 19945, 12485	59119, 10597, 8176
R_{int}	0.081	0.149	0.062
***R*[$F^2 > 2\sigma(F^2)$], *wR*(F^2), *GOF on* F^2**	0.127, 0.311, 1.08	0.087, 0.247, 1.03	0.045, 0.116, 1.05
No. of reflections	57947	19945	10597
No. of parameters	2569	1012	775
No. of restraints	122	0.087, 0.247, 1.03	8
Δ>max, Δ>min (e Å^{-3})	1.97, -1.06	1.43, -1.70	1.44, -1.26

Table A7.2 Data collection and crystallographic parameters for complexes **21**, **22** and **23**·xMeCN·yH_2O.

Chemical formula	$C_{56}H_{41}Cl_{0.7}Co_2LaN_{13.3}O_{14.9}$ (**21**)	$C_{56}H_{41}CeCl_{0.7}Co_2N_{13.3}O_{14.9}$ (**22**)
M_r	1420.20	1421.41
Crystal system, space group	Monoclinic, $P12_1/m1$	Monoclinic, $P12_1/m1$
Temperature (K)	295	295
***a*, *b*, *c* (Å)**	13.8585 (7), 15.5823 (9), 14.354 (1)	13.8358 (16), 15.5505 (17), 14.3349 (19)
α, β, γ (°)	112.277 (2)	112.131 (3)
***V* (Å^3)**	2868.4 (3)	2857.0 (6)
Z	2	2
Radiation type	Mo *K*α	Mo *K*α
μ (mm^{-1})	1.42	1.47
Crystal size (mm)	0.09 × 0.06 × 0.06	0.16 × 0.07 × 0.03
Diffractometer	Bruker D8 VENTURE	Bruker D8 VENTURE
No. of measured, independent and	53820, 9032, 6995	7350, 7350, 5355

observed [$I > 2\sigma(I)$] reflections		
R_{int}	0.051	0.128
$R[F^2 > 2\sigma(F^2)]$, $wR(F^2)$, GOF on F^2	0.053, 0.175, 0.98	0.082, 0.221, 1.06
No. of reflections	9032	7350
No. of parameters	418	418
No. of restraints	3	3
Δ>max, Δ>min (e Å^{-3})	2.97, -1.52	3.23, -1.03

Table A7.3 Data collection and crystallographic parameters for complexes **23**·xMeCN·yH_2O and **24**·xMeOH·yH_2O.

Chemical formula	$C_{135}H_{99}CoDy_2N_{25}O_{22}\cdot C_6H_{16}N\cdot 4(H_2O)\cdot C_2H_3N$ **23**·MeCN·4H_2O	$C_{116.8}H_{116}Cl_{0.3}Gd_6N_{23.8}O_{44.5}$ (**24**·1.5MeOH·2.75H_2O)
M_r	3023.64	3522.24
Crystal system, space group	Monoclinic, $P2_1/c$	Triclinic, $P\bar{1}$
Temperature (K)	100	100
a, b, c (Å)	22.5114 (4), 29.1424 (12), 29.1566 (8)	13.5326 (3), 13.9584 (3), 35.3977 (6)
α, β, γ (°)	109.838 (3)	87.965 (1), 84.3065 (17), 81.384 (2)
V (Å^3)	17992.7 (10)	6576.9 (2)
Z	4	2
Radiation type	Cu $K\alpha$	Mo $K\alpha$
μ (mm^{-1})	5.61	3.08
Crystal size (mm)	0.06 × 0.04 × 0.03	0.16 × 0.08 × 0.03
Diffractometer	Rigaku 007HF equipped with Varimax confocal mirrors and an AFC11 goniometer and HyPix 6000 detector	Rigaku FRE+ equipped with VHF Varimax confocal mirrors and an AFC12 goniometer and HyPix 6000 detector
No. of measured, independent and observed [$I > 2\sigma(I)$] reflections	161284, 32752, 17559	138824, 138824, 112556
R_{int}	0.132	0.047
$R[F^2 > 2\sigma(F^2)]$, $wR(F^2)$, GOF on F^2	0.084, 0.267, 1.02	0.053, 0.127, 1.09
No. of reflections	32752	138824
No. of parameters	1617	1833
No. of restraints	52	38
Δ>max, Δ>min (e Å^{-3})	0.82, -1.36	1.91, -2.33

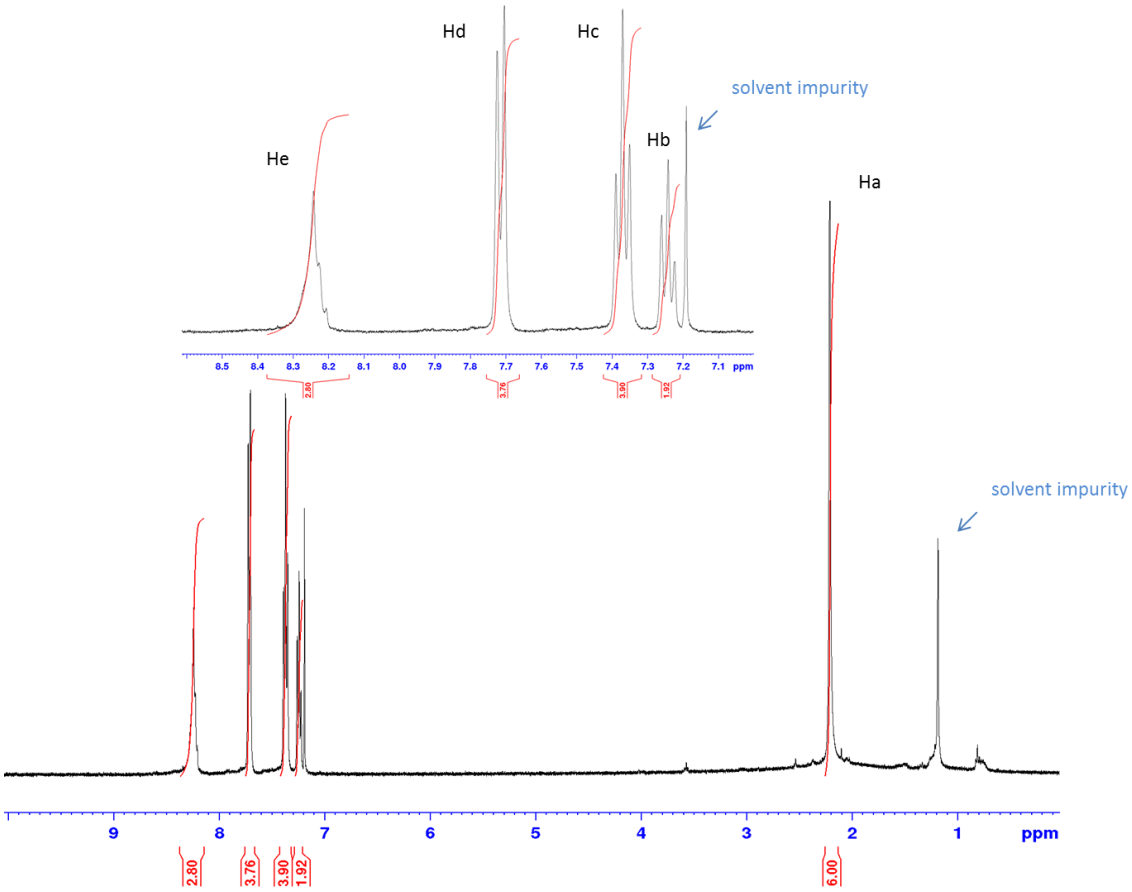

Scheme A7.1 The ^{1}H−NMR spectrum of the ligand $[H_5L]\cdot 3Cl$ in $CDCl_3$.

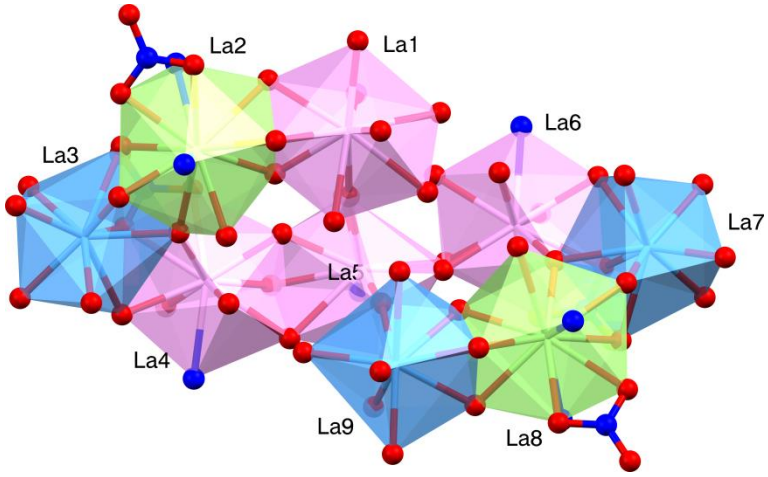

Figure A7.1 Illustration of the different polyhedra of the nine- (blue), ten- (pink) and eleven-coordinate (green) La atoms in complex **18**. Colour code: O: red, N: blue.

Harris notation

Harris notation describes the binding modes as [X.$Y_1Y_2Y_3$…Y_n], where X is the overall number of metals bound by the ligand, and each value of Y refers to the number of metal atoms attached to the different donor atoms. The ordering of Y is listed by the Cahn–Ingold–Prelog priority rules, hence O before N.[8, 9]

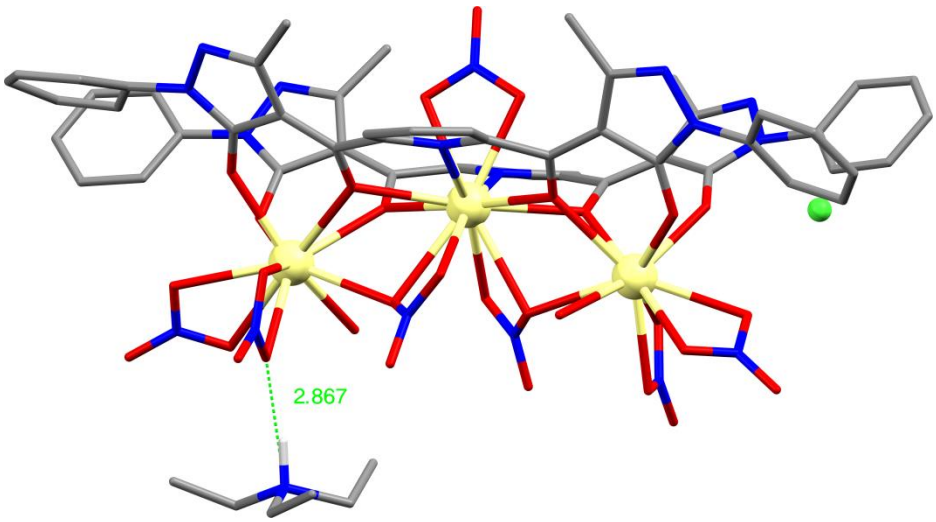

Figure A7.2 The molecular structure of **19**. The green dashed line shows the N···O distance (in Å) between the $[HNEt_3]^+$ and a NO_3^- ligand. Colour code: Ce: light yellow, O: red, N: blue, Cl: green, C: grey, H: white. Hydrogen atoms are omitted for clarity except for the H of the protonated NEt_3.

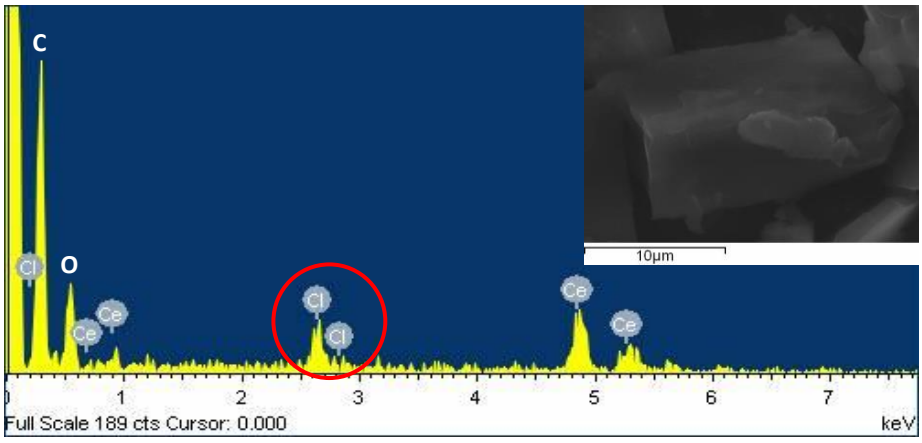

Figure A7.3 EDX spectra of **19**. The inset displays the area of the sample used for the analysis.

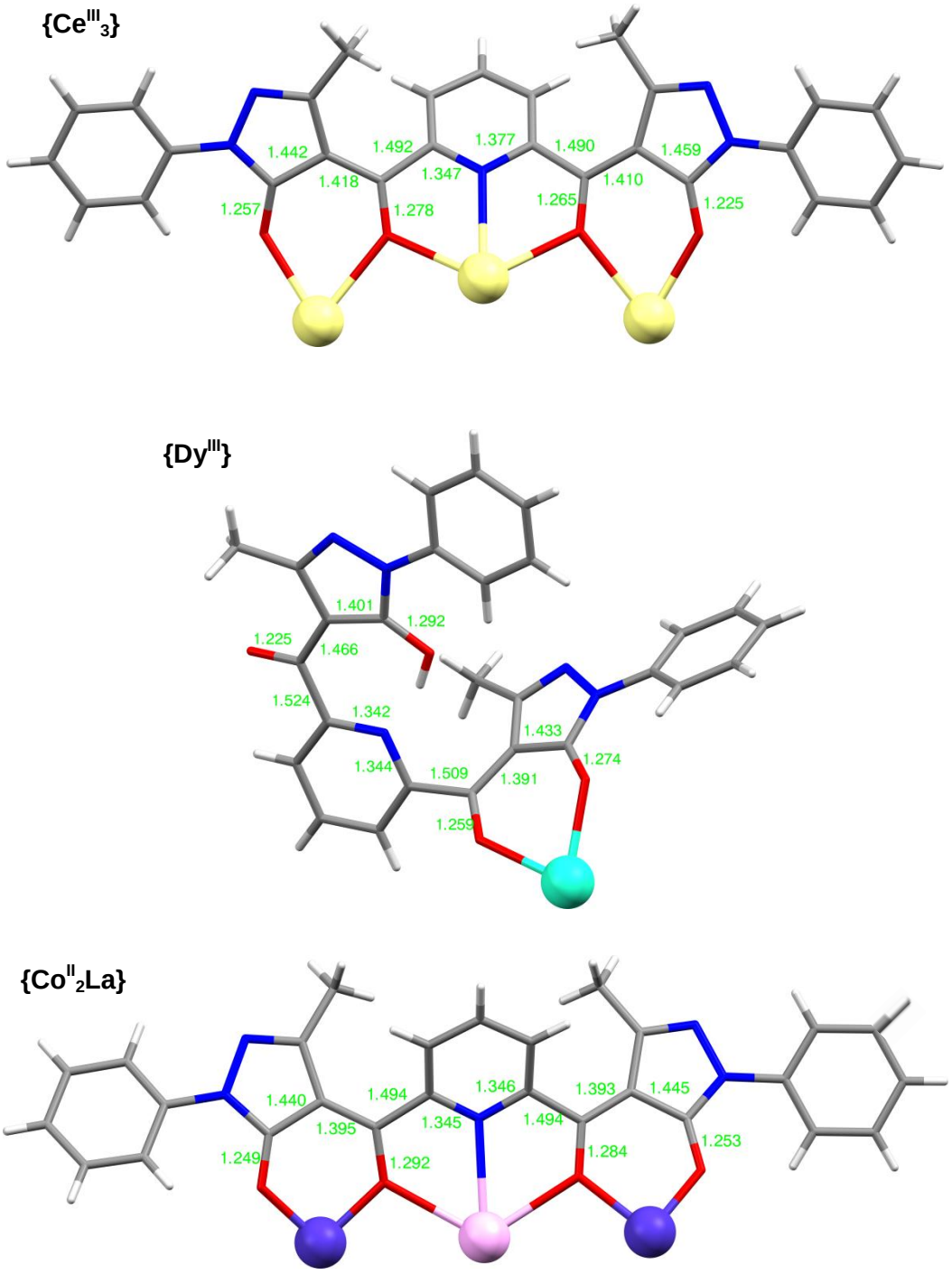

Figure A7.4 Illustration of the bridging mode of the ligands with the metal centres in complexes **19** (HL^- or L^{2-}), **20** (HL^-) and **21** (L^{2-}) (from top to bottom) and the bond distances (in Å) within the ligands. Colour code: Ce: light yellow, Co: violet, La: light pink, Dy: turquoise, O: red, N: blue, C: grey, H: white.

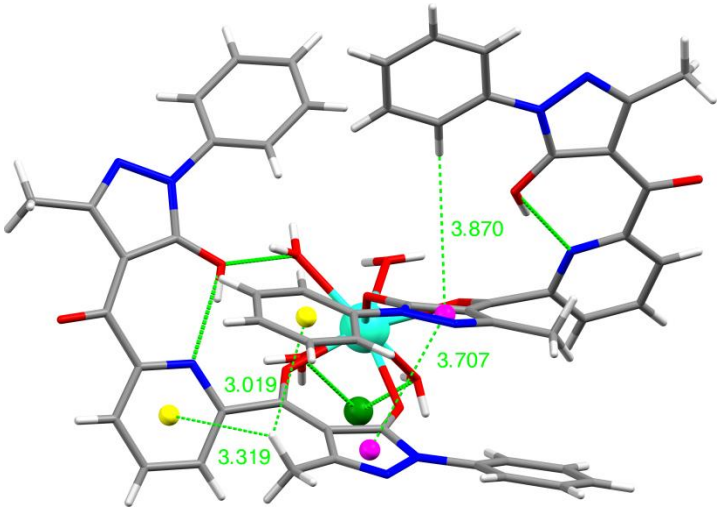

Figure A7.5 Illustration of the intramolecular hydrogen bonds, hydrogen-*π* and *π*-*π* interactions in complex **20**·xMeCN·yH_2O. The dashed green lines show the distances (in Å) between the centroids, and between the centroids and the hydrogens. The yellow spheres represent the centroids of the phenyl rings, while the pink ones represent the centroids of the pyrazolone rings. Colour code: Dy^{III}: turquoise, O: red, C: grey, N: blue, Cl: green, H: white.

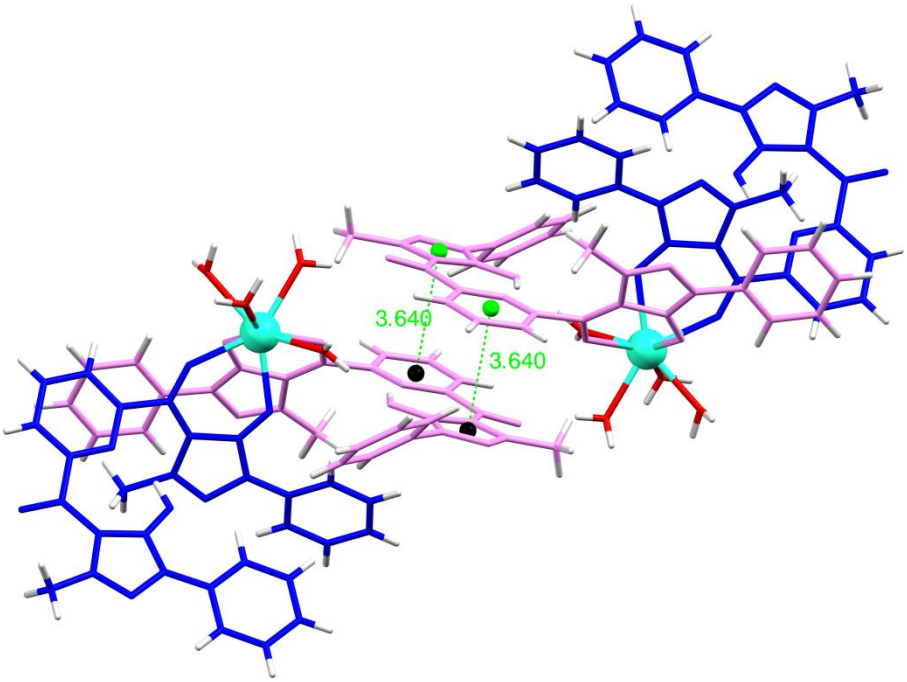

Figure A7.6 Illustration of the intermolecular *π*-*π* interactions in complex **20**·xMeCN·yH_2O. Each ligand in one molecule is represented with a different colour (blue and pink) for clarity. The dashed green lines show the distances (in Å) between the centroids of neighbouring molecules (black and green spheres). Colour code: Dy^{III}: turquoise, O: red, H: white.

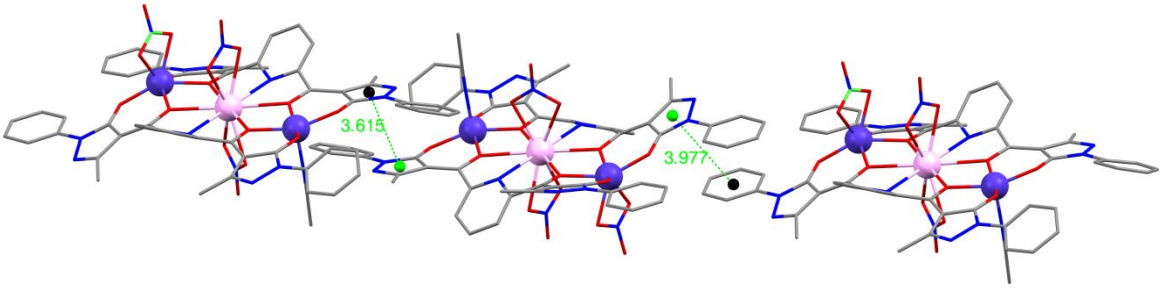

Figure A7.7 Illustration of the intermolecular *π*-*π* interactions between the aromatic pyrazolone and phenyl rings of neighbouring molecules for complex **21**. The green spheres represent the centroids of the aromatic rings in the same molecule and the black one in the neighbouring molecules. The dashed green lines show the distances (in Å) between the centroids. Colour code: Co^{II}: violet, La^{III}: light pink, Cl: green, O: red, N: blue, C: grey. Hydrogen atoms are omitted for clarity.

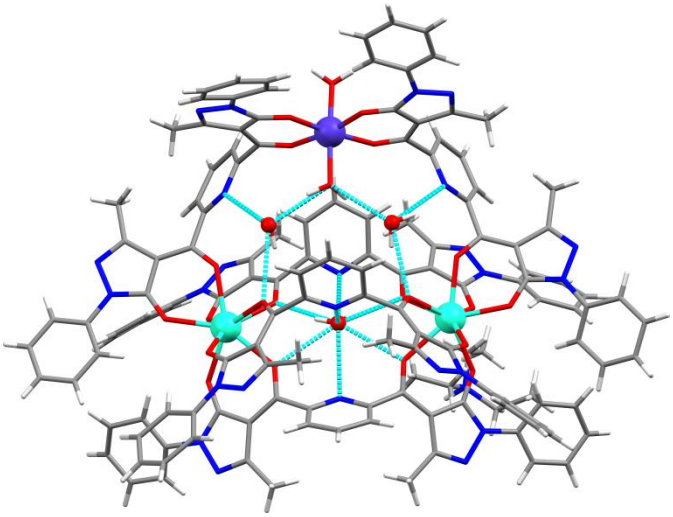

Figure A7.8 Illustration of the intermolecular hydrogen bonds (dashed blue lines) with the three molecules of water crystallised in the centre of the molecule for complex **23**·MeCN·4H_2O (only the modelled molecules of MeCN and H_2O are shown here). Colour code: Co^{II}: violet, Dy^{III}: turquoise, O: red, N: blue, C: grey, H: white.

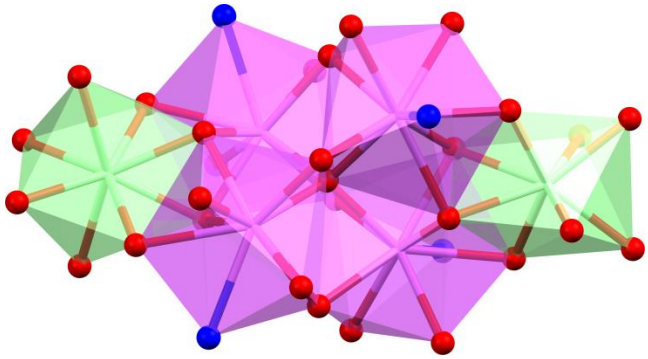

Figure A7.9 Illustration of the different polyhedra of the eight-coordinate (green polyhedra, Gd1 and Gd6) and nine-coordinate (pink polyhedra, Gd2 – Gd5) Gd atoms in complex **24**. Colour code: O: red, N: blue.

Table A7.4 Co^{II} to La^{III} ratio extracted from EDX spectroscopy.

Element	Weight%	Atomic%
Co K	41.57	62.64
La L	58.43	37.36
Totals	100.00	

Table A7.5 Co^{II} to Ce^{III} ratio extracted from EDX spectroscopy.

Element	Weight%	Atomic%
Co K	45.72	66.70
Ce L	54.28	33.30
Totals	100.00	

Table A7.6 Co^{II} to Dy^{III} ratio extracted from EDX spectroscopy.

Element	Weight%	Atomic%
Co K	14.38	31.65
Dy L	85.62	68.35
Totals	100.00	

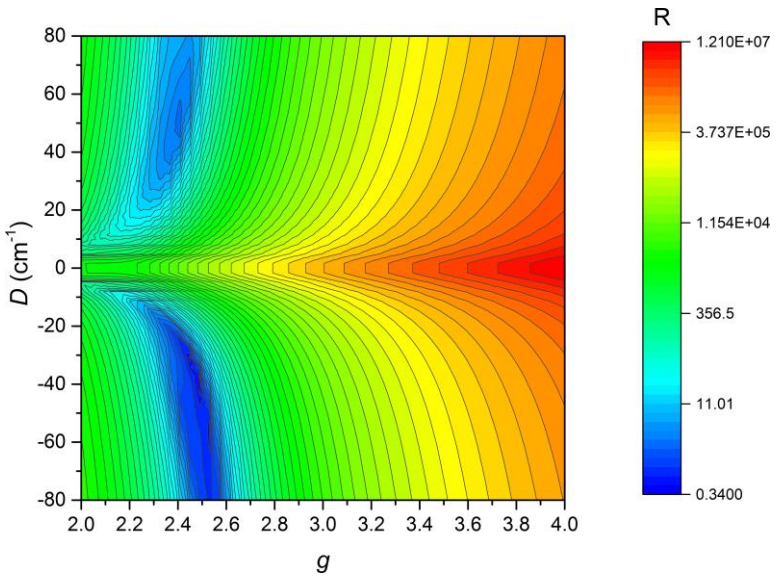

Figure A7.10 The 2D-contour plot of the residual error (R) for the fitting parameters *D* and *g* with the programme PHI[10] for complex **21**·$2H_2O$.

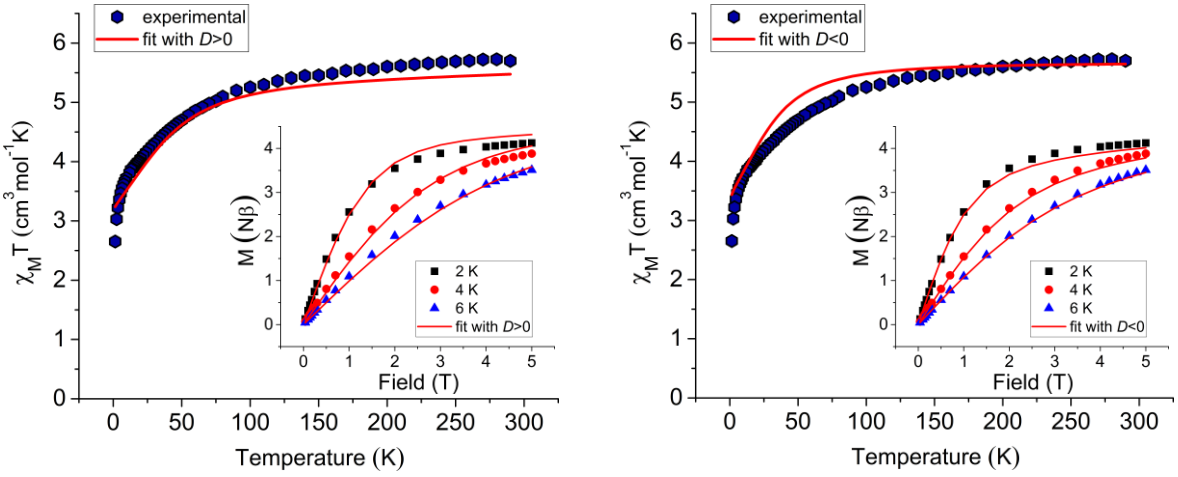

Figure A7.11 $\chi_M T$ versus temperature data for **21**·2H_2O in a field of 1000 Oe from 290–2 K. *Inset*: Magnetisation versus field data at temperatures 2, 4, and 6 K for **21**·2H_2O. The red solid lines represent the fit with **eqn 7.2** (excluding *zj*): fit with *D*>0 (*left*) and *D*<0 (*right*).

Table A7.7 Magnetic parameters for **21**·2H_2O extracted with programme PHI[10] using eqn 7.2 excluding the parameter *zj*.

Equation 7.2			
D **(cm^{-1})**	***g***	χ_{TIP} **(cm^3 mol^{-1})**	**R (%)**
+46.70 (±2.47)	2.39	0.0006	86.06
−36.92 (±0.86)	2.46	-	67.61

A7. References

1. A. Spek, *Acta Crystallographica Section D*, 2009, **65**, 148-155.
2. C. Jordi, A. Pere and A. Santiago, *Chemistry – A European Journal*, 2004, **10**, 190-207.
3. M. Pinsky and D. Avnir, *Inorganic Chemistry*, 1998, **37**, 5575-5582.
4. M. K. Ehlert, S. J. Rettig, A. Storr, R. C. Thompson and J. Trotter, *Canadian Journal of Chemistry*, 1993, **71**, 1425-1436.
5. S. Alvarez, D. Avnir, M. Llunell and M. Pinsky, *New Journal of Chemistry*, 2002, **26**, 996-1009.
6. CC-FIT Copyright © 2014 Nicholas F. Chilton.
7. Y.-N. Guo, G.-F. Xu, Y. Guo and J. Tang, *Dalton Transactions*, 2011, **40**, 9953-9963.
8. R. A. Coxall, S. G. Harris, D. K. Henderson, S. Parsons, P. A. Tasker and R. E. P. Winpenny, *Journal of the Chemical Society, Dalton Transactions*, 2000, 2349-2356.
9. R. E. P. Winpenny, *Journal of the Chemical Society, Dalton Transactions*, 2002, 1-10.
10. N. F. Chilton, R. P. Anderson, L. D. Turner, A. Soncini and K. S. Murray, *Journal of Computational Chemistry*, 2013, **34**, 1164-1175.

Table of complexes 1 – 24.

Complex	Molecular formula
1	$[Co^{II}(H_2bic)Cl]$
2	$[Co^{II}_9(Hbic)_4(bic)_2Cl_4]$
2·12H_2O	$[Co^{II}_9(Hbic)_4(bic)_2Cl_4]\cdot 12H_2O$
3·2THF	$[Co^{II}Co^{III}_2(\mu_3\text{-}OH)(\mu\text{-}pz)_4(DBM)_3]\cdot 2THF$
4·2MeCN	$[Co^{II}Co^{III}_2(\mu_3\text{-}OH)(\mu\text{-}pz)_4(DBM)_3]\cdot 2MeCN$
5	$[Co^{II}Co^{III}_2(\mu_3\text{-}OH)(\mu\text{-}pz)_4(acac)_3]$
6·xMeCN·yH_2O	$[Co^{II}_9(t\text{BuPO}_3)_3(dmpz)_{12}(Hdmpz)_6]\cdot xMeCN\cdot yH_2O$
7	$[Co^{II}_3(t\text{BuPO}_3)_2(Hdmpz)_4Br_2]$
8(MeCN)	$[Co^{II}_8(EtPO_3)_3(dmpz)_{10}(Hdmpz)_6]\cdot xMeCN\cdot yH_2O$
9a(DCM)	$[HNEt_3][Co^{II}_8(EtPO_3)_3(dmpz)_{10}(Hdmpz)_6][ClO_4]\cdot xDCM\cdot yH_2O$
9b(DCE)	$[HNEt_3][Co^{II}_8(EtPO_3)_3(dmpz)_{10}(Hdmpz)_6][ClO_4]\cdot 0.75(Hdmpz)\cdot 2.25DCE\cdot H_2O$
10	$[Co^{II}_3(dmpz)_4(Hdmpz)_2Cl_2]$
11·DCM	$[HNEt_3][Co^{II}_6(PhPO_3)_3(dmpz)_6(Hdmpz)_6][ClO_4]\cdot DCM$
12	$[HNEt_4]_2[Co^{II}_2(dmpz)_2Cl_4]$
13	$[Tb^{III}(Cy_3PO)_2Cl_3(EtOH)]\cdot EtOH$
14	$[Dy^{III}(Cy_3PO)_2Cl_3(EtOH)]\cdot 0.5EtOH$
15	$[Ho^{III}(Cy_3PO)_2Cl_3(EtOH)]\cdot EtOH$
16	$[Er^{III}(Cy_3PO)_2Cl_3(EtOH)]\cdot EtOH$
17	$[Y^{III}(Cy_3PO)_2Cl_3(EtOH)]\cdot EtOH$
18·xMeCN·yH_2O	$[La^{III}_9(L^{2-})_7(NO_3)_4(CO_3)_4(OH)(H_2O)_8]\cdot xMeCN\cdot yH_2O$
19a and **19b**	$[HNEt_3][Ce^{III}_3(HL^-)_2(NO_3)_7(H_2O)_2][Cl]\cdot xMeCN\cdot yH_2O\cdot zEt_2O$ and $[HNEt_3][Ce^{III}_3(HL^{2-})(H_2L)(NO_3)_7(H_2O)_2][Cl]\cdot xMeCN\cdot yH_2O\cdot zEt_2O$
20·xMeCN·yH_2O	$[Dy^{III}(HL^-)_2(H_2O)_4][Cl]\cdot xMeCN\cdot yH_2O$
21	$[Co^{II}_2La^{III}(L^{2-})_2(NO_3)_{2.3}Cl_{0.7}(MeCN)]$
22	$[Co^{II}_2Ce^{III}(L^{2-})_2(NO_3)_{2.3}Cl_{0.7}(MeCN)]$
23·xMeCN·yH_2O	$[HNEt_3][Co^{II}Dy^{III}_2(L^{2-})_4(HL^-)(H_2O)_2]\cdot xMeCN\cdot yH_2O$
24·xMeOH·yH_2O	$[Gd^{III}_6(L^{2-})_4(OH)_4(O^{2-})(MeOH)_6(H_2O)_2][NO_3]_{3.75}[Cl]_{0.25}\cdot xMeOH\cdot yH_2O$

List of starting materials (metal salts)

$CoCl_2 \cdot 6H_2O$	Sigma Aldrich (≥97%)
$Co(NO_3)_2 \cdot 6H_2O$	Sigma Aldrich (98%)
$CoBr_2$	Sigma Aldrich (99%)
$Co(BF_4)_2 \cdot xH_2O$	Alfa Aesar (96%)
$Co(ClO_4)_2 \cdot 6H_2O$	Sigma Aldrich (98%)
$La(NO_3)_3 \cdot 6H_2O$	Sigma Aldrich (≥99%)
$Ce(NO_3)_3 \cdot 6H_2O$	Sigma Aldrich (99%)
$Gd(NO_3)_3 \cdot 6H_2O$	Sigma Aldrich (99.9%)
$TbCl_3 \cdot 6H_2O$	Alfa Aesar (99.9%)
$Dy(NO_3)_3 \cdot xH_2O$	Sigma Aldrich (99.9%)
$DyCl_3 \cdot 6H_2O$	Sigma Aldrich (99.9%)
$HoCl_3 \cdot 6H_2O$	Sigma Aldrich (99.9%)
$ErCl_3 \cdot 6H_2O$	Sigma Aldrich (99.9%)
$YCl_3 \cdot 6H_2O$	Acros Organics (99.9%)